The Dissertation Committee for Claiborne Ott McPheeters certifies that this is the approved version of the following dissertation:

The Application of Light Trapping Structures and of InGaAs/GaAs Quantum Wells and Quantum Dots to Improving the Performance of Single-Junction GaAs Solar Cells

Committee:

Edward T. Yu, Supervisor

Andrea Alù

Seth Bank

Ray Chen

John Zhang

The Application of Light Trapping Structures and of InGaAs/GaAs Quantum Wells and Quantum Dots to Improving the Performance of Single-Junction GaAs Solar Cells

by

Claiborne Ott McPheeters, B.S.; M.S.

Dissertation

Presented to the Faculty of the Graduate School of

The University of Texas at Austin

in Partial Fulfillment

of the Requirements

for the Degree of

Doctor of Philosophy

The University of Texas at Austin

May 2012

Dedication

To my family and my friends

Acknowledgements

I am deeply indebted to my family. Mom and Dad, you provided me with all of the opportunities that a son could want. You gave me the support that I needed, let me pursue my interests, and gave me amazing resources for balancing and enriching my life. I love both of you. Sheridan, you are an amazing brother, and I am very proud of you. Hilary, George, and Diane, thank you for the good times we have shared and for supporting me. To all of you: though we are geographically separated, and that seems to become truer with time, it makes it that much better when we get together. I love y'all!

Education has been a central part of my life. I have had many excellent teachers, though I am most grateful to a handful of them. I credit Mike Gearen for making high school physics supremely interesting and rewarding. The same can be said of the late Bill Wilson and of Richard Baraniuk at Rice University, who dedicated themselves to teaching, and who taught fun, compelling courses. Jun Kono, at Rice, and Tobias Hertel, at Vanderbilt, were excellent advisors on my first forays into scientific research.

It has been a pleasure to work with Prof. Edward Yu. Ed, you are an outstanding thesis advisor and teacher. You provided guidance without restricting what I could do, and your insights helped me both to understand my work and to develop personally. I am tremendously thankful for everything that you have done for me and given to me.

During the past six years, I have developed many personally meaningful relationships. To those people whom I am referring, I am grateful for the time that we have spent together, and I look forward to sharing more.

I spent a lot of time working in graduate school, so it has been my pleasure to work with many outstanding people. This included lab mates: Daniel Derkacs, Swee Hoe

Lim, Peter Matheu, Jeremy Law, Sourobh Raychaudhuri, Keun Woo Park, Lei Zhu, Vaishno Dasika, Ping-Chun Li, Xiaohan Li, and Chengqing Hu; students from other groups: Winnie Chen, Wayne Chen, Jung Park, Arthur Zhang, Karun Vijayraghavan, Robert Adams, Chris Corbet, David Dillen, and Erica Krivoy; professors: S. S. Lau, Paul Yu, Deli Wang, and Seth Bank; and the staff of the Electrical Engineering departments at UCSD and at UT, including at Nano3 (UCSD) and at the MRC/MER (UT), who do fantastic jobs of supporting research activities at each university. I am thankful to my committee members for their advice, which has improved the quality of the work that appears in this dissertation and the document itself.

Finally, I am indebted to my collaborators, who have provided me with the semiconductor materials and supporting measurements necessary to make the solar cells that I work on. Many thanks to Dr. Dongzhi Hu and Prof. Dr. Daniel Schaadt at the Clausthal University of Technology, and Drs. David Ting, Cory Hill, and Sarath Gunapala at the Jet Propulsion Laboratory. It has been a pleasure working with all of you, and I hope that we will have more opportunities to do so.

The Application of Light Trapping Structures and of InGaAs/GaAs Quantum Wells and Quantum Dots to Improving the Performance of Single-Junction GaAs Solar Cells

Claiborne Ott McPheeters, Ph.D.

The University of Texas at Austin, 2012

Supervisor: Edward T. Yu

High efficiency photovoltaic solar cells are expected to continue to be important for a variety of terrestrial and space power applications. Solar cells made of optically thick materials often cannot meet the cost, efficiency, or physical requirements for specialized applications and, increasingly, for traditional applications. This dissertation investigates improving the performance of single-junction GaAs solar cells by incorporating InGaAs/GaAs quantum wells and quantum dots to increase their spectral response bandwidth, and by incorporating structures that confine light in the devices to improve their absorption of it. InGaAs/GaAs quantum dots-in-wells extend the response of GaAs homojunction devices to wavelengths >1200 nm. Nanoparticles that are randomly deposited on the top of optically thick devices scatter light into waveguide modes of the device structures, increasing their absorption of electromagnetic energy and improving their short-circuit current by up to 16%. Multiply periodic diffractive structures have been optimized using rigorous software algorithms and fabricated on the back sides of thin film quantum dot-in-well solar cells, improving their spectral response at wavelengths 850 nm to 1200 nm, where only the quantum dot-in-well structures absorb light, by factors of up to 10. The improvement results from coupling of diffracted light to

waveguide modes of the thin film device structure, and from Fabry-Perot interference effects. Simulations of absorption in these device structures corroborate the measured results and indicate that quantum well solar cells of ~2 μm in thickness, and which are equipped with optimized backside gratings, can achieve 1 Sun Airmass 0 short-circuit current densities of up to ~5 mA/cm^2 (15%) greater than GaAs homojunction devices, and of up to >2 mA/cm^2 (7%) greater than quantum well devices, with planar back reflectors. A combination of Fabry-Perot interference and diffraction into waveguide modes of the thin devices is shown to dominate the simulated device response spectra. Simulations also demonstrate the importance of low-loss metals for realizing optimal light trapping structures. Such device geometries are promising for reducing the cost of high efficiency solar cells that may be suitable for a variety of traditional and emerging applications.

Table of Contents

List of Tables

List of Figures

Chapter 1: The Physics and Operation of Solar Cells

1.1. INTRODUCTION

Electricity is increasingly embedded in modern civilization, with electronics enabling many of the communication and information technologies we rely on. For many years, electricity has been generated predominantly by the combustion of hydrocarbon-based fuels, such as coal and oil. In recent decades, however, concern over gaseous and particulate emissions from the combustion of hydrocarbons, significant accidents retrieving and transporting these fuels, and volatility in the price of oil, have generated interest in alternative sources of energy. An important set of these are renewable sources, which occur and are sustained as part of a natural cycle. Solar energy is one such source, and converting it to electricity is most directly achieved via the photovoltaic effect, on which solar cells are based.

Among alternative energy sources, solar is compelling for numerous reasons. In recent history, approximately 16 terawatts (TW) of electricity are consumed worldwide,[1] while, on average, about 24,800 TW of electromagnetic power are incident on Earth.[2] Energy consumption is greatest during daylight hours, when solar-generated power can be readily consumed. Solar cells can be used for distributed and centralized power generation and can scale from a few watts for personal electronics to megawatts in utility-level installations. Some are flexible and can be attached to movable objects, such as tents or backpacks, to charge mobile electronics. And, though adoption of transportation based on electrically-driven systems continues slowly, even planes powered by photovoltaic cells have been demonstrated.[3-5] Because of their versatility, solar cells are expected to find a diverse range of uses.

In addition to their possibilities for terrestrial use, solar cells have historically been, and remain, important for powering equipment in space and equipment for extra-terrestrial exploration, including the International Space Station and NASA's Mars Exploration Rovers. Solar cells are attractive for use in space because the availability of sunlight is predictable.

For both terrestrial and space purposes, there is a desire to increase the efficiency and robustness of solar cells while minimizing their cost. This has guided the development of *thin film* solar cells, which consume relatively little material in manufacturing, helping to keep their cost relatively low. Thin films are amenable to flexible device geometries and are generally more mechanically robust than thick films, which are rigid and, often, brittle. A thin device typically does not absorb as much light as a thick device, however, and techniques to improve their absorption are an important area of research and development.

Nanotechnology-based solar cells are also receiving a great deal of attention for their potential to reach high efficiencies and, in some cases, low cost. Most of these device technologies are relatively immature and are not yet ready for development; however, they garner significant interest because theoretical calculations indicate that they can achieve higher efficiencies than traditional solar cells based on bulk materials. As with thin film devices, however, the limited volume of absorbing material in nanostructured solar cells may limit light absorption.

This dissertation is broadly about solar cells that incorporate semiconductor nanostructures and photonic structures to improve light absorption and, ultimately, efficiency. Specifically, it investigates the ability of photonic structures to improve absorption of light that is achieved by inclusion of nanostructures in traditional devices. The devices that have been investigated are all solid state solar cells that convert

electromagnetic energy to electrical energy by the photovoltaic effect. As will be discussed, the solar cells presented in this dissertation are potentially useful for both terrestrial and space applications.

This chapter presents several topics that are important to understanding the work discussed in subsequent chapters. Fundamental concepts from solid state physics are presented before discussing the operation of solar cells. Optical properties of solid state materials are then presented, followed by discussion of theoretical limits of energy conversion in solar cells and the potential of novel devices with nanostructured materials to exceed traditional device limits. Finally, techniques to realize such devices are briefly discussed.

1.2. THE PHYSICS OF SOLID STATE DEVICES

Semiconductors are fundamental to modern electronic devices because of their ability, as the name implies, to conduct electricity in some situations and to act as insulators in others. Electrons are obviously essential to current flow, but so are holes, which are vacant electronic states in the valence band of a material which carry a positive charge and interact with electrons electrostatically. Collectively, electrons and holes are *charge carriers*. At the atomic level, the wave and particle properties of charge carriers are both important, including their *wavevectors* ($\mathbf{k}_e$, $\mathbf{k}_h$ for electrons and holes, respectively; where they appear, subscripts of 'e' and 'h' denote "electron" and "hole" unless otherwise specified), which are defined as

$$|\mathbf{k}| = \frac{2\pi}{\lambda}, \tag{1.1}$$

and λ is the wavelength of the particle. In many instances, a scalar k appears in expressions for simplicity, though the expressions apply to each component of $\mathbf{k}$.

As the term "wavevector" implies, the wave nature of charge carriers can be very important. An essential quantity in this respect is the *wavefunction*, denoted $\psi(\mathbf{k}, \mathbf{r})$, which contains probabilistic information about a particle at position $\mathbf{r}$ in a crystal. The wavefunction of a particle is a probability distribution with the property that

$$\int_V \psi^* \psi \, d\mathbf{r} = 1, \tag{1.2}$$

where * denotes the complex conjugate and the integral is performed over the volume of the crystal. Thus, the definition of the wavefunction requires that a particle be contained within a finite volume, but the particle may be distributed spatially by its wave nature, contrasting with the localized view of a particle.

A material's crystal lattice strongly influences the properties of its charge carriers, which are closely connected to its electronic and optical properties. A free particle has a sinusoidal wavefunction of the form

$$\psi(\mathbf{k}, \mathbf{r}) A \exp(i\mathbf{k} \cdot \mathbf{r}) + B \exp(-i\mathbf{k} \cdot \mathbf{r}). \tag{1.3}$$

The atoms of a crystal lattice impose a spatially-dependent electrostatic potential, $V(\mathbf{r})$, on carriers through electrostatic interactions, and this potential is periodic with the same periodicity as the lattice, which is illustrated in Fig. 1.1. If the lattice has a spatial period of $\mathbf{R}$, then the potential is periodic such that $V(\mathbf{r}) = V(\mathbf{r} + \mathbf{R})$. According to Bloch's Theorem, a particle in a periodic potential occupies a Bloch state, denoted $u(\mathbf{k}, \mathbf{r})$, where, $u(\mathbf{k}, \mathbf{r}) = u(\mathbf{k}, \mathbf{r} + \mathbf{R})$. Bloch's Theorem further states that the wavefunction of a particle in a periodic potential has the form of periodic Bloch wave modulated by a plane wave *envelope*:

$$\psi(\mathbf{k}, \mathbf{r}) \propto \exp(\pm i\mathbf{k} \cdot \mathbf{r}) \, u(\mathbf{k}, \mathbf{r}). \tag{1.4}$$

This general form successfully describes the behavior of particles in solid state materials because they have periodic lattices. Deviations from a perfect lattice perturb the potential

function that charge carriers experience, affecting the electronic states that they can occupy and their wavefunctions. Perturbation theory is an approach to calculating the effect of such modifications of an ideal potential function or other parameter by using the matrix formulation of quantum mechanics, which is briefly introduced in Appendix 1. Such perturbations, though they may occur at near-atomic scales, affect the aggregate properties of electronic and optoelectronic devices in significant ways. The influence of several effects, such as spatial confinement of carriers and the application of external electrostatic fields, will be discussed in this work.

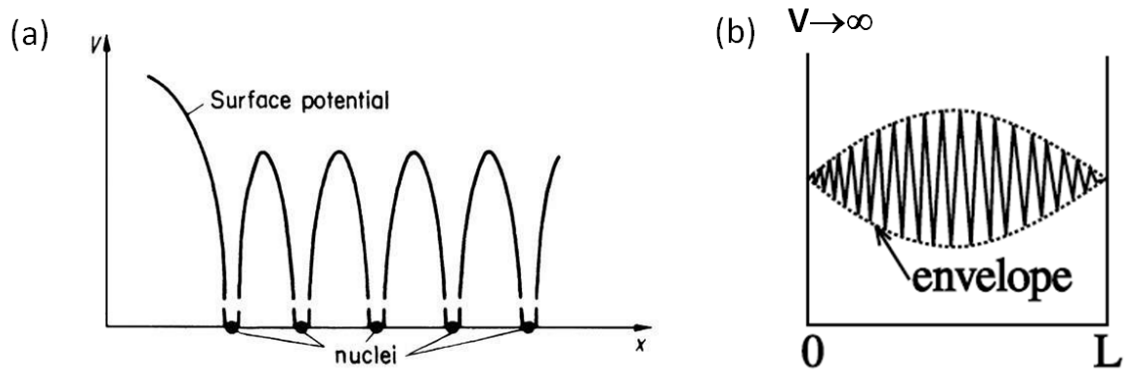

Figure 1.1: (a) An illustration of the periodic potential function experienced by an electron in a linear (one dimensional) crystal lattice. A real crystal can be represented by extending this model to three dimensions. (b) The wavefunction of a particle in a Bloch state in a potential well, where the potential is zero between $x = 0$ and $x = L$ and becomes infinitely large at those points.

Semiconductors, like all crystalline materials, consist of bands of electronic states that result from the interactions of bonded atoms in its crystal lattice. In a semiconductor with no impurities or defects, and at temperature T = 0 K, the highest occupied energy band has all of its states filled by electrons and is called the "valence band," while the next highest band is empty and is called the "conduction band." Using a common, though

over-simplified, treatment of electronic bands as parabolic in shape allows the following simple relation:

$$E(\mathbf{k}) = \frac{\hbar^2 \mathbf{k}^2}{2m}, \tag{1.5}$$

where E is energy and m is the free electron mass. As just discussed, however, particles in a semiconductor lattice are not free and electrostatic interaction of electrons and the ionic nuclei of the lattice atoms, and of electrons with each other, frequently cause electrons to behave as if they are lighter than a free electron. The mobility of electrons within bands varies with their direction of motion based on the geometry of bonds in the crystal, which causes charge carriers to appear to have different masses along different crystal axes. For these reasons, $m*$ often appears instead of m to denote the *effective mass* of charge carriers. Based on anisotropy in the crystal, the effective mass may be different along different spatial dimensions, and is generally written $\mathbf{m}^* = (m_x^*,\ m_y^*,\ m_z^*)$.

Charge carriers undergo regular changes in energy, E, and momentum, $\mathbf{k}$, through a variety of mechanisms. These include particle-particle, particle-lattice, and particle-photon interactions, which may occur because of electrostatic, thermal, or electromagnetic perturbations. At finite temperature, electrons acquire heat energy from the surrounding crystal lattice via interactions with *phonons*, which are collective vibrations of the atoms in the lattice that also have wave- and particle-like properties. Electrons can collide with each other, transferring kinetic energy in the process, and they can absorb the energy of photons comprising electromagnetic radiation, which is the essence of the photovoltaic effect. Each of these interactions can cause an electron to move to a different electronic state if it provides sufficient energy. Transitions within an electronic band (*intraband* transitions) require changes in $\mathbf{k}$, which correspond to changes in momentum ($\mathbf{p}$), because $\mathbf{p} = \hbar\mathbf{k}$. Different electronic bands, such as the valence band

and the conduction band, have states with equivalent momentum (i.e., **k** values) but different energies. Thus, *interband* transitions require a change in energy, and, depending on the band structure, they may or may not require a change in momentum. Electron-phonon interactions and collisions between particles generally change the momentum of the interacting particles; however, the momentum of photons is negligible compared to that of particles with mass. Therefore, electron-photon interactions essentially change the energy of particles but not their momentum.

Though energy bands are parabolic, many electronic and optical phenomena occur through transitions between states at and near the minimum energy (the *band edge*) of electronic bands, since carriers tend to occupy the lowest energy state available. Between the conduction and valence band edges, there is a set of energies where no electronic states exist called the *bandgap*, and it is often denoted by its magnitude, E_g, which equals the separation in energy between the conduction band edge (E_c) and valence band edge (E_v). In a *direct bandgap* semiconductor, the minima in the conduction and valence bands occur at the same value of **k**, which is taken as **k**=0:

$$E_g = E_c(0) - E_v(0). \tag{1.6}$$

With *indirect bandgap* semiconductors, the conduction and valence band minima occur at different values of **k**, which are taken as $\mathbf{k}_2 \neq 0$ and $\mathbf{k}_1 = 0$, respectively:

$$E_g = E_c(\mathbf{k}_2) - E_v(0). \tag{1.7}$$

A change in **k** of a particle corresponds to a change in its momentum, and this signals an important difference in devices made of direct and indirect bandgap materials: transitioning across the bandgap in an indirect gap material requires a change in the momentum of an electron, while it does not in a direct bandgap material. This is especially important for optical devices, including solar cells, because absorption of a photon alone imparts very small $\Delta\mathbf{k}$ that, on its own, is insufficient to change the

momentum of a particle. As illustrated in Fig. 1.2, an indirect transition requires that the electron absorbs a photon and a phonon to gain the required energy and momentum. If the photon and phonon interactions do not occur nearly simultaneously, then light is not absorbed. The result is that indirect bandgap materials typically absorb light more weakly than direct bandgap materials, particularly at energies near the bandgap (E_g).

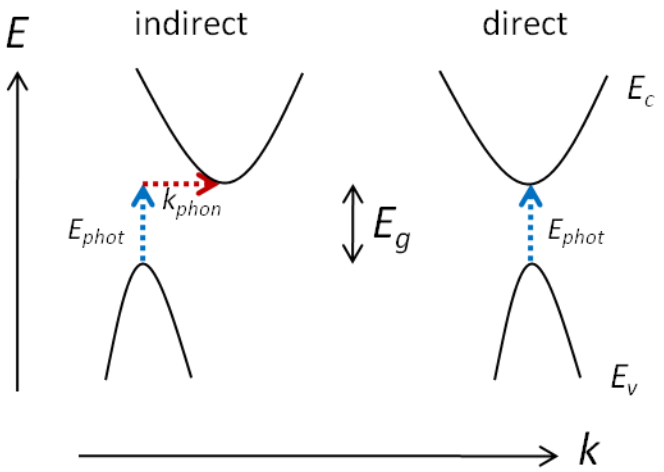

Figure 1.2: Indirect (left) and direct bandgap (right) semiconductor band diagrams with the same bandgap energy (E_g). Transitions across the indirect bandgap require energy from a photon (E_{phot}) and momentum from a phonon (k_{phon}), while just a photon is sufficient for a direct gap transition.

Because of the importance of the band edge states, it is assumed herein that all energy band diagrams represent states at the band edges unless otherwise stated or shown. For example, Fig. 1.3 shows a band diagram for an *intrinsic* (i.e., a crystalline material with no defects or impurities) semiconductor, where the horizontal axis corresponds to spatial position and the vertical axis to energy. On the low side of the energy scale is the valence band edge, at energy E_v, and on the high side is the conduction band edge, at energy E_c. In between the two, at energy E_F, is the *Fermi energy*, which

marks the energy at which there is a 50% probability of an electronic state being occupied by an electron. E_F can lie within the bandgap, where there are no states, because it is a statistical value rather than an actual energy state. Electrons, being fermions, obey Fermi-Dirac statistics, which gives the probability for an electronic state at energy E to be occupied via the Fermi-Dirac distribution function:

$$f_{FD}(E) = \frac{1}{\exp\left[\frac{E - E_F}{k_B T}\right] + 1}, \tag{1.8}$$

where k_B is the Boltzmann constant, and T is the absolute temperature of the material, which is assumed to be in thermodynamic equilibrium.

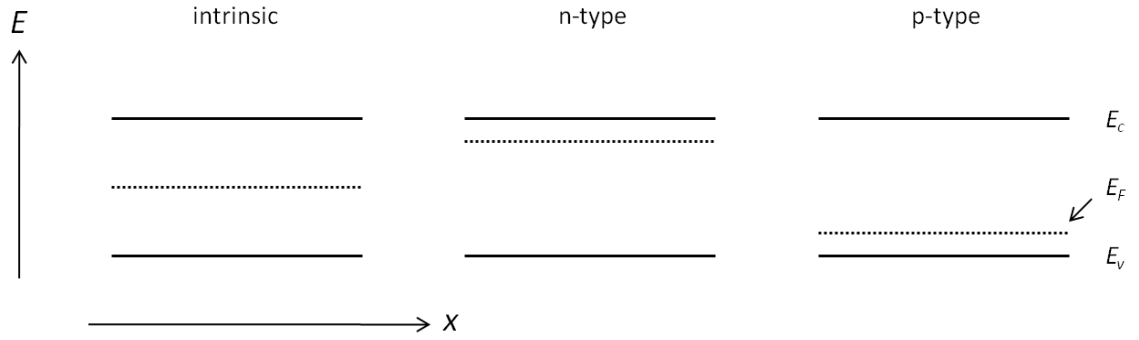

Figure 1.3: Band edge diagrams of (left, "intrinsic") an undoped semiconductor and of a semiconductor doped with (middle, "n-type") electron donor atoms or (right, "p-type") electron acceptor atoms. The Fermi energy (E_F) is close to the middle of the bandgap in intrinsic material and it shifts toward the conduction band edge (E_c) and the valence band edge (E_v) in *n*-type and *p*-type material, respectively.

Though the concept of the Fermi energy is straightforward, many details of the band structure of a material affect its value. Within the energy bands, the total number, or *density of electronic states*, varies as a function of energy, and is denoted $g_e(E)$ and $g_h(E)$ for electrons and holes, respectively. In an intrinsic semiconductor, which contains no

foreign atoms (*impurities*), the number of electrons in the conduction band (n) equals the number of holes in the valence band (p):

$$n = \int_{E_c}^{\infty} g_e(E) f_{FD}(E) dE = p = \int_{-\infty}^{E_v} g_h(E)[1 - f_{FD}(E)] dE \,. \tag{1.9}$$

In bulk materials, with dimensions on the order of one micron or larger,

$$g(E) = \frac{\sqrt{2}}{\pi^2 \hbar^3} m^{*3/2} E^{1/2}, \tag{1.10}$$

and, using the Boltzmann approximation of

$$f_{FD}(E) \approx \exp\left(-\frac{E - E_F}{k_B T}\right), \tag{1.11}$$

expressions for the carrier concentrations become:

$$n = \int_{E_c}^{\infty} g_e(E) f_{FD}(E) dE \equiv N_c \exp\left(-\frac{E_c - E_F}{k_B T}\right) \tag{1.12}$$

$$p = \int_{-\infty}^{E_v} g_h(E)[1 - f_{FD}(E)] dE \equiv N_v \exp\left(-\frac{E_F - E_v}{k_B T}\right), \tag{1.13}$$

where N_c and N_v are the *effective density of states* for electrons and holes, respectively. At room temperature (T = 300 K), $k_B T \approx 0.026$ meV, which is quite small, so $E - E_F \gg k_B T$ is satisfied and the Boltzmann approximation is reasonable.

The Fermi energy relates to the population of electrons and holes, which depends on energy transfer to and between charge carriers. In an intrinsic semiconductor in thermal equilibrium, heat excites electrons from the valence band to the conduction band and the number of electrons in the conduction band equals the number of holes in the valence band. Equating Eqs. 1.12 and 1.13,

$$N_c \exp\left(-\frac{E_c - E_F}{k_B T}\right) = N_v \exp\left(-\frac{E_F - E_v}{k_B T}\right). \tag{1.14}$$

Using the definitions of N_c and N_v, which depend on $g(E)$, the previous expression can be stated:

$$\exp\left(\frac{2E_F - (E_c + E_v)}{k_B T}\right) = \frac{N_v}{N_c} = \left(\frac{m_h^*}{m_e^*}\right)^{\frac{3}{2}}. \quad (1.15)$$

Solving for E_F yields

$$E_F = \frac{E_c + E_v}{2} + \frac{3}{4} k_B T \ln\left(\frac{m_h^*}{m_e^*}\right), \quad (1.16)$$

which shows that in an intrinsic semiconductor at thermal equilibrium, the Fermi level lies at or near the middle of the bandgap.

Controlling the Fermi level in a material is a means of controlling its conductivity, which is an important part of electronic device engineering. It can be seen in Eq. 1.16 that temperature influences the Fermi level; however, the most practical method to control electrical properties of a semiconductor is to *dope* it with foreign atoms (impurities) by incorporating them in the crystal lattice. In crystalline silicon, which has four valence electrons, each Si atom is covalently bonded to four other Si atoms in order to completely fill their partially-occupied, outermost valence orbitals. If a Si atom is replaced with an atom from Group III or lower on the periodic table, having fewer valence electrons than Si, then the crystal is deficient of valence electrons. This adds hole states (such impurity atoms are *electron acceptors*) to the valence band of the crystal, and the Fermi level shifts down in energy. Material doped in this manner is referred to as *p*-type. Alternatively, replacing a Si atom with an atom from Group V or higher adds valence electrons, and those that are not required for bonding with neighboring atoms in the valence band move to conduction band states as the valence band is full. Correspondingly, the Fermi level shifts up in energy in such *n*-type material. These effects are also illustrated in Fig. 1.3. Dopants are essential to engineering the electronic properties of semiconductors because their location and concentration within materials can be precisely controlled. Methods of doping solid-state materials include incorporation of dopants during epitaxial growth, ion implantation, and diffusion from gaseous, solid-state, and spin-on sources.

1.3. PRINCIPLES OF THE OPERATION OF SOLAR CELLS

Any semiconductor diode can function as a solar cell when it is illuminated and biased appropriately. A *p*-*n* junction diode consists of a *p*-type semiconductor joined atomically to an *n*-type semiconductor. For now, we assume that the semiconductors are the same material, with bandgap E_g. As the *p*-type material has an excess of positively charged holes and the *n*-type material has an excess of negatively charged electrons, when the two are atomically joined, the excess charge carriers diffuse in opposite directions to achieve thermal equilibrium. During this process, conduction electrons from the *n* side relax to lower energy hole states in the valence bands of atoms on the *p* side in a process called *recombination*. Diffusion of these charges constitutes current and results in negatively charged acceptor atoms that have acquired an extra valence electron, and positively charged donor atoms that have lost an electron, on the *p* and *n* sides, respectively. A voltage builds up as a result of the electrostatic forces between ionized donor and acceptor atoms and the associated electric field (the *drift field*) accelerates charge carriers in the direction opposite of diffusion, generating a *drift current* opposing the *diffusion current*. This process of carrier diffusion, drift, and recombination continues until a sufficient number of ionized donor and acceptor atoms are present around the *p*-*n* junction that the drift current is equal and opposite to the diffusion current, at which point, the device is said to be in equilibrium, and remains so in the absence of external perturbations. The area near the junction, where mobile charge carriers have recombined and left ionized impurity atoms, is the *depletion region* or *space charge region*, and the built-in voltage across it is essential to the operation of diodes and solar cells.

All of the discussion until now has assumed that a device is in thermodynamic equilibrium, as illustrated in Fig. 1.4(a), which requires that no external forces produce variations in the local carrier concentration. Two examples of such forces are incident

light and an applied electrostatic field, which induce non-equilibrium conditions in which a single Fermi level cannot describe carrier populations. Instead, *quasi-Fermi levels* (QFLs) for electrons and for holes are used, and they are denoted E_{Fn} and E_{Fp}, respectively. A QFL identifies the energy at which the probability of finding its corresponding carrier is 50%.

When an electrostatic potential is applied between the *n* and *p* sides of a diode, the applied voltage, or *bias*, attracts electrons to the cathode while holes are attracted to the anode. At equilibrium, on the *n* side of a device, E_{Fn} is relatively near the conduction band edge and E_{Fp} is relatively near the valence band edge on the *p* side. When a positive potential is applied to the *p* side with respect to the *n* side, electrons on the *n* side and holes on the *p* side diffuse into the junction as the size of the potential barrier there decreases, as shown in Fig. 1.4(b). As the junction potential decreases with additional forward bias, the carriers diffuse further into it, increasing their spatial proximity and, therefore, increasing the probability of an electron and hole recombining. Thus, positive current flow in a diode consists of electrons and holes injected into the depletion region from the *n* and *p* sides, respectively, where they recombine.

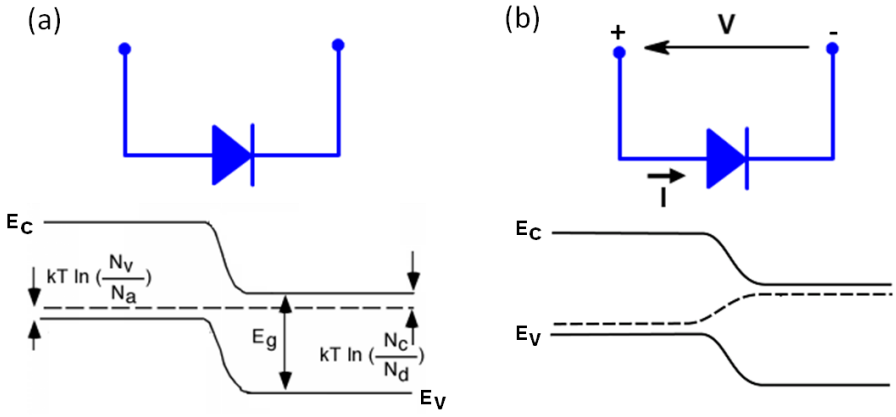

Figure 1.4: A *p*-*n* diode (a) at equilibrium, and (b) under forward bias, which reduces the junction potential so that electrons can be injected from the *n* side and holes can be injected from the *p* side, constituting positive current in the device.

At thermal equilibrium, the built-in voltage opposes carrier injection, though even if a solar cell is not biased (or, if a small reverse bias is applied) a small negative current exists at finite temperature because some electrons are thermally excited into the conduction band. If this occurs close enough to the depletion region that the minority carrier diffuses to it before recombining, then the electric field sweeps it to the other side of the junction, opposite to the direction of positive current. This is known as the *saturation current* of the device and it is denoted I_0. In the context of solar cells, this is a component of the *dark current*, which flows regardless of whether devices are illuminated. The relationship between current, I, and voltage, V, of an ideal diode is given by

$$I = I_0 \left[\exp\left(\frac{eV}{nk_BT}\right) - 1 \right], \tag{1.17}$$

where e is the fundamental electronic charge, n is the *ideality factor* of the diode, k_B is Boltzmann's constant, and T is the temperature. A plot of the *I*-*V* relationship of a diode in the dark is shown in Fig. 1.5(a).

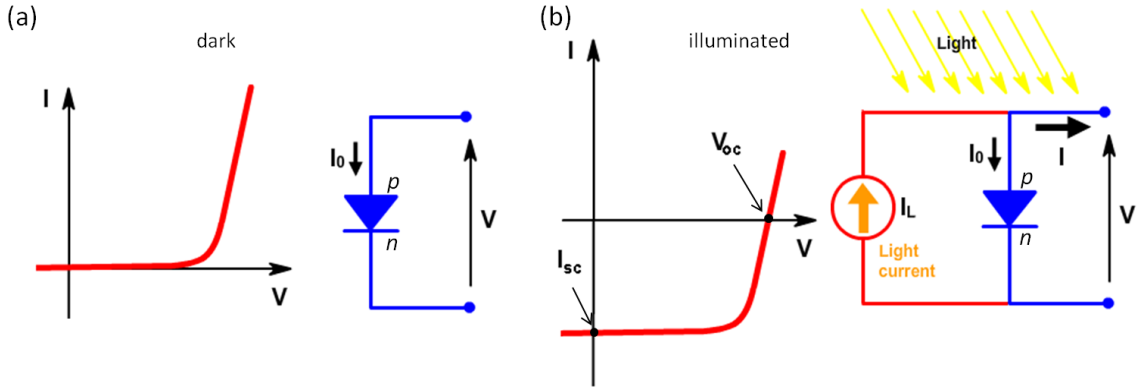

Figure 1.5: Current-voltage (I-V) curves of a diode (a) in the dark and (b) under illumination. Under illumination, the negative current produced at positive bias typifies energy conversion in a solar cell. At high level current injection, corresponding approximately to voltages $V > V_{mp}$, voltage loss due to the series resistance in a diode can be significant, producing the relatively linear character of $I(V)$ seen at large bias voltages in the figure.

The ideality factor is an important parameter that relates to recombination in diodes. In an ideal diode, recombination occurs only in the neutral (n- and p-type) regions of the device (i.e., not in the junction) when an electron relaxes from a conduction band state directly to a valence band state, or by relaxing through a *trap* state at an energy level within the bandgap of the semiconductor. Traps exist because of impurities or defects in the crystal lattice (e.g., *vacancies*, which are locations where atoms are missing and "dangling bonds" on neighboring atoms create low energy states). When carriers relax through direct band-to-band or trap-assisted transitions, this is called *Shockley-Read-Hall* (SRH) recombination. At low bias, few carriers are injected into the junction due to the potential barrier, and carriers recombine in the quasi-neutral regions in a situation that is described by $n = 1$. If recombination in the junction dominates current flow, this is described by $n = 2$, which only occurs at relatively high bias in an ideal diode, when a large number of carriers are injected into the junction. If defects, interfacial states, or

other material issues facilitate junction recombination at lower bias, then current will "leak" through the junction at lower voltages and its ideality factor will be between 1 and 2, indicating non-ideal rectification. Indeed, no real diode performs ideally, and they all have ideality factors between 1 and 2.

When a diode is illuminated by light consisting of photons with energy $E_{ph} > E_g$, carriers are *photogenerated* due to electrons absorbing photons. As with thermally generated carriers, minority photogenerated carriers diffuse toward the depletion region and, on average, reach it before recombining if the junction is located within the *diffusion length* of the carriers. At the junction, carriers are accelerated across the depletion region to the opposite side by the built-in field, which is referred to as carrier *collection*. This *photocurrent*, like the thermally-generated current, is negative in sign, and it is generated as long as the built-in potential is large enough to collect the carriers.

The current-voltage product, $I \times V$, of a solar cell must be negative to produce power, and the functional relationship $I(V)$ indicates much about device performance. Many devices, including solar cells, vary considerably in size, so it is common to refer to current density, J, which is current per unit area of a device. Converting from I to J simply involves dividing or multiplying by the area of a solar cell, respectively. At zero bias, the point on the *I-V* plot of a solar cell is known as the *short-circuit current* (I_{sc}), as indicated in Fig. 1.5(b). The photocurrent of a device under illumination, I_L, is typically much larger than its saturation current even for modest illumination that is much less than the intensity of the sun (i.e., $I_L >> I_0$), and the result is that the *I-V* curve of an illuminated solar cell ideally looks much like its *I-V* curve in the dark, but with the whole curve shifted in the negative direction of the current axis by the amount $-I_L$, as seen in Fig. 1.5(b). At some value of forward bias, the electrically injected forward current equals the magnitude of the reverse photocurrent and the net current through the device is

zero; this is the *open-circuit voltage* (V_{oc}). At voltages between zero and V_{oc}, a solar cell generates power, and its maximum occurs at the maximum power point, (V_{mp}, I_{mp}), where $I \times V$ is largest. In order to achieve optimal performance, solar cells should be operated at their maximum power point, which corresponds to the most efficient conversion of light-to-electrical power conversion.

The efficiency of a solar cell is determined by its ability to absorb electromagnetic radiation and convert that energy to electricity. The power conversion efficiency, η, equals the ratio of output electrical power (P_{out}) to total incident electromagnetic power (P_{in}). Assuming operation at the maximum power point, the efficiency of a solar cell is given by

$$\eta = P_{out}/P_{in} = I_{mp}V_{mp}/P_{in}. \tag{1.18}$$

The efficiency can also be expressed in terms of V_{oc} and I_{sc} as

$$\eta = P_{out}/P_{in} = I_{mp}V_{mp}/P_{in} = FF \times V_{oc}I_{sc}/P_{in} \tag{1.19}$$

where FF is the *fill factor* of the device, and is given by

$$FF = V_{mp}I_{mp}/V_{oc}I_{sc}. \tag{1.20}$$

The fill factor represents the fraction of power that a solar cell generates compared to the amount that would be generated if it could operate at (V_{oc}, I_{sc}). The $I \times V$ product is always less than $I_{sc} \times V_{oc}$, so the FF is always less than unity. Inspecting Eq. 1.19, however, it is evident that higher values of the FF improve power conversion efficiency.

The fill factor is in fact a measure of the quality, or ideality, of the diode, with more ideal/higher quality devices having larger fill factors. Fig. 1.6 demonstrates an equivalent circuit for a solar cell, which features a diode, a photogenerated current in the reverse direction that is non-zero when the diode is appropriately illuminated, and two resistors, one of which is in series (R_s) and the other of which is in parallel with the diode (R_{sh}, also known as *shunt resistance*). Ideally, $R_{sh} = \infty$ and no current flows in the forward

direction until adequate bias is applied for carriers to surmount the junction potential. Finite R_{sh} allows current to "leak" through the diode junction; however, in practice, values of R_{sh} of ~1 kΩ and larger produce nearly ideal behavior. Conversely, an ideal diode has $R_s = 0$, but a real diode has series resistance associated with carrier transport through the junction, through the *n*- and *p*-type regions, and through the electrical contacts to the diode. In practice, values of R_s up to several mΩ do not significantly degrade device performance. Low shunt resistance is most detrimental at low current levels, when leakage of carriers through the junction causes the current to increase at voltages below an ideal device's turn-on voltage, rounding the knee of the *I-V* curve and reducing the *FF*. Series resistance causes voltage loss, which linearizes the *I-V* curve and reduces the *FF*; it is most pronounced at high levels of electrical carrier injection, at voltages between V_{mp} and V_{oc}. These effects are illustrated in Fig. 1.7, which show how they reduce the fill factor of a solar cell. Because they degrade the performance of an ideal device, R_s and R_p are collectively known as *parasitic resistance*, and mitigating their effect is an important aspect of cell design.

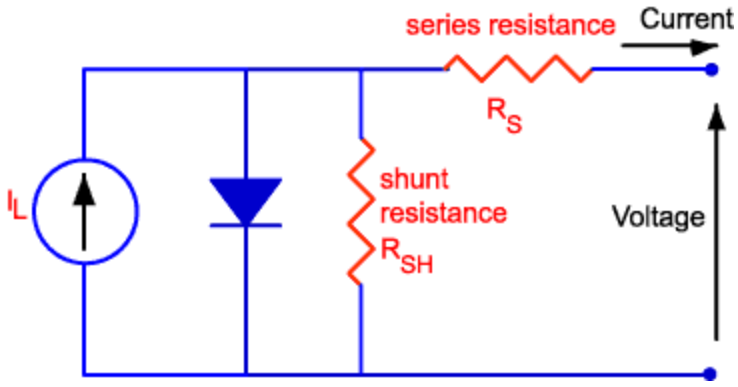

Figure 1.6: The equivalent circuit of a solar cell, indicating parasitic resistance in series (R_s) and in parallel (R_{sh}).

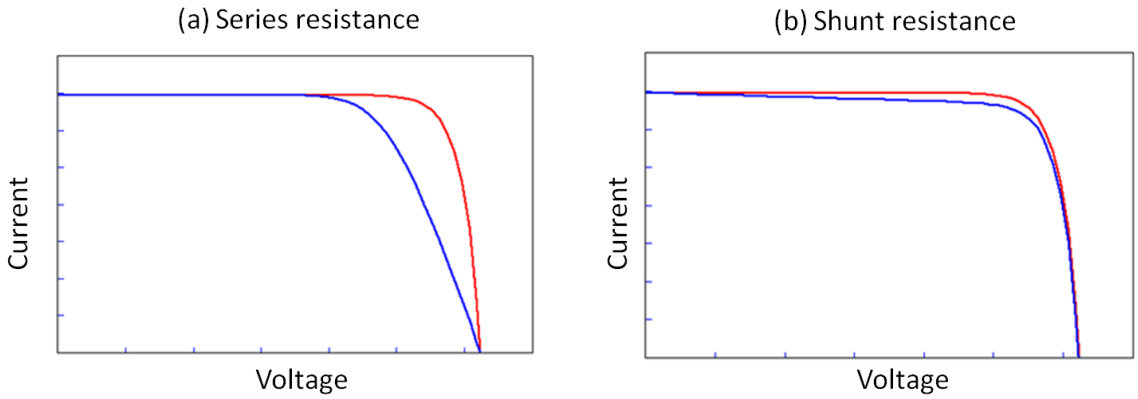

Figure 1.7: Effects of (a) series resistance, which linearizes the *I-V* curve; and (b) shunt resistance, which increases the roundness of the *I-V* curve and can reduce the open-circuit voltage. R_s and R_{sh} both reduce the fill factor.

Two other fundamental figures of merit for solar cells are *spectral response* and *quantum efficiency*. The spectral response is a measure of the photocurrent generated by a device at individual wavelengths. By integrating the product of the spectral response, $SR(\lambda)$ [A/W], and the irradiance, $I(\lambda)$ [W/cm^2/nm], the current density of a device is obtained:

$$J = \int SR(\lambda) \times I(\lambda) d\lambda. \tag{1.21}$$

Quantum efficiency (QE), which is also a function of wavelength, is a measure of the number of electron-hole pairs that are produced per absorbed photon. *External quantum efficiency*, $EQE(\lambda)$, refers to the QE when optical losses due to reflected and transmitted light are included, while *internal quantum efficiency*, $IQE(\lambda)$, excludes them; therefore, $IQE \geq EQE$. $IQE < 1$ indicates recombination loss, and efficient devices exhibit IQE near unity at most wavelengths shorter than that corresponding to their band edge ($\lambda_g = hc/E_g$), where c is the speed of light in vacuum. Notable exceptions include lower QE values at short wavelengths, for which carriers are generated near the top surface of a device where the recombination velocity is high, and at long wavelengths immediately

near the absorption edge, corresponding to the bandgap energy, where the QE of a good device decreases sharply to zero. As inaccuracy is easily introduced in device reflectivity measurements, such as non-detection of diffuse reflections and inclusion of reflection from contacts instead of the semiconductor surface, *EQE* may be more confidently measured, and is a useful measure of both light absorption and carrier collection

1.4. LIGHT-MATTER INTERACTIONS

Interactions between light and the materials that constitute a solar cell play significant roles in the energy losses experienced by the device, which necessitates careful engineering to maximize optical and electrical performance. Everyone experiences certain optical phenomena that occur all around us, such as reflection, refraction, and transmission of light, which determine how we view our surroundings. In fact, these phenomena are aggregate effects of the fundamental process of *scattering* of light. When radiation is incident on matter, it causes electrons and protons to oscillate, and the associated acceleration of the charges results in emission of electromagnetic radiation, which is the scattered light. Simultaneously, some of the energy transferred to the oscillating charges is dissipated as heat. Energy which is transferred from the incident light and not re-emitted as light is therefore *absorbed* by the scattering medium.

At the macroscopic scale, scattering is responsible for the bulk optical properties of materials, such as reflection, refraction, and transmission. The bulk optical properties of a material are described by its *complex refractive index*, $\tilde{n}$, given by

$$\tilde{n}(\lambda) = n(\lambda) + i\kappa(\lambda), \tag{1.22}$$

where n is the *refractive index* and κ is the *extinction coefficient*. n describes how light waves are retarded when they propagate through different media, and κ is a measure of

their attenuation by the medium. When light of intensity I propagates through an absorbing medium ($\kappa > 0$), it is attenuated according to the distance, z, it propagates:

$$I(z) = I_0 \exp(-\alpha z), \tag{1.23}$$

where $I(z = 0) \equiv I_0$ and α is the *absorption coefficient*

$$\alpha = \frac{2\kappa\omega}{c} = \frac{4\pi\kappa}{\lambda}. \tag{1.24}$$

Equivalently, the bulk optical properties of a material are defined by its *dielectric function*, or *relative permittivity*, ϵ_r:

$$\epsilon_r(\lambda) = \epsilon_1(\lambda) + i\epsilon_2(\lambda) \tag{1.25}$$

where

$$\epsilon_1 = n^2 - \kappa^2 \tag{1.26}$$

and

$$\epsilon_2 = 2n\kappa. \tag{1.27}$$

The total permittivity of a material is then

$$\epsilon = \epsilon_r \epsilon_0, \tag{1.28}$$

where $\epsilon_0 = 8.854 \times 10^{-12}$ Farads/m is the permittivity of vacuum. The components of the complex refractive indices of GaAs and InAs are shown in Fig. 1.8 as an example.

The real and imaginary components of the dielectric function (and, equivalently, of the complex refractive index) are related by what are known as Kramers-Kronig relations. These relations encapsulate the principle of causality, which states that the response of a material to a perturbing force may not precede the perturbation. While this statement is intuitively evident, mathematically, it implies that the real and imaginary components of the optical response function of a material are related. Their relationship is given by a pair of Kramers-Kronig relations, which, for the refractive index and extinction coefficient, in terms of one another, are:

$$n(\omega) = 1 + \frac{1}{\pi} P \int_{-\infty}^{\infty} \frac{\kappa(\omega')}{\omega' - \omega} d\omega' \tag{1.29}$$

$$\kappa(\omega) = -\frac{1}{\pi} P \int_{-\infty}^{\infty} \frac{n(\omega') - 1}{\omega' - \omega} d\omega'. \tag{1.30}$$

A similar pair of Kramers-Kronig relations relate the real and imaginary parts of the dielectric function of a material.

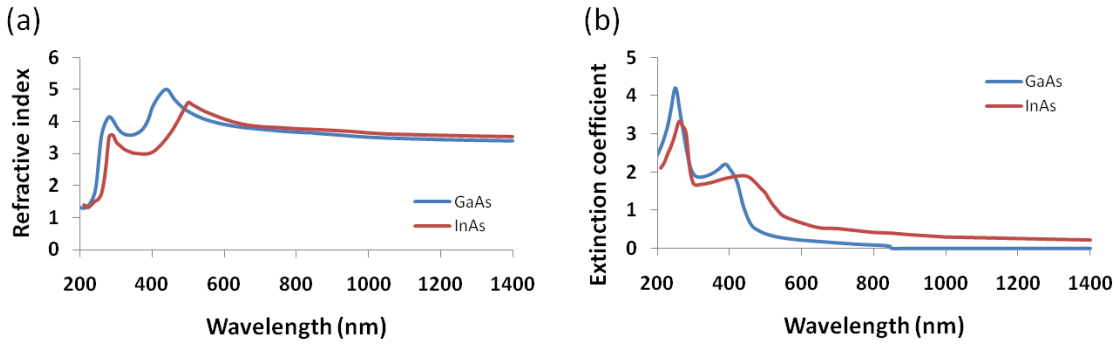

Figure 1.8: (a) The refractive indices, n, and (b) the extinction coefficients, κ, of GaAs (blue line) and InAs (red line), which are similar in value at wavelengths which are relevant to solar performance. Notably, however, $\kappa_{InAs} > 0$ to $\lambda = \sim 3.4$ μm, enabling it to absorb a much broader spectrum of wavelengths of light than GaAs, which has an absorption edge of 850 nm corresponding to $\kappa_{GaAs} = 0$.

While scattering of light occurs at the atomic scale, the aggregate effect of scattering by many particles gives rise to bulk optical properties. In solid state materials, the crystal lattice is highly ordered and all of the atoms scatter light in essentially the same way. Thus, when the atoms are illuminated simultaneously, the scattered field from each is largely coherent with the rest. Light that emerges in the half-plane containing the incident field is *reflected* while light that emerges in the opposite half-plane is

transmitted. Any incident power not accounted for by the reflected and transmitted fields is absorbed. The coherently scattered fields at a planar interface produce *specular* reflection, where the incident and reflected rays have equal angles with respect to the surface normal. This is the type of reflection we see from mirrors, and such materials obey the Fresnel laws of reflection and transmission and Snell's law for refraction of light.

The opposite of specular reflection and transmission is *diffuse*, which describes light scattered by an inhomogeneous material or interface. If a material does not have a regular crystal lattice, the different orientations of atoms correspond to randomly oriented dipoles that scatter light in different directions. If the surface height of a material varies, the facets can produce specular reflection in multiple directions, which, in aggregate, appear diffuse. If surface features vary over distances on the order of the wavelength of light or smaller, an incident wave arrives at the surface at slightly different times. The phase differences between the scattered waves result in constructive or destructive interference, which, combined with the broad angular distribution of scattered light, can produce complicated reflection and transmission characteristics.

The absorption of photons is a statistical process, which is why attenuation of light increases with its distance of propagation in a medium, as seen in Eq. 1.23. Absorption and emission of light involve *radiative transitions* of electrons, which are governed by Fermi's Golden Rule. The quantum mechanical nature of this relationship underlies the statistical nature of absorption:

$$W_{ij} = \frac{2\pi}{\hbar}\left(\frac{eE_0}{m_0\omega}\right)^2 |\langle j|\hat{\mathbf{p}}\cdot\mathbf{e}|i\rangle|^2 g\left(E_j - E_i - \hbar\omega\right), \tag{1.31}$$

where W_{ij} is the radiative transition rate; $|i\rangle$ and $|j\rangle$ are the initial and final electronic states; e is the electronic charge; E_0 is the electric field intensity; m is the mass of the

particle; $\hat{\mathbf{p}}$ is the momentum operator; **e** is the polarization of the incident radiation; and $g(E)$ is the joint density of states. The strength of the oscillator term, $|\langle j|\hat{\mathbf{p}}\cdot\mathbf{e}|i\rangle|^2$, depends on the symmetry of atomic orbitals that comprise valence and conduction band states in the material via the operator $\hat{\mathbf{p}}$.

When a photon is absorbed, the electron and hole are in close spatial proximity immediately after photo-generation, and their opposite electric charges experience Coulombic attraction to each other with an associated *binding energy*. A bound electron-hole pair, or an *exciton*, has properties that are similar to those of a hydrogen atom. The excitonic binding energy is:

$$E_{\mathrm{n}} = -\frac{\mu}{m_0}\frac{1}{\epsilon_r^2}\frac{R_H}{n^2} = -\frac{R_X}{\mathrm{n}^2} \tag{1.32}$$

where E_{n} is the binding energy; n is the exciton level index; m_0 is the rest mass of an electron; ϵ_r is the relatively permittivity of the material; R_H is the Rydberg constant of the hydrogen atom (R_H = 13.6 eV); R_X is the exciton Rydberg constant, which varies by material (for example, R_X = 0.0042 eV in bulk GaAs at 300 K); and μ is the reduced mass of the electron-hole pair,

$$\mu = \left(\frac{1}{m_e^*} + \frac{1}{m_h^*}\right)^{-1}. \tag{1.33}$$

The radius of the exciton also has a similar form to that of the hydrogen atom:

$$r_{\mathrm{n}} = \frac{m_0}{\mu}\epsilon_r \mathrm{n}^2 a_H = \mathrm{n}^2 a_X, \tag{1.34}$$

where $a_H = 5.29\times10^{-11}$ m, which is the Bohr radius of the hydrogen atom, and a_X is the exciton Bohr radius ($a_H = 13\times10^{-9}$ m in bulk GaAs at 300 K).

In bulk materials, thermal energy at room temperature (300 K) and higher rapidly excites the electron and hole to higher energy levels in the continuum of states above the excitonic bound state, causing the exciton to dissociate into a free electron and a free hole, which can contribute to photocurrent in a solar cell. Excitonic effects are therefore

unimportant in most bulk devices at normal operating temperatures. In the devices studied in this work, it will be seen that excitonic effects become important when electrons are confined at length scales on the order of their de Broglie wavelength.

1.5. Theoretical Limits of the Performance of High Efficiency Solar Cells

The efficiency of a solar cell is a function of its absorption of light and collection of photogenerated carriers, which collectively determine the current and voltage it produces, and which can be hampered by numerous loss mechanisms. These mechanisms are classified as *intrinsic* if they are thermodynamically unavoidable, and otherwise as *extrinsic*, which result from non-ideal effects that are typically material- or process-related, including non-radiative recombination and parasitic resistance. Many theoretical calculations of device performance assume only intrinsic losses in order to determine the maximum efficiency of devices. In real solar cells, approaches to minimize intrinsic and extrinsic losses have been, and continue to be, widely investigated.

1.5.1. Loss Mechanisms in Solar Cells

An ideal solar cell would suffer only intrinsic losses, of which there are principally three, and they relate to its energy band structure and the spectrum of incident light. The first is that photons with energy $E_{ph} < E_g$ cannot be absorbed and, therefore, its energy cannot be converted. As Eq. 1.18 indicates, the efficiency of a device depends on the total power of *all* light incident upon it, including that which cannot be absorbed. The second intrinsic loss follows the excitation of an electron from the valence band to the conduction band by a photon of energy $E_{ph} > E_g$, which promotes the electron to a state that is above the band edge energy. In order to achieve thermal equilibrium, this "hot" electron can emit phonons to dissipate the excess energy $E - E_g$, which is lost to heating of the device. The third intrinsic loss is radiative recombination of carriers, or *emission*.

According to the principle of blackbody emission, all materials at a finite temperature emit light. Thus, solar cells are both absorbers and emitters of light, and recombination fundamentally limits the open-circuit voltage of a solar cell to less than its bandgap because it decreases the electron and hole quasi-Fermi energies. In calculations of the maximum theoretical efficiencies of solar cells, only intrinsic losses are considered, because they are unavoidable.

Extrinsic losses occur because of issues with material quality or with the design or manufacturing of a solar cell. Radiative recombination of carriers is inevitable in a device at a finite temperature, but if it occurs via a defect or trap state in the bandgap, or via an Auger process, such transitions often involve emission of phonons instead of a photon because of momentum mismatch between the initial, intermediate, and final states. Non-radiative recombination heats solar cells and prevents the possibility of an emitted photon being re-absorbed in the device. Other non-ideal losses include the reflection of light at the surface of a device; *shadowing* of the top surface of a solar cell by metal contacts, which decreases the amount of light that enters the cell; voltage loss due to series resistance associated with the contacts as well as the device material; and voltage and current losses from shunt resistance associated with defect states that allow current to leak through the junction.

1.5.2. Detailed Balance Calculations of Solar Cell Efficiency

Many aspects of solar cell design require compromise between essential but opposing factors in order to optimize device performance. The efficiency of a solar cell depends on the current and voltage that it generates. Current and voltage cannot, however, increase independent of one another. The solar spectrum is broad and generating maximum photocurrent from it requires a material with a very small bandgap

to absorb the infrared wavelengths. On the other hand, the voltage at the terminals of a solar cell are given by the separation of the electron and hole quasi-Fermi levels, which cannot be larger than the bandgap. Typically, the maximum achievable open-circuit voltage of a device is a few hundred millivolts less than its bandgap, and the operating voltage is slightly less than V_{oc}. Too large or too small of a bandgap is therefore detrimental to the current or to the voltage of the cell, respectively, and optimal materials have bandgaps that allow them to absorb light at energies where the incident irradiance is high, and to extract photocurrent at a useful voltage. Identifying ideal materials for solar cells and their maximum power conversion efficiencies is the subject of numerous theoretical studies that continue to motivate research and development.

Theoretical analyses often seek the maximum efficiency of a solar cell so that different materials and configurations can be evaluated as evenly as possible. All solar cells suffer the same intrinsic losses that have just been discussed, though the magnitude of each intrinsic loss mechanism varies according to the balance of energy transfer between the radiation source (typically, the sun) and the solar cell, which form a coupled thermodynamic system. By evaluating equations based on the steady-state transfer of energy in that system, which must be balanced in observance of energy conservation, and assuming only intrinsic losses, the current and voltage generated by a solar cell can be calculated. Known as "detailed balance" calculations, these have become essential to the prediction of solar cell efficiencies.

1.5.2.1. Single-Junction Device Efficiency Limit

One such analysis, which was reported in 1960 by Shockley and Queisser,[6] calculated the maximum theoretical efficiency of a *p-n* junction solar cell. Their calculation assumes that the device incurs only intrinsic losses; that the Sun is a

blackbody emitter at a temperature of 6000 K; that the solar cell is a blackbody at a temperature of 300 K; that all photons with energy $E > E_g$ are absorbed; and that absorbed photons each produce one electron-hole pair. With these assumptions, the maximum photovoltaic energy conversion efficiency is approximately 30% and it is achieved with a bandgap of 1.1 eV. This limit is often referred to as the "Shockley-Queisser limit."

1.5.2.2. Multiple-Junction Device Efficiency Limit

Limits on the efficiency of photovoltaic conversion of sunlight derive from the large spectral breadth of solar irradiance. A single-bandgap device can only fully convert the energy of photons with energy of $h\nu = E_g$; intrinsic losses reduce the energy converted at other frequencies, which implies that connecting multiple cells with different bandgaps is a route to efficiencies greater than 30%. In 1980, Henry used the detailed balance framework to calculate limiting efficiencies for multiple-bandgap devices in a *tandem multi-junction* configuration,[7] where the individual cells are stacked on each other, as illustrated in Fig. 1.9. The solar cell was again considered a blackbody at 300 K, though Henry used a terrestrial solar spectrum designated *air mass* 1.5 (AM 1.5) as the incident spectrum.[8] His results indicate that significant increases in the maximum theoretical efficiency of devices can be achieved by using multiple semiconductors with optimal bandgaps: assuming that the sunlight incident on a device is concentrated by a factor of 1000 (see Sec. 5.2.3), limiting efficiencies are 37% for a single-bandgap device; 50% for a two-bandgap device; 56% for a three-bandgap device; and 72% for a 36-bandgap device, which are presented in Ref. 7. The overall record for power conversion efficiency of solar cells has for years been held by tandem MJ devices under concentrated light, and currently stands at 43.5%, held by a three-junction device.[9]

Two important points about the performance of photovoltaic cells are highlighted by Henry's analysis. First, solar concentration is an important consideration for creating viable photovoltaic systems with expensive but efficient solar cells. Secondly, increasing the number of bandgaps in the system enables considerable increases in efficiency; however, doing so has practical limits because the differential improvement of efficiency decreases as the number of bandgaps increases and there is significant cost associated with increasing the number of bandgaps.

1.5.2.3. Practical Aspects of Multi-Junction Solar Cells

Multi-junction (MJ) solar cells use multiple materials with different bandgaps to improve their spectral response bandwidth and to reduce intrinsic losses compared to single-bandgap devices. MJ devices consist of multiple solar cells of different bandgaps connected in series (*tandem* configuration) or in parallel. Tandem devices have enhanced voltage equal to the sum of the voltages of the individual *sub-cells* while the current is equal to the lowest current of the sub-cells. If the devices are connected in parallel, then the currents sum and the voltage is limited. As a result of fabrication and integration considerations, and because resistive losses are significant at high current densities, such as those found in parallel-connected devices, the tandem configuration dominates MJ cell design.

The multiple sub-cells in a MJ stack generally consist of direct bandgap materials for their strong absorptivity, and they are typically grown on the same substrate with thin *tunnel junctions* that connect them in series. As illustrated in Fig. 1.9, light passes vertically through the sub-cells. The top cell has the largest bandgap and the bottom cell has the smallest bandgap, so that each sub-cell absorbs a specific portion of the solar spectrum. This is essential to matching the current generated in each sub-cell, which is

limited by the lowest current producing sub-cell. Appropriate choice of the materials and sub-cell thicknesses based on anticipated irradiance is essential to achieving the high efficiencies of which MJ devices are capable.

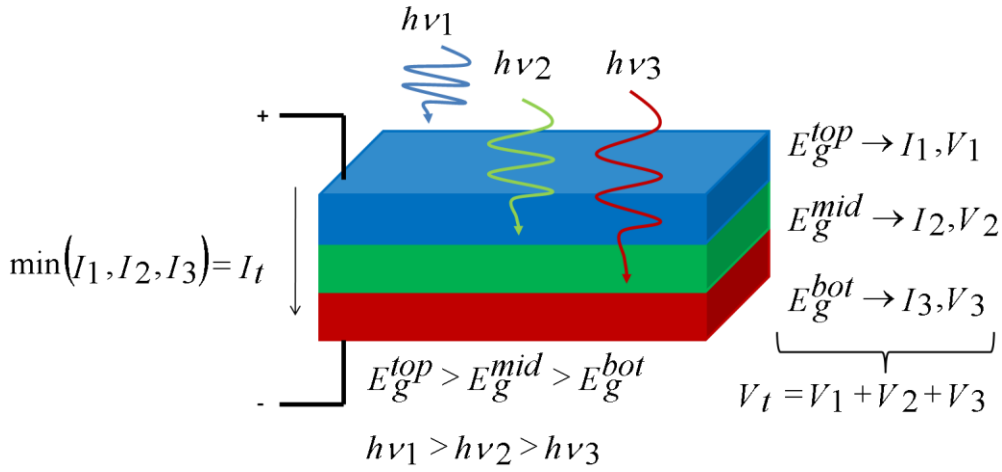

Figure 1.9: A series-connected, three-junction tandem solar cell, in which three distinct solar cells are connected in series. In these devices, the top sub-cell has the highest bandgap (E_g^{top}), and the bandgaps of sub-cells decrease monotonically to the smallest one, which is on the bottom (E_g^{bot}). Correspondingly, the top sub-cell absorbs the highest energy photons while the lowest pass through to the bottom cell. The voltages of the sub-cells add while the net current through the tandem device equals the smallest of the sub-cell currents.

The cost of manufacturing MJ solar cells originally limited their use to space equipment, such as satellites, where areal restrictions necessitate the use of very efficient devices. However, *concentrator photovoltaics* (CPV) have garnered interest in MJ cells for terrestrial applications. In this approach, concentrating optics made of relatively cheap materials collect light from a relatively large area and focus it onto small, but efficient, solar cells, which are often tandem MJ devices. In this way, the quantity of expensive device material required for a system is minimized, which improves the economics of CPV for terrestrial power generation, especially at utility-scale levels.

While tandem MJ devices have already been adopted for terrestrial systems, the current-matching requirement is a barrier to their performance in locations with variations in weather and spectral variations based on the time of day and year. The cells are designed for a prevailing spectral condition and deviations from it produce sub-cell current mismatch, which can significantly reduce MJ device efficiencies. This generally limits their use to dry, sunny locations where spectral variation throughout each day and the year are minimized. Terrestrial MJ cells are also typically mounted on mechanical tracking systems to maximize capture of the *direct component* of incident light as it is more intense and regular than the *diffuse component*, which is light scattered in the atmosphere. Thus, MJ-based CPV systems are well-suited for utility-scale generation in parts of the world, but they are not a universal solution for high power, low-area systems that demand efficient devices.

1.6. Multi-Bandgap Device Alternatives to the Multi-Junction Solar Cell

One route past the current-matching requirement imposed by tandem multi-junction solar cells is to incorporate multiple materials in a single-junction device. *Epitaxial growth* of semiconductors (see Sec. 1.7), which is the method of constructing III-V tandem multi-junction devices, enables precise control of the composition of materials that are deposited to form a device, and of their thickness, which can be less than 1 nm. Quantum confined materials can thus be made in order to specifically tailor the electronic and optical properties of devices. Semiconductor *heterostructures* consist of different semiconductors that are deposited, or epitaxially grown, on a substrate such that they are atomically bonded at their interface. This enables materials with different bandgaps to be assembled in one structure.

1.6.1. Energy Bands in Semiconductor Heterostructures

At the interface between two materials, an electrostatic potential must compensate differences in band alignment. Depending on the electron affinity and on the bandgap of each material, this can lead to several different configurations of the bands at hetero-interfaces, which are classified as type I, II and III. Structures featuring these hetero-interfaces are shown in Fig. 1.10, where a layer of one material (B) is sandwiched between two layers of another material (A). In the type I structure, the B layer acts as a *well* for electrons and holes because it has conduction and valence band states that are lower in energy than those of material A. In the type II and III structures, the B layer acts as a well for electrons but not for holes. Each structure is suitable for different devices and guides the choice of which materials to use.

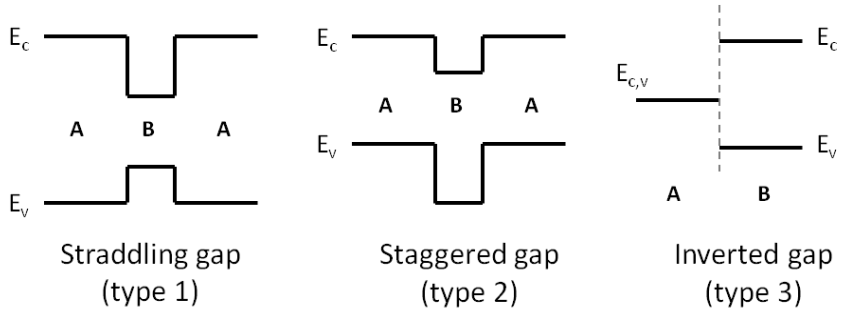

Figure 1.10: Three types of semiconductor heterostructures, of which types 1 and 2 can provide confinement in a low-bandgap "well" with a potential barrier created by an adjacent, high-bandgap "barrier." In type 1 and 2 heterostructures, material B is a potential well for (type 1) electrons and holes and (type 2) electrons only. The "inverted" gap of type 3 heterostructures occurs at the interface between some semimetal-semiconductor structures, which are not used as light absorbing materials in solar cells, but are mentioned to illustrate the different band alignments at heterojunctions.

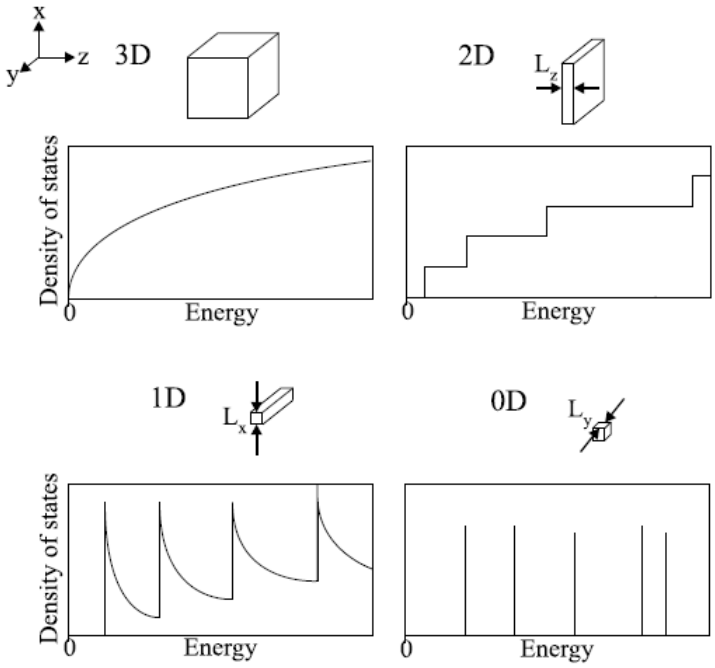

Figure 1.11: Qualitative illustrations of the density of states function, $g(E)$, for materials with no quantum confinement (3D) and varying degrees of confinement (i.e., '2D' is analogous to a quantum well, '1D' is analogous to a quantum wire or nanowires, and '0D' is analogous to a quantum dot).

Numerous semiconductor heterostructures have become technologically important. In many cases, heterostructures feature quantum confinement in one or more dimension, which affects the material's electronic and optical properties. A *quantum well* (QW), for example, consists of a "well" layer that is thin in the direction of growth, but unconfined in the transverse directions, that has lower potential energy than the surrounding "barrier" material. A *quantum dot* (QD) is the same concept as a QW, but with confinement of the "dot" material in all three dimensions. Among their other differences with bulk semiconductors, quantum confined structures have reduced densities of states, $g(E)$, compared to bulk materials, as illustrated in ... because confinement reduces the dimensionality of the crystal, which reduces the number of

electronic states available at a given energy (or, equivalently, at a given wavevector). The rate of radiative transitions is directly proportional to the density of states, as indicated in Eq. 1.31, and scattering of carriers from one electronic state to another by non-optical processes also depends highly on $g(E)$, implying that the reduced density of states in quantum confined materials has an important effect on the optoelectronic behavior of devices.

1.6.2. Quantum Wells and Quantum Dots for Solar Cells

In 1990, Barnham and Duggan proposed the quantum well solar cell (QWSC), which contains type I QWs to increase the spectral response of a single-junction solar cell.[10] The device consists of a *p-i-n* diode with QWs inserted in the *i* ("intrinsic," meaning nominally undoped) layer, where the built-in electric field assists collection of carriers that are photogenerated in the sub-bangap states of QWs. The QWs absorb a larger bandwidth of the solar spectrum than the barriers; thus, if carriers are extracted from the QWs and collected at the same potential as an analogous device without QWs (a *homojunction* reference device), the additional photocurrent produced by the QWs increases the efficiency of a QWSC compared to the homojunction cell. These principles are illustrated in the schematic of a device that has QDs embedded in QWs, shown in Fig. 1.12.

Quantum dots have also been proposed for improving the performance of solar cells via numerous physical mechanisms. Most straightforwardly, QDs can generate photocurrent at wavelengths longer than the homojunction band edge, improving performance in the same way as was just discussed for QWSCs.[11,12] The use of QDs in such a manner is the primary focus of quantum dot solar cells (QDSCs) in this dissertation. Less straightforwardly, QDs have been proposed for realizing an

intermediate band solar cell (IBSC),[13-16] which enables sub-band photon absorption via a band of intermediate states in the homojunction bandgap, and to improve device efficiency via multiple carrier generation from absorption of single photons, which would reduce thermal losses via phonon emission by carriers excited by high energy photons.[17,18] The realization of devices that demonstrate performance benefits as a result of these principles has, however, been challenging. In this work, QWs and QDs are intended solely to improve photocurrent by enabling sub-band absorption of radiation.

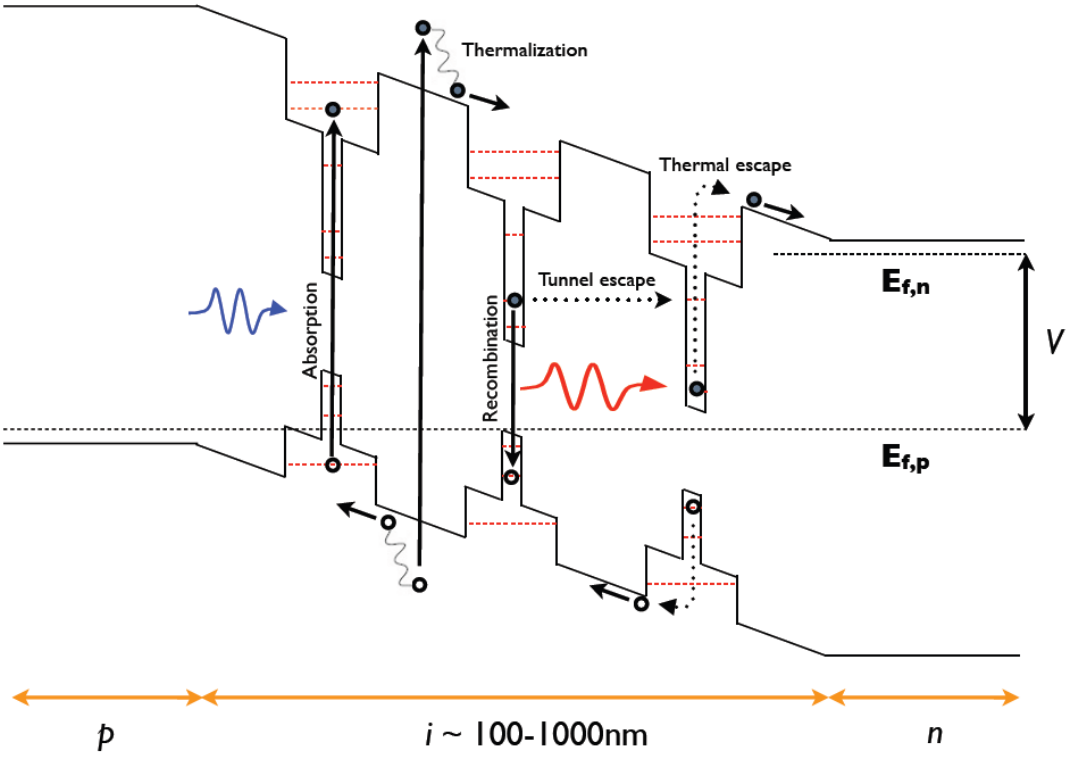

Figure 1.12: An illustration of a *p-i-n* quantum dot-in-well solar cell with radiative transitions and mechanisms of carrier escape from sub-band states labeled. The voltage across the terminals of the device equals the separation between the electron and hole quasi-Fermi levels.

1.6.3. Theoretical Efficiency of Nanostructured Solar Cells

When they proposed the QWSC, Barnham and Duggan argued that the voltage of the cell would be determined by the larger bandgap material, enabling its photocurrent to increase without voltage degradation and, correspondingly, improving its efficiency compared to a homojunction device. They estimated the maximum theoretical efficiency of a QWSC to be $\eta > 40\%$, larger than the Shockley-Queisser limit for a homojunction device.

The theoretical maximum efficiency of QWSCs became a topic of debate following additional theoretical analyses. Marti, et al., argued that the QWs would increase absorption in a device, but that they would also increase luminescence (i.e., radiative recombination).[19-21] They suggested that electron and hole quasi-Fermi levels would be reduced in energy in an ideal QWSC relative to a device without QWs as a result of carriers recombining through the QW sub-band states. The voltage of the device would therefore be reduced by an amount commensurate with the benefit of increased absorption. Based on this, Marti, et al. argued that QWSCs could not exceed the Shockley-Queisser limit for single-junction devices.

Subsequent detailed balance analyses have demonstrated that variations in the quasi-Fermi level of a QWSC between the QW and barrier are essential to enabling high efficiency. A study of solar cells containing generic quantum confined sub-bandgap absorbers (e.g., QWs, QDs, nanowires) found that if carriers in the barriers do not equilibrate with carriers in sub-band states, and assuming all sub-band carriers are collected, a maximum efficiency of ~44% can be achieved with unconcentrated sunlight.[22] Another study, which specifically considered QWSCs, determined a maximum efficiency of ~64% under maximum solar concentration.[23] These prospects, and the possibility of using QWs[24,25] and QDs[26,27] to tailor the absorption in sub-cells of tandem

MJ devices to increase their net photocurrent, has sustained considerable interest in nanostructures for high efficiency solar cells.

1.6.4. Practical Issues with Nanostructured Solar Cells

While many demonstrations of nanostructured solar cells have been reported, realizing very efficient devices has been challenging. QWSCs have a highest reported efficiency of ~28%[28] and QDSCs have a highest reported efficiency of 13.5%.[29] Improving their performance is likely to require novel approaches to improving light absorption and carrier transport in the devices. Improving light absorption can be achieved by optical or photonic structures that increase the path length of photons passing through a device, while efficient carrier transport and collection are achieved through careful device engineering.

Carriers that are photogenerated in QW or QD sub-band states must be collected at the electrode potential, requiring additional energy so that they can transit the barriers in the intrinsic region. That additional energy may be supplied thermally, radiatively, or carriers can tunnel through the barriers. Thermal escape results from carriers absorbing phonons and moving to higher energies in the continuum of bulk states that begins near the barrier band edge, while radiative escape achieves the same end through absorption of photons. Once in the continuum, the built-in potential sweeps carriers through the intrinsic region to the electrodes. The time required for carriers to escape from sub-band states must be less than their lifetimes; if it is not, they recombine.

The thickness of the depletion region and the strength of its built-in electric field are important for carrier collection from sub-band states. The field affects the confinement potential of the quantum wells, which in turn affect the probability of carrier

escape from sub-band states. In the depletion approximation, the voltage drop across the depletion region with an externally applied bias, V_a, is

$$V_{bi} = \frac{kT}{e}\ln\left(\frac{N_A N_D}{n_i^2}\right) - V_a. \tag{1.35}$$

The electric field strength is then

$$E = \frac{V_{bi} - V_a}{t}, \tag{1.36}$$

where t is the thickness of the depletion region. From Eq. 1.35, it can be seen that higher base and emitter doping yields a higher built-in potential and, therefore, a stronger electric field for a given applied bias. In GaAs solar cells, base and emitter doping levels on the order of $N_A = 10^{17}$ cm^{-3} and $N_D = 10^{18}$ cm^{-3}, respectively, are typical because they are low enough to limit absorption of light by free carriers and high enough to achieve reasonably low contact resistance and high carrier collection efficiency.[30,31]

Numerous studies have investigated the dependence of QWSC performance on factors that affect sub-band carrier escape and collection from QWs. These include the built-in field in the intrinsic region[32,33] and the depth of the potential well.[34] Embedding heterostructures in an excessively thick undoped i region may impede carrier transport across the junction, while excessively high base or emitter doping may increase recombination and free carrier absorption loss in the neutral regions. Thus, a compromise between the doping levels and the thickness of the i region is necessary for optimal device performance.

The probability of carriers tunneling through QW barriers is also a function of electric field strength in the QWs. For a triangular potential barrier, which is the shape of QW barriers in the depletion region, tunneling is analogous to Fowler-Nordheim tunneling, which occurs with probability that increases with electric field strength:

$$\Theta = \exp\left(-\frac{4}{3}\frac{\sqrt{2em^*}}{\hbar}\frac{\phi^{3/2}}{\mathcal{E}}\right), \tag{1.37}$$

where ϕ is the potential at the top of the barrier, yielding a triangular potential function of

$$V(z) - E = e\phi\left(1 - \frac{z}{L}\right). \tag{1.38}$$

with E being the carrier energy and $\mathcal{E}$ the magnitude of the electric field. Studies have attributed photocurrent at high electric fields in InAs/GaAs QDs to tunneling escape from sub-band states.[35] Additionally, when multiple periods of QD layers are used, the interaction of carrier wavefunctions in vertically-[36] and laterally-adjacent QDs[37] is influenced by the electric field[38] and affects carrier transport and recombination.[39]

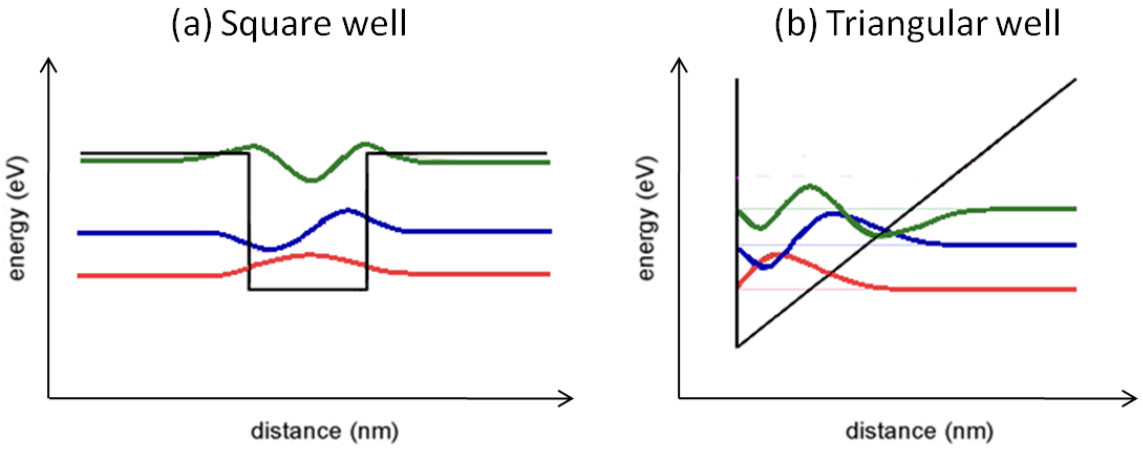

Figure 1.13: The first three sub-band states of (a) a square well and (b) a triangular well, where (a) is representative of a quantum well at flat band and (b) is representative of a quantum well in an electric field, such as in a quantum well solar cell.

In the intrinsic region of a solar cell, several factors affect carrier dynamics. The presence of a built-in electric field implies that the band edge in QWs and QDs slopes such that the lowest sub-band state may lie in a triangular potential well, as illustrated in Fig. 1.13(b), as opposed to the flat, "square" well of Fig. 1.13(a), which corresponds to zero field. A triangular potential well supports states with different energies than a square well, and the QW or QD potential most resembles a triangular well at strong fields, when

the band edge slope is large. The field also pushes low energy electron and hole states to opposite sides of the QW or QD in the direction of the field; in Fig. 1.13(a), the average position of a particle is in the center of the quantum well, whereas it is shifted to the low-potential edge of the triangular well in Fig. 1.13(b), decreasing the overlap of electron and hole wavefunctions compared to flat band because the field pushes electrons and holes in opposite directions. Known as the quantum-confined Stark effect, this shift induces an electric dipole associated with the spatial offset of the electron and hole, and the dipole shifts the energy of sub-band states according to

$$\Delta E = -p_z E_z \tag{1.39}$$

where

$$p_z = -e\langle z \rangle, \tag{1.40}$$

and

$$\langle z \rangle = \int \varphi^* z \varphi dz. \tag{1.41}$$

E_z is the magnitude of the electric field in the z direction, which is the direction of epitaxial growth. This shift reduces rates of radiative absorption and recombination via QW and QD sub-band states because of reduced wavefunction overlap; however, the effect is generally small, and the energy shift is often negligible compared to the un-shifted sub-band state energy.

1.7. Epitaxial Growth of Solar Cells

Realization of tandem multi-junction, quantum well, and quantum dot solar cells, as well as electronic and optical devices that incorporate semiconductor heterostructures, is enabled by *epitaxial growth* of solid state materials. Epitaxial growth refers to depositing solid state materials on a substrate where the crystal of the epitaxial material has a regular structure. This enables growth of mono-crystalline wafers consisting of one

or more materials. Common methods of epitaxial growth for electronic and optical devices include chemical vapor deposition (CVD); metal-organic CVD (MOCVD); and molecular beam epitaxy (MBE). MOCVD and MBE are often used to grow optoelectronic device wafers because of the numerous source materials available to them and the high controllability of layer thickness and doping that they offer. Of the two, MBE typically offers greater precision in epitaxial growth because it can abruptly control the incidence of material for growth with shutters in front of the source material cells. MOCVD uses inert gas to transport source materials to the substrate, which cannot be controlled as precisely.

1.7.1. Epitaxial Growth of Device Structures Used in this Dissertation

All of the devices prepared in this work have been grown by collaborators in the Infrared Photonics Group at the NASA Jet Propulsion Laboratory (Pasadena, CA) or in the lab of Prof. Daniel Schaadt, formerly located at the Karlsruhe Institute of Technology (Karlsruhe, Germany) and presently at the Technical University of Clausthal (Clausthal, Germany). Both groups use solid source MBE systems, in which source materials consist of ultra high-purity, solid state materials that are placed in heated elements known as effusion cells. The materials are heated to temperatures sufficient to cause them to sublimate and subsequently effuse into the central chamber, where they condense on one or more growth substrates. Mechanical shutters control passage of the effusing materials into the growth chamber. An example of a MBE system in this configuration is shown in Fig. 1.14.

The chamber of the MBE system is pumped to very low pressures, which are typically on the order of 10^{-8} Torr, to remove potential contaminants. Samples sit on a temperature-controlled, rotatable chuck. Temperature control is necessary to achieve the

growth kinetics required to produce a given material, while rotating the substrate improves the uniformity of the deposited materials. During growth, reflection high-energy electron diffraction (RHEED) can be used to monitor the surface characteristics of the grown material *in-situ*, potentially observing abnormalities when they occur. These features make MBE a precise growth technique that is capable of producing highly crystalline materials with thicknesses, material profiles, and doping profiles at atomic scale precision.[40]

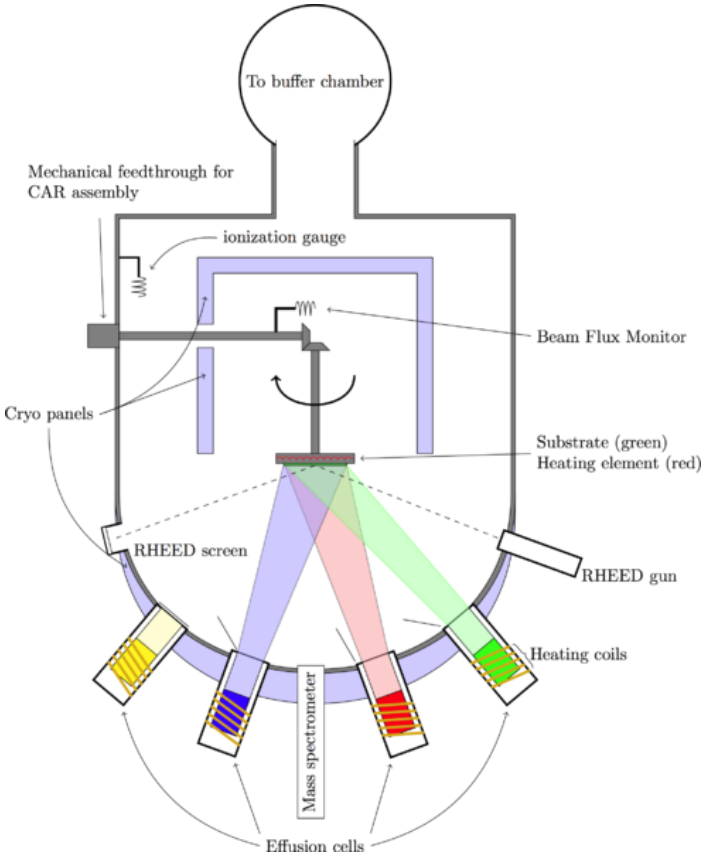

Figure 1.14: A schematic of a solid source molecular beam epitaxy system. The figure is freely licensed under Creative Commons, and was retrieved from http://en.wikipedia.org/wiki/File:MBE.png on 16 January 2012.

1.7.2. Strain in Semiconductor Heterostructures

An important aspect of heterostructures is that the lattice constants of two materials are not, in general, equal, so that when they are grown, strain exists as a result of tensile or compressive stress in the epitaxial layers. If the thickness of the growth substrate is much larger than that of the epitaxial layers, which is generally the case, then the lattice of the epitaxial layers will stretch or compress to conform to the lattice constant of the substrate. If the thickness of the epitaxial layers exceeds a critical value however, energy stored in the strained bonds of the epitaxial layer will be released by the formation of *dislocations*. A dislocation is a line of vacancies at sites where atoms are normally located, and it forms when it is energetically favorable to break bonds between neighboring atoms than to store additional strain energy in the bonds.

From a device performance standpoint, it is often necessary to minimize the density of dislocations. Unsatisfied bonds on atoms adjacent to a dislocation have large electron affinities and create deep level traps within the bandgap of a material, which facilitate non-radiative recombination. Dislocations must terminate at a surface or interface, so dislocation lines often extend through entire device layers or, worse, entire devices. Balancing the strain in heterostructures with layers of tensile- and compressively-strained materials is an approach that has been demonstrated to reduce dislocations in thick structures.[41-43]

Quantum wells and dots made of $In_xGa_{1-x}As$ with GaAs barriers, grown on GaAs substrates, are used in devices throughout this work. This is because GaAs is a nearly optimal single-junction solar cell material, and InGaAs has a lower bandgap than GaAs, enabling absorption of additional infrared light. As indicated by Fig. 1.15, the lattice constant of InAs is larger than that of GaAs. Thus, when InGaAs is grown on a thick GaAs substrate, the InGaAs is compressively strained if its lattice constant is reduced to

that of GaAs or an intermediate value. Data for the critical thickness of InGaAs coherently strained to GaAs is provided in Fig. 1.16.

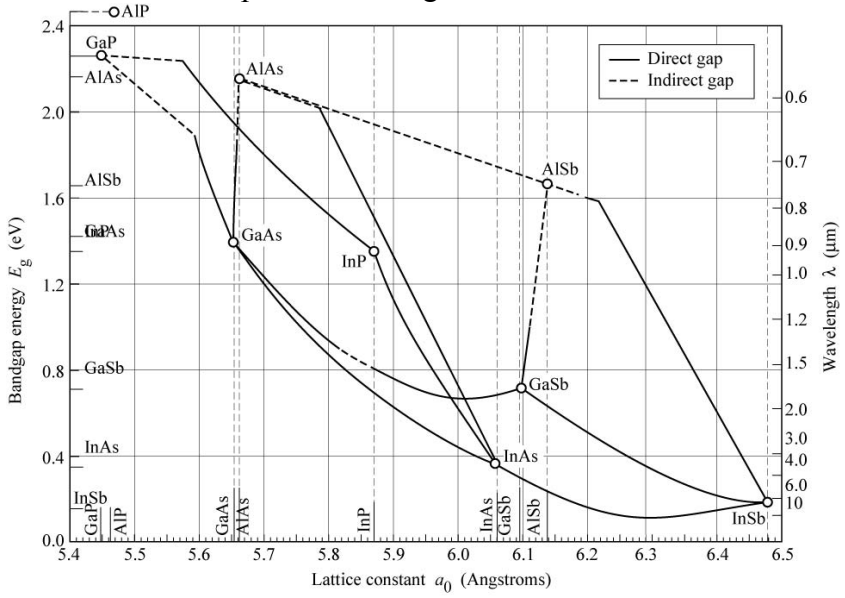

Figure 1.15: Bandgaps of compound semiconductors as a function of lattice constant. Figure adapted from Ref. 44.

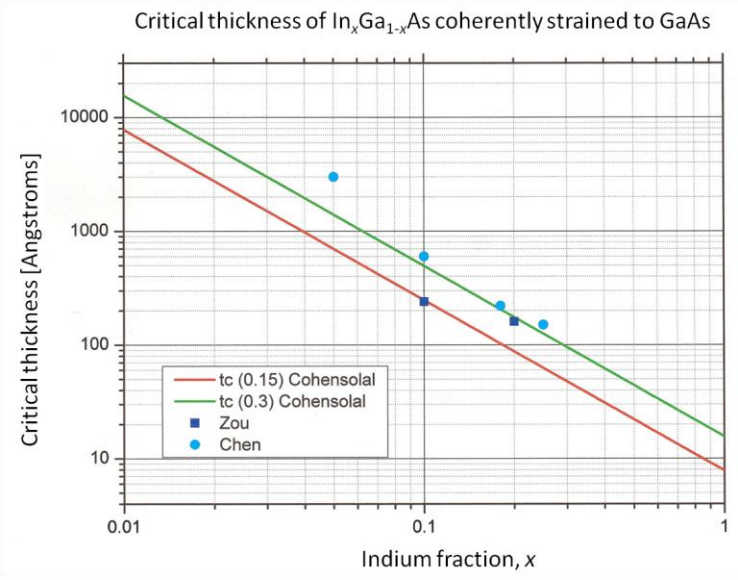

Figure 1.16: The critical thickness for dislocation formation in $In_xGa_{1-x}As$ coherently strained to GaAs. Graph courtesy Dr. Dongzhi Hu, TU-Clausthal. The data for 'Zou' and 'Chen' may be found in Refs. 45 and 46, respectively.

1.8. Chapter Summary and Overview of the Dissertation

This chapter has introduced concepts from solid state physics that are relevant to understanding the operation of solar cells. Basic principles of how solar cells function were also presented, and several of their key figures of merit were discussed, including the open-circuit voltage (V_{oc}), the short-circuit current (I_{sc}), and the fill factor (FF), which largely determine the efficiency (η) of a solar cell. The optical properties of materials were discussed; they are highly relevant to understanding the material in subsequent chapters. Finally, brief overviews have been provided of calculating the efficiency of solar cells; of high efficiency cell designs; of nanostructured materials and their use in high efficiency solar cell; and of experimental realization of such devices, including those investigated in this dissertation.

In chapter two, optical effects related to light trapping in solar cells are discussed, with an emphasis on light trapping in solar cells containing semiconductor heterostructures, such as quantum wells and quantum dots. Principles of electromagnetic waveguiding and criteria for coupling light into such confined modes in solar cells are presented, and the importance of simulations that model such effects are discussed. A quantum mechanical model for calculating the anisotropic optical properties, including the absorption coefficient, of strained quantum wells and quantum dots is presented and demonstrated for InGaAs/GaAs quantum wells.

Chapter three demonstrates absorption enhancement in optically thick InGaAs quantum dot-in-well solar cells, and corresponding increases in the photocurrent generated by the devices, which improves their power conversion efficiencies. Metal and dielectric nanoparticles deposited on the surface of the devices scatter light into guided modes of the device structure, producing broadband photocurrent enhancement, including at infrared wavelengths longer than the GaAs absorption edge, where only quantum dots

are absorbing. The short-circuit current density of a device increases by up to 16% with no reduction in its fill factor or open-circuit voltage. Results from finite element simulations corroborate the experimental results and illustrate how different phenomena related to optical scattering by nanoparticles affect device performance.

In chapter four, a light trapping approach for improving the performance of thin film InGaAs/GaAs quantum dot-in-well solar cells is demonstrated computationally and experimentally. Thin film devices are shown to have benefits for improving the coupling of incident radiation to waveguide modes of a device structure compared to optically thick devices. Devices with planar, symmetric, multiply periodic reflection gratings located on their back sides are shown to have broadband photocurrent generation of up to a factor of 10 larger than devices with planar back contacts/reflectors at wavelengths of 850 nm to 1200 nm. The improvement results from light trapping in the thin devices. A software-based procedure for optimizing the photocurrent of devices, given arbitrary illumination, and incorporating the anisotropic optical response of quantum wells, is presented and applied to the aforementioned gratings. A process for fabricating thin film devices with such light trapping structures is described, and results of measurements of such devices demonstrate photocurrent enhancement relative to control devices. Techniques to evaluate and characterize the performance of solar cells, and approaches to improving the performance of the types of devices investigated here, are also discussed.

The optical response of thin film photovoltaic devices represents the aggregate of numerous optical effects, which are discussed in chapter five. Incomplete absorption on the first pass of light through a thin film results in Fabry-Perot interference between incident and reflected waves. This phenomenon occurs both in devices with planar back contacts/reflectors and in devices with diffractive structures. It is shown that the photoresponse of grating-equipped quantum dot-in-well solar cells improves from

diffraction of light into the device structure and from reduction of optical absorption by metal in the gratings compared to planar reflectors. Considerations for the design of thin film devices and light trapping structures are illustrated based on the simulated performance of devices with different active layer thicknesses and for different metals used on the back surface.

Chapter six summarizes the work presented in this dissertation and concludes with discussion of the outlook for quantum wells and dots in solar cells. It discusses their application both to single- and multi-junction devices structures, as well as promising areas for work related to these devices.

---

[1] *Annual Energy Review*, US Energy Information Administration (2011).
[2] S. Hegedus and A. Luque, *Handbook of Photovoltaic Science and Engineering (2 ed.)* (Wiley, 2011) p. 6.
[3] "UFM/Mauro Solar Riser," accessed 11 February 2012 from http://www.airventuremuseum.org/collection/aircraft/UFM-Mauro%20Solar%20Riser.asp
[4] A. Cowell, "Solar-Powered Planes Flies for 26 Hours." *New York Times*, 8 July 2010.
[5] "Electric Aircraft," accessed 11 February 2012 from http://en.wikipedia.org/wiki/Electric_aircraft.
[6] W. Shockley and H.J. Queisser *J. Appl. Phys.* **32,** 510 (1961).
[7] C.H. Henry, *J. Appl. Phys.* **51**, 4494 (1980).
[8] C. Riordan and R. Hulstron, *Record of 21st IEEE PV Spec. Conf.*, 1085 (1990).
[9] M.A. Green, K. Emery, Y. Hishikawa, W. Warta and E.D. Dunlop, *Prog. Photovolt:. Res. Appl.* 19, 565 (2011).
[10] K.W.J. Barnham and G. Duggan, *J. Appl. Phys.* **67**, 3490 (1990).
[11] R.B. Laghumavarapu, M. El-Emawy, N. Nuntawong, A. Moscho, L.F. Lester and D.L. Huffaker, *Appl. Phys. Lett.* **91**, 243115 (2007).
[12] S.M. Hubbard, C.D. Cress, C.G. Bailey, R.P. Raffaelle, S.G. Bailey and D.M. Wilt *Appl. Phys. Lett.* **92**, 123512 (2008).
[13] A. Luque and A. Martí, *Phys. Rev. Lett.* **78**, 5014 (1997).
[14] V. Popescu, G. Bester, M.C. Hanna, A.G. Norman and A. Zunger *Phys. Rev. B* **78**, 205321 (2008).
[15] G. Wei and S.R. Forrest, *Nano Lett.* **7**, 218 (2007).
[16] A.S. Lin, W. Wang and J.D. Phillips, *J. Appl. Phys.* **105**, 064512 (2009).
[17] A. Luque, A. Martí and A.J. Nozik *MRS Bulletin* **32**, 236 (2007).
[18] J.B. Sambur, T. Novet and B.A. Parkinson, *Science* **330**, 63 (2010).
[19] G.L. Araujo and A. Martí, *Solar Energy Mater. and Solar Cells* **33**, 213 (1994).
[20] G.L. Araujo, A. Martí, F.W. Ragay and J.H. Wolter, *Proc. 12th European Communities Solar Energy Conf.* p. 1481 (1994).
[21] G.L. Araujo and A. Martí, *Appl. Phys. Lett.* **66**, 894 (1995).
[22] G. Wei, K.T. Shiu, N.C. Giebink and S.R. Forrest *Appl. Phys. Lett.* **91**, 223507 (2007).
[23] S.P. Bremner, R. Corkish and C.B. Honsberg, *IEEE Trans. Elec. Devices* **46**, 1932 (1999).
[24] N.J. Ekins-Daukes, J. Barnes, K.W.J. Barnham, J.P. Connolly, M. Mazzer, J.C. Clark, R. Grey, G. Hill, M. Pate and J.S. Roberts, *Solar Energy Mater. and Solar Cells* **68**, 71 (2001).
[25] D.B. Bushnell, T.N.D. Tibbits, K.W.J. Barnham, J.P. Connolly, M. Mazzer, N.J. Ekins-Daukes, J.S. Roberts, G. Hill and R. Airey, *J. Appl. Phys.* **97**, 124908 (2005).

[26] J.F. Wheeldon, et al., *Proc. SPIE* **7750**, 77502Q-1 (2010).
[27] J.F. Wheeldon, et al., *AIP Conf. Proc.* **1407**, 220 (2011).
[28]J.G.J. Adams, W. Elder, G. Hill, J.S. Roberts, K.W.J. Barnham and N.J. Ekins-Daukes, *Proc. SPIE* **7597***,* 759705 (2010).
[29] C.G. Bailey, D.V. Forbes, R.P. Raffaelle and S.M. Hubbard, *Appl. Phys. Lett.* **98**, 163105 (2011).
[30] G.J. Bauhuis, P. Mulder, J.J. Schermer, E.J. Haverkamp, J. van Deelen and P.K. Larsen, *Proc. 20th European Photovolt. Solar Energy Conf.*, p.468 (June 2005).
[31] G.J. Bauhuis, P. Mulder, E.J. Haverkamp, J.C.C.M. Huijben and J.J. Schermer, *Solar Energy Mater. Solar Cells* **93**, 1488 (2009).
[32] I. Serdiukova, C. Monier, M. F. Viela, A. Freundlich, *Appl. Phys. Lett*. **74**, 2812 (1999).
[33] A. Alemu, J. A. H. Coaquira, and A. Freundlich, *J. Appl. Phys*. **99**, 084506 (2006).
[34] J. M. Mohaidat, K. Shum, W. B. Wang, and R. R. Alfano, *J. Appl. Phys.* **76**, 5533 (1994).
[35] P.W. Fry, J.J. Finley, L.R. Wilson, A. Lemaitre, D.J. Mowbray, M.S. Skolnick, M. Hopkinson, G. Hill and J.C. Clark, *Appl. Phys. Lett.* **77**, 4344 (2000).
[36] P. Miska, J. Even, C. Paranthoen, O. Dehaese, A. Jbeli, M. Senes, and X. Marie, *Appl. Phys. Lett*. **86**, 111905 (2005).
[37] L. Höglund, C. Asplund, Q. Wang, S. Almqvist, H. Malm, E. Petrini, J. Y. Andersson, P. O. Holtz, and H. Pettersson, *Appl. Phys. Lett*. **88**, 213510 (2006).
[38] A.F.G. Monte, F. Qu and M. Hopkinson, *Appl. Phys. Lett*. **92**, 182102 (2008).
[39] J. M. Smith, P. A. Dalgarno, B. Urbaszek, E. J. McGhee, G. S. Buller, G. J. Nott, R. J. Warburton, J. M. Garcia, W. Schoenfeld, and P. M. Petroff, *Appl. Phys. Lett.* **82**, 3761 (2003).
[40] E.H.C. Parker, ed., *The Technology and Physics of Molecular Beam Epitaxy* (Springer, 1985).
[41] D.C. Houghton, *J. Appl. Phys.* **70**, 2136 (1991).
[42] J.W. Matthews and A.E. Blakeslee, *J. Cryst. Growth* **27**, 118 (1974).
[43] N.J. Ekins-Daukes, K.W.J. Barnham, J.P. Connolly, J.S. Roberts, J.C. Clark, G. Hill and M. Mazzer, *Appl. Phys. Lett.* **75**, 4195 (1999).
[44] E.F. Schubert, *Light-Emitting Diodes* (Cambridge Univ. Press, 2003).
[45] J. Zou, D.J.H. Cockayne and B.F. Usher, *J. Appl. Phys.* **73**, 629 (1993).
[46] Y.C. Chen, P.K. Bhattacharya and J. Singh, *J. Vac. Sci. Tech. B* **10**, 769 (1992).

Chapter 2: Semiconductor Heterostructure Solar Cells and Light Trapping

A straightforward approach to reducing the cost and weight of a solar cell, and to potentially increase its mass-specific power density, is to reduce its thickness. However, in doing so, the amount of light absorbed by the solar cell generally decreases. Semiconductor heterostructures, such as quantum wells and dots, can be particularly beneficial in a thin film device compared to a thick one because they can absorb light more strongly than the bulk material surrounding them. Light management also becomes more important for maximizing absorption in thin film solar cell, and, specifically, for maximizing absorption in the relatively small volume of sub-band absorbing material (i.e., the quantum wells and dots). Furthermore, it is challenging to produce thin film devices when, as with III-V devices, they are epitaxially grown on expensive, brittle substrates.

Despite these challenges, III-V thin film solar cells are attractive for applications that require high mass-specific [W/kg] and areal [W/m^2] power density. For example, the large absorption coefficient of GaAs enables absorption of ~92% of solar photons with energy greater than its bandgap that are incident on a 1 μm thick GaAs film, which is approximately twice as many as are absorbed by a 1 μm crystalline Si film. Increasing the GaAs film thickness to 2 μm enables absorption of >99% of photons with energy greater than the bandgap. The benefit of direct bandgap materials, such as GaAs and InAs, can be seen in Fig. 2.1, which shows their absorption coefficients and that of crystalline Si with the Airmass (AM) 1.5 global solar spectrum for reference.*

* The AM 1.5 spectrum is a terrestrial solar reference spectrum, which is also known by its designations from two standards organizations: ASTM G173-03 and ISO 9845-1.

In addition to the impressive light absorbing ability of III-V thin films, photogenerated carriers can be efficiently collected in thin film solar cells made of these materials. As a result of their excellent radiative properties, carrier transport, and nearly ideal bandgap for photovoltaic energy conversion,[47] high quality thin film GaAs solar cells produce large open-circuit voltages of near 1.0 V and current densities >20 mA/cm^2. Thus, the world record single-junction cell efficiency has been held by GaAs thin film devices for many years, and it is currently ~28%.[48] It is therefore attractive to incorporate quantum wells and dots in GaAs solar cells to potentially reach efficiencies greater than are achievable with homojunction devices, as discussed in Sec. 1.6.3. This chapter focuses on the design of single-junction quantum well and dot solar cells, structures for light trapping in photovoltaic devices, and optical effects in thin films that can significantly influence the response of such devices.

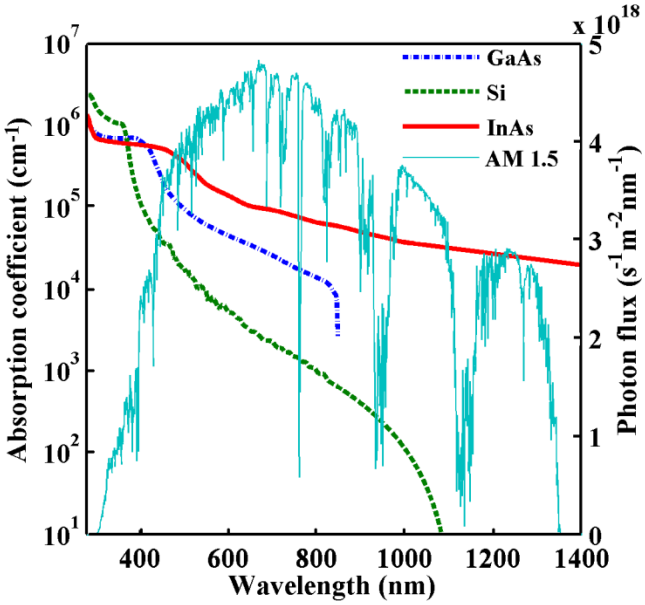

Figure 2.1: The absorption coefficients (left axis) of GaAs (dot-dashed, blue line), Si (dashed, green line), and InAs (solid, red line) against the photon flux (right axis) of the portion of the Airmass 1.5 global solar spectrum from 300 nm to 1400 nm in wavelength (solid, cyan line).

2.1. LIGHT MANAGEMENT AND TRAPPING IN SOLAR CELLS

Because the probability that light transmitted into a solar cell will be absorbed increases with the path length of photons in the device, materials and structures that increase photon path lengths can be effective at improving the performance of photovoltaic devices. Solid state semiconductors have relatively high refractive indices, with common values of $n \approx 3$ to 5. Therefore, a solar cell made of such a material, and which has no anti-reflection coating (ARC) on its top surface, loses between 25% and 50% of normally incident power to reflection at the top surface. Of the light that enters a device, some will be absorbed in the semiconductor, while the rest will be transmitted out its back side. These optical losses significantly reduce the photocurrent generated by a solar cell and compel approaches to minimize them.

2.1.1. Anti-reflection Coatings and Back Side Reflectors

The simplest approach to light management in solar cells has been to add planar materials on the front and back surfaces of devices using standard processing techniques. A planar back side reflector ideally consists of low loss metal and simultaneously serves as an electrical contact to the back bottom electrode of a device. Thus, it is important to pick a metal (or an alloy, as are many semiconductor contacts) that achieves low contact resistance. The optical function of the metal is simply to reflect light back into the device for at least a second pass through the cell, completing a "round trip" through the structure. When light reflected at the bottom of a cell reaches the top of the device, some of its intensity transmits out of the device, and some reflects back into the device. This series of reflections inside a solar cell is a fundamental effect and, as discussed in Sec. 2.2.1, and demonstrated in Secs. 4.2 and 5.1.2, interference between the reflected waves can be an important factor in the performance of thin film solar cells.

Another fundamental structure for light management in solar cells is a planar ARC, which typically consists of a dielectric material with a refractive index ideally close to $\sqrt{n_{\text{semi}}}$ that is deposited on top of a device, where n_{semi} is the refractive index of the underlying semiconductor. An ARC use interference of the waves reflected at its front and rear surfaces to minimize reflection at a particular free space wavelength (λ). If the ARC thickness equals $\lambda/4$ ('quarter-wave'), then the normally incident and quarter-wave reflected fields are 90° out of phase, maximizing destructive interference. Thus, a simple quarter-wave ARC maximizes transmission of light into the device, but only at one wavelength. Multiple-layer ARCs can improve the breadth of transmission enhancement, but, like single-layer ARCs, they have poor angular response. Further, multi-layer ARCs are often considerably more expensive than single-layer ARCs. Thus they are principally used with expensive multi-junction solar cells, which require maximum transmission over a broad spectral width. Finally, because all planar ARCs exhibit poor angular response, devices equipped with them must accept variable performance as the position of the sun changes, or they must be mounted on equipment that mechanically tracks the sun to achieve more consistent performance.

2.1.2. Traditional Approaches to Light Trapping

Another approach to maximizing light absorption in a device is to dramatically increase the path lengths of photons compared to their values in devices with planar ARCs and reflectors. All light that transmits into a planar, symmetric device (i.e., a device with flat interfaces) enters radiation modes of the device structure that allow only a round-trip pass through the device for the majority of photons before they couple out to radiation modes in the surrounding medium. As a result, a majority of the light that is reflected at the back surface of such a device, and is not absorbed before reaching the top

surface, transmits out of the cell. Decoupling the external (i.e., in the surrounding medium) and internal (i.e., in the device) radiation modes requires an asymmetric structure that scatters light, or otherwise redirects it, into the larger set of electromagnetic modes of a device structure. These include confined *waveguide* modes, in which photons propagate transverse to the surface normal of a device, and can be effectively induce many internal reflections. Techniques for achieving this may be referred to as *light trapping* techniques.

Traditionally, light trapping has been achieved by the use of micron-sized features, often with random geometries, to scatter incident radiation into a device structure. These features are often produced by anisotropic chemical etching of the top surface of a semiconductor. Yablonovitch identified the ability of textured surfaces to increase absorption in weakly absorbing materials by a factor of up to $4n^2$,[49] where n is the refractive index of the material. Thin film devices, however, are often too thin to permit etching of micron-scale features, which continues to motivate investigations of novel light trapping techniques. Subsequent analyses have shown that enhancement factors $>4n^2$ are possible in thin-films,[50-52] though realizing them over a wide range of wavelengths, polarization, and incident angles has only been theoretically demonstrated, and, to-date, requires complicated nanoscale structures.[53] Nevertheless, modern fabrication technologies enable the realization of structures with intricate micro- and nanoscale features, which may result in significant improvement of light transmission into, and absorption within, photovoltaic devices.

2.1.3. Advanced Techniques for Light Trapping

Semiconductor fabrication and manufacturing equipment have enabled the realization of devices with feature sizes of <10 nm. Electron-beam lithography,[54,55]

interference lithography,[56] nanoimprint lithography,[57,58] and extreme ultraviolet (EUV) lithography[59] are examples of techniques for creating very fine patterns. Naturally, such equipment spurs investigation of sub-wavelength structures and nanostructured materials to improve absorption in photovoltaic devices, often by increasing the path length of light as a result of scattering or diffraction. Myriad photonic structures containing sub-wavelength features have been proposed for improving photovoltaic device performance, including diffraction gratings,[60-62] nanoparticles,[63-67] and photonic crystals.[68-71] Advanced light trapping structures, such as these, are expected to play an important role in the development of future generations of photovoltaic devices.

Nanoscale particles, which can be relatively easily fabricated and integrated onto solar cell surfaces, have been of considerable interest for scattering and trapping of light in photovoltaics.[63-67] Studies of the effects of both metal and dielectric nanoparticles deposited on the surface of photovoltaic devices have demonstrated broadband enhancement of photogenerated current and increased power conversion efficiencies relative to devices without nanoparticles[65,66,72-74] and provided substantial initial understanding of these and related effects. Such particles can be deposited or fabricated on the surface of a device in random[63-66] or geometric patterns.[75-77] In most cases, their essential function is to scatter light such that photon path lengths increase compared to those of photons that are directly transmitted at normal incidence into the device, thereby increasing the fraction of absorbed radiation. The scattering cross-sections of nanoparticles can exceed their geometric cross-sections, and their angular scattering distributions can be tuned with their size, shape, and composition,[78] making nanoparticles a versatile option for studying light management in photovoltaics. Nanowires can also exhibit scattering properties and greater-than-unity interaction cross-sections,[79-81] which, combined with their potential to achieve superior carrier transport and collection

compared to bulk devices, has inspired studies of nanowires for photovoltaic applications.

Numerous studies of nanoparticles for enhancement of photovoltaics have focused on metal particles that exhibit surface plasmon polariton (SPP) resonances. This is partly a result of indications that the strong evanescent fields associated with SPPs, if they exist near the active region of a device, can increase photocurrent generation. The oscillating surface charges and evanescent field associated with SPPs are illustrated in Fig. 2.2. The possibility of destructive interference between the scattered and directly transmitted waves to inhibit photocurrent generation, which results from a phase difference between the waves near the SPP resonance,[82] can be minimized or eliminated by careful choice of the material and size of nanoparticles with respect to the local dielectric environment.

Plasmonic effects and their application to improving photovoltaic device performance continue to be subjects of concerted research efforts. In addition to potential photocurrent enhancement associated with their strong evanescent fields, SPPs can mediate coupling to waveguide modes of photovoltaic devices, and they support confined plasmonic modes. The absorption and scattering cross-sections of sub-wavelength metallic structures are typically large near SPP resonant wavelengths, and efficient coupling of scattered light to waveguide modes of a thin-film device can occur if the momentum of scattered light matches that of a confined mode. The evanescent field of SPPs may also increase the intensity of radiation that couples to waveguide modes relative to light scattered at non-resonant wavelengths. Plasmonic effects do, however, increase absorption by the metal and will generally result in greater ohmic loss of energy than would occur in their absence. For this reason, and because of the potential for scattered fields associated with them to destructively interfere with others, the use of

plasmonic structures for solar cell enhancement must be carefully engineered based on material and device properties and the spectral illumination of a solar cell.

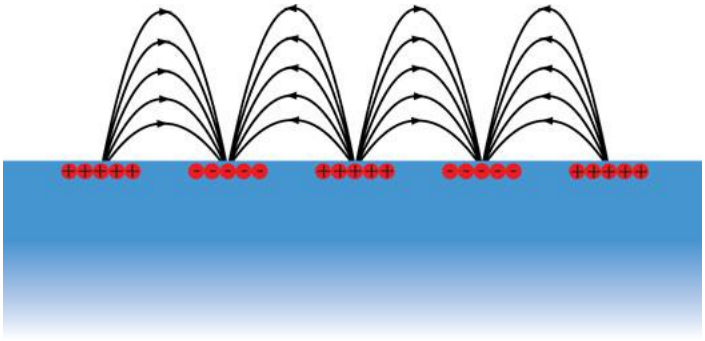

Figure 2.2: An illustration of a point in time of the charge oscillations associated with a surface plasmon polariton. The electric field amplitude decreases exponentially with distance from the surface of the SPP-supporting medium.

The rational design of sub-wavelength structures for light-trapping in solar cells is also an extremely active area of research. These structures typically exhibit variations on length scales similar to the wavelengths targeted for diffraction or scattering. Despite their small feature sizes, advanced lithographic techniques can be used to pattern such structures over large areas.[83-85] Their design and optimization are typically performed numerically and both periodic[70,86-88] and pseudo-random structures[89,90] can be investigated with such approaches. As a result of the fact that periodic structures, such as diffraction gratings,[88,91,92] typically have narrow response bands, optimal periodic structures for scattering of solar radiation are likely to have intricate geometries to handle a relatively broad band of wavelengths, different polarizations and angles of incidence. Rigorous simulation of truly random structures is challenging, in particular because of the significant computational requirements to perform electromagnetic field calculations over large areas. Calculations that use periodic boundary conditions with random geometries

to simulate pseudo-random structures are generally more feasible. As optimal structures are likely to vary depending on the absorbing material of a solar cell and its operating conditions, the rational design of light-scattering structures is likely to be a topic of interest for the foreseeable future.

2.2. Electromagnetic and Optical Effects Related to Light Trapping in Solar Cells

Numerous electromagnetic phenomena affect light trapping in solar cells. Some of these are photonic in nature, such as the propagation of a scattered wave in a bulk device, while others involve evanescent fields and, potentially, coupling between propagating and evanescent modes. This section discusses such effects and how they impact light trapping in a solar cell.

2.2.1. Fabry-Perot Interference

Thin film solar cells, which are assumed to consist of absorber layers on the order of one to several microns in thickness, are unable to absorb all of the light which enters them. Absorption of light that transmits into the devices generally must occur in one round trip through the cell, in the absence of light trapping. A reflective structure on the bottom of a solar cell is required to enable the second pass of the round trip. When such a reflection occurs, the incident and reflected fields interfere, which has an important impact on absorption in thin film devices.

Interference between specular reflected waves in a film is known as Fabry-Perot interference. If the thickness of a film is an integer multiple of the wavelength of light, then the incident and reflected waves are in-phase and constructively interfere. If the waves are out of phase, destructive interference can diminish the incident and reflected

fields. The phase difference, δ, between the incident and reflected waves in a thin film cavity is:

$$\delta = \left(\frac{2\pi}{\lambda_1}\right) 2n_2 l\cos(\theta) \tag{2.1}$$

where λ_1 is the wavelength of light in medium 1, which has an index of refraction n_1; and n_2 is the refractive index of the medium, l is the thickness of the film, and θ is the angle of incidence with respect to the surface normal. This situation is illustrated in Fig. 3.3. For most wavelengths, interference between the incident and reflected waves is somewhere between totally constructive and totally destructive.

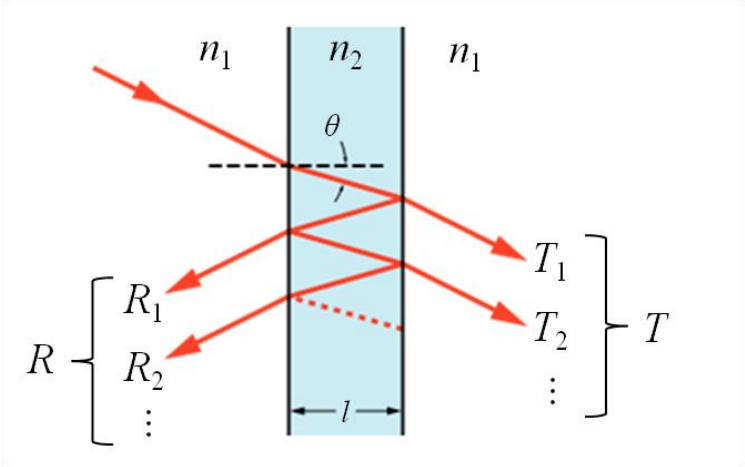

Figure 2.3: Fabry-Perot interference in a thin film with refractive index n_2, surrounded by a dielectric environment of refractive index n_1. The total steady-state reflection, R, and transmission, T, equal the sums of the magnitudes of each reflection and transmission event that occur when incident light propagates in the thin film.

Constructive Fabry-Perot interference cannot be achieved for every wavelength in the solar spectrum, or even for most of them, suggesting that broadband absorption can be improved by scattering incident light such that fields are redirected to laterally-propagating paths before interfering reflections occur. In principle, the best case is to

scatter incident light into a waveguide mode supported by a device such that: (1) light couples efficiently into the waveguide mode; (2) maxima in the electromagnetic field distribution overlap spatially with the semiconductor absorber; and (3) parasitic loss of power in the waveguide mode, such as by metal absorption or leakage through non-conductive waveguide boundaries, is minimized.

2.2.2. Coupling of Light to Waveguide Modes of a Solar Cell

Fabry-Perot interference occurs for light in radiating modes of a device structure and considerable field intensity may be lost each time the field encounters an interface, due to absorption at a metal-dielectric interface or to transmission at a dielectric-dielectric interface. It is, therefore, compelling to employ techniques that increase the path length of photons in a device beyond those associated with specular reflections that give rise to Fabry-Perot resonances, and to minimize transmission and parasitic absorption losses. Coupling incident radiation to waveguide modes of solar cells can potentially meet both of those goals, and this section discusses the properties of waveguides and principles for coupling light to guided modes of solar cells.

2.2.3. Modes of Slab Waveguides

A planar dielectric structure, such as the one shown in Fig. 2.4, supports discrete, laterally-propagating waveguide modes that are confined to the dielectric film. These contrast to radiating modes in the structure, which may have lateral components of propagation (i.e., waves propagating at non-normal angles with respect to the surface of a device), but which partially couple out of the device each time light encounters an interface, as shown in Fig. 2.3. The properties of guided modes depend on the permittivity of the waveguide and its thickness. The permeability is also important,

though, in the following discussion, it may be assumed that materials are non-magnetic (i.e., $\mu = \mu_0$).

To simplify the analysis of guided modes, we assume that a thin film consists of a planar, charge-free dielectric medium surrounded by planar boundaries that are perfectly conducting. While this is not representative of the conditions in a thin film solar cell, these assumptions provide a convenient analytical framework, and the results of calculations that use them are generally similar to those of arbitrary structures. A wave can propagate in the waveguide with either transverse electric (TE), transverse magnetic (TM), or transverse electromagnetic (TEM) polarization, and the polarization determines the boundary conditions that must be satisfied. The electric and magnetic field intensities in the dielectric region must satisfy the homogeneous Helmholtz equations:

$$\nabla^2 \mathbf{E} + k^2 \mathbf{E} = 0 \tag{2.2}$$

$$\nabla^2 \mathbf{H} + k^2 \mathbf{H} = 0 \tag{2.3}$$

where $\mathbf{E}$ and $\mathbf{H}$ are the vector electric and magnetic fields, and $k = \omega\sqrt{\mu\epsilon}$ is the wavenumber.

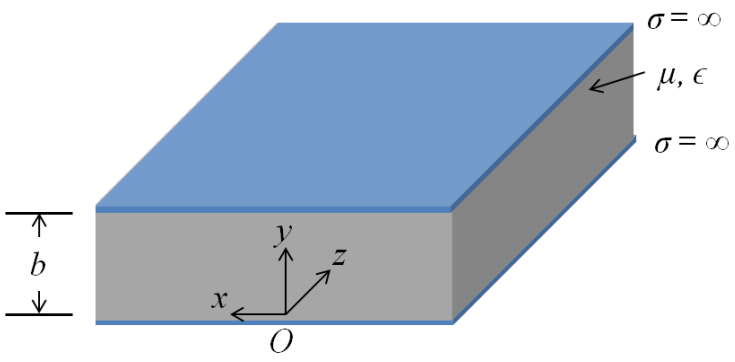

Figure 2.4: A parallel-plate waveguide consisting of two perfectly conducting boundaries ($\sigma = \infty$) separated by a medium of thickness, b, with dielectric permittivity, ϵ, and magnetic permeability, $\mu = \mu_0$. The film extends infinitely in the $\pm\boldsymbol{x}$ and $\pm\boldsymbol{z}$ directions.

We assume that waves propagate in the +z direction, according to the geometry of Fig. 2.4, and that they have a propagation constant $\gamma = \alpha + i\beta$, where $i = \sqrt{-1}$. The harmonic time dependence of electric and magnetic fields corresponding to light with angular frequency ω acquires a phase of $e^{-j\omega t}$ and is attenuated according to $e^{-\gamma z}$ as it propagates along the guide. Thus, the electric field may be written:

$$E(x, y, z, t) = Re\left[\mathrm{E}_0(x, y)e^{(j\omega t - \gamma z)}\right], \tag{2.4}$$

where E_0 is the initial electric field amplitude and *Re*[ ] denotes the real part of the bracketed expression. A similar expression may be written for the **H** field according to the Maxwell relation

$$\boldsymbol{\nabla} \times \mathbf{E} = -i\omega\mu\mathbf{H}. \tag{2.5}$$

The first term of Eq. 2.2 can be written in terms of the longitudinal (z) and transverse (x, y) electric field components:

$$\boldsymbol{\nabla^2}\mathbf{E} = \left(\boldsymbol{\nabla}_{xy}^2 + \boldsymbol{\nabla}_z^2\right)\mathbf{E} = \left(\boldsymbol{\nabla}_{xy}^2 + \frac{\partial^2}{\partial z^2}\right)\mathbf{E} = \boldsymbol{\nabla}_{xy}^2\mathbf{E} + \gamma^2\mathbf{E}. \tag{2.6}$$

Combining Eqs. 2.2 and 2.6 gives:

$$\boldsymbol{\nabla}_{xy}^2\mathbf{E} + (\gamma^2 + k^2)\mathbf{E} = 0. \tag{2.7}$$

Similarly, for the magnetic field:

$$\boldsymbol{\nabla}_{xy}^2\mathbf{H} + (\gamma^2 + k^2)\mathbf{H} = 0, \tag{2.8}$$

where

$$h \equiv \gamma^2 + k^2. \tag{2.9}$$

Each guided wave has a profile that is determined by the frequency of light, the dielectric and magnetic properties of the waveguide medium, and the boundary conditions. A TM wave propagating in the z direction has a modal field profile that varies in the y direction, due to confinement by the guiding layer. Assuming that the electric field varies only with the y coordinate, Eq. 2.7 can be written:

$$\frac{d^2E_z^0(y)}{dy^2} + h^2E_z^0(y) = 0. \tag{2.10}$$

The perfectly conducting waveguide boundaries require that

$$E_z^0(y = 0) = E_z^0(y = b) = 0, \tag{2.11}$$

where b is the waveguide thickness, as shown in Fig. 2.4. Based on the second-order differential form of Eq. 2.10 and on the conditions of Eq. 2.11, the electric and magnetic fields of a TM guided wave ($H_z = 0$) in a parallel-plate slab waveguide are sinusoidal in the y direction, with

$$E_z^0(y) = A_n \sin\left(\frac{n\pi y}{b}\right) \tag{2.12}$$

$$H_x^0(y) = \frac{i\omega\epsilon}{h} A_n \cos\left(\frac{n\pi y}{b}\right) \tag{2.13}$$

$$E_y^0(y) = -\frac{\gamma}{h} A_n \cos\left(\frac{n\pi y}{b}\right) \tag{2.14}$$

where A_n depends on the strength of excitation of a TM mode, the mode index is given by the integer n = 1, 2, 3, ..., where

$$h = n\pi/b, \tag{2.15}$$

and, based on Eqs. 2.9 and 2.15, the propagation constant of the TM mode is given by:

$$\gamma = \sqrt{\left(\frac{n\pi}{b}\right)^2 - \omega^2\mu\epsilon} \tag{2.16}$$

The cutoff frequency of a mode, f_c, is the frequency at which $\gamma = 0$, indicating that the field no longer propagates (i.e., it is evanescent):

$$f_c = \frac{n}{2b\sqrt{\mu\epsilon}}. \tag{2.17}$$

By similar analysis, it can be demonstrated that the TE modes of a parallel-plate waveguide have the same cutoff frequencies as TM modes. Importantly, thick

waveguides support more propagating modes at a given frequency of light than thin films because the modes cut off at lower frequencies as b increases, as illustrated by Eq. 2.17. Thus, relatively thick guiding layers can be beneficial for waveguiding to trap light in solar cells because they support more modes to which scattered light may couple.

Quantifying the net effect of schemes for light trapping on the performance of solar cells is essential to their thorough evaluation. Simulations that calculate the distribution of electromagnetic energy within a device structure, which consists of the aggregate of scattered/diffracted fields and those transmitted directly into a device, enable such quantitative evaluation. These simulations can compute quantities associated with the overlap of electromagnetic fields and the absorbing layers of a solar cell, such as the rate of dissipation (i.e., absorption) of electromagnetic energy, which can be a means of evaluating how coupling to different waveguide modes influences photocurrent generation and the short-circuit current of a device. To understand how different guided modes can affect photocurrent generation, consider Eq. 2.12, from which it can be seen that high order modes (large n) have more nodes in their field patterns than low order modes (small n). This means that high order modes have more minima and maxima in their spatial electric field distribution than low order modes. The overlap of the active region of a solar cell and the electric field is important because absorption in the semiconductor is largest at field maxima.

The net distribution of electromagnetic energy within a solar cell is a function of many wavelengths of light, and each has different field characteristics. Thus, for optimizing device performance, it is, in general, more useful to calculate the net photocurrent generation (i.e., the short-circuit current, if assumptions about carrier collection are made) in a device structure than just the photocurrent generated at an individual wavelength. In that regard, a primary quantity of interest is the volume-

integrated absorbed power in the active layers of a device, which can be calculated according to:[93]

$$U_A(\omega) = \frac{\omega}{2} \int_V \mathrm{Im}[\epsilon(\omega, \mathbf{r})] \, |\mathbf{E}(\mathbf{r})|^2, \tag{2.18}$$

where $\mathbf{r} = (x, y, z)$ is the position in the device, ω is the frequency of the electromagnetic incident radiation, $\epsilon(\omega, \mathbf{r})$ is the complex dielectric function in the device structure, which may vary spatially, such as in quantum well or dot solar cells, where multiple materials are present, and V denotes integration over the volume of semiconductor that comprises the active device. The calculation of Eq. 2.18 is useful because of its generality: it incorporates absorption of light in radiation and evanescent modes, including waveguide modes, and the spatial overlap of all of these modes with the absorbing materials.

Finally, although it has been assumed that a waveguide consists of two parallel, conducting plates with a dielectric layer in between, it will be seen in the following chapters that the solar cells studied in this work deviate from this geometry. The devices have one conducting boundary, which is on the bottom of the device, and are bound on the top by a low-index dielectric layer, such as SiO_2, or by air. The properties of the TE and TM waves supported by the devices are nominally similar to those just presented. However, Ampere's circuital law states that the magnitudes of the longitudinal conduction and displacement currents (i.e., currents in the direction of propagation) are related to the integrated transverse magnetic field along a closed loop. A TEM mode has $E_z = 0$, which, therefore, means that it has no longitudinal displacement current, implying that no closed magnetic field loops exist in any transverse plane. Thus, TEM modes cannot be supported without a second conductor to enable a longitudinal current in the waveguide, and scattered or diffracted light must couple to TE or TM modes in the solar

cells studied in this dissertation. Scattering and diffraction of light into the modes of quantum well and dot solar cells will be demonstrated as a means to light trapping in solar cells in the following chapters.

2.2.4. Periodic and Random Structures for Coupling Light to Waveguide Modes

As discussed in Sec. 1.4, all materials scatter light. If the materials contain features of sizes less than a wavelength of light, or if the materials are themselves of that size, then the scattering properties will be considerably different from those of the corresponding bulk material. Similarly, if the physical shape or composition of a structure varies, then light incident on different portions can reflect and transmit with different phases, producing an interference pattern in the total reflected and transmitted fields. That phenomenon is referred to as *diffraction*.

Diffractive structures have periodic, spatially varying dielectric composition and are commonly referred to as *diffraction gratings*. Two examples are *surface relief gratings* and *volume gratings*. The physical profile of a surface relief grating varies, with a period Λ, and several examples appear in Fig. 2.5(a-c). Volume gratings consist of planar structures with internally varying dielectric profile, as illustrated in Fig. 2.6. Fig. 2.5(d) illustrates random scattering features, which comprise disordered surface relief and do not induce typical diffraction of light, in contrast to gratings.

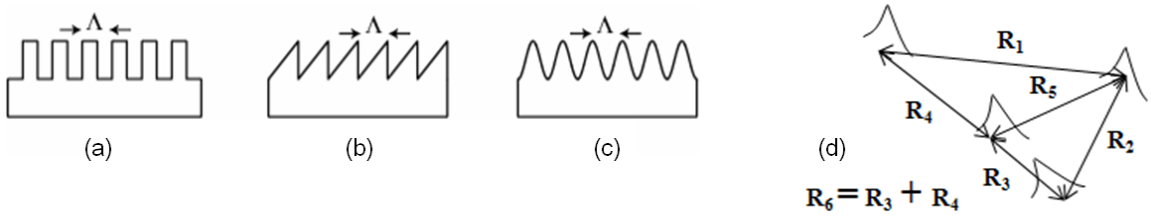

Figure 2.5: (a-c) Surface relief gratings of period Λ, with (a) binary, (b) blazed, and (c) sinusoidal profiles. (d) Random scattering features with distances labeled by position vectors **R**.

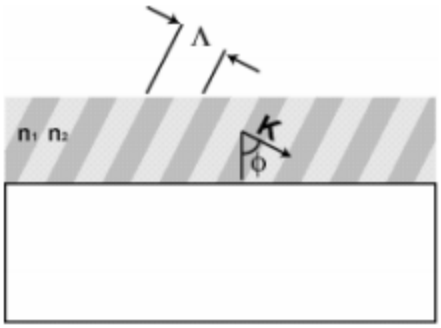

Figure 2.6: A volume grating, which consists of a planar surface with internal alternating layers of refractive index n_1 and n_2, aligned at an angle, ϕ, with respect to the surface normal of the grating.

Gratings are characterized by their grating vector, **K**, which is analogous to the lattice constant of a crystalline material. Just as an electron can experience a change in momentum when it scatters from one energetic state to another, which is mediated by lattice phonons, gratings change the momentum of light via diffraction. This is expressed in the grating equation:

$$\mathbf{k}_q = \mathbf{k}_u - q\mathbf{K}, \tag{2.19}$$

where $q = 0, \pm1, \pm2, \ldots$ is the order of diffraction, $\mathbf{k}_u$ is the wavevector of the undiffracted wave, corresponding to $q = 0$ (i.e., the wave that undergoes specular reflection or transmission), and $\mathbf{k}_q$ is the wavevector of the q^{th} diffracted order. The diffraction equation relates the direction of propagation of incident and diffracted waves:

$$n_t \sin\theta_q = n_i \sin\theta_i - q\frac{\lambda}{\Lambda} \tag{2.20}$$

where n_i is the refractive index of the incident medium, n_t is the refractive index of the transmitted medium, and λ is the wavelength of light.

Gratings are strongly dispersive, as demonstrated in Eq. 2.20. The diffraction order and angle are highly sensitive to the wavelength of light, grating period, angle of incidence, and the refractive indices of the incident medium and grating. In particular,

Eq. 2.20 indicates that if the grating period is small compared to the wavelength, then the grating orders cut off, beginning with the highest indices. Cut off orders are indicated by complex-value θ_q, implying that diffracted waves are evanescent. Fig. 2.7 illustrates a binary surface relief grating where, for a wave incident at angle θ_i, the labeled reflected and transmitted diffraction orders propagate away from the grating at various angles, which are θ_q in Eq. 2.20. Orders that do not appear in the illustration are cut off and do not propagate. Using a large dielectric contrast (i.e., large n_t compared to n_i) enables smaller periods to be used without cutting off high diffraction orders.

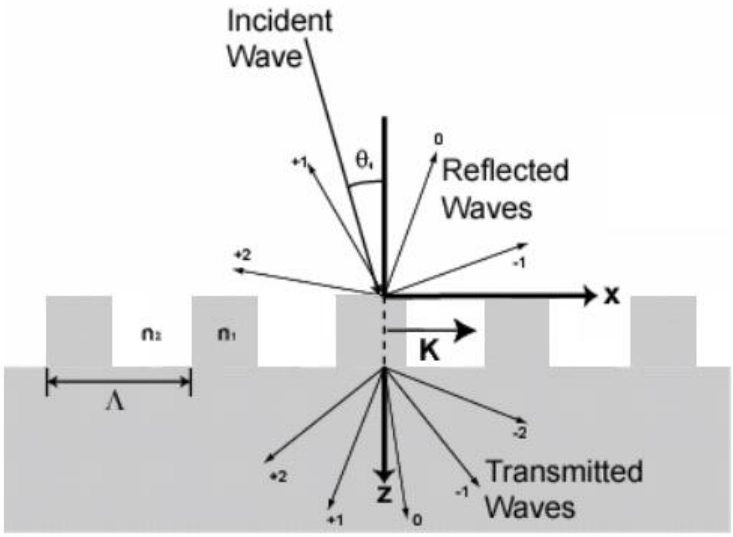

Figure 2.7: A binary dielectric surface relief grating with the reflected and transmitted diffraction orders labeled.

2.2.4. Requirements for Coupling of Scattered Light to Waveguide Modes

Diffracted light can couple to a waveguide mode of a guiding structure if the effective index of refraction of the diffracted light matches the effective index of a waveguide mode. The effective index of diffracted light is the ratio of the tangential

component of the diffracted wave, which is denoted by k_{qx} based on the geometry of Fig. 2.7, to the free space wavevector, k, where the former is given by:

$$k_{qx} = \frac{2\pi n_t}{\lambda}\sin\theta_q. \tag{2.21}$$

The effective index of order q is then:

$$n_{eff}^{q} = \frac{k_{qx}}{k} = \frac{\frac{2\pi n_t}{\lambda}\sin\theta_q}{\frac{2\pi}{\lambda}} = n_t\sin\theta_q, \tag{2.22}$$

and the condition for coupling to guided modes is found by substituting Eq. 2.22 into Eq. 2.20:

$$n_{eff}^{q} = n_i\sin\theta_i - q\frac{\lambda}{\Lambda}. \tag{2.23}$$

It is evident from Eq. 2.23 that guided mode coupling is sensitive to the incident angle for a given wavelength and grating period. Relatively little mismatch between the effective indices of a diffracted wave and that of a waveguide mode can be tolerated for the diffracted wave to couple efficiently to the mode. Therefore, the combination of broad spectral width, and, ideally, wide angular distribution over which coupling to waveguide modes is desired for light trapping in solar cells poses a significant challenge for optimal design of gratings and similar structures.

One approach to addressing that challenge is to use a randomly structured light scattering object (or set of objects), such as the one represented by Fig. 2.5(d). These structures can potentially satisfy the mode coupling requirement of Eq. 2.23 for a greater number of guided modes than a grating because they have many more "grating" wavenumbers resulting from the random positions of features. However, the relatively low frequency with which any given wavenumber occurs for a random surface means that the net scattering amplitude for any one of them may be much smaller than it is for a grating with that wavenumber. There is, therefore, an open question of what degree of

order, or disorder, is most beneficial for light trapping in solar cells. Because it is difficult to rigorously optimize the geometry of random and pseudo-random structures, this work focuses on planar, periodic scattering structures with multiple periods. Such structures are promising for light trapping in solar cells,[94] and they lend themselves to rigorous optimization using software algorithms because they are periodic, enabling boundary conditions to be used that minimize computational requirements. The optimization approach used in this work is discussed in Sec. 4.2.

2.3. Selection Rules on Optical Transitions in Nanostructured Materials

Absorption of light involves the interaction of electromagnetic waves with electric dipoles formed by atomic particles. The direction of the electric field of interacting radiation and the orientation of electric dipoles in an illuminated material in part determine the strength of their interaction, which relates to the polarizability of the material. The orientation of the dipoles is determined by orbital configurations of the valence electrons that form bonds between atoms in a material. These are fundamentally based on quantum mechanical properties, including spin and angular momentum, which influence the geometry of dipoles and atomic bonds. Consequently, there can be restrictions on the strength of optical transitions in a material that depend on its structural symmetry and bonding geometry. These *selection rules*, and their effect on absorption and emission in nanostructured solar cells, are the focus of this section.

2.3.1. Anisotropic Absorption and Emission of Light in Quantum Confined Semiconductors

Optical transitions are governed by Fermi's Golden Rule, which is given by Eq. 1.31. Based on Fermi's Golden Rule, it is evident that the overlap of wavefunctions in the initial and final states and the result of the polarization-momentum operator acting on the

transition are key determinants of transition strength. For the solar cells in this dissertation, we are principally interested in interband transitions between the valence and conduction bands, because they correspond to energies that are prominent in the solar spectrum. It has been assumed that these bands have simple parabolic shapes, according to Eq. 1.5. Optical phenomena, however, are sensitive to the band structure, and a more detailed model is needed to accurately compute their influence in the performance of solar cells investigated in this dissertation.

The structure of a material's valence band is more complicated than that of the conduction band, and its properties result from how atoms bond in the material. Si, for example, has four valence electrons: two in a filled *s* orbital, and two within the three *p* orbitals, which can have a total of six electrons. In crystalline Si, the *s* and *p* orbitals of neighboring Si atoms hybridize to form four sp^3 orbitals, creating the diamond lattice of Si. The valence band results from "bonding" combinations of sp^3 orbitals, and the conduction band results from "anti-bonding" combinations of the same orbitals. States with energies near the top of the valence band have the symmetry of *p* orbitals, while states near the bottom of the conduction band have *s*-like symmetry.

The crystal lattices of compound semiconductors, such as GaAs and InAs, are less symmetric than those of elemental crystals because they consist of multiple atoms. As a result, the bonds are somewhat weaker, and the valence band splits into one band, from hybridization of *s* orbitals, which is lower in energy than the triple band formed by the three *p* orbitals. The *s*-based band is too low in energy to be accessed for interband transitions, so it is omitted from the set of electronic states that are considered to be the valence band, which is taken as the three *p*-based bands.

The geometry of orbitals that form a band strongly determines its dispersive properties. For example, if a material with a simple cubic crystal structure has bonded *p*

orbitals that are aligned in the z direction, as illustrated in Fig. 2.8, then the wavefunctions overlap strongly in the z direction and they overlap weakly in the x-y plane. This makes electronic transport *anisotropic*: electrons and holes move relatively easily in the z direction compared to the x and y directions. Their effective masses are therefore lower in the z direction than in the transverse directions. Correspondingly, the threefold p orbital valence band splits into a 'light hole' band and doubly degenerate 'heavy hole' bands, as shown in Fig. 2.9(a) and (b), respectively. The picture is complicated by the relativistic effect of "spin-orbit splitting," in which one of the two heavy hole bands shifts to a lower energy, leaving one light and one heavy hole band that are degenerate in energy, as shown in Fig. 2.9(c).

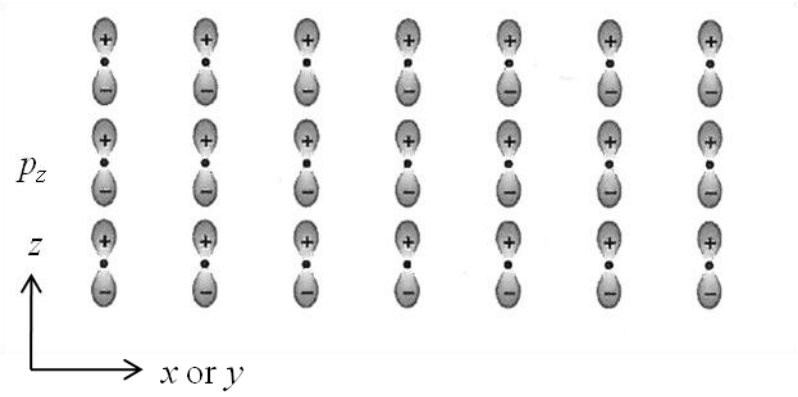

Figure 2.8: p_z orbitals of atoms in a simple cubic crystal, illustrating that the bonds facilitate efficient charge transport between atoms in the z direction but not in the transverse directions. Thus, the z direction corresponds to a light hole band and the transverse directions correspond to doubly degenerate heavy hole bands.

The valence bands are, in fact, still more complicated than has been described to this point, and a more comprehensive model is needed for the sake of evaluating optical transitions. To that end, the Kane model is applied to determine structures of the

conduction and valence bands in semiconductors.[95] The Kane model is based on $\mathbf{k} \cdot \mathbf{p}$ theory† and it can calculate the band structure near the conduction and valence band edges ($\mathbf{k} = 0$), including E-$\mathbf{k}$ dispersion relations and wavefunctions of the states, from a limited set of basis states. As will be shown, the symmetry of the basis states is a key determinant of the strength of radiative transitions. In this work, which uses a four band Kane model, the set of basis states is chosen as one wavefunction with s orbital symmetry, $|S\rangle$, corresponding to the conduction band state, and three valence band wavefunctions, $|X\rangle$, $|Y\rangle$, and $|Z\rangle$, which have the symmetry of p_x, p_y, and p_z orbitals, respectively.

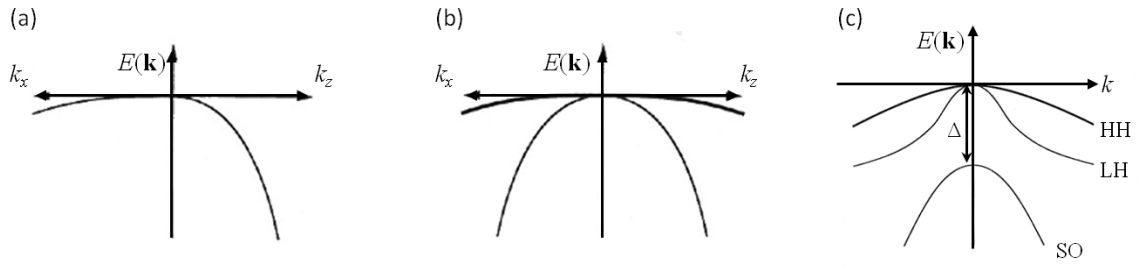

Figure 2.9: Dispersion diagrams of the valence band in a compound semiconductor, such as GaAs, InAs, or $In_xGa_{1-x}As$ that is formed by the p_z-bonded orbitals of Fig. 2.8: (a) a heavy hole band along k_x and a light hole band along k_z (the band is also heavy along k_y, which is not shown); (b) the single light hole band and doubly degenerate heavy hole bands arising from all of the p orbitals; and (c) a more accurate picture of the valence band, in which the split-off band (SO) is at energy Δ below the valence band maximum, where the heavy hole (HH) and light hole (LH) bands are degenerate.

Spin-orbit coupling must be considered in the Kane model of the valence band because of its effect on bonding. This phenomenon occurs because of interaction between the magnetic moment associated with the spin of an electron and the magnetic field

† Refer to Appendix 1 for more information about $\mathbf{k} \cdot \mathbf{p}$ theory.

produced by the electron, which results in different energetic states, depending on their alignment. Suppose an electron has orbital angular momentum **l** and spin **s**; the spin-orbit coupling energy is proportional to $\mathbf{l} \cdot \mathbf{s}$. The spin-angular momentum state of an electron depends on its bonding behavior: spin, which is assumed to be oriented along z, is $s_z = \pm\frac{1}{2}$, and s-symmetric states have $l = 0$, while p-symmetric states have $l = 1$ and $m = l_z = -1, 0, 1$, where m describes the magnetic moment of an electron.

The different combinations of spin and magnetic moment correspond to distinct p-symmetric valence band states that are labeled according to their spin and angular momentum. For example, $|{+1}\uparrow\rangle$ denotes the state with $m = +1$ and $s_z = +\frac{1}{2}$ (i.e., spin up, which is indicated by the upward pointing arrow). In the conduction band, the s-symmetric state supports both up and down spins, and its $l = 0$ designation precludes spin-orbit effects from influencing conduction band states. The conduction band state is therefore denoted $|S\uparrow\downarrow\rangle$, where only one arrow normally appears, to indicate the spin. The spin-orbit valence band states are designated by their magnetic moment index, and they relate to the valence band basis states as follows:

$$|0\rangle = |Z\rangle, \qquad |\pm 1\rangle = \sqrt{\frac{1}{2}}(|X\rangle \pm i|Y\rangle). \tag{2.24}$$

The valence band states are characterized by their total angular momentum, $\mathbf{j} = \mathbf{l} + \mathbf{s}$, where quantum mechanics requires, as in the cases of **l** and **s**, that **j** be quantized. The allowed combinations for $l = 1$ and $s = \frac{1}{2}$ are either $j = \frac{3}{2}$ with corresponding $j_z = \pm\frac{3}{2}, \pm\frac{1}{2}$, or $j = \frac{1}{2}$ with corresponding $j_z = \pm\frac{1}{2}$. Thus, valence band states are designated $|j, j_z\rangle$ as follows:

$$|\tfrac{3}{2}, +\tfrac{3}{2}\rangle = |{+1}\uparrow\rangle,$$
$$|\tfrac{3}{2}, +\tfrac{1}{2}\rangle = \sqrt{\tfrac{1}{3}}|{+1}\downarrow\rangle - \sqrt{\tfrac{2}{3}}|0\uparrow\rangle,$$

$$
\begin{aligned}
|\tfrac{3}{2},-\tfrac{1}{2}\rangle &= -\sqrt{\tfrac{1}{3}}|-1\uparrow\rangle - \sqrt{\tfrac{2}{3}}|0\downarrow\rangle,\\
|\tfrac{3}{2},-\tfrac{3}{2}\rangle &= |-1\downarrow\rangle,\\
|\tfrac{1}{2},+\tfrac{1}{2}\rangle &= \sqrt{\tfrac{2}{3}}\left|+1\downarrow\right\rangle - \sqrt{\tfrac{1}{3}}\left|0\uparrow\right\rangle,\\
|\tfrac{1}{2},-\tfrac{1}{2}\rangle &= -\sqrt{\tfrac{2}{3}}\left|-1\uparrow\right\rangle + \sqrt{\tfrac{1}{3}}\left|0\downarrow\right\rangle.
\end{aligned}
\tag{2.25}
$$

The heavy holes correspond to states $|\frac{3}{2},\pm\frac{3}{2}\rangle$, and light hole states correspond to $|\frac{3}{2},\pm\frac{1}{2}\rangle$.

Now, we apply the Kane model to optical transitions. Assume that the direction of the epitaxial growth of quantum wells in a device is *z*. Carriers are confined in the *z* direction by the quantum well potential, while they are unconfined in the transverse directions. The influence of the quantum well potential on carriers must be considered in additional to the periodic potential imposed by the atoms of the crystal lattice. Because of the separability of the terms associated with the quantum well potential and the lattice potential, the wavefunction in quantum well sub-band states can be factored into Bloch waves, corresponding to bulk crystal states, which are modulated by an envelope produced by the quantum well confinement potential:

$$\psi(\mathbf{r}) \propto \chi(\mathbf{r})u_{n\mathbf{0}}(\mathbf{r}). \tag{2.26}$$

Here, χ is the envelope function, $u_{n\mathbf{0}}$ is the Bloch wave at $\mathbf{k}=0$, and *n* is the band index. Denote the volume of a crystal by Ω, over which the wavefunction must be normalized. Then the optical matrix element in Eq. 1.31 can be written:

$$\langle j|\mathbf{e}\cdot\hat{\mathbf{p}}|i\rangle = \Omega\int_{\Omega}\chi_{\mathrm{c}}^{*}(\mathbf{r})u_{\mathrm{c}}^{*}(\mathbf{r})(\mathbf{e}\cdot\hat{\mathbf{p}})\chi_{\mathrm{v}}(\mathbf{r})u_{\mathrm{v}}(\mathbf{r})d^{3}\mathbf{r}, \tag{2.27}$$

where ‘c’ and ‘v’ denote conduction and valence band states, respectively. The Bloch functions vary within each unit cell of the crystal because the spacing of atoms is on the order of one Angstrom. The envelope functions vary over length scales of one to two orders of magnitude greater than the Bloch functions, corresponding to typical quantum

well thicknesses of several to tens of nanometers. The envelope function is, therefore, essentially constant within a unit cell and Eq. 2.27 can be simplified by summing over the unit cells in a crystal and, for each cell, integrating over its volume:

$$\langle j|\mathbf{e}\cdot\hat{\mathbf{p}}|i\rangle \approx \Omega \sum_{j}^{\text{cells}} \chi_{\text{c}}^{*}(\mathbf{r})\chi_{\text{v}}\,(\mathbf{r}) \int_{\text{cell } j} u_{\text{c}}^{*}(\mathbf{r})(\mathbf{e}\cdot\hat{\mathbf{p}})u_{\text{v}}\,(\mathbf{r})d^{3}\mathbf{r}\,. \tag{2.28}$$

The transition is assumed to occur between states at the conduction and valence band edges, where $\mathbf{k}=0$. Denote the integral over a unit cell $(\Omega_{\text{cell}}/\Omega)\mathbf{e}\cdot\mathbf{p}_{\text{cv}}(\mathbf{0})$, where Ω_{cell} is the volume of a unit cell, and

$$p_{\text{cv}}(\mathbf{k}) = \frac{1}{\Omega_{\text{cell}}} \int_{\text{cell}} u_{\text{ck}}^{*}(\mathbf{r})(\mathbf{e}\cdot\hat{\mathbf{p}})u_{\text{vk}}(\mathbf{r})d^{3}\mathbf{r}\,. \tag{2.29}$$

Eq. 2.28 may then be written as:

$$\langle j|\mathbf{e}\cdot\hat{\mathbf{p}}|i\rangle \approx \mathbf{e}\cdot\mathbf{p}_{\text{cv}}(\mathbf{0})\Omega_{\text{cell}} \sum_{j}^{\text{cells}} \chi_{\text{c}}^{*}(\mathbf{r})\chi_{\text{v}}\,(\mathbf{r})\,. \tag{2.30}$$

Finally, because of the large number of unit cells that comprise typical crystalline samples, the sum over the unit cells can be converted to an integral over the volume of the crystal, which absorbs the factor of Ω_{cell} due to normalization of the wavefunctions:

$$\langle j|\mathbf{e}\cdot\hat{\mathbf{p}}|i\rangle \approx \mathbf{e}\cdot\mathbf{p}_{\text{cv}}(\mathbf{0}) \int_{\Omega} \chi_{\text{c}}^{*}(\mathbf{r})\chi_{\text{v}}\,(\mathbf{r})d^{3}\mathbf{r}\,. \tag{2.31}$$

In the simplest case, the envelope functions in a quantum well are unbound plane waves in the x and y directions and a bound wave in the z direction. In the conduction band, the envelope function may then be written:

$$\chi_{\text{c}}\,(\mathbf{r}) = A^{-\frac{1}{2}}\exp(i\mathbf{k}\cdot\mathbf{r})\,\phi_{cn}(z) \equiv |n\mathbf{k}\rangle. \tag{2.32}$$

Eq. 2.31 then becomes:

$$\langle j|\mathbf{e}\cdot\hat{\mathbf{p}}|i\rangle = \langle n\mathbf{k}'|\mathbf{e}\cdot\hat{\mathbf{p}}|m\mathbf{k}\rangle \approx \mathbf{e}\cdot\mathbf{p}_{cn,\text{v}m}\delta_{\mathbf{k},\mathbf{k}'} \int \phi_{cn}^{*}(z)\phi_{\text{v}m}(z)dz\,, \tag{2.33}$$

where m and n are valence and conduction sub-band indices, and $\mathbf{k}$ and $\mathbf{k}'$ are the transverse wavevectors, respectively. The Dirac delta function, $\delta_{\mathbf{k},\mathbf{k}'}$, appears because integrating over orthogonal plane waves, for which $\mathbf{k} \neq \mathbf{k}'$, evaluates to zero. Eq. 2.33 shows that there are two selection rules on interband optical transitions in a quantum well. One relates to the polarization-momentum matrix element, which will simply be referred to as the "interband optical matrix element." The second selection rule relates to the overlap of quantum well bound state envelope functions for the initial and final states. These are each discussed in the following three sections.

2.3.2. The Interband Optical Matrix Element

The first selection rule relates to the polarization of light, $\mathbf{e}$, and the symmetry of dipoles formed by interacting states in the valence and conduction bands. The strengths of optical transitions depend on the overlap of initial and final state wavefunctions, which are related by the following interaction matrix, with the conduction band state labeling the row and three valence band states listed in the column headers:

$$\begin{matrix} & |\frac{3}{2},\frac{3}{2}\rangle & |\frac{3}{2},\frac{1}{2}\rangle & |\frac{1}{2},\frac{1}{2}\rangle \\ \langle S\uparrow| & 0 & -i\sqrt{\frac{2}{3}}Pk & i\sqrt{\frac{1}{3}}Pk \end{matrix}, \tag{2.34}$$

where P is a material dependent parameter that is defined by the relations

$$\langle S|p_x|X\rangle = \langle S|p_y|Y\rangle = \langle S|p_z|Z\rangle \equiv (im_0/\hbar)P, \tag{2.35}$$

while all other combinations are zero by symmetry (e.g., $\langle S|p_y|X\rangle = 0$).

The heavy hole band corresponds to $|\frac{3}{2},\frac{3}{2}\rangle$ states, which, according to Eqs. 2.24 and 2.25, are equivalent to $|+1\uparrow\rangle = \sqrt{\frac{1}{2}}(|X\uparrow\rangle \pm i|Y\uparrow\rangle)$. We assume for the moment that light is polarized in the x direction, so that $\mathbf{e}\cdot\hat{\mathbf{p}} = p_x$. The optical matrix element for transitions from a heavy hole state to a conduction band state then has the form:

$$\langle S\uparrow|p_x|\frac{3}{2},\frac{3}{2}\rangle = \sqrt{\frac{1}{2}}(\langle S\uparrow|p_x|X\uparrow\rangle + i\langle S\uparrow|p_x|Y\uparrow\rangle) = \frac{im_0P}{\hbar\sqrt{2}}. \quad (2.36)$$

It is evident that the magnitude of the transition is the same for *y*-polarized light (for which the operator p_y replaces p_x in Eq. 2.36) because the heavy hole wavefunction has equal contributions from *x* and *y*-symmetric orbital states. However, for *z*-polarized light, both terms on the right hand side of Eq. 2.36 equal zero and radiative transitions cannot occur, or are 'forbidden.'

Transitions to and from the light hole band involve $|\frac{3}{2},\frac{1}{2}\rangle$ states, which, according to Eqs. 2.24 and 2.25, may be written as:

$$|\frac{3}{2},\frac{1}{2}\rangle = \sqrt{\frac{1}{3}}|+1\downarrow\rangle - \sqrt{\frac{2}{3}}|0\uparrow\rangle = \sqrt{\frac{1}{6}}|X\downarrow\rangle + i\sqrt{\frac{1}{6}}|Y\downarrow\rangle - 2\sqrt{\frac{1}{6}}|Z\uparrow\rangle. \quad (2.37)$$

It can be seen from Eq. 2.37 that radiative transitions between the light hole band and conduction band occur for all polarizations of light. The strength of a transition is proportional to the square of the optical matrix element, so absorption and emission of photons via transitions that involve light hole states occurs four times as strongly for *z*-polarized light than for *x*- and *y*-polarized light. These results are summarized in Table 2.1.

2.3.3. Strain in Heterostructures and its Effect on Optical Transition Selection Rules

The analysis of the interband optical matrix element in the preceding section applies to both bulk materials and quantum confined materials, because confinement does not change the orbital symmetry of valence and conduction band states. The difference arises because of the effect of strain on the bands of heterostructures.[96] Hydrostatic strain, which corresponds to a change in the volume of a material without affecting the symmetry of the crystal lattice, produces equal shifts in band energies such that any degeneracy is unaffected. Uniaxial or biaxial stress breaks the symmetry of a *crystal*

(which is to be distinguished from the symmetry of the orbitals), causing bands that are degenerate in energy to become non-degenerate.

In a quantum well consisting of lattice mismatched materials, hydrostatic and uniaxial and/or biaxial stress may be present. For example, when pseudomorphic (i.e., strained) InGaAs is epitaxially grown on GaAs, the InGaAs experiences biaxial compressive strain, which shifts the energy of the conduction band and the average energy of the valence bands relative to their energies in unstrained material. The biaxial strain also induces different shifts in energy for the light and heavy hole bands such that they become non-degenerate. The result is that there are effectively two bandgaps: one that is associated with the heavy hole band, and one that is associated with the light hole band. In the case of InGaAs/GaAs quantum wells, the strain splitting produces a larger bandgap for the light hole band than for the heavy hole band, in contrast to bulk InGaAs, which has degenerate light and heavy hole bands. As a result of the fact that in quantum wells, generally, the heavy and light hole bands are non-degenerate, and because of the anisotropy in the strength of interband optical transitions, which depends on the type of hole state involved and on the polarization of light, absorption and emission of light in quantum wells is, in general, anisotropic.

2.3.4. Envelope Function Overlap and Quantum Well Selection Rules

The second selection rule on optical transitions in quantum wells relates to the overlap of the bound state envelope functions of the conduction and valence band states. The envelope function overlap appears in Eq. 2.33:

$$\int \phi_{cn}^{*}(z)\phi_{\mathrm{v}m}(z)dz\,, \tag{2.38}$$

where the conduction and valence band envelope functions, denoted $\phi_{cn}(z)$ and $\phi_{\mathrm{v}m}(z)$, respectively, depend on the type of a heterostructure according to the classifications listed

in Fig. 1.10, and on the associated band offsets. We assume a type 1 heterostructure, in which the valence and conduction band potential wells are symmetric, such as in InGaAs/GaAs quantum wells. Calculation of the envelope functions of bound states in a finite quantum well is relatively straightforward and is discussed in many quantum mechanics texts. The most important property of the envelope functions with regard to the evaluation of Eq. 2.38 is their symmetry.

	$\mathbf{e} = \hat{\mathbf{x}}$	$\mathbf{e} = \hat{\mathbf{y}}$	$\mathbf{e} = \hat{\mathbf{z}}$	**Transition type**
$\mathbf{k} \,//\, \hat{\mathbf{z}}$	$\frac{{m_0}^2 P^2}{2\hbar^2}$	$\frac{{m_0}^2 P^2}{2\hbar^2}$	Impossible	HH to CB
$\mathbf{k} \,//\, \hat{\mathbf{z}}$	$\frac{{m_0}^2 P^2}{6\hbar^2}$	$\frac{{m_0}^2 P^2}{6\hbar^2}$	Impossible	LH to CB
$\mathbf{k} \,//\, \hat{\mathbf{x}}$	Impossible	$\frac{{m_0}^2 P^2}{2\hbar^2}$	*Forbidden*	HH to CB
$\mathbf{k} \,//\, \hat{\mathbf{x}}$	Impossible	$\frac{{m_0}^2 P^2}{6\hbar^2}$	$\frac{2{m_0}^2 P^2}{3\hbar^2}$	LH to CB
$\mathbf{k} \,//\, \hat{\mathbf{y}}$	$\frac{{m_0}^2 P^2}{6\hbar^2}$	Impossible	*Forbidden*	HH to CB
$\mathbf{k} \,//\, \mathbf{y}$	$\frac{{m_0}^2 P^2}{2\hbar^2}$	Impossible	$\frac{2{m_0}^2 P^2}{3\hbar^2}$	LH to CB

Table 2.1: Relative values of the strengths of optical transitions between valence band (heavy hole, abbreviated 'HH,' and light hole, abbreviated 'LH') and conduction band ('CB') states in a quantum well, evaluated using the optical matrix element $|\langle \boldsymbol{n}\mathbf{k}'|\mathbf{e}\cdot\hat{\mathbf{p}}|\boldsymbol{m}\mathbf{k}\rangle|^2$, which is the square of Eq. 2.33. The table is organized by the direction of propagation of light (given by the wavevector, k, which is listed as parallel ('//') to the direction of propagation) and its polarization vector, e.

The envelope functions of quantum well bound states are somewhat more complicated than those of infinite-barrier potential wells, though, for simplicity, assume that electron and hole envelope functions in quantum wells are either symmetric or anti-symmetric,‡ and that one set essentially consists of harmonic cosine functions while the other set essentially consists of harmonic sine functions. The assignment of cosine or sine to symmetric and anti-symmetric states is somewhat arbitrary and depends on the location of $z = 0$ on the quantum well growth axis. Because of their finite barriers, the envelopes of quantum wells are sinusoidal within the well, but they decay exponentially into the barriers, in contrast to the pure sinusoids of wells with infinite potential barriers. Fig. 2.10 illustrates several of the lowest valence and conduction sub-band state wavefunctions in a type 1 quantum well, where strain-induced splitting of the heavy and light hole bands results in a smaller bandgap for transitions involving the former than the latter. Valence sub-band states are labeled by a positive integer, *m*, and *n* labels conduction sub-band states. It can be seen in Fig. 2.10(a) that increasing or decreasing *m* by one selects a state with parity opposite to that of the initial state. Conversely, increasing or decreasing *m* by two selects a state with parity equal to that of the initial state. These parity rules apply to all conduction and valence sub-band states in a quantum well, but they can only be observed in the heavy hole band of the shallow quantum well illustrated in Fig. 2.10 because it supports only one sub-band in both the conduction band and the light hole band.

Based on Eq. 2.38, it can be seen that the overlap of symmetric and anti-symmetric states integrates to zero, so radiative transitions between opposite parity sub-band states are impossible. This is the '*same parity*' selection rule. In an infinite-barrier

‡ The symmetry of wavefunctions is also referred to in terms of their 'parity:' symmetric wavefunctions have the same parity, while symmetric and anti-symmetric functions have opposite parity.

quantum well, transitions between conduction and valence sub-bands with different sub-band indices are impossible even if the states have the same parity, because the sinusoidal envelope functions have harmonic frequency factors equal to integer multiples of π / L, where L is the width of the quantum well. Thus, if $n \neq m$, the envelope functions are orthogonal and the overlap integral equals zero. This is the '$n = m$' selection rule. However, in finite quantum wells, the exponential tails of envelope functions near the barriers result in finite, but small, overlap between states of the same parity for which $n \neq m$, and weak transitions can occur. The thickness of arrows in Fig. 2.10 denotes the strength of optical transitions between valence and conduction sub-band states.

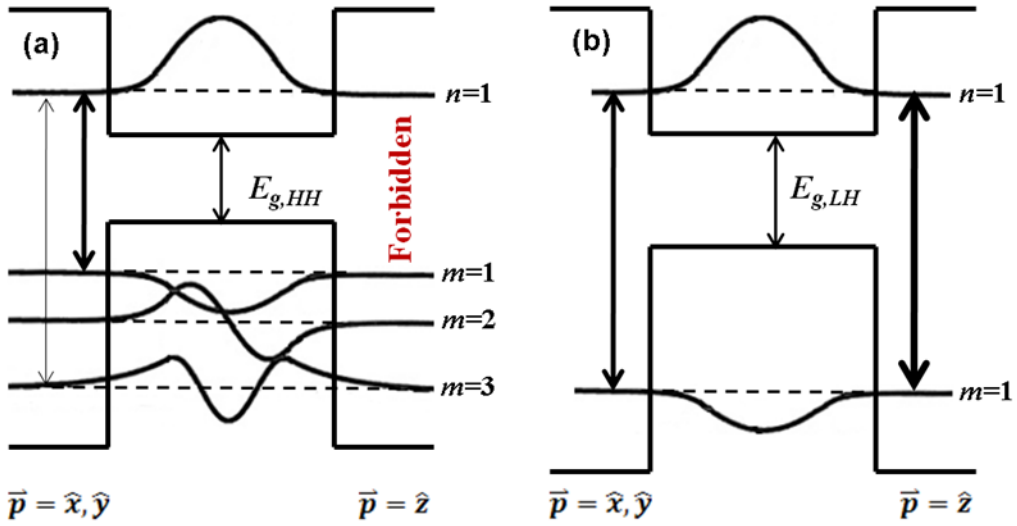

Figure 2.10: Radiative transitions in a type 1 (e.g., InGaAs/GaAs) quantum well involving (a) heavy hole states and (b) light hole states. The energy band gap for heavy holes is smaller than for light holes as a result of strain in the quantum well. Relative transition strengths for *x*-, *y*-, and *z*-polarized light are indicated by the weight of arrows. Note that no heavy-hole transitions are allowed in the quantum well for *z*-polarized light as a result of the momentum-polarization selection rules discussed in Secs. 2.3.2 and 2.3.3.

2.3.5. Selection Rules for Optical Transitions in Quantum Dots

The physics that determine selection rules on optical transitions apply equally to quantum wells and dots. However, the selection rules for optical transitions in quantum dots are frequently different from those for quantum wells because of their geometries. If quantum dots are assumed to be boxes, as illustrated in Fig. 2.11, then they may be thought of as a quantum well in each direction. In this model, the wavefunction of a quantum dot with infinite barriers in each direction can be written as the product of the bound state envelope functions for each direction:

$$\psi(\mathbf{r}) \propto \phi_{n_x}(x)\phi_{n_y}(y)\phi_{n_z}(z), \tag{2.39}$$

with corresponding wavevector

$$\mathbf{k} = k_{n_x}\hat{\mathbf{x}} + k_{n_y}\hat{\mathbf{y}} + k_{n_z}\hat{\mathbf{z}}. \tag{2.40}$$

Thus, the total overlap integral to be evaluated for optical interband transitions in such quantum dots equals the product of the overlap integrals along each direction. In a quantum dot, because carriers are confined in all three directions, the $n = m$ selection rule applies threefold compared to a quantum well, with the result that an ideal quantum dot has sharp absorption and emission lines at certain frequencies of light. This is representative of the 0D density of states in an ideal quantum dot, which is illustrated in Fig. 2.11. Inhomogeneous broadening of the shape, size, and composition in real quantum dots reduce their 0D character and produce broader absorption and emission spectra.[97,98]

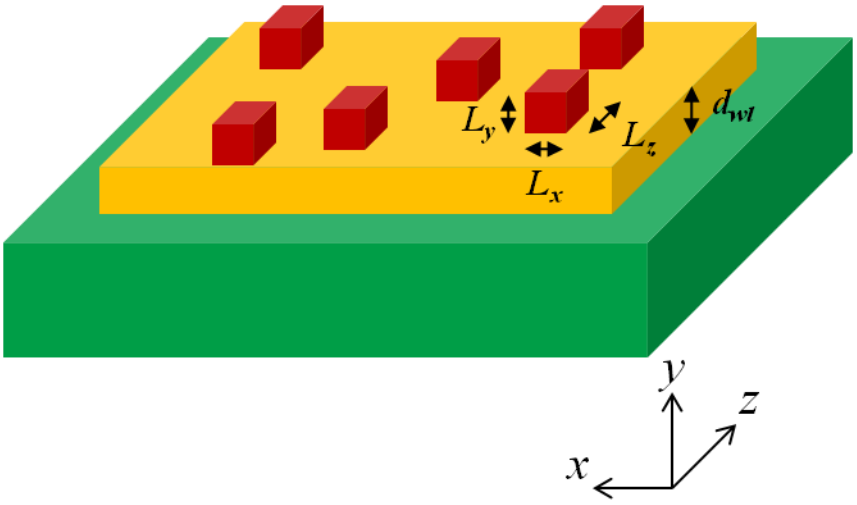

Figure 2.11: An illustration of quantum dots (red boxes) grown on a substrate (green) such that a wetting layer (yellow) exists between the dots and the substrate. The dimensions of the dots and wetting layer are labeled. The quantum dots and wetting layer are assumed to be uniform in composition, and not necessarily of the same composition, in this model.

Strain in quantum dots is typically different from strain in quantum wells. It is assumed that the quantum dots are self-assembled, as in the Stranski-Krastanov growth mode,[99] and that they consist of islands sitting atop a wetting layer.[100,101] The composition of a real quantum dot can vary over its volume, but at the point of contact between dots and the wetting layer, they have the same composition. The wetting layer, therefore, generally experiences strain because of lattice mismatch between it and the substrate, but the dots are not necessarily strained by the wetting layer. Thus, in an actual quantum dot, biaxial strain may not be present, and the heavy and light hole bands may be degenerate at $\mathbf{k} = \mathbf{0}$. Measuring the polarization-dependent absorption,[102,103] photocurrent,[104,105] or photoluminescence[106] spectrum, in order to inspect light hole and heavy hole transitions, can confirm their effective band gaps in quantum confined structures. X-ray diffraction spectroscopy can confirm the presence or absence of strain in the structures, and the magnitude of splitting of light and heavy hole bands in a

structure, as measured by polarization-dependent optical spectroscopy, can be compared to the x-ray result. Though real quantum dots do not have the box geometry shown in Fig. 2.11, for the sake of computation, the dots may be idealized as boxes of a single composition, enabling straightforward application of a formalism similar to the one used for quantum well calculations. The optical properties of quantum wells and dots, including absorption coefficients, are presented and discussed in Refs. 107 and 108.

2.4. Selection Rules and Absorption in Quantum Confined Structures

Calculations based on the preceding analysis have been performed to model the effects of quantum confinement and strain on the optical properties of quantum wells and dots. We consider $In_xGa_{1-x}As/GaAs$ quantum wells that are assumed to be coherently strained to GaAs. The magnitudes of strain-induced shifts in the band edge energies of quantum confined structures can be calculated using Van de Walle's approach of deformation potentials in the framework of the model solid theory.[96] Values of the material parameters for bulk InGaAs have been calculated by linear interpolation between the values for InAs and GaAs that are presented in Ref. 96, including the lattice and elastic constants, shear modulus, and deformation potentials.

The effects of quantum confinement are incorporated using the envelope function approximation. We assume that a quantum well consists of a finite amount of well material surrounded by barrier material with semi-infinite spatial extent, and that there is an abrupt interface between them defined by the offsets at the valence and conduction band edges. Bulk material properties are assumed to apply up to each interface. The conduction and valence bands are treated using a four-band Kane model[109] with parabolic bands and no mixing of heavy and light hole states. The finite barrier heights are accounted for in calculations of bound state energies, though it is assumed in the

calculation of the optical matrix element that the envelope functions are sinusoidal over the entire width of a quantum well, and do not extend into the barriers. Calculations of the quantum confined Stark shift in sub-band state energies assume an electric field in the intrinsic region of devices of 35 kV/cm at an operating voltage of 0.8 V, based on doping in the *p* and *n* regions, and on the *i* layer thickness for quantum well solar cells in this work. The resulting shifts in energy are on the order of 0.1 meV, which are negligible.

A semi-empirical approach has been taken with these calculations. Adapting the calculation of Nelson,[108] the absorption coefficient for a quantum well is found to be given by

$$\alpha(\hbar\omega) = \zeta\alpha_b \sum_{m,n} \gamma_h \left|\langle F_{e,n} | F_{h,m}\rangle\right|^2 \left[\theta\left(\hbar\omega - E_g - E_n - E_m\right) + r_n \delta\left(\hbar\omega - E_g - E_n - E_m + E_b\right)\right], \quad (2.41)$$

where α_b is the bulk absorption coefficient at the band edge of the quantum well, γ_h is the relative strength of the transition, as illustrated in Fig. 2.10, $\theta(E)$ is the Heaviside function that describes the quantum well density of states, r_n is the exciton oscillator strength relative to the continuum, δ is the Dirac delta function, and ζ is a scaling factor that can be used to fit the semi-empirical calculation to measured data, though this has not been done here (i.e., in this work, $\zeta = 1$) . Homogeneous broadening of excitonic transitions is modeled with a Lorentzian having a full-width at half-maximum of 2Γ.

Related optical parameters, such as the semi-empirical, wavelength-dependent refractive index or dielectric function, may be calculated via the relationships between the different optical functions. Here, the extinction coefficient is obtained directly from α using Eq. 1.24, and Kramers-Kronig relations are used to calculate the complex index of refraction from the extinction coefficient. Thus, Eqs. 1.29 and 1.30 can be used to derive the semi-empirical complex index of refraction of quantum confined structures.

To use an example that is relevant to the solar cell structures investigated in subsequent chapters, consider the complex index of refraction of an 8 nm $In_{0.12}Ga_{0.88}As$/20 nm GaAs quantum well coherently strained to a GaAs substrate. To demonstrate the versatility of the semi-empirical calculations, first, the absorption coefficient of the quantum well was calculated using Eq. 2.41. Subsequently, the complex refractive index was calculated using Kramers-Kronig relations, as described in the preceding paragraph, and it was converted to the corresponding dielectric function using Eqs. 1.26 and 1.27. The resulting semi-empirical, anisotropic function $\epsilon_2(\lambda)$ is shown in Fig. 2.12, which illustrates that absorption of light in the quantum well depends on the polarization of the light. The calculation assumes that the absorption coefficient of bulk $In_xGa_{1-x}As$ is a linear interpolation between the absorption coefficients of bulk InAs[110] and GaAs[111] in order to determine the value of α_b used in Eq. 2.41. The linear interpolation is likely to be overly simplistic; however, limited useful data on the optical parameters of InGaAs strained to GaAs have been found. Strained $In_xGa_{1-x}As$ grown on InP substrates, which typically contains modest strain for x~0.45-0.5, exhibits relatively little bandgap bowing, resulting in only slight non-linear variation of its bandgap as a function of the atomic fraction of indium, x, in $In_xGa_{1-x}As$.[112,113] Thus, for consistency in the optical data used in this work for simulations of InGaAs/GaAs quantum wells with different atomic fraction of indium, linear interpolation between bulk GaAs and InAs has been performed, though it is likely to produce some inaccuracy.

The interpolated bulk absorption coefficient does not include effects of strain or quantum confinement, which enter through the semi-empirical calculations. The calculations assume excitonic broadening of $\Gamma = 3$ meV, which is approximately the value observed for a similar multi-quantum well sample.[114] The peaks in ϵ_2 at 965 nm and just below 950 nm in Fig. 2.12 correspond to excitonic absorption at the first heavy

hole transition and at the only light hole transition supported by the quantum well, respectively. At energies above the bandgap of the barrier material (in this case, GaAs), the quantum well is assumed to have the optical properties of bulk InGaAs. This is a poor assumption at energies near the barrier band edge, but it improves at higher energies as quantum effects diminish. Finally, this approach may also be used to compute the optical properties of quantum dots by assuming that they are three-dimensional, finite quantum boxes (refer to Sec. 2.3.5).

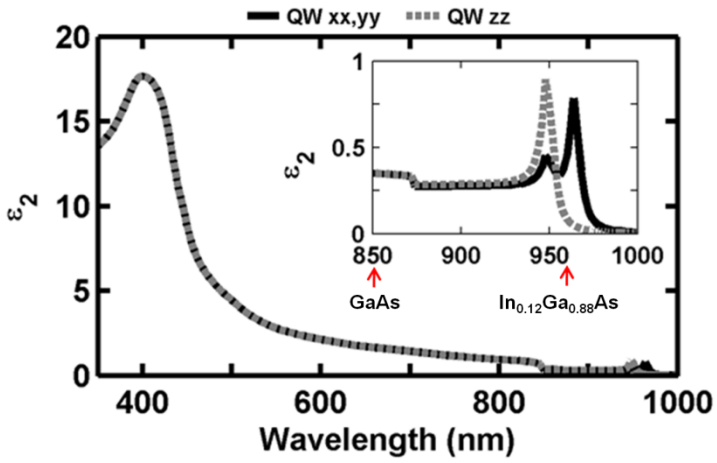

Figure 2.12: The component ϵ_2 of an 8 nm $In_{0.12}Ga_{0.88}As$/20 nm GaAs quantum well calculated using the semi-empirical method described in this section, resulting in anisotropic permittivity with (black, solid line) $\epsilon_{2,xx} = \epsilon_{2,yy} \neq$ (gray, dashed line) $\epsilon_{2,yy}$. Inset: the value of ϵ_2 at wavelengths longer than the GaAs band edge, where peaks occur due to excitonic absorption near quantum well sub-band edges. Arrows indicate the band edges of bulk GaAs and $In_{0.12}Ga_{0.88}As$ at 850 nm and 965 nm, respectively.

2.5. SUMMARY

Many options exist for light trapping in solar cells, which is a promising approach to optimizing their efficiency by using relatively thin device structures that facilitate efficient carrier collection while using light trapping to efficiently absorb light. Coupling

of incident radiation to waveguide modes of device structures is particularly attractive for increasing the absorption of light in solar cells. However, such coupling requires a scattering or diffractive structure to match the effective index of the scattered wave to the effective index of a waveguide mode. Achieving such index matching over a broad band of wavelengths is challenging due to the multiple periodicities required for the scattering/diffractive structure. Thus, random and multiply periodic structures are of particular interest for light trapping in solar cells.

Accurate modeling and analysis of many of the electromagnetic effects discussed in this chapter, including plasmonic effects, interactions of light with sub-wavelength structures, and waveguiding, requires rigorous solutions of the vectorial Maxwell's equations. Therefore, in this work, such simulation techniques are used to analyze absorption in devices equipped with structures for light trapping.

Absorption and emission of light in quantum confined structures is anisotropic as a result of the polarization dependence of optical transitions between light hole states, or heavy hole states, and the conduction band. These bands are degenerate in bulk, unstrained materials, but the strain in quantum wells and dots can lift the degeneracy, which results in anisotropic absorption and emission of light by the nanostructures. The symmetry of bound-state wavefunctions in quantum wells and dots places additional restrictions on allowed optical interband transitions. These selection rules have been implemented to calculate the optical properties of 8 nm $In_{0.12}Ga_{0.88}As$/20 nm GaAs quantum wells used in the solar cells presented in subsequent chapters based on a four-band Kane model, and using the envelope function approximation. These semi-empirical calculations use measured material parameters to arrive at realistic data for quantum wells.

[47] C. H. Henry, *J. Appl. Phys.* **51**, 4495 (1980).
[48] M.A. Green, K. Emery, Y. Hishikawa, W. Warta and E.D. Dunlop, *Prog. Photovolt.: Res. Appl.* **19**, 565 (2011)
[49] E. Yablonovitch *J. Opt. Soc. Am.* **72** 899 (1982).
[50] P. Campbell and M.A. Green, *J. Appl. Phys.* **62**, 243 (1987).
[51] J.M. Gee, *Proc. 29th IEEE Photovolt. Spec. Conf.* p.150 (2002).
[52] P.N. Saeta, V.E. Ferry, D. Pacifici, J.N. Munday and H.A. Atwater, *Opt. Express* **17**, 20975 (2009).
[53] Z. Yu, A. Raman and S. Fan, *Proc. Natl. Acad. Sci. U.S.A*. **107**, 17491 (2010).
[54] A.A. Tseng, K. Chen, C.D. Chen and K.J. Ma, *IEEE Trans. Elec. Packaging Manuf.* **26**, 141 (2003).
[55] M. Altissimo, *Biomicrofluidics* **4**, 026503 (2010).
[56] C. Lu and R.H. Lipson, *Laser and Photonics Reviews* **4**, 568 (2010).
[57] L.J. Guo, *Adv. Mater.* **19**, 495 (2007).
[58] S. Zankovych, T. Hoffmann, J. Seekamp, J.-U. Bruch and C.M. Sotomayor-Torres, *Nanotech.* **12**, 91 (2001).
[59] B. Wu and A. Kumar, *J. Vac. Sci. Tech. B* **25**, 1743 (2007).
[60] C. Heine and R.H. Morf, *Appl. Opt.* **34**, 2476 (1995).
[61] Y.C. Lee, C.F. Huang, J.Y. Chang and M.L. Wu, *Opt. Express* **16**, 7969 (2008).
[62] A. Naqavi, K. Söderström, F.J. Haug, V. Paeder, T. Scharf, H.P. Herzig and C. Ballif, *Opt. Express* **19**, 128 (2011).
[63] D.M. Schaadt, B. Feng and E.T. Yu, *Appl. Phys. Lett.* **86**, 063106 (2005).
[64] K.R. Catchpole and S. Pillai, *J. Appl. Phys.* **100**, 044504 (2006).
[65] D. Derkacs, S.H. Lim, P. Matheu, W. Mar and E.T. Yu, *Appl. Phys. Lett.* **89**, 093103 (2006).
[66] K. Nakayama, K. Tanabe and H.A. Atwater, *Appl. Phys. Lett.* **93**, 121904 (2008).
[67] S. Mokkapati, F.J. Beck, A. Polman and K.R. Catchpole, *Appl. Phys. Lett.* **95**, 053115 (2009).
[68] P.G. O'Brien, N.P. Kherani, S. Zukotynski, G.A. Ozin, E. Vekris, N. Tetreault, A. Chutinan, S. John, A. Mihi and H. Míguez, *Adv. Mater.* **19**, 4177 (2007).
[69] P. Bermel, C. Luo, L. Zeng, L.C. Kimerling and J.D. Joannopoulos, *Opt. Express* **15**, 16986 (2007).
[70] D. Duché, L. Escoubas, J. Simon, P. Torchio, W. Vervisch and F. Flory, *Appl. Phys. Lett.* **92**, 193310 (2008).
[71] T. Suezaki, H. Yano, T. Hatayama, G.A. Ozin and T. Fuyuki, *Appl. Phys. Lett*. **98**, 072106 (2011).
[72] T.H. Chang, P.H. Wu, S.H. Chen, C.H. Chan, C.C. Lee, C.C. Chen and K.Y. Su, *Opt. Express* **17**, 6519 (2009).
[73] D. Derkacs, W.V. Chen, P.M. Matheu, S.H. Lim, P.K.L. Yu and E.T. Yu, *Appl. Phys. Lett.* **93**, 091107 (2008).
[74] P. Matheu, S.H. Lim, D. Derkacs, C.O. McPheeters and E.T. Yu, *Appl. Phys. Lett.* **93**, 113108 (2008).
[75] C.H. Chan, C.C. Chen, C.K. Huang, W.H. Weng, H.S. Wei, H. Chen, H.T. Lin, H.S. Chang, W.Y. Chen, W.H. Chang and M.T. Hsu, *Nanotechnology* **16**, 1440 (2005).
[76] P. Jiang, T. Prasad, M.J. McFarland and V.L. Colvin *Appl. Phys. Lett.* **89**, 011908 (2006).
[77] S. Jeong, L. Hu, H.R. Lee, E. Garnett, J.W. Choi and Y. Cui *Nano. Lett.* **10**, 2989 (2010).
[78] C.F. Bohren and D.R. Huffman, *Absorption and Scattering of Light by Small Particles* (Wiley, 1984).
[79] L. Hu and G. Chen *Nano Lett.* **7**, 3249 (2007).
[80] L. Tsakalakos, *et al*. *J. Nanophotonics* **1**, 013552 (2007).
[81] R. Tena-Zaera, J. Elias and C. Lévy-Clément, *Appl. Phys. Lett.* **93**, 233119 (2008).
[82] S.H. Lim, W. Mar, P. Matheu, D. Derkacs and E.T. Yu, *J. Appl. Phys.* **101**, 104309 (2007).
[83] S.Y. Chou, P.R. Krauss and P.J. Renstrom, *Appl. Phys. Lett.* **67**, 3114 (1995).
[84] J.C. Hulteen and R.P. Van Duyne *J. Vac. Sci. Technol. A* **13**, 1553 (1995).
[85] Y. Xia and G.M. Whitesides, *Annu. Rev. Mater. Sci*. **28**, 153 (1998).
[86] J.G. Mutitu, S. Shi, C. Chen, T. Creazzo, A. Barnett, C. Honsberg and D.W. Prather, *Opt. Express* **16**, 15238 (2008).
[87] V.E. Ferry, M.A. Verschuuren, H.B.T. Li, R.E.I. Schropp, H.A. Atwater and A. Polman, *Appl. Phys. Lett.* **95**, 183503 (2009).

[88] A. Naqavi, K. Söderström, F.J. Haug, V. Paeder, T. Scharf, H.P. Herzig and C. Ballif, *Opt. Express* **19**, 128 (2011).
[89] S. Fahr, C. Rockstuhl and F. Lederer, *Appl. Phys. Lett*. **92**, 171114 (2008).
[90] A. Lin and J. Phillips, *Solar Energy Mater. and Solar Cells* **92**, 1689 (2008).
[91] C. Heine and R.H. Morf, *Appl. Opt.* **34**, 2476 (1995).
[92] Y.C. Lee, C.F. Huang, J.Y. Chang and M.L. Wu, *Opt. Express* **16**, 7969 (2008).
[93] RSoft Design Group, *DiffractMOD User Guide (v. 3.2)* p.39 (2011).
[94] Z. Yu, A. Raman and S. Fan, *Opt. Express* **18**, A366 (2010).
[95] E.O. Kane, *Handbook on Semiconductors*, vol. 1, ed. T.S. Moss (North-Holland, 1982).
[96] C.G. Van de Walle, *Phys. Rev. B*. **39**, 1871 (1989).
[97] M.A. Cusack, P.R. Briddon and M. Jaros, *Physica B* **253**, 10 (1998).
[98] M. Hjiri, F. Hassen and H. Maaref, *Mater. Sci. and Eng.: B* **69**, 514 (2000).
[99] I. N. Stranski and L. Krastanow, "Zur Theorie der orientierten Ausscheidung von Ionenkristallen aufeinander," in *Sitzungsberichte d. Akad. D. Wissenschaften in Wien*, vol. 146, pp. 797–810 (Mathnaturwiss, Klasse, 1937).
[100] K. Shiramine, S. Muto, T. Shibayama, H. Takahashi, T. Kozaki, S. Sato, Y. Nakata and N. Yokoyama, *J. Vac. Sci. Technol. B* **21**, 2054 (2003).
[101] M. Yakimov, V. Tokranov, G. Agnello, J. van Eisden and S. Oktyabrsky, *J. Vac. Sci. Technol. B* **23**, 1221 (2005).
[102] J.-P. Reithmaier, R. Hoger, H. Riechert, P. Hiergeist and G. Abstreiter, *Appl. Phys. Lett.* **57**, 957 (1990).
[103] P. Ridha, L. Li, A. Flore, G. Patriarche, M. Mexis and P.M. Smowton, *Appl. Phys. Lett.* **91**, 191123 (2007).
[104] P.W. Fry, *et al*., *Phys. Rev. B* **62**, 16784 (2000).
[105] M. Schardt, *et al.*, *Physica E* **32**, 241 (2006).
[106] J.-Y. Marzin, M.N. Charasse and B. Sermage, *Phys. Rev. B* **31**, 8298 (1985).
[107] S.L. Chuang, *Physics of Photonic Devices* (Wiley, 2009).
[108] J. Nelson, *Low-dimensional Semiconductor Structures: Fundamentals and Device Applications*, ed K. Barnham and D. Vvedensky, p.209 (Cambridge University Press, 2001).
[109] E.O. Kane, *J. Phys. Chem. Solids* **1**, 249 (1957).
[110] S. Adachi, *Phys. Rev. B* **35**, 7454 (1987).
[111] E.D. Palik, *Handbook of Optical Constants of Solids* (Academic Press, 1998).
[112] C.P. Kuo, S.K. Vong, R.M. Cohen and G.B. Stringfellow, *J. Appl. Phys.* **57**, 5428 (1985).
[113] W. Porod and D.K. Ferry, *Phys. Rev. B* **27**, 2587 (1983).
[114] W.Z. Shen, S.C. Shen, W.G. Tang, S.M. Wang and T.G. Andersson, *J. Appl. Phys.* **78**, 1178 (1995).

Chapter 3: Nanoparticle Scattering into InGaAs/GaAs Quantum Dot-in-Well Solar Cells

Solar cells based on low-dimensional semiconductor structures are of great interest for development of high-efficiency photovoltaics.[115-118] In particular, quantum well- and quantum dot solar cells have been proposed as a means of exceeding the Shockley-Queisser limit of ~31% power conversion efficiency for homojunction devices.[115,116,119] Incorporation of quantum dots in the solar cells investigated here is attractive for absorbing infrared light because they are not limited by certain selection rules for optical transitions in quantum wells (refer to Sec. 2.3). While quantum dots (QDs) have been proposed for use in a variety of photovoltaic concepts, such as the intermediate band solar cell[120] and multi-exciton generation devices,[121] they serve here to extend the absorption of InGaAs quantum well solar cells (QWSCs) to longer infrared wavelengths that are essential for realizing high efficiency, while maintaining the waveguiding characteristics of QWSCs[122] to enhance infrared photocurrent generation. In order to compare devices as directly as possible, InAs QDs have been embedded in InGaAs/GaAs QWs, creating quantum dot-in-well solar cells (QDWSCs). This chapter demonstrates photocurrent and short-circuit current density enhancement in InGaAs/GaAs QDWSCs via scattering of light by metal and dielectric nanoparticles into waveguide modes of the quantum dot device structure. The improvement results from coupling of radiation into said modes, which can improve photocurrent at all infrared wavelengths in the device response spectrum.

3.1. Particle Scattering and Radiative Coupling to Waveguide Modes of Dielectric Films

In the 1990s, Hall and co-workers studied the effects of nanoparticles located on the surface of silicon photodetectors that were fabricated on silicon-on-insulator (SOI) wafers.[123] The air above the device layer, and low permittivity insulator below it, made the silicon device layer an effective electromagnetic waveguide. The monochromatic photocurrent response of devices improved by a factor of up to 20, which resulted from increased absorption of light due to optical scattering by nanoparticles into modes of the device structure.[124] These experiments, and theoretical calculations of radiative coupling of light scattered by particles, spurred considerable interest in nanoparticle scattering to improve solar cells.

3.1.1. Nanoparticle Scattering as Electric Dipole Emission

If an isolated particle that is located near the surface of a dielectric structure is illuminated by light of wavelength larger than the diameter of the particle, the particle radiates light in a manner analogous to an electric dipole. The scattering and absorptive properties of the particle are determined by its size, shape, composition, and the surrounding dielectric environment. With appropriate combinations of those parameters, a significant fraction of the radiation scattered by such a particle can couple into modes of the underlying structure, potentially including waveguide modes that it supports.

Soller and Hall have analyzed dipole emission into dielectric device structures,[125] and their results are applied here to the case of nanoparticle scattering into QDWSC structures. For light that is incident normal to the surface of a device with the geometry illustrated in Fig. 3.1(a), horizontal electric dipoles (HEDs) are excited in nanoparticles situated on top of the device. The position vector **r** makes an angle θ with the x axis, as illustrated in Fig. 3.1(b). For coupling into lateral propagation modes, including

waveguide modes, the transverse component of the wavevector of radiation emitted by the dipole (i.e., scattered by a nanoparticle) is an important metric. The normalized transverse wavevector is given by $u = k_\rho/k_s = \sin(\theta)$, where k_ρ is the wavevector in the dielectric medium (i.e., in the device structure) and $k_s = \sqrt{\epsilon_s}\omega/c$ is the wavevector in the source medium, which is typically air [i.e., $k_s = \omega/c$, as in Fig. 3.1(b)]. Thus, for electric dipole emission, *u* is analogous to the effective index of a diffracted wave, which is defined in Eq. 2.23.

Light emitted by an electric dipole can couple to both radiation and evanescent modes of a device structure. Radiation modes are defined as those that can couple between radiating states in the source medium and in the device structure (i.e., states that are not guided by the device structure). Therefore, if a photon in a radiation mode is not absorbed on a round trip through a device, a significant portion of its power exits through the top surface. Radiation modes are characterized by real-valued wavevectors. In the context of the normalized wavevector, this means that radiating waves have values of $u \in (0,1)$, corresponding to real-valued k_ρ and to waves that have non-zero wavevectors in the $\pm x$ direction, according to the geometry of Fig. 3.1(b). Evanescent waves have complex-valued *u* and consist of two types: *substrate radiation modes*, which propagate in the dielectric medium below the dipole, including the semi-infinite substrate, but are evanescent in the source medium, and *waveguide modes*, which are confined to the epitaxial layers, which are bound on the top by a capping layer or the source medium, and which are bound on the bottom by the substrate. In the context of InGaAs/GaAs heterostructure devices of the form shown in Fig. 3.1(a), substrate radiation modes are characterized by $u \in (1, n_{\mathrm{GaAs}})$, and waveguide modes are characterized by $u \in (n_{\mathrm{GaAs}}, \infty)$.

Modal power spectra are useful quantities for analyzing the coupling of dipole emission into the different types of modes supported by a device structure. These spectra are proportional to the rate of damping of dipole emission by its environment, which is defined by the complex-valued Fresnel reflection coefficients of the dielectric device stack below the dipole. The Fresnel coefficients are r_p and r_s for transverse magnetic (TM) and transverse electric (TE) polarization, respectively. Here, it is assumed that the source region is air or vacuum (i.e., $n = 1$). The modal power spectrum for a HED in the geometry of Fig. 3.1(b) is given by the following expression:[125]

$$S(u)_{\mathrm{HED}} \propto \frac{u}{(1-u^2)^{1/2}}\left\{(1-u^2)\left[1-r_p \exp(2ik_{sx}x_s)\right]+\left[1+r_s \exp\left(2ik_{sx}x_s\right)\right]\right\} \quad (3.1)$$

where k_{sx} is the x component of the wavevector in the source medium. It is unimportant that Eq. 3.1 is inexact because it can still be used to calculate the fraction of light emitted into each type of mode. Two quantities of particular interest for enhancing absorption in solar cells via nanoparticle scattering are the fraction of scattered/emitted light that couples to substrate radiation modes, and the corresponding fraction that couples to waveguide modes, of a device structure. These are given by:[125]

$$\gamma_{\mathrm{sr}} = \frac{\int_1^{n_{\mathrm{GaAs}}} S(u)du}{\int_0^{\infty} S(u)du} \qquad \gamma_{\mathrm{wg}} = \frac{\int_{n_{\mathrm{GaAs}}}^{\infty} S(u)du}{\int_0^{\infty} S(u)du}, \quad (3.2)$$

where γ_{sr} and γ_{wg} are the fractions corresponding to substrate radiation and waveguide modes, respectively.

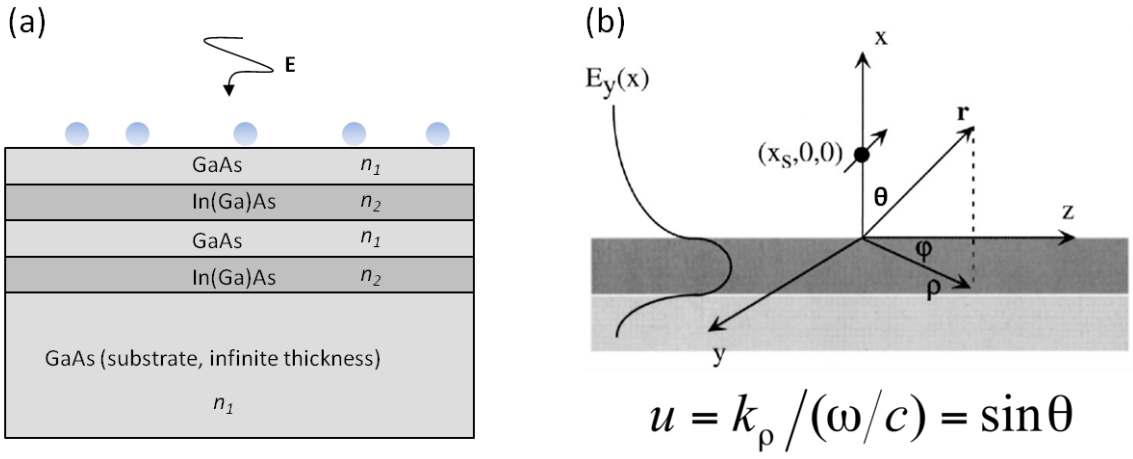

Figure 3.1: (a) A representation of nanoparticles deposited on the surface of a InGaAs/GaAs quantum well/dot solar cell structure, which is illuminated by light incident normal to the surface of the device and has an electric field vector, **E**. (b) The coordinates used in dipole radiation analysis. The dipole is situated a distance x_s above the surface of a device and the position vector, **r**, makes an angle θ with the x axis. The normalized transverse wavevector is denoted by u, and is defined as shown.

3.1.2. Dipole Emission into InGaAs/GaAs Quantum Dot-in-Well Solar Cells

The use of nanoparticles to improve absorption in InGaAs/GaAs *p-i-n* QDWSCs has been investigated using the dipole emission framework presented in the previous section. The device structure considered in this work appears in Fig. 3.2(a). The modal power spectrum and associated quantities have been calculated using the Matlab code "sollerhall_com.m," provided in Appendix A2.1, which is modified from a program authored by Daniel Derkacs.[126]

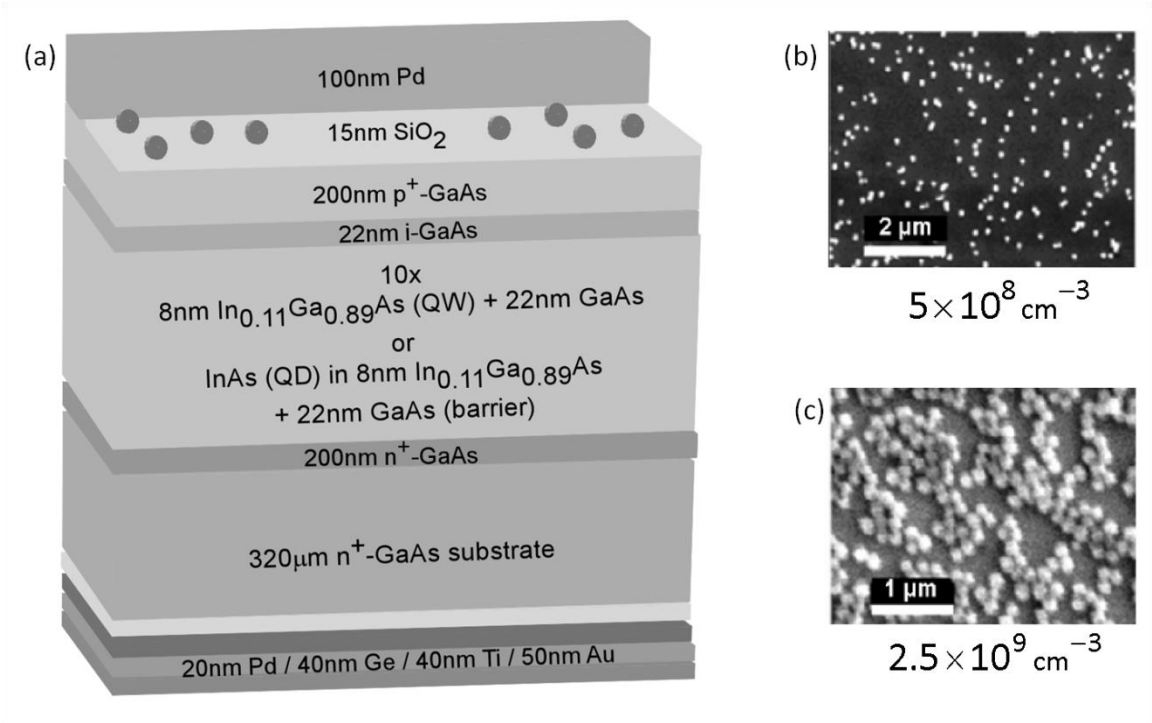

Figure 3.2: (a) Schematic of the device structures of quantum dot-in-well and quantum well solar cells employed in this study. Scanning electron micrographs of typical deposition results for (b) 100 nm diameter Au (left) and (c) 150 nm diameter SiO_2 particles (right), with concentrations of ~5×10^8 cm^{-2} and ~2.5×10^9 cm^{-2}, respectively.

Fig. 3.3 shows the calculated fraction of light scattered into substrate radiation modes and waveguide modes of the device structure as a function of the wavelength of normally incident light. Over 80% of light at all wavelengths, and ~90% of light at $\lambda > 850$ nm, couples to substrate radiation modes of the device. A majority of the remaining fraction of light (~10-15%, depending on the wavelength) couples to propagating modes and, therefore, escapes from the device after one round trip.

It is notable that essentially zero light couples to waveguide modes at wavelengths that are absorbed only in the quantum wells and dots (i.e., $\lambda > 850$ nm). For maximal absorption of light by quantum wells and dots, it is desirable for scattered light to couple

to waveguide modes. When that occurs, light is confined strictly to the region of the device where the quantum wells/dots are located. In practice, a good waveguide consists of a guide layer and boundary layers with maximal difference in their indices of refraction, which reduces the critical angle necessary to achieve total internal reflection in the guiding layer. The real components of the complex refractive indices of GaAs and InAs, which appear in Fig. 1.8, are quite similar, and are much closer in value than those of the Si-SiO_2 photodetector structures investigated by Soller and Hall in Refs. 123-125. Thus, it is not surprising that a small fraction of light scattered into the QDWSC and QWSC structures of this investigation couples to waveguide modes. Nevertheless, the fact that a large fraction of the scattered light couples to substrate radiation modes provides useful enhancement, which is demonstrated experimentally in Sec. 3.3.3 of this chapter.

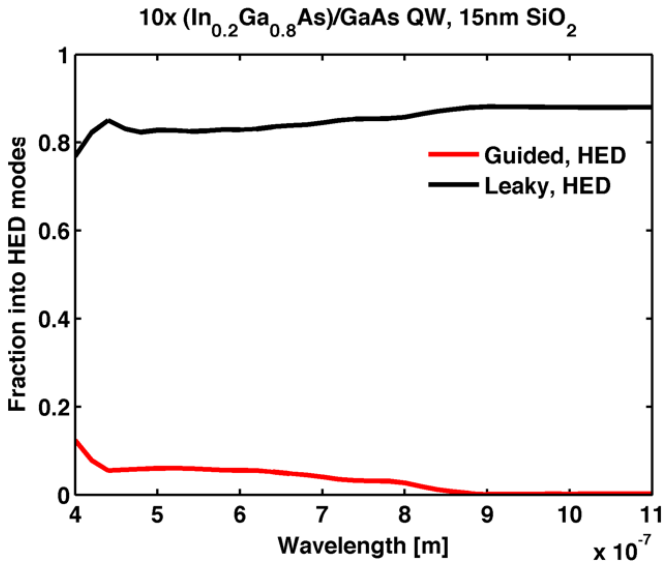

Figure 3.3: The fraction of light emitted by a horizontal electric dipole (HED) into substrate radiation modes ("Leaky, HED") and waveguide modes ("Guided, HED") of the device structure shown in Fig. 3.2(a).

3.2. Experimental Studies of Nanoparticle Scattering into Quantum Dot-in-Well Solar Cells

The effect of scattering by sub-wavelength metal and dielectric nanoparticles into InGaAs/GaAs QDWSCs has been investigated experimentally. This section discusses the device structures and experimental techniques used in the work.

3.2.1. Growth of Device Structures and Device Fabrication

Epitaxial layer structures, shown schematically in Fig. 3.2(a), were prepared by molecular beam epitaxy on 2-inch n^+-GaAs (001) substrates on which a buffer layer of 200 nm n^+-GaAs was grown first. The active regions of the QDWSCs nominally consist of ~300 nm of intrinsic material: specifically, 10 iterations of the sequence {22 nm GaAs, 4 nm $In_{0.11}Ga_{0.89}As$, 2.6 monolayers InAs, 4 nm $In_{0.11}Ga_{0.89}As$}. The InAs was annealed at 500°C to form quantum dots, as described in detail elsewhere.[127] Reference devices with 300 nm of either intrinsic GaAs, or with 8 nm $In_{0.11}Ga_{0.89}As$ QWs (no QDs) with 22 nm GaAs barriers, were also grown.

3.2.2. Characterization of Device Structures

Photoluminescence (PL) has been used to inspect the lowest energy sub-band of the quantum dot-in-well structure. The lowest sub-band is nominally located in the quantum dot, which has the highest atomic fraction of indium in the structure. As seen in Fig. 3.4, the quantum dot-in-well structures exhibit a room temperature photoluminescence peak wavelength of 1175 nm with a full-width at half max of 100 nm. The relatively large spectral width of the luminescence implies inhomogeneity in the size and/or composition of the quantum dots, which is supported by composition evaluation by lattice fringe analysis (CELFA) data of similarly grown quantum dots that have been provided by collaborators in the research group of Prof. Daniel Schaadt at TU-Clausthal. CELFA is a transmission electron microscope-based technique for determining material

composition. These data appear in Fig. 3.5, which indicate that as-grown dots have a concentration gradient with a typical peak indium fraction of ~30% near their centers.

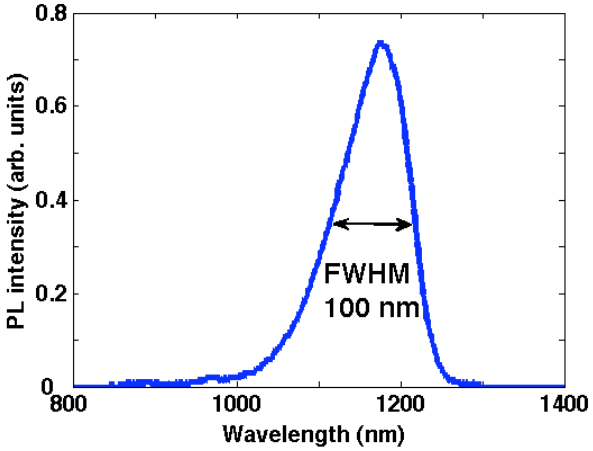

Figure 3.4: Room temperature photoluminescence from the InGaAs/GaAs quantum dot-in-well solar cell structures depicted in Fig. 3.2(a).

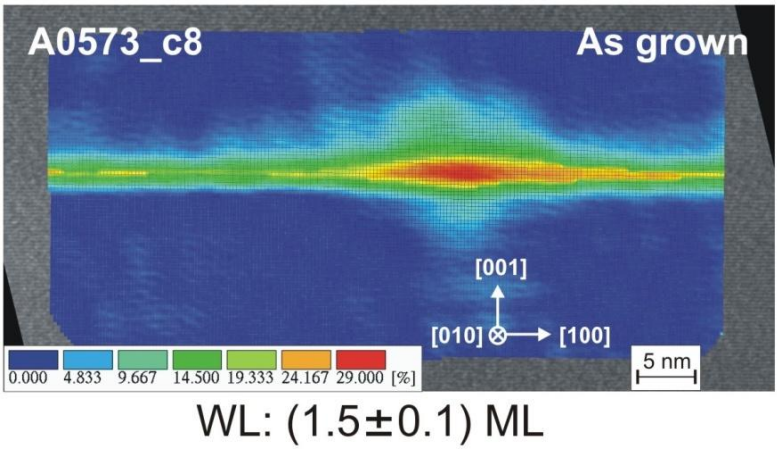

Figure 3.5: Compositional data of InAs/GaAs quantum dots formed in the Stranski-Krastanov mode via molecular beam epitaxy, as obtained by composition evaluation by lattice fringe evaluation (CELFA). The wetting layer (WL) has an approximate thickness of 1.5 monolayers and the color scale indicates the atomic percent of indium in the InGaAs/GaAs structure. While the sample from which the data shown in this figure were taken is not the same as the quantum dot-in-well device structure investigated in this chapter, this figure is intended to illustrate the fact that InAs/GaAs quantum dots grown in the Stranski-Krastanov mode by MBE can be irregular in size and composition.

Management of strain in InGaAs/GaAs heterostructures is important to preventing material dislocations, which can degrade device performance. Therefore, strain in as-grown wafers has been inspected. Topographic data acquired using an atomic force microscope appear in Fig. 3.6 and show no evidence of cross-hatching on the wafer surface, implying that strain relaxation in the material is negligible.

X-ray diffraction (XRD) rocking curves for the quantum well reference structure and for the quantum dot-in-well structure appear in Fig. 3.7. The peak at $\Delta\theta = 0$, which is known as the "substrate peak," represents zero strain with respect to the GaAs lattice, and is, therefore, produced by diffraction from GaAs. Satellite peaks appear to the left of the substrate peak, and their position to the left of the substrate peak indicates that they are compressively strained, as expected, while the fact that there are multiple peaks in the spectrum indicates that multiple periods of the heterostructure are present in the structure.

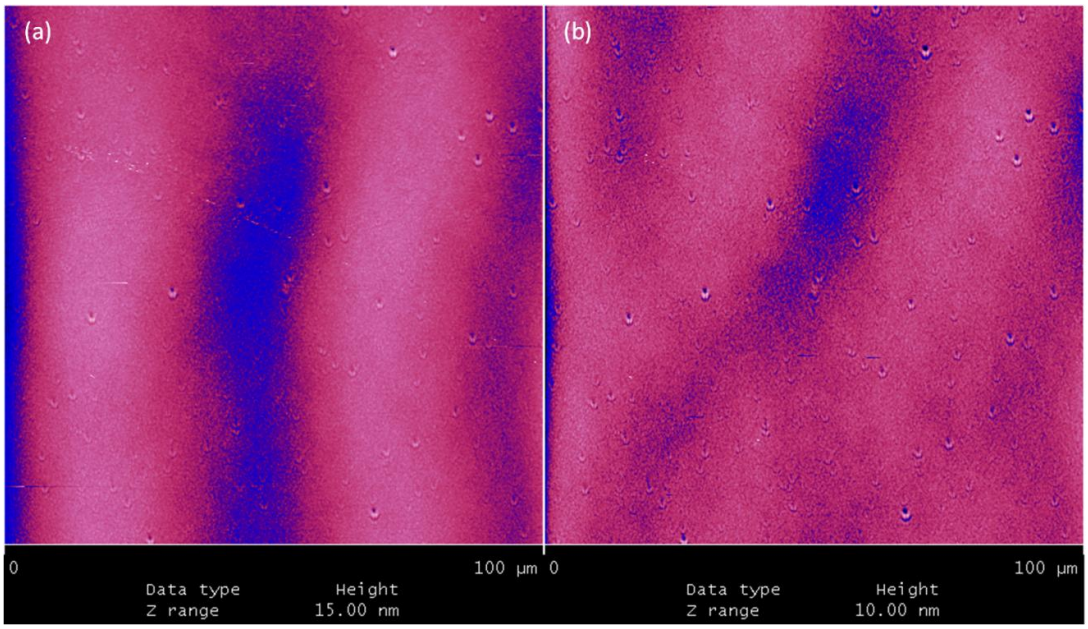

Figure 3.6: Large area atomic force microscope topographs of two different areas (labeled 'a' and 'b') of the as-grown device wafers corresponding to the quantum dot-in-well solar cells depicted in Fig. 3.2.

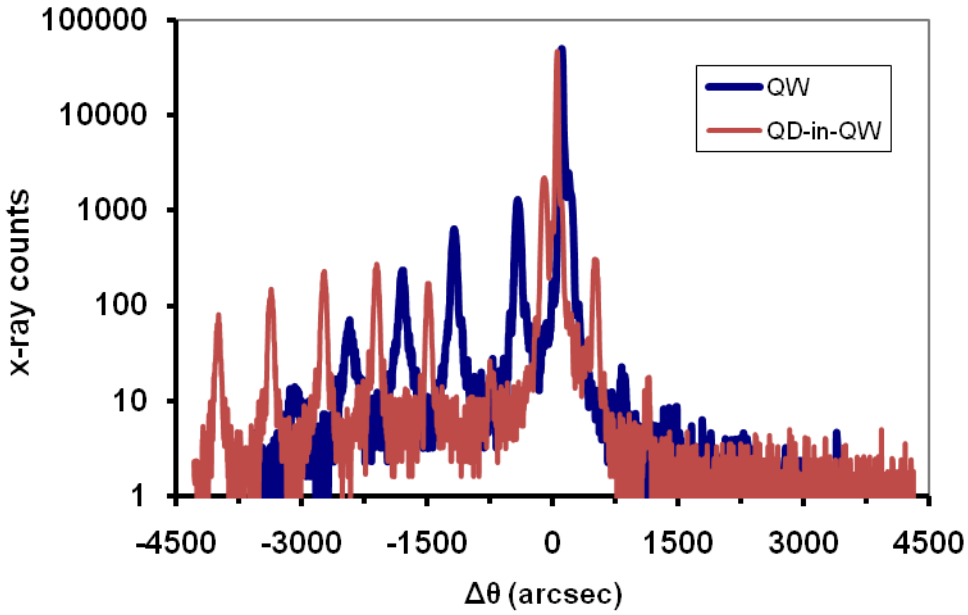

Figure 3.7: X-ray diffraction data for the InGaAs/GaAs quantum well ('QW') and InAs/InGaAs/GaAs quantum dot-in-well ('QD-in-QW') devices prepared for this work.

3.2.3. Fabrication of Quantum Dot-in-Well Solar Cells

The n^+-GaAs bottom contact metallization consisted of 20 nm Pd/40 nm Ge/40 nm Ti/50 nm Au, based on the contact of Ref. 128, and the p^+-GaAs contact consisted of 100 nm Pd. All metals were deposited by electron beam evaporation. Photolithography and a standard liftoff using acetone were used to fabricate windows in the top contact and to enable sputter deposition of a 15 nm thick SiO_2 passivation layer on the windows of the solar cells.

The literature indicates that Pd is useful for contacting GaAs[129] due to its reactivity at low temperature, which facilitates formation of tunneling ohmic contacts. The *n*-type GaAs contact in Ref. 128 is intended to be annealed. In so doing, nominally, Pd reacts with Ga, enabling Ge to diffuse into the top region of GaAs, filling Ga vacancies and creating a heavily *n*-type surface layer that facilitates ohmic contact.

Experiments with rapid thermal annealing of solar cells processed with this contact, according to the annealing procedure of Ref. 128, did not show changes in the short-circuit current density, open-circuit voltage, or fill factor of devices beyond typical variation between devices made in proximity to one another on a device wafer, which was by up to 6%. Thus, unless otherwise specified, contacts have not been annealed in devices in this work. Despite this particular non-effect of annealing, it is important to understand the contact properties of electronic devices because they can significantly affect device performance. Anyone considering using the aforementioned *n*-type GaAs contact is advised to conduct annealing tests to determine an appropriate process.

3.3. Experiments of Nanoparticle Scattering into Optically thick Quantum Dot-in-Well Solar Cells

3.3.1. Measurements

Devices were evaluated at room temperature in terms of their short-circuit photocurrent response (I_{ph}) and illuminated current density vs. voltage (*J-V*) characteristics, both with and without nanoparticles deposited on the top surface. Photocurrent measurements were performed using a custom monochromator system and illuminated *J-V* measurements were taken using normally incident light from a Newport Oriel 96000 solar simulator operating at 150 W with an AM 1.5 global spectral filter.

3.3.2. Deposition of Nanoparticles

In this study, 100 nm diameter Au (AuNP) or 150 nm diameter SiO_2 (SNP) colloidal particles from nanoComposix, Inc., have been used. Prior to particle deposition on the window areas on the top sides of devices, the top surface was cleaned with acetone, methanol and isopropyl alcohol, and blown dry with nitrogen gas. Next, the particle adhesion promoter, poly-l-lysine, was applied, which is an organic molecule with

a positive charge. Many colloidal particles, and, in particular, metal particles, have negative surface charge as a result of their synthesis processes.[130] Thus, poly-l-lysine electrostatically attracts the colloidal particles to the surface of the device. Further, poly-l-lysine is attractive for easy and benign deposition: an aqueous solution containing the adhesion promoter was drop-coated onto the surfaces of clean devices and remained on the surface for 180 seconds before being blown off with nitrogen gas. Particles were then deposited in a humid environment for 30 to 60 min by using a pipette to drop-coat typically 5-20 μL of solution containing nanoparticles at concentrations between 1×10^{10} and 4×10^{12} mL^{-1}.

Scanning electron micrographs of AuNPs and SNPs deposited at typical concentrations of ~5×10^{8} cm^{-2} and ~2.5×10^{9} cm^{-2}, respectively, are shown in Fig. 3.2(b) and (c). Both types of particles scatter light strongly, but they exhibit different wavelength-dependent behavior: for AuNPs, around 500 nm (near the surface plasmon polariton resonance), destructive interference between the scattered and incident fields reduces the magnitude of the transmitted field.[131] This loss mechanism, which is associated with a dipolar mode of the AuNPs, is insignificant for SNPs at the wavelengths of interest. Clusters of metal particles also reduce the transmitted field amplitude by reducing scattering compared to individual particles, while the effects of dielectric particle clustering are much less severe.

3.3.3. Measurement Results

Photocurrent response spectra were measured at short-circuit and used to calculate the internal quantum efficiency (IQE) of devices, which are shown in Fig. 3.8. These results confirm that the addition of QDs enables additional carrier generation and collection at infrared wavelengths. A calibrated Newport 818UV photodiode was

measured under the same conditions as our test devices, and calculated surface reflection losses were subtracted in order to estimate IQE. In Fig. 3.8, it can be seen that the response of the GaAs cell and QWSC cut off abruptly at 890 nm and 940 nm, respectively. The photocurrent response of the QDWSC extends well above the peak at 980 nm, reaching zero at 1150 nm. We attribute the tail in the QDWSC spectrum to inhomogeneous broadening of QD absorption associated with variations in dot size[132] and composition, which is corroborated by the PL data in Fig. 3.4 and the CELFA data in Fig. 3.5.

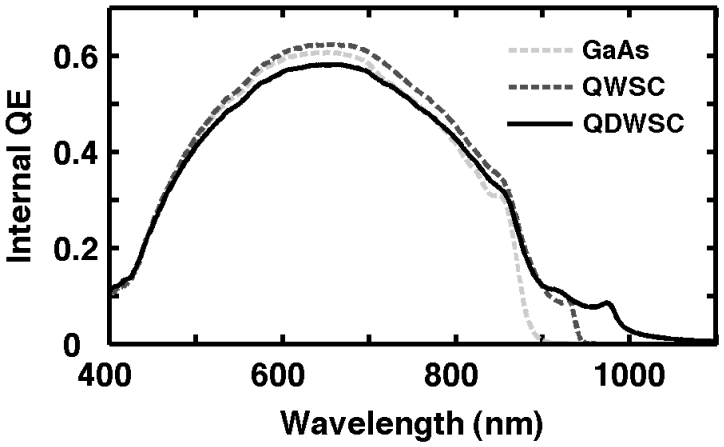

Figure 3.8: Calculated internal quantum efficiency spectra, indicating effective absorption edges for the GaAs reference ('GaAs'), quantum well ('QWSC'), and quantum dot-in-well devices ('QDWSC').

Following nanoparticle deposition, improvements in short-circuit current density (J_{sc}) have been observed for QDWSCs. Fig. 3.9 shows current density *J-V* measurement results for QDWSCs, where calculation of *J* used the unmetallized device area. As these device structures were not optimized for photovoltaic performance, the J_{sc} of devices is somewhat lower than typical values for high efficiency cells. Furthermore, the measurements used illumination intensity less than standard AM 1.5 conditions, so the

relative performance of devices with and without nanoparticles is the most useful metric. Following deposition of SNPs and AuNPs, respective J_{sc} increases of 16% and 3% have been achieved for QDWSCs relative to devices with no nanoparticles. Open-circuit voltages and fill factors exhibited negligible changes following particle deposition, so J_{sc} enhancement corresponds to an equal factor of improvement in cell efficiency.

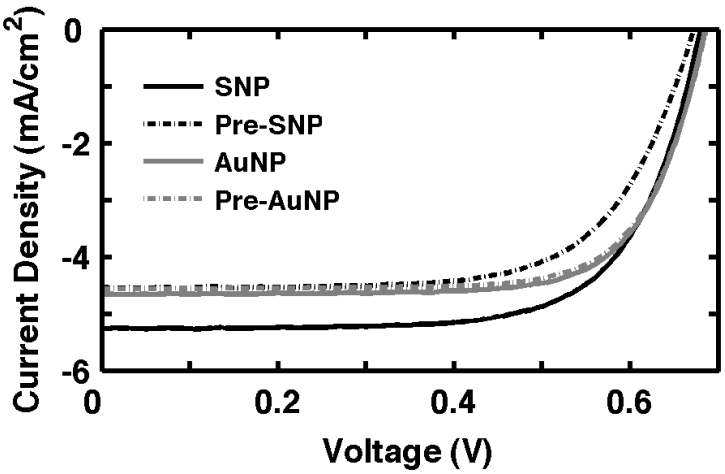

Figure 3.9: *J-V* data for quantum dot-in-well solar cells before (dashed lines) and after (solid lines) deposition of 150 nm diameter silica particles (black) and 100 nm diameter gold nanoparticles (gray).

3.4. Simulations of Nanoparticle Scattering to Improve the Photoresponse of Quantum Dot-in-Well Solar Cells

Finite-element electromagnetic simulations using Comsol Multiphysics software were performed in three dimensions to analyze the mechanisms responsible for the improved J_{sc} and efficiency demonstrated in the previous section. In the simulations, the integrated magnitude-squared of the electric field in the semiconductor volume, $|\mathbf{E}|^2$, was computed as a function of wavelength for devices with and without nanoparticles on the surface to obtain quantities G_{np} and G_{bare}, respectively. These quantities are expected to be proportional to optical transition rates and, consequently, to photocurrent generation,

assuming unity carrier collection efficiency. Fig. 3.10(a) and (b) show G_{np}/G_{bare} in the curves labeled 'sim,' which we take as an estimate of the expected photocurrent ratio in QDWSCs due to the presence of AuNPs or SNPs. With regard to the simulations, we see that photocurrent enhancement is generally expected in the range of 550 nm to 1100 nm for AuNPs and 400 nm to 1100 nm for SNPs. These improvements result, in part, from forward scattering of incident electromagnetic radiation by the nanoparticles, which increases light transmission through the air-semiconductor interface compared to a bare device. As discussed in the next section, some of the forward scattered light couples to confined modes of the device structure, improving absorption compared to light which couples to radiation modes.

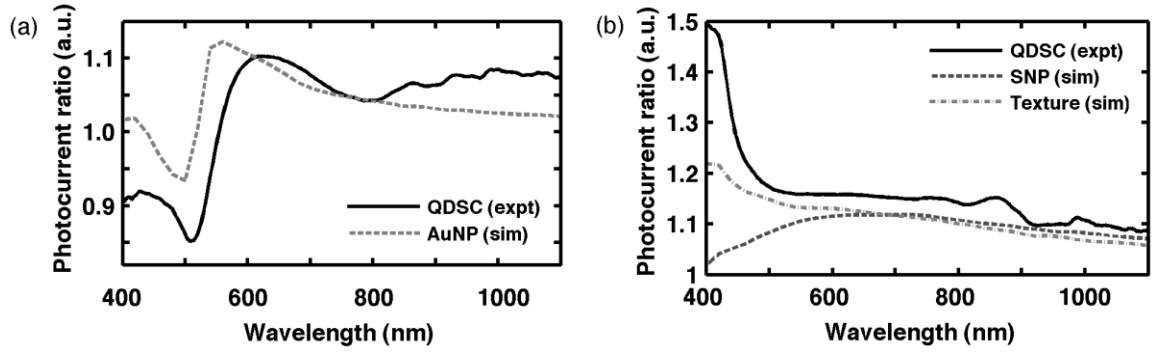

Figure 3.10: Photocurrent ratios, relative to bare devices prior to nanoparticle deposition, for quantum dot solar cells (a) with deposited 100 nm diameter Au particles (black, solid line) and simulated Au nanoparticles (grey, dashed line); and (b) with deposited 150 nm diameter SiO_2 particles (black, solid line), simulated SiO_2 nanoparticles (dark grey, dashed line), and simulated 150 nm tall random surface texturing (light grey, dashed line).

3.5. Analysis and Comparison of Simulation and Experimental Results

For both AuNPs and SNPs, the measured photocurrent enhancement was typically greater than simulations predicted. Specifically, the experimental spectra show additional broad enhancement of photocurrent due to light coupling into substrate radiation modes

(refer to Sec. 3.1.1), including substantial improvements at infrared wavelengths. In most cases where the simulations underestimate enhancement, it is because the simulation volume is not large enough for waveguide modes to be modeled. The actual device structures, however, are thick, and they support many optical modes. With the majority of scattered light entering substrate radiation modes, this effect is primarily responsible for the observed photocurrent enhancement. Secondary gains result from light below 900 nm coupling weakly into true guided modes, but with a peak efficiency of ~10% (refer to Fig. 3.3) due to the small difference between the refractive indices of InGaAs and GaAs. Since the simulations do not accurately model the effects of waveguiding, differences between simulation and experimental results highlight the benefit of optical waveguiding for QDWSCs.

Experimental results also reveal substantial enhancement at short wavelengths when SNPs are used, as seen in Fig. 3.10(b)**,** where there is a prominent increase in I_{ph} of ~50% at 400 nm in the experimental data that is not predicted by modeling. In fact, the simulation of a randomly textured SiO_2 surface with 150 nm tall features qualitatively predicts the experimental result more accurately than the nanoparticle simulation. This is because the deposited SNPs, which, as seen in Fig. 3.2(c), are densely clustered, are more akin to a rough film than to individual particles. The similarity is not unexpected, as scattering of light by textured surfaces is a well-known method for increasing its transmission into device structures,[133,134] and, here, nanoparticles perform the same function. SNPs are not a homogeneous film, however; their anti-reflective behavior is weaker than that of a true thin film, and it is ultimately of secondary importance to the I_{ph} and J_{sc} enhancements observed. The scattering provided by the nanoparticles is essential for coupling light into waveguide modes of the device structure, and, indeed, the most

significant benefit of SNPs is photocurrent enhancement of 10-20% due to partial trapping of light in substrate radiation modes between 500 nm and 1100 nm.

3.6. SUMMARY

In summary, it has been shown that InAs quantum dots are effective in extending the photocurrent response of InGaAs quantum well solar cells to wavelengths well beyond the QW absorption edge, and that optical scattering from nanoparticles can substantially enhance the performance of InGaAs/GaAs quantum dot-in-well solar cells by coupling light into waveguide modes of the device structure. Photocurrent at infrared wavelengths increased by ~10% following deposition of SiO_2 nanoparticles on bare devices, resulting in an enhancement factor of 16% in short-circuit current density and power conversion efficiency. It is encouraging that these improvements were achieved even though ~80% of scattered light entered substrate radiation modes rather than true guided modes. This suggests that even greater enhancement should be possible with a better waveguide structure, which is the subject of the next chapter.

---

[115] K.W.J. Barnham and G. Duggan, *J. Appl. Phys*. **67**, 3490 (1990).
[116] A. Luque and A. Martí, *Phys. Rev. Lett*. **78**, 5014 (1997).
[117] R. Dahal, B. Pantha, J. Li, J.Y. Lin, and H.X. Jiang, *Appl. Phys. Lett*. **94**, 063505 (2009).
[118] R. Oshima, A. Takata, and Y. Okada, *Appl. Phys. Lett*. **93**, 083111 (2008)
[119] G. Wei, K.-T. Shiu, N.C. Giebink, and S.R. Forrest, *Appl. Phys Lett*. **91**, 223507 (2007).
[120] A. Martí, L. Cuadra, and A. Luque, *Proc. of the 28th Photovolt. Spec. Conf.* ,p.940 (2000).
[121] A. J. Nozik, *Chem. Phys. Lett*. **457**, 3 (2008).
[122] D. Derkacs, W.V. Chen, P.M. Matheu, S.H. Lim, P.K.L. Yu, and E.T. Yu, *Appl. Phys. Lett*. **93**, 091107 (2008).
[123] H.R. Stuart and D.G. Hall, *Appl. Phys. Lett.* **69**, 2327 (1996).
[124] H.R. Stuart and D.G. Hall, *Appl. Phys. Lett.* **73**, 3815 (1998).
[125] B.J. Soller and D.G. Hall, *J. Opt. Soc. Am. A* **18**, 2577 (2001).
[126] D. Derkacs, Ph.D. thesis, Univ. of California, San Diego (2009).
[127] S.D. Gunapala, S.V. Bandara, C.J. Hill, D.Z. Ting, J.K. Liu, S.B. Rafol, E.R. Blazejewski, J.M. Mumolo, S.A. Keo, S. Krishna, Y.-C. Chang, and C.A. Shott, *IEEE J. Quantum Electronics* **43**, 230 (2007).
[128] W.Y. Han, et al. *J. Appl. Phys.* **74**, 754 (1993).
[129] E. Yablonovitch, T. Sands, D.M. Hwang, I. Schnitzer, T.J. Gmitter, S.K. Shastry, D.S. Hill and J.C.C. Fan, *Appl. Phys. Lett.* **59**, 3159 (1991).
[130] S.H. Brewer, W.R. Glomm, M.C. Johnson, M.K. Knag and S. Franzen, *Langmuir* **21**, 9303 (2005).
[131] S.H. Lim, W. Mar, P. Matheu, D. Derkacs, and E.T. Yu, *J. Appl. Phys*. **101**, 104309 (2007).
[132] H.T. Johnson, V. Nguyen, and A.F. Bower, *J. Appl. Phys*. **92**, 4653 (2002).

[133] J. Zhao, A. Wang, M. A. Green, and F. Ferrazza, *Appl. Phys. Lett*. **73**, 1991 (1998).
[134] L.L. Ma, Y.C. Zhou, N. Jiang, X. Lu, J. Shao, W. Lu, J. Ge, X.M. Ding, and X.Y. Hou, *Appl. Phys. Lett*. **88**, 171907 (2006).

Chapter 4: Demonstration of Light Trapping in Thin Film Quantum Dot-in-Well Solar Cells

Thin film device structures are attractive for reducing the cost of solar cells and because they can enable more efficient carrier collection than thick films. Thin film GaAs solar cells with embedded InGaAs/GaAs quantum wells and/or dots also benefit from the higher absorption coefficient of InGaAs relative to GaAs. Furthermore, at solar wavelengths, thin structures are superior waveguides to the optically thick devices of Chapter 3. While the low dielectric contrast between GaAs and InGaAs makes it difficult to guide light strictly in the intrinsic region of *p-i-n* solar cell structures made of those materials, where quantum wells and/or dots are located, the entire device structure can be an effective waveguide if it is bounded by layers with low refractive indices. Using a thin film, on the order of one to several microns thick, cuts off the substrate radiation modes that dominate the modal spectrum of optically thick device structures, such as those investigated in the previous chapter. In general, thick device structures poorly confine scattered light to the area near the intrinsic region, where it can be absorbed by quantum wells/dots. Utilizing a thin geometry, where quantum wells/dots occupy a significantly larger fractional volume of devices, increases the spatial overlap of guided waves and sub-band absorbing materials, improving the effectiveness of light trapping.

In addition to light trapping, which maximizes absorption of light, it is also essential to achieve as close to unity transmission of light into devices as possible. To that end, placing scattering structures on the rear of devices and using an anti-reflection coating (ARC) on the top is promising. This approach attempts to separate the tasks of maximizing transmission of light and light trapping. Ideally, the light scattering features do not damage the back surface of the semiconductor, nor do they degrade the back

contact properties. In that respect, light trapping structures that are compatible with standard device and thin film processing are highly desirable. To that end, this chapter presents numerical and experimental results of thin film In(Ga)As/GaAs quantum dot-in-well solar cells with software-optimized diffractive structures (i.e., planar, symmetric grating-like structures) located on their rear sides.

4.1. THIN FILM DEVICE LAYER STRUCTURE AND DESIGN

Producing thin films of sufficiently high quality to make optoelectronic devices requires that the films be epitaxially grown on a rigid substrate, followed by removal of the thin film from the growth substrate. One approach to doing so is to attach the epitaxial device film to a support and then destructively remove the growth substrate. That method has been utilized in this work to minimize the number of process steps required to fabricate thin devices. An economically preferable method is to non-destructively "lift off" the epitaxial device film from the growth substrate. This process, which is frequently called "epitaxial liftoff" (ELO), allows the substrate to be re-used for additional growths, reducing the cost of producing devices.[135-137] Another process, referred to as "controlled spalling," has been demonstrated for removing thin film multi-junction solar cells from a growth substrate, which may enable re-use of the substrate.[138]

The epitaxial layer structures of thin film devices investigated in this chapter are shown in Fig. 4.1. All devices are grown on 2 inch (100) GaAs wafers by molecular beam epitaxy (MBE; refer to Sec. 1.7.2). A principal issue in the design of these structures is to enable substrate removal without damaging the epitaxial devices. Device structures were grown by MBE in Prof. Daniel Schaadt's group at the Karlsruhe Institute of Technology. The source materials available for MBE growth were Ga, In, Al, As, and N, with dopants Si and Be. Based on the source materials, $Al_xGa_{1-x}As$ is used as a stop

etch material for selective removal of GaAs substrates by the aqueous etch solution of hydrogen peroxide (H_2O_2) and ammonium hydroxide (NH_4OH). This etchant has demonstrated selectivity in etch rates of GaAs:AlAs from 493:1[139] up to 1000:1.[140] $Al_{0.85}Ga_{0.15}As$ is chosen for the stop etch layer in this work because AlAs oxidizes at room temperature and can become brittle,[141] potentially resulting in physical damage to devices. The selectivity of the etch rate for GaAs:$Al_{0.85}Ga_{0.15}As$ is likely less than for GaAs:AlAs, and may be considerably lower than 500:1. In consideration of that possibility, a thick stop etch layer of 800 nm $Al_{0.85}Ga_{0.15}As$ is used.

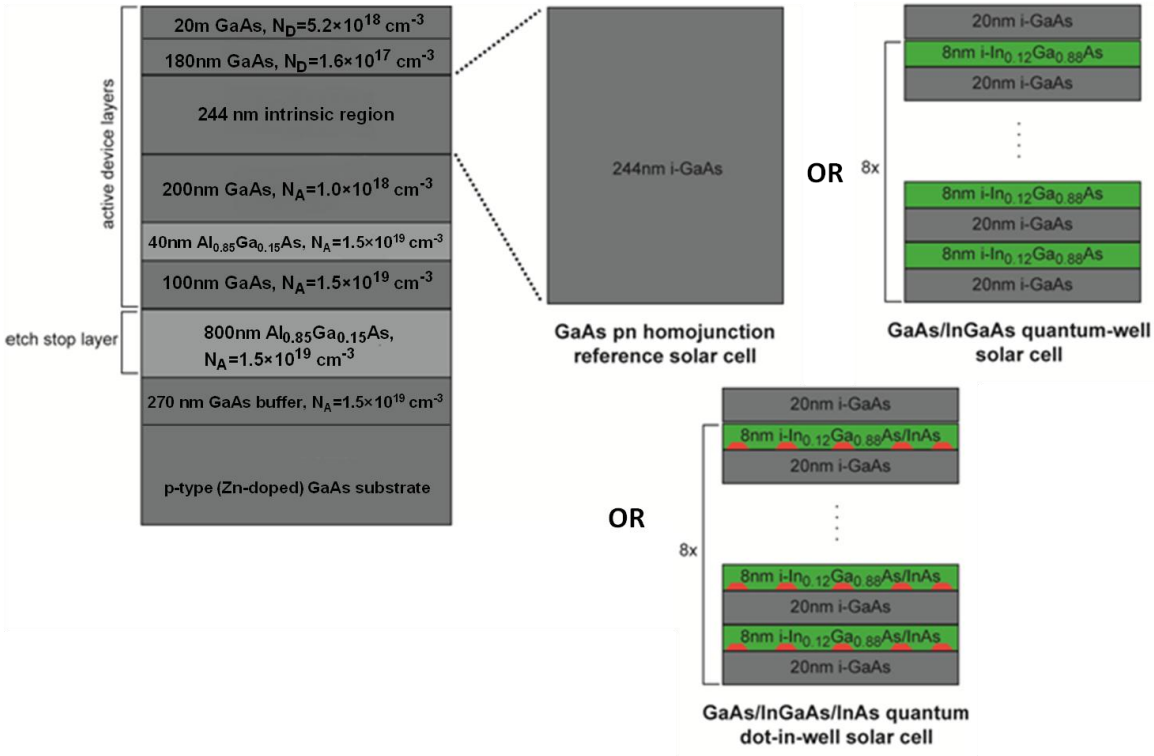

Figure 4.1: Layer structures of wafers used for thin film device experiments. Three device configurations are investigated, which are shown: a GaAs homojunction structure, an $In_{0.12}Ga_{0.88}As$/GaAs quantum well structure, and a structure with InAs quantum dots inserted in $In_{0.12}Ga_{0.88}As$/GaAs quantum wells. Both the quantum well and quantum dot-in-well devices contain 8 periods of the heterostructure.

The polarity of these thin film solar cells was chosen based on the *p*-type doping of the growth substrate. In order to be able to test the devices with the substrate and stop etch layer intact, an *n*-*i*-*p* growth configuration was selected, as illustrated in Fig. 4.1. The stop etch layer was grown after a p^{++}-GaAs buffer layer. These are followed by the epitaxial device layers, which begin with p^{++}- and p^{+}-GaAs contact layers of 100 nm and 200 nm, respectively that are separated by a 40 nm p^{++}-$Al_{0.85}Ga_{0.15}As$ window layer. The high aluminum fraction of 85% results in a window bandgap of 2.1 eV, corresponding to a wavelength of 590 nm, and has been chosen, along with a thickness of 40 nm, to minimize absorption of incident light while adequately passivating the underlying GaAs. The passivation is important for minimizing surface recombination, which is the essential function of a window. Instead of a window layer, the *n*-type side features 20 nm n^{+}-GaAs with higher doping than the bulk of the *n*-type contact. This *back surface field* (BSF) creates a potential barrier for minority holes that are photogenerated in the quasi-neutral *n* region, increasing the probability that they diffuse toward the junction and are collected.

The window is grown on the bottom of the layer structure and the BSF is grown on the top of the layer structure because the epitaxial wafers are intended to be inverted and bonded to a support during fabrication of thin film devices, which is illustrated in Fig. 4.2. After removing the GaAs growth substrate, the final polarity of the solar cell is *p*-*i*-*n*, and the window layer is near the top side of the thin film structure. Nominally, in the inverted geometry, contact would be made to the 200 nm p^{+}-GaAs layer located below the AlGaAs window by selectively removing the 100 nm p^{++}-GaAs and window layers. However, these layers have been heavily doped to enable contact to the top 100 nm p^{++}-GaAs without removing it or the window. The high doping (N_A=1.5×10^{19} cm^{-3}) minimizes the resistance for hole transport across the wide-bandgap window in such a situation.

The thickness of the remaining layers was chosen to give a total active device thickness of ~1 μm in order to confine light reasonably near to the intrinsic region. Eight periods of the quantum well structure {8 nm $In_{0.12}Ga_{0.88}As$/20 nm GaAs}, or of the quantum dot-in-well structure {8 nm $In_{0.12}Ga_{0.88}As$/0.69 nm InAs/20 nm GaAs}, were grown in the intrinsic region, which nominally totaled 244 nm in thickness. With the 200 nm base and emitter layers and the 40 nm window layer, the total device thickness is approximately 700 nm. If the p^{++}-GaAs layer is not removed, the device is ~800 nm thick. The 200 nm thickness of the base and emitter is chosen to provide adequate separation between the surface depletion region and the intrinsic region, which may be wider than they are expected to be, particularly if devices are tested at reverse bias.

The doping of the base and emitter layers, and the thickness of the intrinsic region, were selected to facilitate carrier collection from quantum well sub-band states. Studies of InAsP/InP multiple quantum well solar cells, including ones with barrier heights comparable to those of $In_{0.12}Ga_{0.88}As$/GaAs, found that a critical built-in field of $E_{bi} > 35$ kV/cm in the intrinsic region was necessary for complete collection of carriers from quantum well sub-band states.[142,143] Based on the depletion approximation, and using the specified base and emitter doping, these devices have $E_{bi} > 35$ kV/cm at forward biases of up to 500 mV.

The depletion approximation is expected to over-estimate the built-in field by not accounting for the higher intrinsic doping or the background doping of the intrinsic region. Thus, it is possible that incomplete collection of carriers from quantum well sub-band states begins at biases below the maximum power voltage of the thin film quantum well solar cells in this work. The larger band offsets associated with InAs quantum dots in the $In_{0.12}Ga_{0.88}As$/InAs/GaAs quantum dot-in-well structure means that a critical field of >35 kV/cm is likely required for complete collection of carriers from quantum dot sub-

band states. Studies of a single layer of InAs/GaAs quantum dots grown similarly to those in the quantum dot-in-well devices of this work found that photocurrent due to tunneling escape of carriers from the quantum dots began to increase from zero at an electric field of ~100 kV/cm, and saturated at ~150 kV/cm.[144] As these fields are inaccessible without reverse biasing the thin film quantum dot-in-well solar cells, carrier escape from quantum dot states is expected to be dominated by phonon absorption.

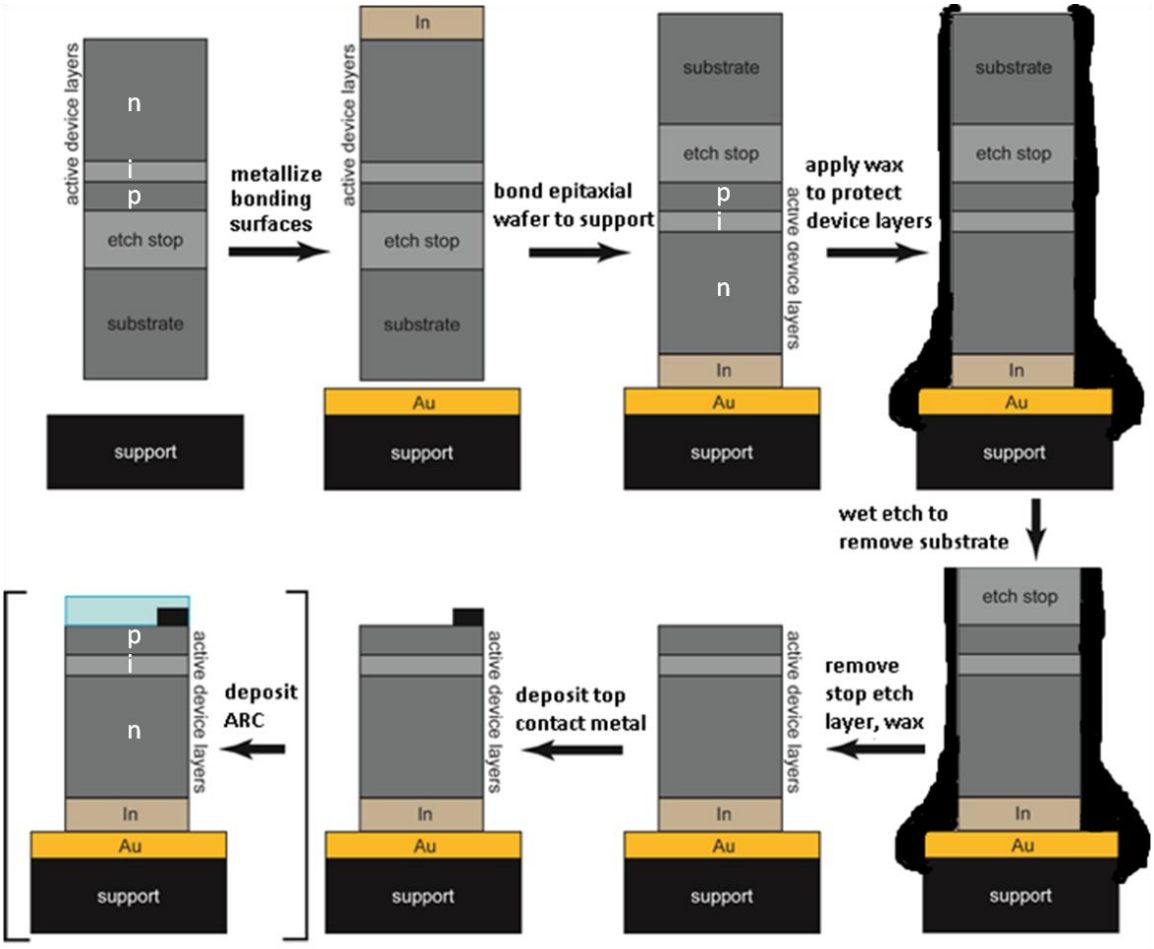

Figure 4.2: Illustration of the thin film device fabrication process used in this work. Note that the as-grown epitaxial device, on top of the substrate, has *n-i-p* polarity, which is inverted during fabrication so that the final thin film device has *p-i-n* polarity.

4.2. Optimization of Periodic Structures for Light Trapping

Both randomly and periodically structured materials can be effective for light trapping, though the geometry of a periodic structure can be rigorously optimized by simulation and it can be fabricated consistently using lithographic techniques. A periodic structure that is optimized for one wavelength does not perform well at most other wavelengths, however, and the large number of iterations required to manually configure it over the broad parameter space of potentially useful geometries makes such an approach unattractive, and potentially infeasible. Software-based optimization offers an efficient means of maximizing solar cell performance by considering the broadband response of a device.

Simulations of periodic structures, such as diffraction gratings, can be efficiently performed using rigorous coupled-wave analysis (RCWA). Algorithms based on this frequency-domain method of solving Maxwell's equations use relatively simple spatial representations of a simulated structure, dividing it into layers in the direction transverse to its periodicity. Each layer consists of a spatial dielectric function that is modeled using Fourier harmonics, which generally requires much less computational memory than constructing a geometric mesh over the same volume. The electromagnetic fields in a simulation are also represented by a sum over coupled waves, and each coupled wave relates to a Fourier harmonic. With models for the dielectric structure and fields that are both composed of Fourier harmonics, Maxwell's equations can be solved efficiently in the frequency domain. RCWA solutions can provide the steady-state spatial distribution of the electromagnetic field and related quantities, such as energy density, absorption, reflection, and transmission. Refs. 145-148 contain additional information about modeling and simulations that use RCWA.

Here, the performance of solar cells is estimated based on the net absorption of light by device structures as calculated by RCWA simulation using DiffractMOD software from RSoft Design Group. Since RCWA solutions yield the steady-state spatial electric and magnetic field amplitudes, the normalized absorptivity *in the semiconductor layers of a device* at a given wavelength, $A_s(\lambda)$, assuming unity incident power, is given by:[149]

$$A_s(\lambda) = \frac{\omega}{2} \int_{V_s} \epsilon_2(\omega, \mathbf{r}) |\mathbf{E}(\mathbf{r})|^2 d\mathbf{r}, \tag{4.1}$$

where ω is the angular frequency of the incident radiation, $\mathbf{r}$ is the position vector, $\epsilon(\omega, \mathbf{r}) = \epsilon_1(\omega, \mathbf{r}) + i\epsilon_2(\omega, \mathbf{r})$ is the dielectric function, which varies according to the materials in the simulated volume of the device, V, and $\mathbf{E}(\mathbf{r})$ is the electric field vector. The integral in Eq. 4.1 is performed over the volume of semiconductor that comprises the active device, V_s, which is a subset of V. The simulated device structure is likely to include metals or other lossy materials that do not contribute to the photocurrent of a device, so it is important to exclude the power absorbed in them from the calculation. Based on these quantities, the photocurrent density generated at a given wavelength, $j(\lambda)$, is a function of $A_s(\lambda)$, the incident photon flux at that wavelength, $\Phi_{ph}(\lambda)$, and the carrier collection efficiency, $\mathfrak{f}_{eh}(\lambda)$, where it is assumed that each absorbed photon produces one electron-hole pair:

$$j(\lambda) = \Phi_{ph}(\lambda) \times A_s(\lambda) \times \mathfrak{f}_{eh}(\lambda). \tag{4.2}$$

The short-circuit current density of a solar cell, J_{sc}, is then obtained by integrating over the full range of its spectral response:

$$J_{sc} = \int j(\lambda) d\lambda. \tag{4.3}$$

In general, light trapping structures should seek to maximize J_{sc}. If it is assumed that, for a given device structure, incorporating light trapping features does not affect the

open-circuit voltage or fill factor of a device, then maximizing J_{sc} is equivalent to maximizing the efficiency. Quantifying changes in V_{oc} and *FF* that result from incorporating light trapping structures requires information about the electronic properties of the materials that comprise a device structure in order to solve the Boltzmann transport and Poisson's equations. This includes the band offsets at interfaces, intrinsic carrier and dopant concentrations, dopant ionization energies, the relative positions of Fermi energies in materials, carrier effective masses and lifetimes, dielectric constants of materials, and more. Ideally, these calculations are performed with simultaneous optical excitation, which requires the complex refractive indices or complex dielectric functions of materials. In the absence of software that performs such calculations, it is reasonable to assume that light trapping designs that (1) do not alter the semiconductor layer structure or surface, and (2) do not significantly affect the contact resistance, will not affect the V_{oc} or the *FF* of a device.

Rigorous electromagnetic simulations that are capable of modeling both photonic and plasmonic phenomena, such as those based on RCWA, finite-element calculations (refer to Ch. 3), and finite difference time-domain (FDTD), are well-suited to optimizing light trapping structures. The optimization process used here maximizes the J_{sc} of a device under the Airmass (AM) 0 solar spectrum[§] according to Eqs. 4.1-4.3. In the optimization, light is assumed to be incident normal to the device with 45° linear polarization to, in an average sense, account for the unpolarized nature of sunlight. Variable parameters included the period, pitch, and height of the light trapping structure, which was positioned immediately below the GaAs base layer of devices, and the thickness of a SiO_2 ARC on top of the device. This geometry is illustrated in Fig. 4.3.

[§] The AM 0 spectrum is also known as the "extra-terrestrial" solar spectrum (i.e., in space) and by its designation as standard ASTM E490.

The optimization consisted of a search with a genetic algorithm[150] over a broad parameter space for several periodic geometries, including rectangular, triangular, hexagonal, spherical, and semi-spherical structures. The range of the parameters allowed in the optimization was dictated by the photocurrent spectra of InGaAs/GaAs quantum dot-in-well solar cells in Ch. 3. After the genetic algorithm finished, local optimization of the result was performed using a simplex algorithm, which is described in Ref. 151. By using a broad optimization followed by local refinement, as was done here, the complex parameter space of the performance of a solar cell with light trapping can be investigated reasonably thoroughly and efficiently.

The optimized periodic structure that provided the best J_{sc} of the investigated geometries is illustrated in Fig. 4.3. Though the structure is not a traditional reflection grating, it may be thought of as a multiply periodic, grating-like structure, which exhibits more complicated diffraction than typical gratings. The parameters of the structure that have been optimized are the pitch (parameters L_1, L_2, W_1, and W_2), the period in the x and y directions (D_1 and D_2, respectively), and the height (H_2). The thickness of the ARC (H_1) was also optimized. The RCWA simulations performed during optimization used a dielectric function for 8 nm $In_{0.12}Ga_{0.88}As$/20 nm GaAs quantum wells that was calculated according to the method of Sec. 2.4. While the AM 0 spectrum was chosen in this instance, the optimization procedure is general and can be applied with any incident spectrum. Finally, though the performance of the optimized structure, with dimensions given in Fig. 4.3, was the best of several geometries that were simulated, there are likely to be designs that offer similar or better performance, in particular for different spectral conditions.

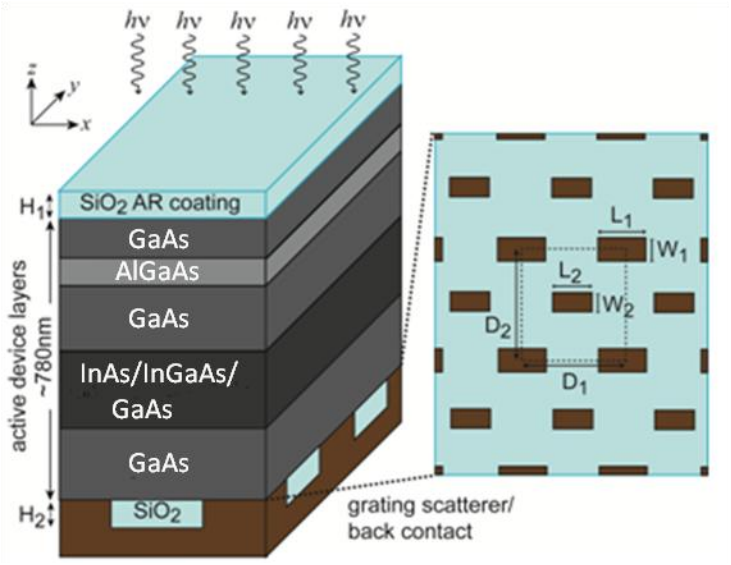

Figure 4.3: Diagram of the simulated device, which has a broadband, two-dimensional diffractive structure located on its back side. The optimization procedure produced the following dimensions: W_1 = 184 nm, L_1 = 474 nm, W_2 = 168 nm, L_2 = 356 nm, D_1 = 900 nm, and D_2 = 1.13 μm.

The result of the optimization process is evaluated in terms of the spectral absorption response and the J_{sc} of a device for a given illumination condition. Assuming collection of all photogenerated carriers [i.e., $f_{eh}(\lambda) = 1$ in Eq. 4.2], the J_{sc} of a thin-film GaAs homojunction device (i.e., a device with the structure shown in Fig. 4.3 that contains no quantum wells or dots) with a planar metal back side is 28.4 mA/cm^2. The quantum well solar cell, which has eight periods of 8 nm $In_{0.12}Ga_{0.88}As$/20 nm GaAs, with a planar Pd back side, generates 28.6 mA/cm^2, and the quantum well solar cell with the back side diffractive structure shown in Fig. 4.3 generates 30.2 mA/cm^2. The results demonstrate that the slight benefit of adding a relatively small number of relatively weakly absorbing quantum wells to a GaAs device without any light scattering structure increases substantially with the addition of the diffractive structure. We note that the relatively low indium content (12%) of the quantum wells can be increased both to

increase their absorption coefficient and to enable absorption of additional infrared wavelengths, further improving photocurrent generation, and has been demonstrated for long-wavelength photodiodes.[152] Additionally, though Pd has been used in the fabrication of these devices, it is a relatively lossy metal, which considerably limits its usefulness in light trapping. Simulations that demonstrate the benefit of using strongly absorbing InGaAs/GaAs quantum wells, and of using Ag or other relatively low-loss materials to improve light trapping, are presented in Chapter 5.

Using the interpolated bulk and semi-empirical quantum well permittivity functions discussed in Sec. 2.4 (refer to Fig. 2.12), the absorption in the semiconductor layers of the quantum well solar cell has been calculated via RCWA simulations and is shown in Fig. 4.4. The results are presented as a ratio of the total normalized absorptivity in a device with a Pd-SiO_2 back side diffractive structure relative to absorption in a device with a planar Pd back side. The ratios are equal at wavelengths shorter than 850 nm, which is expected, because the semi-empirical model assumes that bulk optical properties apply to the quantum well at wavelengths shorter than the GaAs band edge. At wavelengths shorter than 500 nm, GaAs and InGaAs are very strongly absorbing and all light that transmits into the device is absorbed before reaching the back surface of the device. At wavelengths between 500 nm and 850 nm, the absorption varies due to Fabry-Perot interference in the thin device structure. As these wavelengths are smaller than the *x*- and *y*-periods of the diffractive structure, it is essentially transparent to them, and diffraction is negligible. However, the structure adds ~140 nm of dielectric material to the device structure, which shifts the Fabry-Perot resonances with respect to the planar device, producing the oscillations observed in the absorption ratio between wavelengths 500 nm to 850 nm.

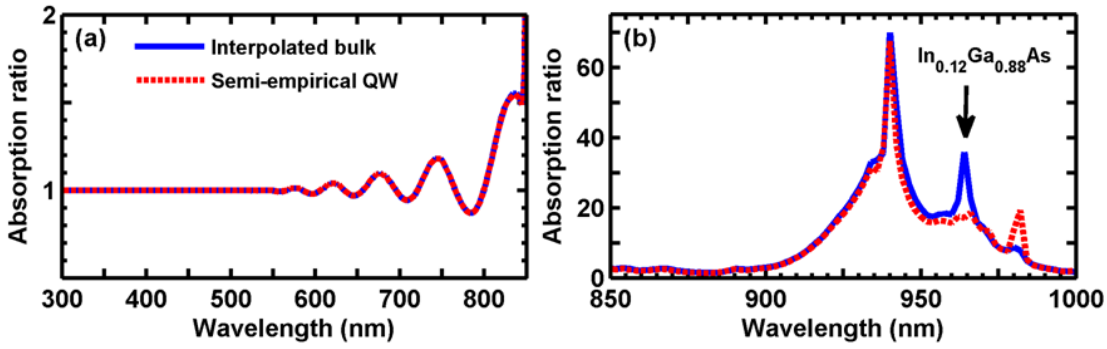

Figure 4.4: Ratios of the simulated spectral absorption by a quantum well solar cell with a Pd-SiO_2 diffractive structure, as illustrated in Fig. 4.3, relative to the same device with a planar back side of Pd, at wavelengths (a) shorter and (b) longer than the GaAs band edge, respectively. The device contained eight periods of 8 $In_{0.12}Ga_{0.88}As$/20 nm GaAs quantum wells. The ratio is shown for simulations that used (blue, solid line) interpolated bulk and (red, dashed line) semi-empirical quantum well permittivity functions to model the optical properties of the quantum wells. The absorption edge of semi-empirical 8 nm $In_{0.12}Ga_{0.88}As$/20 nm GaAs quantum wells is marked at 965 nm. However, due to inhomogeneous broadening of excitonic absorption, the semi-empirical quantum well absorbs light very weakly at wavelengths longer than 965 nm, as seen in Fig. 2.12.

Turning to longer wavelengths, shown in Fig. 4.4(b), the effects of the diffractive structure are evident. Most prominent are the peaks at wavelengths of 940 nm, 965 nm, and 980 nm, indicating increased absorptivity in the quantum wells by up to a factor of 70. The spatial distribution of electric field components has been calculated and illustrates the effect of waveguiding for absorption enhancement. Radiation is incident normal to the device surface, polarized with the electric field in the *x*-*y* plane. Therefore, a non-zero value of E_z indicates a diffracted or scattered wave. In Fig. 4.5(a), which shows the steady-state value of E_z in the *y*-*z* plane of the device at an incident wavelength of 940 nm, a distinct modal pattern is seen corresponding to a wave confined to the device structure. A representative cross-section of the same field component in the *x*-*y* plane is shown in Fig. 4.5(b), confirming the presence of a confined wave propagating in

the y direction. Comparison of the E_x, E_y, and E_z components in Fig. 4.5 reveals that the strength of the confined wave can be comparable to those of radiating waves, shown in Fig. 4.5(c) and (d), indicating strong coupling to the waveguide mode. The strength of coupling of incident radiation to waveguide modes of the device varies with wavelength, but the structure diffracts light into propagating modes of the device over a broad band of wavelengths greater than the GaAs band edge (at λ=850 nm), and the effect of this is evident in the improved absorption demonstrated in Fig. 4.4.

The absence of a peak in Fig. 4.4 at 965 nm in the "semi-empirical QW" absorption ratio results from the polarization dependence of optical transitions in the quantum wells. While large absorption enhancement can result from coupling of incident radiation to waveguide modes with substantial E_z fields, $\epsilon_{2,zz}$ for the semi-empirical permittivity is essentially zero at λ=965 nm (refer to Fig. 2.12) because of a selection rule that forbids optical transitions involving heavy hole states and z-polarized fields (refer to Table 2.1). The confined wave with a large E_z component is, therefore, weakly absorbed, leading to only a modest increase in absorption in a realistically modeled quantum well compared to the unrealistic case of bulk material, which absorbs light of all polarizations equally. Note that, as the interpolated bulk permittivity does not account for excitonic effects, it is coincidental that the peak in the absorption ratio modeled using it occurs at the same wavelength as the heavy-hole exciton transition, seen at 965 nm in Fig. 2.12. The peak at 965 nm for interpolated bulk permittivity in Fig. 4.4 results from diffraction of light into modes of the thin film device that increase its absorption of light.

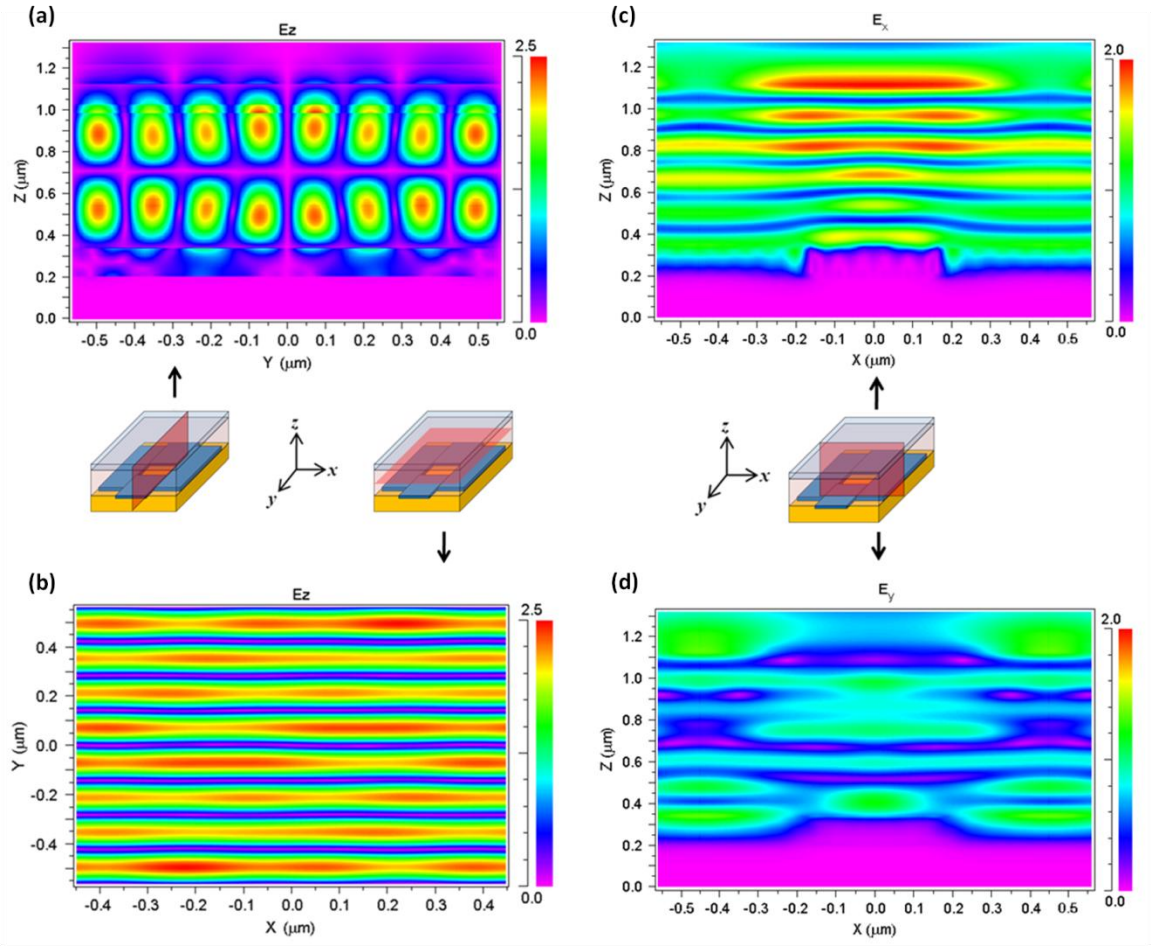

Figure 4.5: Calculated steady-state spatial distributions of (a,b) the E_z field component, (c) the E_x field component, and (d) the E_y field component at an incident wavelength of 940 nm in a thin film quantum well solar cell with a diffractive structure, as illustrated in Fig. 4.3. The simulations used the semi-empirical quantum well permittivity data shown in Fig. 2.12. Plots are cross-sectional cuts of (a) the *y*-*z* plane, (b) the *x*-*y* plane, and (c,d) the *x*-*z* plane. The fields in (a,b) illustrate that incident radiation at this wavelength strongly couples to a confined mode of the device structure via diffraction.

At an incident wavelength of 980 nm, the semi-empirical quantum well absorption ratio exhibits a considerably larger peak than the interpolated bulk ratio, as seen in Fig. 4.4. As seen in Fig. 2.12, at that wavelength, the semi-empirical ϵ_2 approaches zero for all polarizations of light, though it is finite due to homogeneous

broadening of excitons. The quantum well, therefore, absorbs light weakly. While the "interpolated bulk" value of ϵ_2 for $In_{0.12}Ga_{0.88}As$ is also small at 980 nm, it is more than an order of magnitude larger than the corresponding value determined by semi-empirical quantum well calculations. As Yablonovitch demonstrated for textured surfaces,[153] large absorption enhancement factors can be achieved with weakly absorbing materials, which we observe here as well: the relatively large peak in the semi-empirical quantum well absorption ratio at λ=980 nm in Fig. 4.4 is a product of large absorption enhancement due to light trapping in a waveguide mode, but at a wavelength where the quantum well is very weakly absorbing. Indeed, J_{sc} increases by less than 0.1 mA/cm^2 when Eq. 4.3 is evaluated to an upper wavelength limit of 1000 nm, instead of the effective upper limit on absorption of the quantum wells, which is ~970 nm. It is, therefore, likely that quantum well solar cells would benefit from diffractive or scattering structures that facilitate strong coupling to waveguide modes at additional wavelengths shorter than the absorption edge of quantum wells, and, in particular, that correspond to peaks in excitonic absorption.

4.3. Thin Film Device Processing and Fabrication

Fabrication of thin film III-V solar cells requires removal of epitaxial devices from their growth substrate. From an economic point of view, it is preferable to achieve this using a non-destructive technique, such as epitaxial liftoff.[135-137] In this work, the substrate has been destructively removed from the epitaxial device in order to minimize process complexity. This section describes the process utilized in this work to fabricate thin film devices.

4.3.1. Au-In Wafer Bonding

In any III-V thin film fabrication process, the epitaxial device film should be attached to a support prior to removing it from the growth substrate. Unsupported thin

films tend to curl over themselves, potentially rendering them useless in subsequent process steps. In this work, a metal bond between the epitaxial device and a support has been used to facilitate electrical connection and to provide mechanical support for thin films. The bond is one of Au and In, which alloy when they are placed in contact and heated to a temperature greater than the melting point of In (156° C).[154,155] The melting points of the alloys that form are in excess of 400° C,[156] so the bond is robust in subsequent high temperature process steps.

Devices were fabricated on samples that measured ~1 cm by 1 cm and were cleaved from a thin film device wafer. Pieces of single-side polished silicon wafers measuring ~1.2 cm by 1.2 cm or larger were used as supports to which thin devices were bonded. Both the III-V and Si samples were initially cleaned by rinsing them sequentially in acetone, methanol, and isopropyl alcohol to remove residual organic material, and then blown dry with nitrogen gas. Immediately prior to loading the samples into the metal evaporation system, native oxide was removed by dipping the wafer pieces in buffered oxide etch for 30 seconds, followed by rinsing them in running de-ionized water for 60 seconds, and blowing them dry with nitrogen gas.

Immediately following oxide removal etching, samples were loaded into an electron beam evaporator. The metals deposited on the III-V samples and on the Si support are different, so they required separate deposition runs. In order to achieve contact uniformity, and to improve process repeatability, the system was allowed to pump until it was close to its minimum base pressure before beginning deposition. In the CHA evaporators at UT, this corresponds to a pressure of ~3.2×10^{-6} Torr.

III-V device samples were loaded such that metal was deposited on the epitaxial growth side. In the device structures of Fig. 4.1, the top device layer is *n*-type GaAs, so the first metals that were deposited were those required for the *n*-type contact. As

mentioned in Sec. 3.2.3, Pd/Ge contacts to GaAs are intended to be annealed so that they alloy, producing tunneling ohmic barriers. However, annealing tests of Pd/Ge contacts to similar quantum well and dot solar cells found negligible differences between annealed and unannealed contacts. Therefore, the contacts used here have not been annealed. The *n*-type GaAs contact consisted of, in order of deposition, from the metal listed first: Pd (25 nm)/Ge (10 nm)/Pd (25 nm)/In (1200 nm). Even when they are not annealed, Pd-based contacts to GaAs are attractive because Pd reacts at room temperature to displace native oxide at the semiconductor surface, forming Pd_4GaAs.[157] The final layer of indium in the metallization was used in subsequent In-Au bonding to Si support pieces. Care was taken to prevent In oxidation by storing the III-V samples in isopropyl alcohol after metal deposition. Alternatively, metals that can oxidize may be stored in a nitrogen gas ambient or other non-reactive environment.

For metallization of the Si support pieces, samples were loaded such that metal was deposited on their polished faces. After the evaporation chamber reached its minimum base pressure, samples were coated with Ti (20 nm) / Au (800 nm). The choice of thick In (1200 nm, on the device wafer) and Au (800 nm, on the Si support) layers for bonding ensures that an adequate amount of each metal is available to form a robust bond. Nominally, the weight percent of In in the high temperature Au-In alloys varies from 24-42%,[154] and the atomic weights are 197 for Au and 115 for In. If all of the In and Au reacted during the formation of bonds in this work, the resulting mixture would be 47% In by weight, which is sufficient to form each of the high temperature alloys. It is desirable that all of the In incorporates into alloys in the bonding process so that the bond is as resistant to high temperature as possible. It is unknown to what extent the amounts of elemental In and Au were consumed in the bonding process. However, when

proportionally thinner layers of each metal were used in bonding attempts, the bond was relatively easily broken by a mechanical test, as will be described.

Samples were cleaned immediately prior to bonding to promote high quality. Au-coated Si pieces were rinsed with solvents, blown dry with nitrogen, and cleaned in an oxygen-plasma system at 150 W and 350 mTorr for 10 minutes. III-V samples, which were stored in solvent to prevent In oxidation and to maintain cleanliness, were blown dry with nitrogen just prior to bonding.

To bond the samples, first, the cleavage planes of the wafers were aligned, with the In and Au in contact. Pressure was applied manually to the wafer stack while it was heated to 250° C on a hot plate in a class 1000 clean room, and the pressure was maintained until the temperature indicator on the hot plate displayed less than 130° C. The wafer stack was then allowed to cool on the hot plate until the indicator displayed room temperature. Lateral pressure was applied manually to each side of the III-V sample using plastic tweezers to confirm that it had bonded to the Si support.

4.3.2. Fabrication of Back Side Diffractive Structures on Thin Film Devices

When a light-scattering structure was included on the rear of thin-film devices, it had to be fabricated before bonding a III-V sample to its support. To accomplish this for the optimized diffractive structures of Sec. 4.2, first, the same cleaning and oxide removal steps used in Sec. 4.3.1 were performed on the III-V sample. Then, 140 nm of SiO_2 was deposited on an area of 5 mm by 5 mm in the center of the sample by covering the outer portions with Kapton tape. The oxide was deposited by plasma-enhanced chemical vapor deposition at 200° C or by electron beam evaporation. Following oxide deposition, samples were soaked in acetone to facilitate gentle removal of the Kapton

tape and to remove any residue from it. Sample cleaning was completed by rinsing them in acetone, methanol, and isopropyl alcohol, before blowing them dry with nitrogen gas.

Next, electron beam lithography was used to pattern an etch mask on the oxide. ZEP 520A positive e-beam resist was spun on the oxide in the center of III-V samples at 4000 rpm for 60 seconds, which were then immediately baked on a hot plate at 180° C for 120 seconds. The pattern of the diffractive structure was written in the resist in a grid of 1 mm by 1 mm elements using a JEOL JBX 6000F/S system with a beam current of 100 pA and an acceleration voltage of 50 kV. Each grid element contained approximately 1000 periods of the diffractive structure. After the write finished, the pattern was developed in n-amyl acetate for 60 seconds, rinsed in isopropyl alcohol, and blown dry with nitrogen gas. A scanning electron microscope (SEM) was used to image numerous portions of the developed pattern and to record the sizes of its features, an example of which appears in Fig. 4.6(a).

ZEP 520A is supposed to function well as a dry etch mask, which was a large part of the reason for using it here. After developing the resist pattern, the partially-masked SiO_2 was etched via reactive ion etching to transfer the grating pattern to it. The etch mixture consisted of gaseous CF_4/H_2 which was ionized at an RF power of 100 W and a pressure of 100 mTorr. Based on Dektak measurements of the step height of oxide layers before and after that etch, oxide removal occurred at ~15 nm/minute. Following the etch, typically none of the ZEP 520A resist was visible, indicating that it, too, was substantially etched. However, SEM imaging confirmed that oxide was removed predominantly in the regions where openings were present in the resist pattern, as seen in Fig. 4.6(b). Fig. 4.6(c) confirms that reasonable diffractive structure patterns were produced over relatively large areas. Following SiO_2 pattern etching, samples were

soaked in Remover PG to remove residual resist. Samples remained in Remover PG until they were ready for metal deposition, and always for at least one hour.

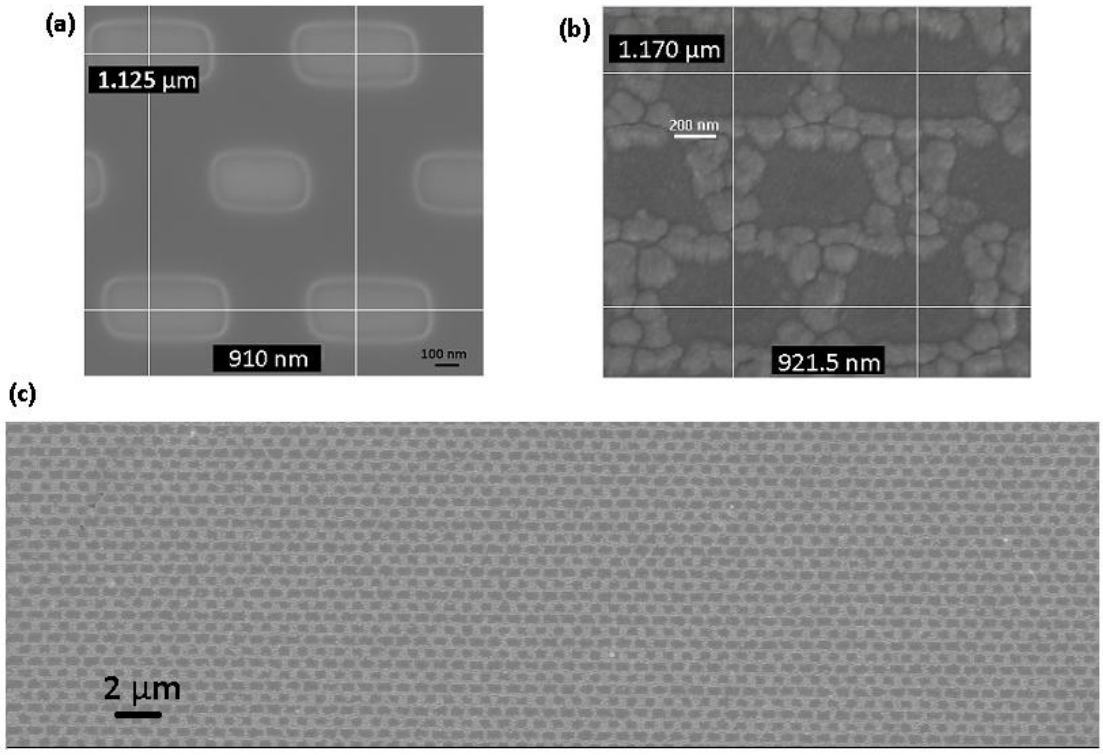

Figure 4.6: Scanning electron micrographs of (a) the developed ZEP 520A diffractive structure etch mask pattern; (b) the post-CF_4/H_2 dry etch, where SiO_2 grains are visible in between the spaces where metal is to be deposited; (c) a wide area of the resulting post-dry etch pattern seen at higher magnification in (b).

Finally, e-beam evaporation was used to fill in the metallic portions of the diffractive structures and, simultaneously, to deposit the back contacts to thin film devices. Immediately prior to loading them into the deposition system, samples were taken from the Remover PG, rinsed with acetone, methanol and isopropyl alcohol, and blown dry with nitrogen. The metal deposition consisted of the following sequence: Ti (5 nm)/Pd (25 nm)/Ge (10 nm)/Pd (25 nm)/In (1200 nm), which, with the exception of the

thin Ti adhesion layer, is identical to the *n*-type GaAs contact and bonding metal sequence in Sec. 4.3.1. Ti is used as an adhesion layer because, when it was not used, the subsequent metals were found to adhere poorly, or not at all, to SiO_2. The grating must be coated by metal to enable a reflective diffraction structure. The use of the Ti adhesion layer likely changed the electrical properties of the contact; however, as it was not annealed, and because a large area contact nominally formed where metal deposited on the outer portion of the III-V sample, which surrounded the central area with the diffractive structure, sufficient contact was made to the thin devices for the sake of measurements. Following metal deposition, these devices were bonded according to the procedure of Sec. 4.3.1, and the processing both of these samples and of reference samples with planar metal contacts continued as described in the next sections.

4.3.3. Substrate Removal Etching

Following bonding of III-V samples to Si holders, Apiezon Wax W ('black wax') was melted on the sides of the wafer stack at 110° C to protect them during substrate removal etching. Black wax is resistant to a number of chemicals, which guided selection of it for protecting the epitaxial device during etching. The etch solution consisted of hydrogen peroxide (H_2O_2) and ammonium hydroxide (NH_4OH) mixed in the volumetric ratio 19:1 of H_2O_2:NH_4OH, which etches GaAs preferentially to AlGaAs.[139,140,158] The mixture used in this work consisted of 190 mL of H_2O_2 and 10 mL of NH_4OH, which was mixed in an uncovered beaker at 150 rpm, at room temperature, by a magnetic stirrer. The sample was suspended in the etch solution using a Teflon basket attached to a vertical stand. A protective material (in this case, black wax) was necessary to protect GaAs layers in the epitaxial device structure during removal of the GaAs substrate, which occurred at rates of 2-3 μm/minute.

When the AlGaAs stop etch layer was exposed following consumption of the GaAs substrate by the etch reaction, colorful patches of material became visible, due to oxidation of the AlGaAs. When colorful areas were visible across the majority of the area where the GaAs substrate was previously seen, samples were removed from the etch solution, rinsed for 60 seconds in de-ionized water, and blown dry with nitrogen gas. Samples were then immersed in hydrofluoric acid (HF) until the epitaxial GaAs layer below the stop etch layer was visible, which took approximately 5 seconds. The black wax was not removed prior to HF etching because doing so likely would have resulted in damage to the AlGaAs window layers in the device structures. No evidence has been found of damaged window layers, but, due to that possibility when HF etching is used, InGaP may be preferable as a window material if it is available for growth.

4.3.4. Mesa Etching and Top Contact Lithography

Following substrate removal, mesas of 1 mm^2 or 4 mm^2 are patterned via photolithography and isolated by wet etching. Illustrations of mesa devices are shown in Fig. 4.7(a) and an optical micrograph of a fabricated mesa device appears in Fig. 4.7(b). First, AZ 5209E photoresist was spun onto III-V device films at 3000 rpm for 60 seconds and, immediately thereafter, samples were baked on a hot plate at 90° C for 45 seconds. The resist was exposed to a mesa device etch mask pattern for a time that nominally provided a dose of 100 mJ/cm^2. Immediately following exposure, the resist was developed in AZ 726 MIF for 25 seconds, rinsed in de-ionized water for 30 seconds, and blown dry with nitrogen gas.

Mesa etching of GaAs devices was performed using the peroxide-ammonia solution used for substrate removal, which was discussed in Sec. 4.3.3. After removing the top 100 nm of *p*-type GaAs during mesa etching of III-V devices, the underlying

AlGaAs window layer was removed by immersing them in HF for 3 seconds. Finally, mesa etching was completed in the peroxide-ammonia solution, where samples were held until the contact metal (Pd or Ti) beneath the GaAs device layers was visible around, and in between, the mesas. Samples were then rinsed in de-ionized water and blown dry with nitrogen gas.

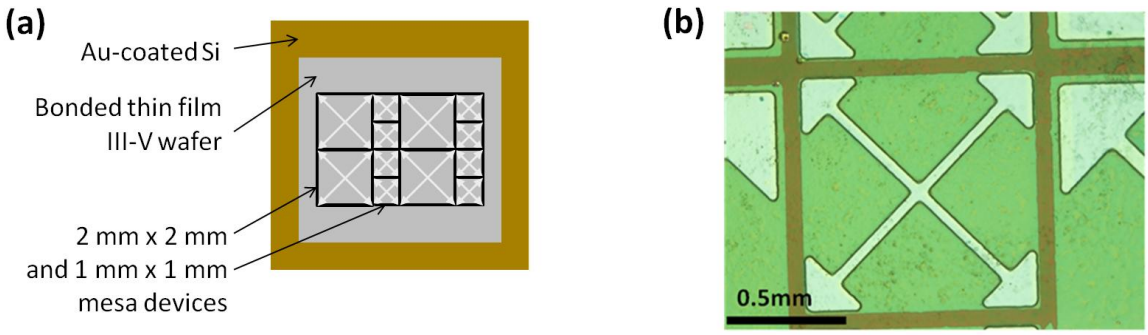

Figure 4.7: (a) An illustration of the geometry of thin film devices, where the footprint (i.e., the area) of the Au-coated Si support is larger than that of the III-V sample bonded to it, allowing an electrical probe to be placed on the Au to make contact to the back of the device via the conductive In-Au bond. A second probe contacted the tops of mesa devices at one of the four triangular pads seen in the corners in (a) and in (b). (b) An optical micrograph of a 1 mm by 1 mm mesa device.

Next, the black wax removed from samples by soaking them in chlorobenzene, which is a solvent for the wax. When wax was no longer visible on the samples, they were rinsed with acetone, methanol, and isopropyl alcohol, and blown dry with nitrogen gas. Photolithography was performed again, using the same procedure as for mesa pattern lithography (refer to the first paragraph of this section) with a pattern that produces the 'X-shaped' finger contacts that appear in Fig. 4.7(a, b). Immediately before loading samples into the metal evaporator, oxide etching of the exposed GaAs was performed by immersing samples in a mixture of hydrochloric acid:de-ionized water, in the ratio 1:1 by

volume, for 10 seconds. After etching them, samples were rinsed in de-ionized water and dried with nitrogen gas. 100 nm of Pd was evaporated to contact the top *p*-type GaAs contact. Finally, lift off was performed in acetone, which removed the remaining photoresist and metal deposited on it, yielding the top finger contacts, and completing the mesa devices.

It should be noted that, as discussed in Sec. 4.1, the top contact to thin film devices should nominally be made to the 200 nm p^{+}-GaAs emitter, which is located below the AlGaAs window layer. Doing so would require at least one additional photolithography step, followed by removal of the top 100 nm of p^{++}-GaAs cap layer, and removal of the AlGaAs window, both potentially using the same etch solutions described above for GaAs and AlGaAs, in order to access the GaAs emitter. Due to what appear to be material issues with some thin film devices that potentially occurred during device fabrication (refer to Sec. 4.6.3), the additional process steps required to access the GaAs emitter were omitted in this work and contact has been made to the top 100 nm p^{++}-GaAs cap layer. Some implications of that decision, and of not depositing an ARC on the devices investigated here, are discussed in the next section.

4.4. Measurements of Thin Film Devices and Comparison of Results with Simulation

The spectral response of thin film devices with and without diffractive structures has been measured at zero bias. Measurements were performed with a single-grating monochromator-based system that used AC lock-in signal detection. The spectral response of several reference devices, with planar Pd rear surfaces, and of a quantum dot-in-well device with the optimized Pd-SiO_2 diffractive structure discussed in Sec. 4.2, are shown in Fig. 4.8. It can be seen that the response of all devices oscillates at wavelengths shorter than the GaAs band edge (~850 nm), with obvious photocurrent generation up to

~950 nm for the quantum well device and up to ~1000 nm for the quantum dot-in-well device. The magnitude of the response of quantum well and dot-in-well devices with planar metal back reflectors/contacts is quite low at wavelengths from 900 nm to 1000 nm, which is due to the lack of light trapping and to a combination of strong absorption by Pd and reflections at the top surfaces. The importance of those effects is discussed in detail in the next chapter. Here, of primary interest is the result that the measured response of the quantum dot-in-well device with a back side diffractive structure ("QD-g") is larger than the dot-in-well device with a planar Pd back side ("QD-p"), which is particularly relevant at wavelengths of 850 nm and longer.

Also, with regard to the spectral response of quantum dot-in-well devices at wavelengths longer than 850 nm, carrier escape from quantum dot sub-band states at zero bias and at forward bias is likely to be inefficient. This is assumed because the electric field in the dots has been calculated at 27 kV/cm using a one dimensional Poisson solver.[159] This field is only modestly larger than the ~22 kV/cm necessary for efficient carrier escape from quantum wells with barrier heights similar to those of $In_{0.12}Ga_{0.88}As/GaAs$,[142,143] and it is likely inadequate for the much larger InAs/GaAs barriers with quantum dots. Thus, as seen in the inset of Fig. 4.8, very little photocurrent is generated at wavelengths of 1000 nm to ~1250 nm. Nevertheless, the measurements demonstrate that using quantum dots enabled photocurrent generation at much longer wavelengths than the quantum wells, and the results are useful for analyzing the effect of light trapping.

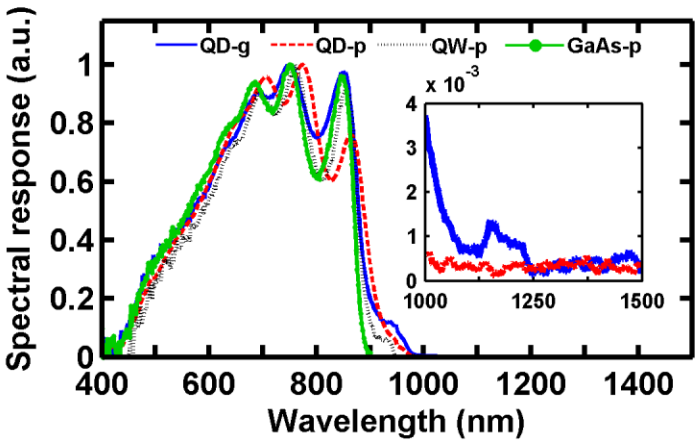

Figure 4.8: Normalized spectral response of the following types of thin film devices: ("GaAs-p") a GaAs homojunction solar cell with planar metal back side; ("QW-p") an eight-period {8 nm $In_{0.12}Ga_{0.88}As$/20 nm GaAs} quantum well solar cell with planar Pd back reflector/contact; ("QD-p") an eight-period {8 nm $In_{0.12}Ga_{0.88}As$/0.69 nm InAs/20 nm GaAs} quantum dot-in-well solar cell with planar Pd back reflector/contact; and ("QD-g") the same quantum dot-in-well device structure, but with a back side Pd-SiO_2 diffractive structure with nominal parameters indicated in Fig. 4.3. Inset: the "QD-g" and "QD-p" device response at wavelengths longer than the quantum well absorption edge.

The effect of the diffractive structure on the spectral response of thin-film devices is illustrated in Fig. 4.9, which shows the ratio "QD-g"/"QD-p" based on the spectra of Fig. 4.8. Also shown in Fig. 4.9 is the corresponding ratio of simulated absorption in the device structures. The measurement and simulation results agree well at wavelengths shorter than 850 nm, where the only effect of the diffractive structure is to modify the thickness of the thin-film cavity, as discussed in Sec. 4.2, resulting in the oscillations observed in the ratios.

At wavelengths longer than 850 nm, the spectral response of the device with the diffractive structure ("QD-g") increases compared to the device with a planar back reflector ("QD-p") due to enhanced absorption in quantum wells and dots, which results from increased photon path lengths subsequent to diffraction. Differences in the positions

of maxima and minima in the measured and simulated response ratios (see Fig. 4.9) likely result from differences between the nominal thin film device thickness and diffractive structure feature sizes, and their values in fabricated devices. Further, the waveguide consists of the semiconductor structure bounded by air on the top and metal on the bottom. Imperfections at these boundaries, including roughness of the top surface produced by substrate removal, may degrade the quality of the waveguide, resulting in lower enhancement of the spectral response in measured devices compared to simulations. Nevertheless, the simulations demonstrate that large absorption enhancement can be achieved over a broad range of wavelengths longer than the GaAs absorption edge with an appropriately designed light trapping structure, which has been confirmed through experiment.

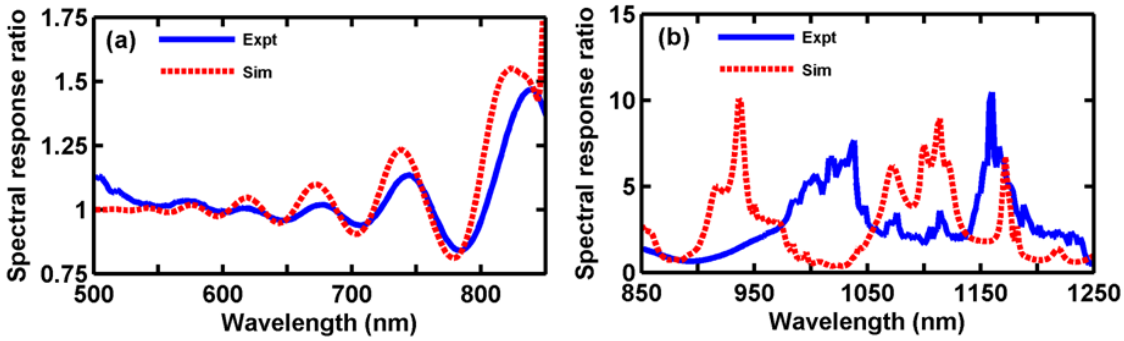

Figure 4.9: Ratios of ("Expt") the measured spectral response and ("Sim") the simulated absorption spectra of a thin film quantum dot-in-well solar cell with the optimized Pd-SiO_2 diffractive structure, seen in Fig. 4.3, relative to the same device structure with a planar Pd back reflector/contact. The ratios are shown at wavelengths (a) shorter and (b) longer than the GaAs band edge, respectively. The measured ratio is defined by "Expt" = "QD-g"/"QD-p," according to the spectra shown in Fig. 4.8.

Illuminated current density-voltage (*J-V*) measurements of thin film devices with planar metal back sides have also been performed. The results, shown in Fig. 4.10, are

based on illumination by a xenon lamp at an intensity of ~100 mW/cm^2 and without a spectral filter. As can be seen, the short-circuit current (J_{sc}) improves from 5.66 mA/cm^2 for the quantum well solar cell, to 5.83 mA/cm^2 for the quantum dot-in-well solar cell. Both improved upon a GaAs homojunction reference devices (the spectral response of which appears as "GaAs-p" in Fig. 4.8), for which J_{sc} was measured to be 5.05 mA/cm^2. As the measured devices all had planar Pd back sides, which has no light trapping benefit, the J_{sc} increases nominally result from additional photocurrent generation at wavelengths longer than the GaAs band edge in quantum wells and dots.

The reduced V_{oc} of quantum dot-in-well solar cells relative to quantum well solar cells cannot be ignored (refer to Fig. 4.10), and quantum well devices generally exhibit voltage losses relative to control devices consisting of only barrier material in the undoped region.[160] "Strain-balancing" has been demonstrated to mitigate such losses in quantum well[161] and quantum dot solar cells.[162] It has also been observed that dark current increases linearly with the number of periods of a quantum well inserted in the undoped region in similar solar cells.[163] This may be indicative of multi-quantum well effects that could increase carrier recombination. Therefore, the use of light trapping with devices containing few quantum well and/or dot layers is promising for maximizing performance.

The devices in this work are intended to illuminate key design considerations for thin film quantum well and dot solar cells incorporating light trapping, and they have not been optimized for overall performance. One of the primary reasons that the measured performance of thin film devices deviates from their simulated performance is that measured devices do not have an anti-reflection coating (ARC). The device structure of Fig. 4.3 has an approximately 100 nm thick SiO_2 ARC, which minimizes reflectivity at 580 nm, where the AM 0 spectral photon flux is greatest. Simulations indicate that

devices without an ARC have reflectivities of ~42% at 580 nm while devices with 100 nm SiO_2 ARCs exhibit reflectivities of ~14% at 580 nm. Also, as seen in Fig. 4.8, the spectral response of fabricated devices increases gradually over wavelengths 400 nm to 700 nm, which are absorbed strongly in the top 100 nm of GaAs. Simulations suggest that transport of electrons across the p^{++}-$Al_{0.85}Ga_{0.15}As$ window is poor, which may result from the large potential barrier for electrons at the GaAs/AlGaAs interface. Due to the fact that solar irradiance peaks below 700 nm, the combined effects of having no ARC and of poor carrier transport across the window significantly diminish the short-circuit currents of measured devices from their optimal values, which simulations indicate should approach 30 mA/cm^2.

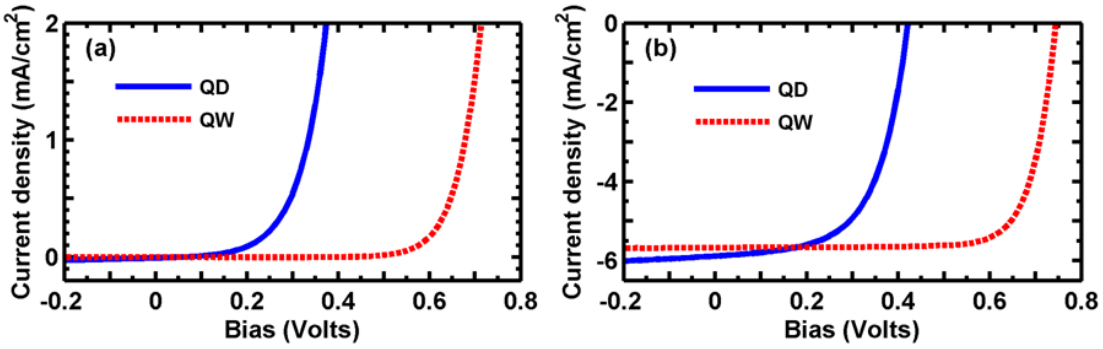

Figure 4.10: Current density-voltage measurements (a) in the dark and (b) under unfiltered illumination from a xenon lamp corresponding to an intensity of ~100 mW/cm^2. Data are shown for a thin film ("QW") quantum well solar cell and for a ("QD") quantum dot-in-well solar cell, corresponding to curves "QW-p" and "QD-p," respectively, in Fig. 4.8.

4.6. Avenues for Improving Device Performance

Numerous approaches may be taken to improving the performance of the solar cells presented in this chapter. Some of them relate to the design of devices, while others relate to improving the fabrication process. Fundamentally, more can be understood

about the electrical performance of the devices, which is relatively complicated by the multiple interfaces in quantum well and dot structures and by strain in the materials. It is important to consider the likelihood that the principles and methods discussed in the following sub-sections of 4.6 may be most usefully applied, to the extent possible, in parallel. Doing so should help to prevent one from performing an excessive amount of modeling or experiments before realizing that a fundamental problem exists in some part of the work that significantly compromises one or more other aspects.

4.6.1. Device Design Improvements

The author has no knowledge of high efficiency solar cells in which absorption of light in the quasi-neutral base and emitter regions, and collection of the resulting photogenerated carriers, is unimportant. This is because it is difficult to create wide *p*-*n* junctions in the one-sided diodes produced using typical base and emitter doping levels for GaAs-based solar cells (see Sec. 1.6.4). In such devices, the base can be around an order of magnitude thicker than the junction width, with the result that much more light is absorbed in the base than in the junction. A GaAs emitter layer also strongly absorbs light, though the emitter is typically closer in thickness to the junction than to the base, due to its relatively high doping and the correspondingly shorter minority carrier diffusion lengths. In *p*-*i*-*n* devices, the undoped region can, in principle, be grown arbitrarily thick. However, intrinsic material inevitably contains background impurities that incorporate during growth,[164,165] which could potentially diminish the built-in potential across the depletion region or increase junction recombination. Thus, there is a strong impetus to have relatively thin depletion/undoped regions in solar cells, and to choose the base and emitter doping and thickness on the basis that a large fraction of incident light will be absorbed in those layers.

PC1D is a free numerical solver created by researchers at the University of New South Wales that simulates the performance of solar cells and similar optoelectronic devices.[166] It incorporates realistic models of carrier transport and recombination to solve for the dark and illuminated current-voltage relationship of a device, its spectral response, and related quantities. The software is limited by the number of material layers that it can simulate in one device structure, however, which makes it essentially impossible to realistically simulate quantum well or dot solar cells using PC1D. However, it is useful for determining appropriate thicknesses, doping concentrations and compositions of the base, emitter, intrinsic (if included), back surface field, and window layers. Based on the junction potential necessary for carrier escape from heterostructure sub-band states and their subsequent collection, these quantities can be varied to optimize the performance of a device structure in the absence of the heterostructures, but in consideration of their requirements. If adding the heterostructure layers does not increase parasitic losses, then this approach can be useful for designing quantum well and/or dot solar cells.

Compared to the PC1D approach of the last paragraph, a superior approach could use commercial software, such as Silvaco ATLAS and ATHENA, or Synopsys TCAD. These programs include more comprehensive models of carrier transport, including quantum tunneling, and support more complicated devices, such as complete heterostructure solar cells.

On the experimental side, numerous studies have demonstrated improved V_{oc} in quantum well and quantum dot solar cells when the heterostructures are "strain-balanced," which has not been done for the devices in this work. Strain-balancing uses alternating layers of quantum well (and/or quantum dot) and of barrier material that experience compressive and tensile strain (or vice versa), respectively, due to lattice mismatch to the substrate and to each other. The thickness and composition of those

layers are selected such that the average lattice constant of the epitaxial structure equals that of the substrate. As a result, in principle, the *complete heterostructure* can be arbitrarily thick without risk of dislocations occurring. However, each quantum well/dot and barrier layer has a critical thickness based on the strain it experiences, and if dislocations occur in any one of these layers, they may extend into other layers.[167,168] The strain conditions in strain-balanced structures, therefore, should be thoroughly analyzed and characterized.

Referring to Fig. 1.15, two materials that could be used to strain-balance InGaAs quantum wells/dot structures grown on GaAs are AlGaP and GaAsP. $Ga_xAs_{1-x}P$ transitions from a direct bandgap to an indirect bandgap at $x \cong 0.5$ and $Al_xGa_{1-x}P$ has an indirect bandgap for all values of x. In *p-i-n* solar cells, the strain-balanced heterostructure, which is located in the *i*-region, comprises part of the active device. Thus, it is beneficial to select x such that all of the active layer materials have direct bandgaps, in order to maximize absorption of light. If device processing steps have the potential to damage aluminum-containing materials, such as by their use of fluorine-based compounds for etching, then it is likely to be preferable to use GaAsP for strain-balancing. As demonstrated in Sec. 4.3.3, however, chemically resistant wax, or other materials, can be used to protect device layers during processing with chemicals that are potentially harmful to them.

As demonstrated in Sec. 5.2, increasing the atomic fraction of indium in $In_xGa_{1-x}As$/GaAs quantum wells can also significantly benefit photocurrent generation in thin film GaAs solar cells. However, increasing x for a given barrier composition and thickness increases the probability of dislocations occurring. Additionally, large values of x may reduce the probability of carriers escaping from quantum well/dot sub-band states compared to lower values of x. Strain-balancing may enable $In_xGa_{1-x}As$ quantum wells

and/or quantum dots with relatively high x to be used to effectively improve photocurrent generation in a solar cell without significantly degrading V_{oc} or the fill factor.[163,169]

4.6.2. Methods for Material and Device Characterization

Unless the reader thoroughly understands how the materials, structures, and interfaces present in his or her devices affect their performance, it is advisable to characterize the materials and device performance before using a considerable amount of time to completely optimize them. This is because materials and device processing often affect device performance in unforeseen ways that cannot be entirely (and, in some cases, may not at all be) predicted by simulations. In heterostructure-based devices, strain and numerous interfaces make that especially true. Optimizing the performance of such devices requires knowledge of the quality and characteristics of the material, as well as the optoelectronic properties, of fabricated devices.

With regard to materials, a standard set of measurements should be used to evaluate wafers. These may include a subset of the following:

(1) Material morphology/structure: scanning electron microscopy (SEM), transmission electron microscopy (TEM), atomic force microscopy (AFM), and x-ray diffraction (XRD).

(2) Bulk chemical composition: energy dispersive x-ray spectroscopy (EDS/EDX/EDAX), XRD [see (1), above], Auger electron spectroscopy (AES), and secondary ion mass spectroscopy (SIMS).

(3) Surface chemical composition: x-ray photoemission spectroscopy (XPS) and glancing (or grazing) incidence x-ray diffraction (GIXRD).

(4) Optoelectronic characterization: optical absorption spectroscopy, ellipsometry, Raman scattering, photoluminescence (PL), and electroluminescence (EL).

(5) Junction analysis: current-voltage versus illumination and temperature (*J-V*, *J-V-T*), photocurrent (or spectral response, or quantum efficiency), capacitance-voltage (*C-V*), optical beam induced current (OBIC), electron beam induced current (EBIC), and cathode luminescence (also, "cathodoluminscence," or CL).

A considerable amount of additional data could be useful for more completely understanding the performance of the solar cells investigated in this dissertation. In particular, because the quantum well/dot solar cells contain numerous strained heterointerfaces, measurement of minority carrier lifetimes in bulk regions of the device, and of carrier lifetimes in quantum well/dot sub-band states, would be particularly valuable to assessing the measured quantum efficiency of devices. Time-resolved PL and temperature-dependent *I-V* measurements may be useful for determining carrier lifetimes[170,171] and for recombination characterization,[172,173] respectively.[174] Measurements of heterostructure devices can be compared to homojunction reference devices, and both should be compared to the same measurements taken from a calibrated GaAs solar cell with performance measured according to NIST-traceable standards. This will help to determine if issues are present in as-grown wafers, or if they are introduced during processing. To that end, contactless characterization techniques, which can be used both on as-grown wafers and on processed devices, are particularly useful. Ref. 175 may be a valuable resource for III-V device characterization.

4.6.3. Thin Film III-V Device Fabrication

To the author's knowledge, the process used to make the thin film GaAs solar cells discussed in this chapter has not been used before. From an economic perspective, it is preferable to use techniques that preserve the growth substrate so that it can be used for multiple growth runs.[135-138] When strained device structures (including ones that contain

quantum wells and/or dots) are used, such as those in this work, various structural or mechanical changes could occur during thin film processing. Thus, it may be useful to perform the device characterization measurements described in Sec. 4.6.2 on devices before and after substrate removal.

It appears that the thin film device fabrication process described in this chapter introduces electrically active shunts in the device wafer. Electrically conductive features have been imaged by conductive AFM, for which topographic and conduction micrographs appear in Fig. 4.11. As seen in the figure, many small features exhibiting relatively large currents, which appear as 'pinholes,' are active at near zero bias, indicating that they likely thread through the junctions of the thin film devices. This is corroborated by the fact that many thin film devices exhibit relatively linear *I-V* characteristics compared to the typical rectifying shape of good diodes. Though the origin of the current shunts has not been identified, conductive AFM scans of device wafers that have only been metal bonded to Si support pieces, without undergoing any of the subsequent thin film processing, revealed no pinhole features. Thus, it is assumed that some aspect of the subsequent thin film device processing causes the shunts to appear. Despite the shunts, mesa isolation has been used to produce high quality, small-area devices, as demonstrated by the measured *I-V* performance of thin film quantum well and dot-in-well solar cells, which is shown in Fig. 4.10. However, in its current state, the thin film fabrication technique used in this work should be considered most useful for thin film device demonstration purposes, as it is not currently useful for producing high quality devices in large quantities.

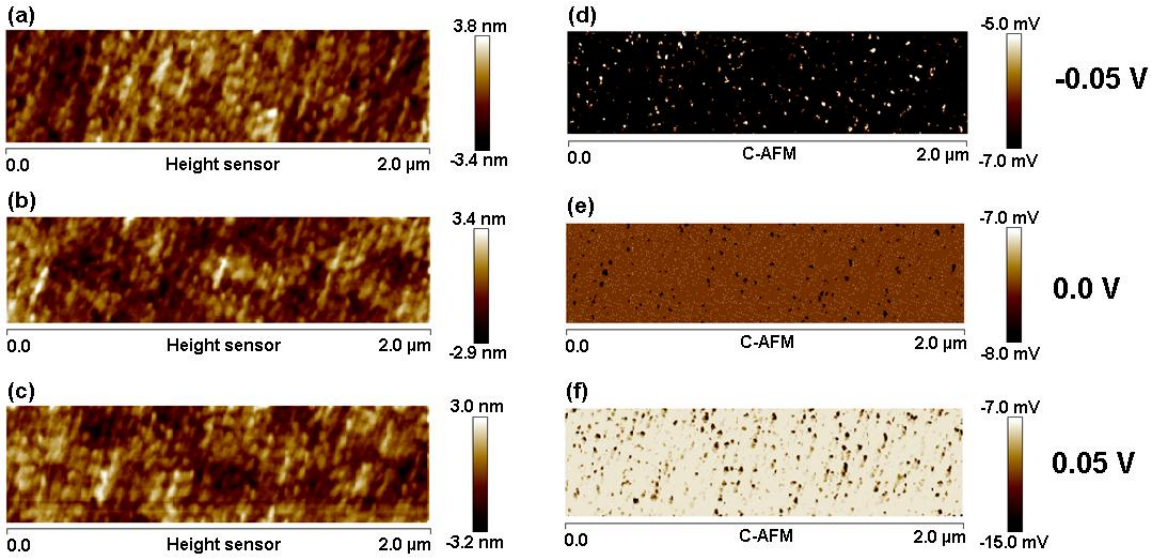

Figure 4.11: Images obtained by AFM scans of a thin film *p-i-n* GaAs homojunction device, showing (a-c) the topography and (d-f) the electrical conduction micrograph for applied biases of (d) -0.05 V, (e) 0.0 V, and (f) 0.05 V, respectively. The sensitivity of the conductive measurements equals 10^{-7} A/V. 'Pinholes' in the C-AFM images are assumed to represent shunts through the junction of the device and do not appear to have an obvious correlation with the topography of the device.

4.7. SUMMARY

In summary, spectral response measurements of thin film solar cells demonstrate that inserting six to eight periods of an {8 nm $In_{0.12}Ga_{0.88}As$/20 nm GaAs} quantum well, or of the same quantum well with embedded InAs quantum dots, in the active region of a *p-i-n* homojunction GaAs device extends its spectral response appreciable by ~50 nm and ~150 nm, respectively, with corresponding increases in the measured short-circuit current. The response of thin film quantum dot-in-well devices indicates that they produce very small, but non-zero, photocurrent at wavelengths of 1000 nm to 1250 nm. Comparisons of thin film quantum dot-in-well solar cells with optimized gratings to reference devices with planar metal reflectors/contacts demonstrate that the diffractive structure enhances the photogenerated current by up to a factor of 10 over a broad band

of wavelengths from the GaAs absorption edge (~850 nm) to that of the quantum dots (~1250 nm). If the fabricated diffractive structures have the nominal parameter values dictated by the results of their optimization, simulations indicate that the spectral absorption in quantum wells and/or dots could up to a factor of 70 greater than in devices with planar reflectors/contacts. Simulations further indicate that the thin film quantum well solar cell with an optimized back side diffractive structure exhibits a 6% increase in short-circuit current under the AM 0 spectrum relative to the same device with a planar reflector/contact. Thus, additional improvements to these devices should be achievable by realizing device structures that improve collection of carriers from quantum dots, by fabricating light trapping structures more precisely, and by further optimization of the device and light trapping structures that use realistic parameters for absorption in quantum wells and quantum dots, and for carrier collection from, and transport across, them.

This chapter has attempted to demonstrate that solar cells benefit greatly from approaches that combine efficient light absorption and charge carrier collection, which can be addressed simultaneously with thin film devices that use photonic structures for light trapping and semiconductor nanostructures to engineer the device structure for optimal absorption of light. Rigorous electromagnetic and electrical simulations that account for material properties and for the complete spectral conditions to which solar cells are exposed are required to optimize their performance over the total range of their spectral response. In this chapter, electromagnetic simulations that use a realistic model of absorption in quantum wells have been employed to demonstrate the usefulness of such an approach. Further, the experimental and simulation results strongly suggest that the use of quantum wells or quantum dots, combined with optimal light trapping schemes, is a promising route to creating efficient thin film devices.

[135] J.J. Schermer, P. Mulder, G.J. Bauhuis, M.M.A.J. Voncken, J. van Deelen, E. Haverkamp and P.K. Larsen, *Phys. Stat. Sol. (a)* **202**, 501 (2005)
[136] Y. Yazawa, K. Tamura, S. Watahiki, T. Kitatani, J. Minemura and T. Warabisako, *Solar Energy Materials and Solar Cells* **50**, 229 (1998).
[137] K. Lee, K.-T. Shiu, J.D. Zimmerman, C.K. Renshaw and S.R. Forrest, *Appl. Phys. Lett.* **97**, 101107 (2010).
[138] D. Shahrjerdi, *et al.*, *Appl. Phys. Lett.* **100**, 053901 (2012).
[139] R. Zhao, W.S. Lau, T.C. Chong and M.F. Li, *Jpn. J. Appl. Phys.* **35**, 22 (1996).
[140] K. Fobelets, R. Vounckx and G. Borgs, *J. Micromech. Microeng.* **4**, 123 (1994).
[141] J. Cheng and N.K. Dutta, eds., *Vertical-cavity Surface-emitting Lasers: Technology and Applications*, p. 302 (Overseas Publishers, 2000).
[142] I. Serdiukova, C. Monier, M.F. Viela and A. Freundlich, *Appl. Phys. Lett*. **74**, 2812 (1999).
[143] A. Alemu, J.A.H. Coaquira and A. Freundlich, *J. Appl. Phys*. **99**, 084506 (2006).
[144] P.W. Fry, J.J. Finley, L.R. Wilson, A. Lemaitre, D.J. Mowbray, M.S. Skolnick, M. Hopkinson, G. Hill and J.C. Clark, *Appl. Phys. Lett.* **77**, 4344 (2000).
[145] R. Petit, *Electromagnetic Theory of Gratings*, p. 174 (Springer-Verlag, 1989).
[146] M.G. Moharam and T.K. Gaylord, *J. Opt. Soc. Am. A*. **3**, 1780 (1986).
[147] L. Li, *J. Opt. Soc. Am. A*. **13**, 1870 (1996).
[148] L. Li, *J. Opt. Soc. Am. A*. **14**, 2758 (1997).
[149] RSoft Design Group, *DiffractMOD User Guide (v. 3.2)*, p.39 (2011).
[150] D.E. Goldberg, *Genetic Algorithms in Search, Optimization, and Machine Learning* (Addison-Wesley, 1989).
[151] W.H. Press, S.A. Teukolsky, W.T. Vetterling and B.P. Flannery, *Numerical Recipes in C*, 2 ed., Ch. 10 (Cambridge University Press, 1995).
[152] J.G. Dries, M.R. Gokhale and S.R. Forrest, *Appl. Phys. Lett.* **74**, 2581 (1999).
[153] E. Yablonovitch, *J. Opt. Soc. Am.* **72**, 899 (1982).
[154] C.C. Lee, C.Y. Wang and G. Matijasevic, *IEEE Trans. Comp., Hybrids, Manuf. Technol.* **16**, 311 (1993).
[155] T.B. Wang, Z.Z. Shen, R.Q. Ye, X.M. Xie, F. Subhan and J. Freytag, *J. Elec. Mater.* **29**, 443 (2000).
[156] H. Okamoto and T.B. Massalski, *Binary Alloy Phase Diagrams*, ed. T.B. Massalski, pp. 381-383 (ASM International, 1990).
[157] E. Yablonovitch, T. Sands, D.M. Hwang, I. Schnitzer, T.J. Gmitter, S.K. Shastry, D.S. Hill and J.C.C. Fan, *Appl. Phys. Lett.* **59**, 3159 (1991).
[158] C. Carter-Coman, R. Bicknell-Tassius, R.G. Benz, A.S. Brown and N.M. Jokerst, *J. Electrochem. Soc.* **144**, L29 (1997).
[159] G. Snider, *1D Poisson*, http://www.nd.edu/~gsnider/. Accessed 7 August 2011.
[160] K. Barnham, I. Ballard, J. Barnes, J. Connolly, P. Griffin, B. Kluftinger, J. Nelson, I. Tsui and A. Zachariou, *Appl. Surf. Sci.* **113-114**, 722 (1997).
[161] N.J. Ekins-Daukes, K.W.J. Barnham, J.P. Connolly, J.S. Roberts, J.C. Clark, G. Hill and M. Mazzer, *Appl. Phys. Lett.* **75**, 4195 (1999).
[162] C.G. Bailey, D.V. Forbes, R.P. Raffaelle and S.M. Hubbard, *Appl. Phys. Lett.* **98**, 163105 (2011).
[163] D.B. Bushnell, T.N.D. Tibbits, K.W.J. Barnham, J.P. Connolly, M. Mazzer, N.J. Ekins-Daukes, J.S. Roberts, G. Hill and R. Airey, *J. Appl. Phys.* **97**, 124908 (2005).
[164] A.Y. Polyakov, *et al.*, *J. Elec. Mater.* **30**, 147 (2001).
[165] A.J. Ptak, D.J. Friedman and S. Kurtz, *J. Vac. Sci. Tech. B* **25**, 955 (2007).
[166] "PC1D," http://www.pv.unsw.edu.au/info-about/our-school/products-services/pc1d. Accessed 5 February, 2012.
[167] K.H. Chang, P.K. Bhattacharya and R. Gibala, *J. Appl. Phys.* **66**, 2993 (1989).
[168] L. Lazzarini, L. Nasi, C.E. Norman, G. Salviati and S. Bertoni, *J. Cryst. Growth* **126**, 133 (1993).
[169] G. Wei and S.R. Forrest, *Nano Lett.* 7, 218 (2007).

[170] R.R. King, J.H. Ermer, D.E. Joslin, M. Haddad, J.W. Eldredge, N.H. Karam, B. Keyes and R.K. Ahrenkiel, *Proc. 2nd World Conf. Photovolt. Solar Ener. Conversion*, Vienna, Austria, p. 86 (1998).
[171] W.K. Metzger, D. Albin, D. Levi, P. Sheldon, X. Li, B.M. Keyes and R.K. Ahrenkiel, *J. Appl. Phys.* **94**, 3549 (2003).
[172] P. Mialhe, J.P. Charles, A. Khoury and G. Bordure, *J. Phys. D.: Appl. Phys.* **19**, 483 (1986).
[173] M.-C. Tseng, R.-H. Horng, Y.-L. Tsai, D.-S. Wuu and H.-H. Yu, *IEEE Elec. Dev. Lett.* **30**, 940 (2009).
[174] K. Emery, *Handbook of Photovoltaic Science and Engineering (2nd ed.)*, ed. A. Luque and S. Hegedus, Ch. 18 (Wiley, 2011).
[175] R.K. Ahrenkiel and M.S. Lundstrom, *Minority Carriers in III-V Semiconductors: Physics and Applications* (Academic Press, 2003).

Chapter 5: Analysis of Light Trapping for Thin Film Quantum Well and Dot Solar Cells

In this chapter, electromagnetic simulations of the thin film devices investigated in the previous chapter, and of similar device structures, are performed to understand how device and light scattering structures affect overall device performance. Fabry-Perot interference effects in thin film devices and optical absorption losses in the metal used in diffractive structures are shown to be important factors that determine the efficacy of light trapping. The results point to promising approaches to improving diffractive structures and device structures for high efficiency photovoltaics incorporating quantum wells and/or quantum dots.

5.1. The Influence of Individual Optical Phenomena on the Response of Devices with Diffractive Structures

5.1.1. Thin Film Device Thickness

The thickness of a thin film device affects its ability to absorb light, to collect carriers, and the number of waveguide modes that it supports. The design of an optimal solar cell, and particularly one with heterostructures, therefore requires careful modeling. In the case of the ~800 nm thick device structure investigated in the previous chapter, and illustrated in Fig. 5.1(a), Fabry-Perot interference influences its absorption, and, therefore, its photocurrent response, at wavelengths of 600 nm and longer, as observed by the oscillations in experimental (see Fig. 4.8) and simulated (Fig. 5.2) response spectra.

The most straightforward way to improve light absorption in a solar cell is to make it thicker. In quantum well and quantum dot solar cells, the thickness of the intrinsic region is constrained by the built-in electric field required to collect carriers from sub-band states, and, therefore, it should not be excessively thick. The base and the

emitter layers offer more flexibility, though their doping concentrations and thicknesses should be chosen to limit minority carrier recombination and free carrier absorption. The short-circuit current of devices with variable total thickness, including an invariant intrinsic region of six quantum well periods of {8 nm $In_{0.12}Ga_{0.88}As$/20 nm GaAs}, has therefore been calculated using RCWA simulations and by assuming 100% carrier collection under 1 Sun Airmass (AM) 0 illumination.

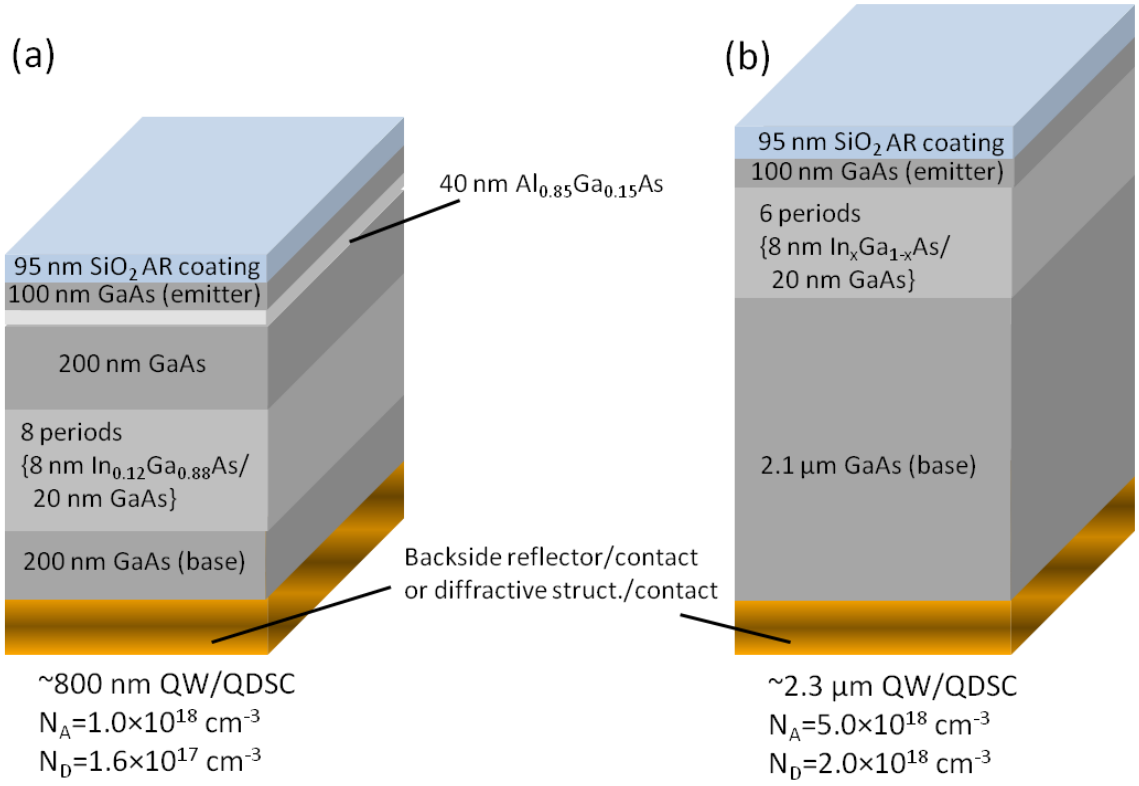

Figure 5.1: (a) The ~800 nm thick device structure of the previous chapter and (b) a ~2.3 µm thick quantum well/dot device structure. The thicker device was designed with two fewer quantum well periods, and higher base and emitter doping, to accommodate quantum wells with atomic indium fractions of up to 30% (i.e., $In_{0.3}Ga_{0.7}As$). Higher indium fractions correspond to deeper quantum wells, which are expected to require larger fields to achieve efficient carrier collection from quantum well sub-band states.

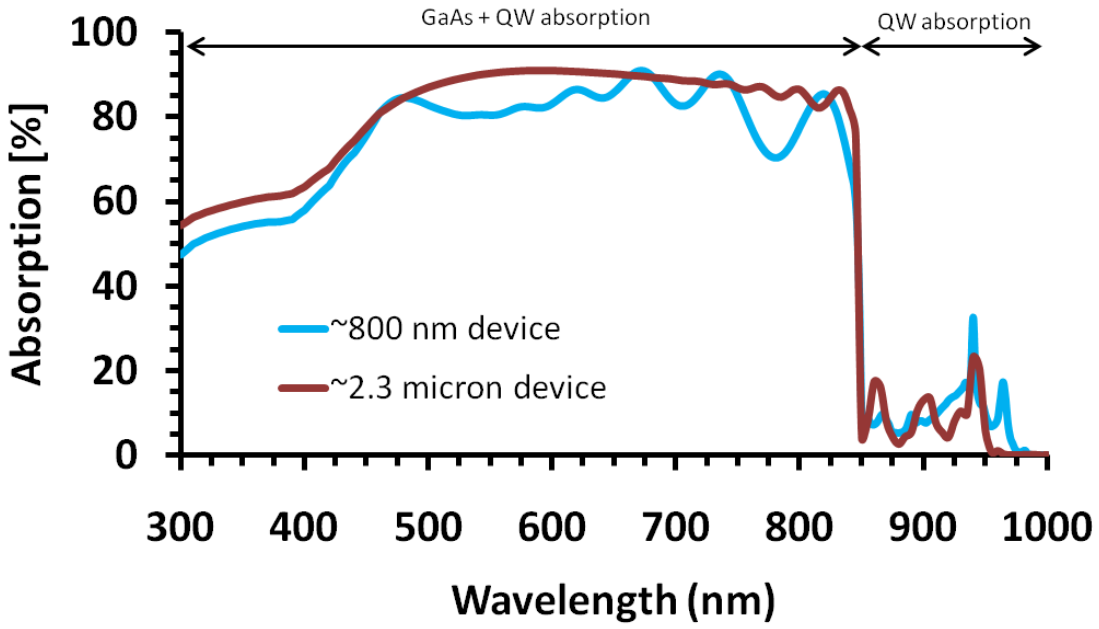

Figure 5.2: The absorption spectra of a ~800 nm thick quantum well solar cell (blue) and a ~2.3 μm thick quantum well solar cell (red). Both devices contain 8 nm $In_{0.12}Ga_{0.88}As$/20 nm GaAs quantum wells, as illustrated in Fig. 5.1. Arrows with labels mark the wavelength ranges at which both GaAs and the InGaAs quantum wells absorb light, and at which only quantum wells are absorbing.

As seen in Fig. 5.3, as the base and emitter thicknesses increase, so does the short-circuit current density (J_{sc}). In fact, J_{sc} converges rapidly to ~31.5 mA/cm^2 as the base thickness increases to 0.6 μm or larger. The changes in J_{sc} as a function of base and emitter thicknesses are asymmetric because of how they affect the position of the intrinsic region within the device structure. Ideally, the quantum wells spatially overlap with electric field maxima, producing maximum absorption. Even at wavelengths shorter than the GaAs band edge, it is desirable to have field maxima overlap the quantum wells because InGaAs has a larger absorption coefficient than GaAs. This consideration is somewhat minor, however, because $J_{sc} \approx 31.5$ mA/cm^2 as long as the base thickness is 1.0 μm or greater, as demonstrated in Fig. 5.3. For comparison, the simulation of a reference

thin film GaAs homojunction solar cell indicates that it produces J_{sc}=31.2 mA/cm^2. All of these simulations use Pd in the rear reflector/diffractive structure for consistency with previous simulations and with fabricated devices. However, Pd is sub-optimal because it strongly absorbs light, in particular at wavelengths $\lambda > 850$ nm that are absorbed exclusively in quantum wells. The benefit of using less lossy metals, such as Ag or Au, is discussed in Secs. 5.1.3 and 5.2.

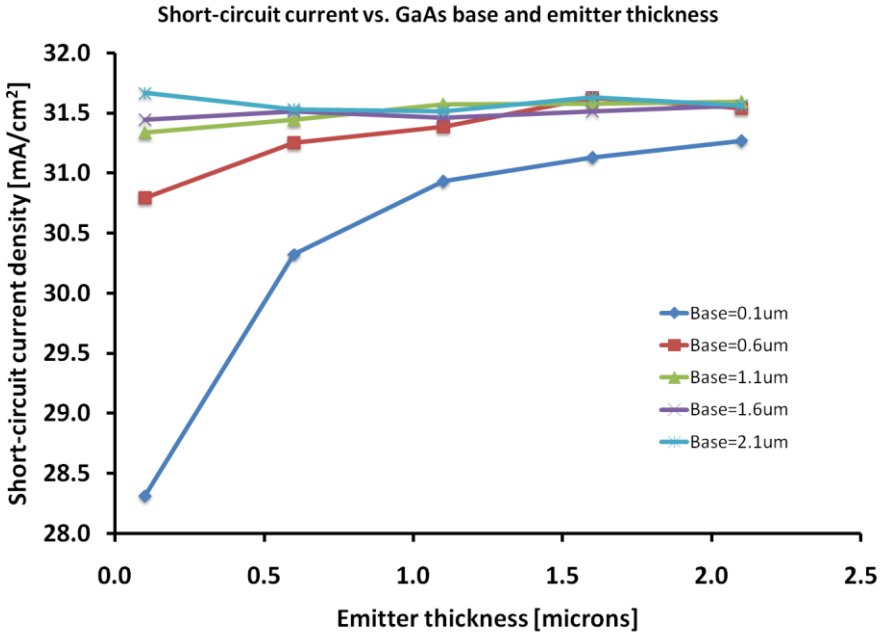

Figure 5.3: The short-circuit current density of thin film quantum well solar cells, as a function of the GaAs base and emitter thickness, based on the structure shown in Fig. 5.1(b). The calculation assumes 1 Sun AM 0 illumination and 100% carrier collection. The intrinsic region contains six periods of 8 nm $In_{0.12}Ga_{0.7}As$/20 nm GaAs quantum wells, and all simulations use the diffractive structure shown in Fig. 4.3.

As discussed in Sec. 1.6.4, base and emitter doping should be chosen to produce low contact resistivity and to minimize free carrier absorption. Typical doping levels are on the order of $N_A = 10^{17}$ cm^{-3} and $N_D = 10^{18}$ cm^{-3} in the base and emitter,

respectively.[176,177] At those doping levels, minority electron and minority hole diffusion lengths in the base and emitter are approximately 3 μm and 2 μm, respectively.[178-180] Fig. 5.3 indicates an optimal J_{sc} of 31.7 mA/cm^2, within the range of base and emitter thicknesses simulated, is achieved with a base thickness of 2.1 μm and an emitter thickness of 0.1 μm. Nominally, these thicknesses are compatible with efficient carrier collection because they are significantly less than the previously listed minority carrier diffusion lengths. *In subsequent thin film device simulations, therefore, a base thickness of 2.1 μm and an emitter thickness of 0.1 μm are used. This device geometry is referred to as the "~2.3 μm" quantum well solar cell throughout the remainder of this dissertation. Similarly, the device structure used in experiments, which was discussed in Sec. 4.1 and is illustrated in* Fig. 5.1(a)*, is referred to as the "~800 nm" device. Unless otherwise specified, the ~2.3 μm device structure consists of six periods of {8 nm $In_{0.3}Ga_{0.7}As$/20 nm GaAs} quantum wells in the intrinsic region, which is in between the base and emitter; a 95 nm SiO_2 ARC on the top surface; and the Pd-SiO_2 diffractive structure illustrated in* Fig. 5.4(d).

Fig. 5.2 compares the simulated spectral absorption of the ~2.3 μm quantum well solar cell to that of the ~800 nm device, where both devices are equipped with back side diffractive structures. It can be seen that the thicker base of the ~2.3 μm device improves its response at wavelengths shorter than the GaAs band edge by absorbing more light, which is manifest in the reduced magnitude of Fabry-Perot oscillations in its response compared to the simulated response of the ~800 nm quantum well solar cell. The net difference is $J_{sc} = 31.6$ mA/cm^2 for the ~2.3 μm device and $J_{sc} = 29.5$ mA/cm^2 for the ~800 nm device under normal incidence illumination at 1 Sun AM 0 and assuming 100% carrier collection.

It is worth noting that the improvement achieved by using the ~2.3 μm device structure is an increase in the simulated J_{sc} by ~2 mA/cm^2 compared to the ~800 nm device structure. While the improvement is non-trivial, the thinner device produces nearly 30 mA/cm^2, which is a considerable amount of photocurrent. The power, area, and cost requirements for a system utilizing this type of solar cell dictates the suitability of a device, and the ~800 nm device structure could be the more appropriate of the two in some situations.

5.1.2. Fabry-Perot Interference

It has been shown that Fabry-Perot interference can significantly influence the absorptive properties of a planar thin film solar cell with a reflective surface on its back side. Fabry-Perot interference can also significantly affect the response of a thin film solar cell in which the back side reflector is replaced by a light scattering structure. As discussed in Sec. 2.2.4, coupling of diffracted light to waveguide modes of a device structure occurs efficiently only when momenta of scattered/diffracted waves match the momentum of a guided mode, which is stated as Eq. 2.23, and which is satisfied only by one wavelength for a given incident angle and period of a diffractive structure. For the rest of this discussion, the light scattering structure is assumed to be a periodic diffractive structure with geometry similar to that shown in Fig. 5.4(d). Thus, light that is not diffracted undergoes a combination of absorption in metallic features of the structure and specular reflection (zero order diffraction). The zero order diffracted fields interfere with the incident field, producing Fabry-Perot characteristics similar to those of a structure with a standard back reflector.

Zero order diffraction is equivalent to specular reflection of a wave at the metal surface of a diffractive structure. In order to reach the metal surface, a portion of the

electromagnetic field must travel through the dielectric in between the metal portions of the diffractive structure, which has thickness equal to the height of the structure (refer to dimension H_2 in Fig. 4.3). Thus, the effective dielectric thickness of a device with a back side diffractive structure is larger than that of a device with a planar back side reflector abutting the semiconductor, by an amount that is correlated to the phase response of the diffractive structure, which is a function of its height. Therefore, the phases of Fabry-Perot reflected waves at a given wavelength are different in the diffractive structure and planar reflector geometries, and the implication of that is discussed below. Here, we simply note that the absorption spectra of both devices exhibit distinct oscillation that result from Fabry-Perot interference, as seen in Fig. 5.4.

The effect of Fabry-Perot interference on the response of thin film quantum well solar cells equipped with diffractive structures has been investigated by simulating the intermediate case of a homogeneous dielectric film of thickness equal to the height of the diffractive structure, which was inserted between the base layer of the device and the metal reflector. Fig. 5.4(a) shows the simulated absorption response of a device with a planar, semi-infinite layer of Pd immediately abutting the base of the device, which serves as a back side reflector/contact; Fig. 5.4(b) shows the response of the same device, but with 165 nm of SiO_2 between the GaAs base layer and the Pd; and Fig. 5.4(c) shows the response of the same device with an optimized diffractive structure, which has the geometry shown in Fig. 5.4(d). Overlaid with the absorption spectra is the polarization-dependent component ϵ_2 of the dielectric function of the quantum well, which has been scaled to fit the vertical axis. Peaks in the dielectric function correspond to excitonic absorption in the quantum wells, and their spectral positions can be compared to the positions of peaks in the simulated absorption spectra of the devices. Due to the relatively large strength of excitonic absorption, a light trapping structure may be particularly

beneficial if it confines photons of energy resonant with that required for photogeneration of excitons to the portion(s) of a device structure where quantum wells and/or dots are located.

Fig. 5.4(a) exhibits regular oscillations in absorptivity that are expected from Fabry-Perot interference, and a peak absorption of ~30% at $\lambda > 850$ nm. Fig. 5.4(b) also exhibits regular oscillations, though the positions of peaks and valleys in absorption are shifted in wavelength with respect to Fig. 5.4(a) because of the phase shift in Fabry-Perot reflected waves that is associated with the increased dielectric thickness from the SiO_2 layer. The peak absorption at $\lambda > 850$ nm also increases to ~45% with the inclusion of the dielectric layer, as seen in Fig. 5.4(b), because light is reflected at the GaAs-SiO_2 interface, reducing the intensity that reaches the Pd and, therefore, that can be absorbed by it.

Fig. 5.4(c) shows the absorption spectrum of the device with an optimized Pd-SiO_2 diffractive structure. Several things are notable about this spectrum at $\lambda > 850$ nm: (1) most of the peaks in absorption occur at the same wavelengths as in Fig. 5.4(b); (2) the exception to (1) is the peak at $\lambda = 1085$ nm, which coincides with the first heavy hole excitonic transition in the quantum well; (3) values of both the maxima and minima of absorption have increased in Fig. 5.4(c) compared to Fig. 5.4(b), by averages of ~5.0% and 5.5% in absolute absorptivity, respectively; (4) the widths of some of the absorption peaks have increased. The net effect is evident in the estimated short-circuit current density for 1 Sun, AM 0 illumination, assuming 100% carrier collection, which is 32.9 mA/cm^2 for the device with just a Pd back reflector/contact; 33.6 mA/cm^2 for the device with SiO_2 between the GaAs base layer and the Pd back reflector/contact; and 34.3 mA/cm^2 for the device with the optimized diffractive structure.

The simulation results indicate that J_{sc} improves by 0.7 mA/cm^2 when a planar SiO_2 layer is added, which has no light trapping benefit, but which reduces loss due to absorption by Pd when using just a Pd reflector/contact. That improvement equals half of the 1.4 mA/cm^2 increase in J_{sc} achieved by using the complete SiO_2-Pd diffractive structure, which, additionally, diffracts light into waveguide modes of the solar cell structure. Thus, the effects of absorption enhancement due to non-zero order diffraction, which can couple to waveguide modes, and of improving the response associated with zero order diffraction, equally benefit the J_{sc} of the simulated devices. The principal benefit of the former effect is increased photon path lengths, while the latter relates to reduced absorption in the metal when a diffractive structure is used compared to a planar Pd reflector/contact.

5.1.3. Metal Absorption Losses

In order to minimize optical absorption loss in materials that do not comprise the active layers of a solar cell, metals with low extinction coefficients are especially useful. Pd, which has thus far been used in experimental and simulated devices because of its utility in forming ohmic contacts to GaAs (refer to Sec. 3.2.3), is strongly absorbing in the infrared compared to some other metals that are potentially useful, such as Au and Ag. Of those two metals, Ag is the least strongly absorbing, though it is much less widely documented as a material for making ohmic contact to GaAs than Au. Thus, for minimizing metal absorption loss, Au or Au-Ge alloys, which have demonstrated low contact resistance,[181-183] may be beneficial *n*-type GaAs contacts. A thin layer of Pd, followed by Au (*p*-type GaAs), Au-Ge (*n*-type GaAs), or alloys with Ag (*n*- and *p*-type GaAs)[184] are also potentially useful for creating contacts with good electrical, physical, and optical properties, and which exhibits significantly less absorption than a bulk Pd

contact. Ti also has a relatively low extinction coefficient compared to Pd. Furthermore, it is relatively inexpensive and, in the author's experience, it adheres to GaAs better than Au.

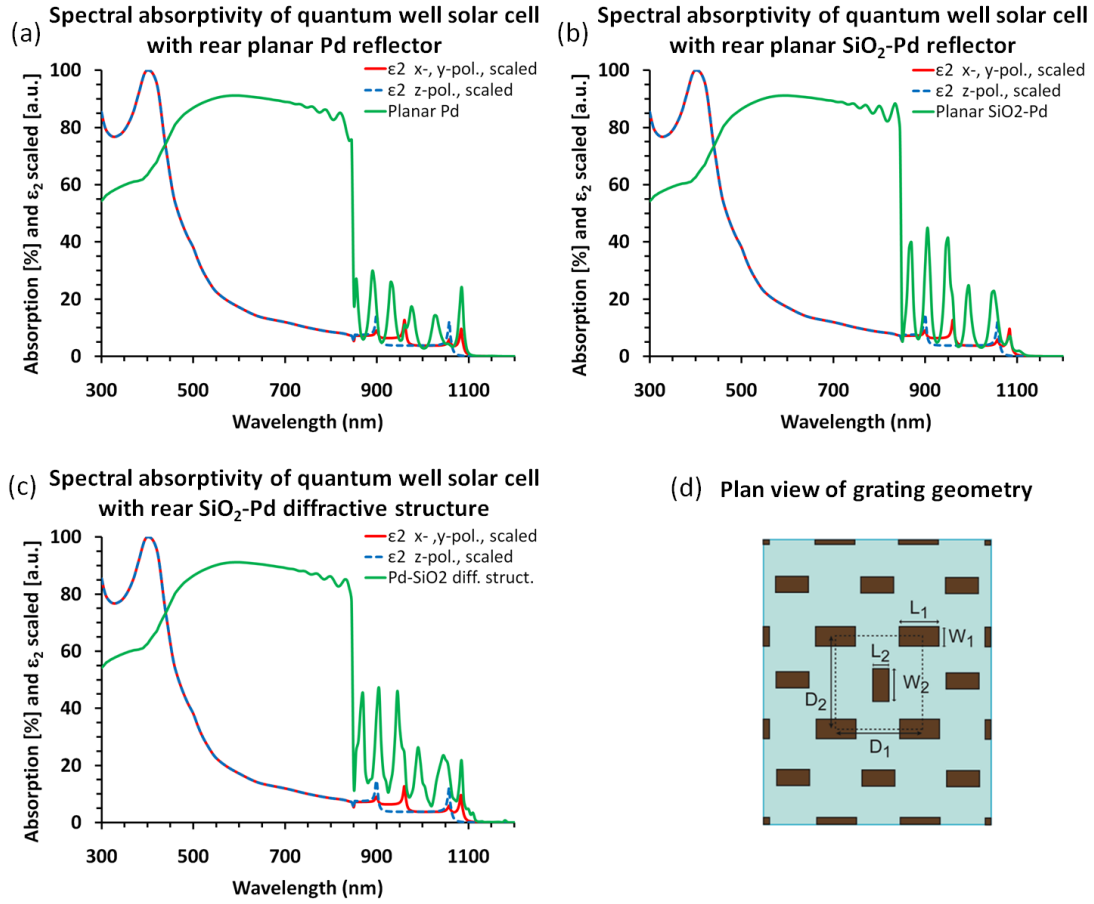

Figure 5.4: Simulated absorption spectra for a ~2.3 μm quantum well solar cell, as illustrated in Fig. 5.1, with quantum wells composed of 8 nm $In_{0.3}Ga_{0.7}As$/20 nm GaAs, where the back side geometry abutting the GaAs base layer consists of (a) semi-infinite Pd, (b) 165 nm SiO_2 followed by semi-infinite Pd; and (c) a SiO_2-Pd diffractive structure (labeled 'diff. struct.') optimized for the quantum wells of this device structure, which has the geometry shown in (d), where W_1 = 268 nm, L_1 = 800 nm, W_2 = 686 nm, L_2 = 205 nm, D_1 = 1355 nm, D_2 = 1070 nm, and H_2 = 165 nm (refer to Fig. 4.3, which indicates that H_2 is the height of the grating). The semi-empirical, anisotropic value of ϵ_2 for an 8 nm $In_{0.3}Ga_{0.7}As$/GaAs quantum well, calculated according to the method of Sec. 2.4, has been scaled and overlaid with the absorption spectra for comparison.

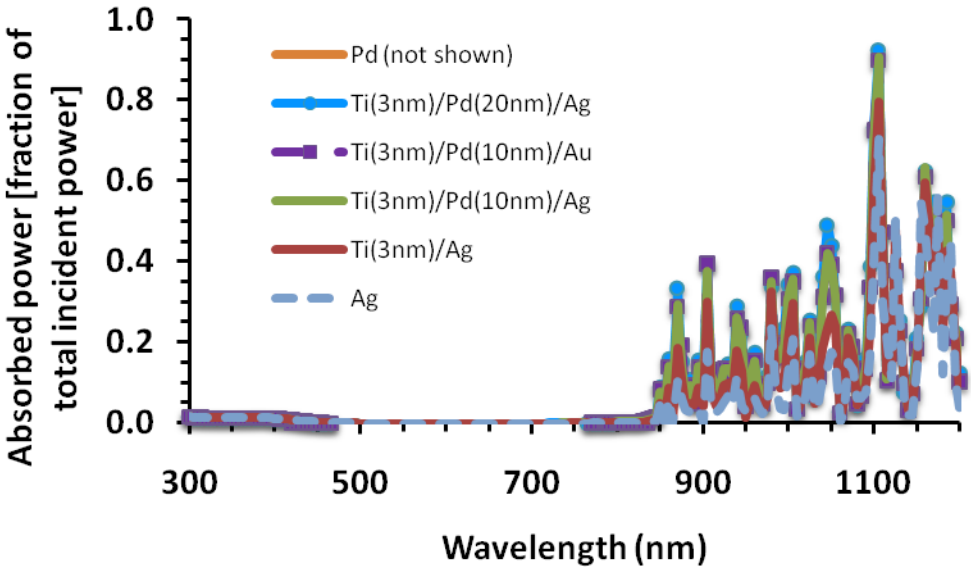

Figure 5.5: The fraction of total incident power absorbed by metal(s) in the back side diffractive structure/contact for use of the same $In_{0.3}Ga_{0.7}As$ quantum well device geometry illustrated in Fig. 5.4. The metal(s) have been selected to illustrate potentially feasible contacts, and to illustrate the relative amount of parasitic absorption by them.

Potentially useful back side reflection/light trapping/contact metallization schemes have been simulated based on the materials discussed in the previous paragraph, and the resulting absorption spectra are compared in Fig. 5.5. Reliable data for the optical properties of the metal alloys considered here could not be found, so the simulations use discrete stacks of elemental metals. In practice, however, the metal stacks may need to be alloyed to achieve adequate electrical performance. The simulation results indicate that several suggested contact schemes improve on one consisting of just Pd, based on the simulated 1 Sun AM 0 short-circuit current density, which is listed for each configuration. The results indicate that any contact that uses Pd is likely to considerably limit the J_{sc} of a thin film solar cell. Though using only Ag is unlikely to produce a true ohmic contact to *n*-type or *p*-type GaAs, due to the difference in the work function of Ag

and the Fermi energy in non-degenerately doped GaAs, the increase in J_{sc} of ~2 mA/cm^2 by switching from only Pd to only Ag indicates the significance of metal absorption in diffractive structures, and it compels the use of contacts which minimizes use of Pd or other highly dissipative metals.

5.1.4. Plasmonic Effects

Resonant excitations in metals by electromagnetic radiation, such as surface plasmon polaritons (SPPs), generally result in greater losses than off-resonance absorption, though they are also a potential source of absorption enhancement for solar cells. The electric field associated with a SPP, which is confined to the surface of a metal, decays exponentially with distance from the metal surface; however, the magnitude of the field within up to ~10 nm from the metal surface can be much larger than the peak magnitude of the electric field of the incident radiation. Therefore, strong optical absorption in the semiconductor adjacent to a metal surface where an SPP is present is possible. The following considerations are relevant when the use of plasmonic effects is attempted to enhance optical absorption in solar cells:

1. Metals are absorbing, and resonant plasma excitations coincide with increases in metal absorption. Additional losses due to metal absorption are therefore expected when resonant excitations occur, and any benefit must overcome them.

2. The magnitude of the evanescent field is largest close to the metal-semiconductor interface and it decays rapidly with distance into the semiconductor. Therefore, carriers generated by evanescent fields will be in proximity to the semiconductor surface, where recombination rates are often relatively high.

3. Minority carriers must diffuse to the junction, which, in a GaAs solar cell, may be between 100 nanometers and several microns from the metal-semiconductor

interface. Plasmonic effects are, therefore, best suited to thin devices. The thinness of such devices, however, is likely to limit their total absorption and efficiency.

For these reasons, plasmonic effects in solar cells must be evaluated thoroughly. Doing so requires rigorous calculation or simulation of absorption in the semiconductor portions (i.e., the active device layers) and in the metal portions of a device structure, which should be performed using algorithms that solve the vector forms of Maxwell's equations. Assuming that a plasmonic structure does not pin the Fermi level at a different position at the metal-semiconductor interface compared to a reference device, it may be assumed that a net increase in absorption in the semiconductor will produce an increase in photocurrent.

5.1.4. Spatial Overlap of Heterostructures and Electromagnetic Fields

As seen in Eq. 2.17, the cutoff frequency of a waveguide mode decreases as the thickness of the waveguide increases, so a thick film supports more waveguide modes than a thin film for a given band of wavelengths. It is the case for heterostructure devices that if light couples to confined modes that occupy the entire device volume, rather than just the heterostructure, then only a fraction of a waveguide mode will overlap with quantum wells/dots in the intrinsic region. That is often true of InGaAs/GaAs heterostructure devices because of the low dielectric contrast between InGaAs and GaAs. Thus, for light that consists of photons with energy less than the bandgap of GaAs, only the portions of the associated fields that overlap with the InGaAs heterostructures can be absorbed, including fields corresponding to light trapped in waveguide modes of such devices. Furthermore, scattering and diffraction of light aside, the maxima and minima in the net electric field associated with the incident and reflected waves also should overlap with quantum wells/dots in order to maximize absorption in the active device layers.

To demonstrate the effect of spatial overlap, the ~2.3 μm thick quantum well solar cell of Sec. 5.1.1 is investigated using RCWA electromagnetic simulations. As seen in Fig. 5.6(a), light at an incident wavelength of 860 nm couples to a high order waveguide mode with many nodes. Fig. 5.6(b) shows light at an incident wavelength of 1105 nm that couples to a lower order mode with fewer nodes. Ideally, a quantum well or dot layer overlaps with the maxima in field intensity between each node. However, the intrinsic region is relatively thin and, therefore, may only overlap with the field between as few as two nodes. Thus, in a practical InGaAs/GaAs quantum well/dot solar cell, where the light is confined to the entire device as opposed to the heterostructure, it may be advantageous to couple to low order waveguide modes, for which the fraction of the total energy contained between each node is larger than for high order modes. Investigating the absorption enhancement resulting from waveguiding in low and high order modes of thin film solar cells is a potential topic for further work.

A device of thickness ~2.3 μm supports more modes than a ~800 nm device. Supporting additional modes is likely to be advantageous because there are more combinations of incident angle and periods of a diffractive structure that satisfy the requirement for coupling to a given waveguide mode, as indicated by Eqn. 2.23. However, as discussed, the modes have varying spatial overlap with the intrinsic layer and the quantum wells/dots within it. The effect of that overlap is investigated in the ~2.3 μm quantum well solar cell structure by adjusting the thickness of the GaAs barriers, y, between the quantum wells while keeping the total device thickness constant. As seen in Fig. 5.7, this has the effect of shifting the position of the quantum wells in the device. The modes supported by the device are not affected in the process because the thickness and refractive index of the waveguide are essentially unchanged. Thus, coupling of light into modes of the device is essentially invariant with quantum well position.

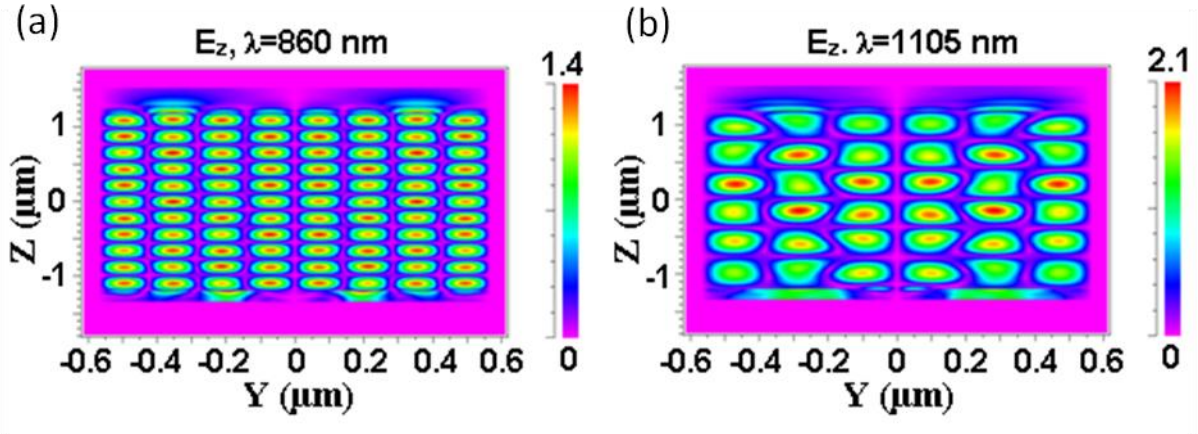

Figure 5.6: Cross-sectional plots at $x = 0$ μm [i.e., through the center of the unit cell of the diffractive structure shown in Fig. 5.4(d)] of the E_z component of the electric field in the ~2.3 μm quantum well solar cell of Sec. 5.1.1, at incident wavelengths of (a) 860 nm and (b) 1105 nm. The incident field is polarized in the *x*-*y* plane, so E_z corresponds to a component of the diffracted field, which is seen to couple to a high order waveguide mode in (a), and to a lower order mode in (b).

The simulated 1 Sun AM 0 J_{sc} of a ~2.3 μm thick InGaAs/GaAs quantum well solar cell is plotted as a function of the GaAs barrier thickness, *y*, in Fig. 5.8. $J_{sc}(y)$ varies by ~0.7 mA/cm^2, in an oscillatory manner, reflecting the movement of the quantum wells through positions of better and worse overlap with the net field in the device structure. The highest J_{sc} occurs for $y = 0$ nm, corresponding to an $In_{0.3}Ga_{0.7}As$ layer 48 nm thick. Implementing no barriers in a device is unrealistic, because doing so is likely to exceed the critical thickness for dislocations for useful atomic fractions of indium in $In_xGa_{1-x}As$ (refer to Fig. 1.15). However, relatively thick (though likely ≤20 nm) InGaAs quantum wells could be strain-balanced, using, for example, GaAsP or AlGaP barriers (refer also to Fig. 1.15, and Refs. 185-187). It would be necessary to verify that carrier escape and collection are not impeded by the larger potential barrier imposed by strain-balancing

layers, or by increased interfacial recombination. If it is not, then using thicker heterostructures could be beneficial.

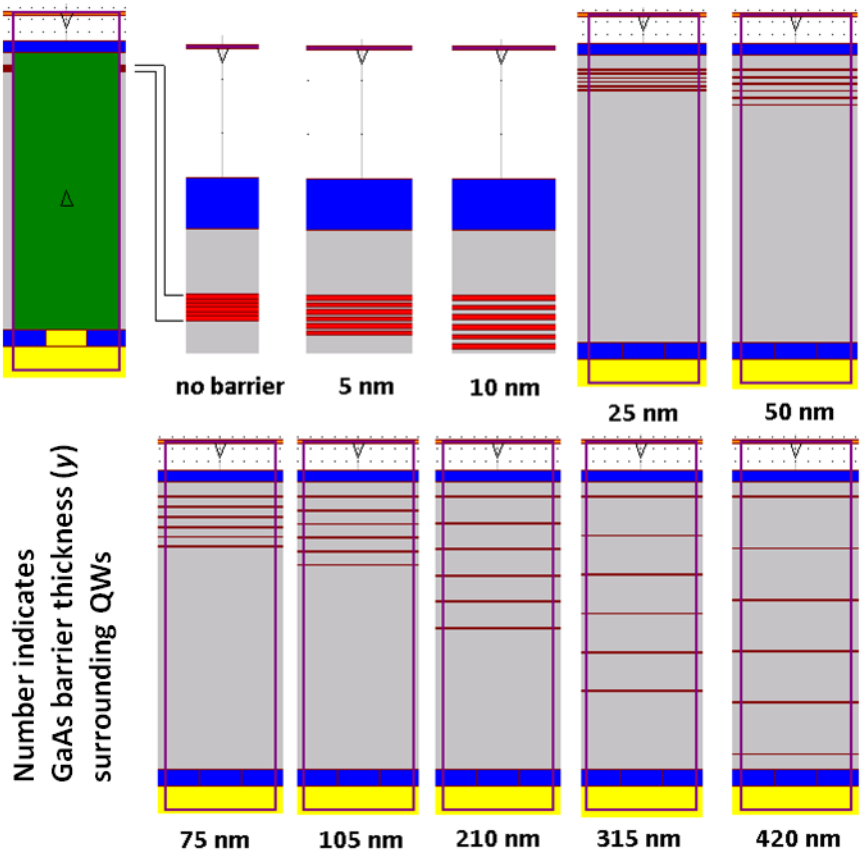

Figure 5.7: An illustration of different device structures that are used in RCWA simulations to determine how the short-circuit current of a quantum well solar cell with six periods of {8 nm $In_{0.3}Ga_{0.7}As$/*y* nm GaAs} varies according to the position of quantum wells in the device. *y* is the thickness of the quantum well barrier, and the total thickness of the device is the same in each case (~2.3 μm). The device is equipped with the optimized diffractive structure specified in Fig. 5.4(d).

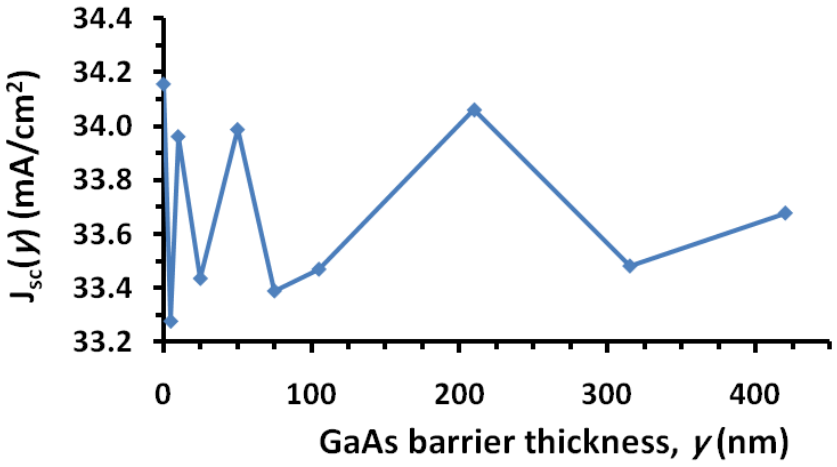

Figure 5.8: Variation of the 1 Sun AM 0 estimated short-circuit current density of devices with optimized back side diffractive structures as a function of the thickness of GaAs barriers, y, in between 8 nm $In_{0.3}Ga_{0.7}As$ quantum wells, as illustrated in Fig. 5.7. Calculations assume illumination at normal incidence and 100% collection of carriers.

5.2. Trends on Enhancement in Thin Film Quantum Well Solar Cells

Quantum wells and quantum dots can be very effective light absorbers, particularly if they consist of direct bandgap materials, such as InGaAs, which are strongly absorbing up to their band edges. Fermi's Golden Rule, given in Eq. 1.31, indicates that the radiative transition rate is directly proportional to the joint density of states in a material, $g(E)$. In quantum wells, the step-wise shape of $g(E)$ produces abrupt increases in their wavelength-dependent absorption coefficients, as seen in Fig. 5.9, which shows the calculated semi-empirical absorption coefficient for an 8 nm $In_{0.3}Ga_{0.7}As$/GaAs quantum well. The absorption coefficient shown in Fig. 5.9, which is qualitatively similar to that of a prototypical quantum well, implies that more light can be absorbed in the quantum well at $\lambda =$ 850-950 nm than at $\lambda >$ 950 nm, assuming that light trapping is not used, because the absorption coefficient is larger at the shorter

wavelengths. In fact, the same can also be true when light trapping is used; namely, that strongly absorbing materials can absorb more light that couples to waveguide modes of a device structure than weakly absorbing materials. This is why the maxima in the absorption spectrum of the ~2.3 μm solar cell with $In_{0.3}Ga_{0.7}As$ quantum wells are larger between 850 nm and 950 nm than at $\lambda > 950$ nm, as seen in Fig. 5.4(a-c): the absorption coefficient of the quantum wells is larger between 850 nm and 950 nm than at $\lambda >$ 950 nm, as seen in Fig. 5.9.

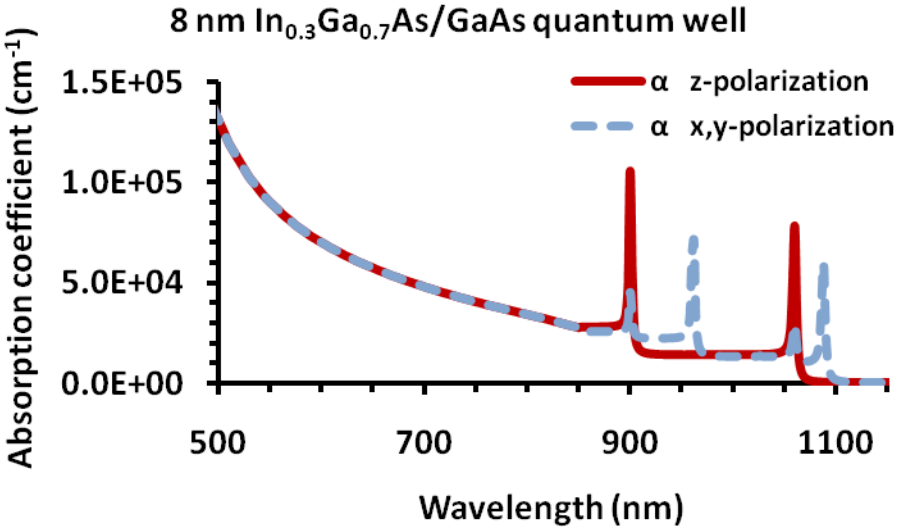

Figure 5.9: The anisotropic absorption coefficient of an 8 nm $In_{0.3}Ga_{0.7}As$/GaAs quantum well for ('α x,y-polarization') x- and y-polarized light and for ('α z-polarization') z-polarized light at wavelengths corresponding to absorption in sub-band states ($\lambda > 850$ nm) and in the continuum of states ($\lambda \leq 850$ nm). The absorption coefficient was calculated using the semi-empirical approach of Sec. 2.4.

Light trapping is particularly effective for increasing absorption in quantum well/dot layers because of their limited thickness. The 1 Sun AM 0 J_{sc} of ~2.3 μm thick quantum well solar cells with six periods of {8 nm $In_xGa_{1-x}As$/20 nm GaAs} in the intrinsic region, as illustrated in Fig. 5.1(b), equipped with optimized diffractive

structures, and the same device structures with planar metal contacts/reflectors, were simulated via RCWA. The relationship between J_{sc} and the atomic fraction of indium, x, of $In_xGa_{1-x}As$ is plotted in Fig. 5.10 for cases where either Ag or Pd are used as the planar reflector/contact or as the metal in the diffractive structure. The case of $x = 0$ corresponds to a GaAs homojunction device.

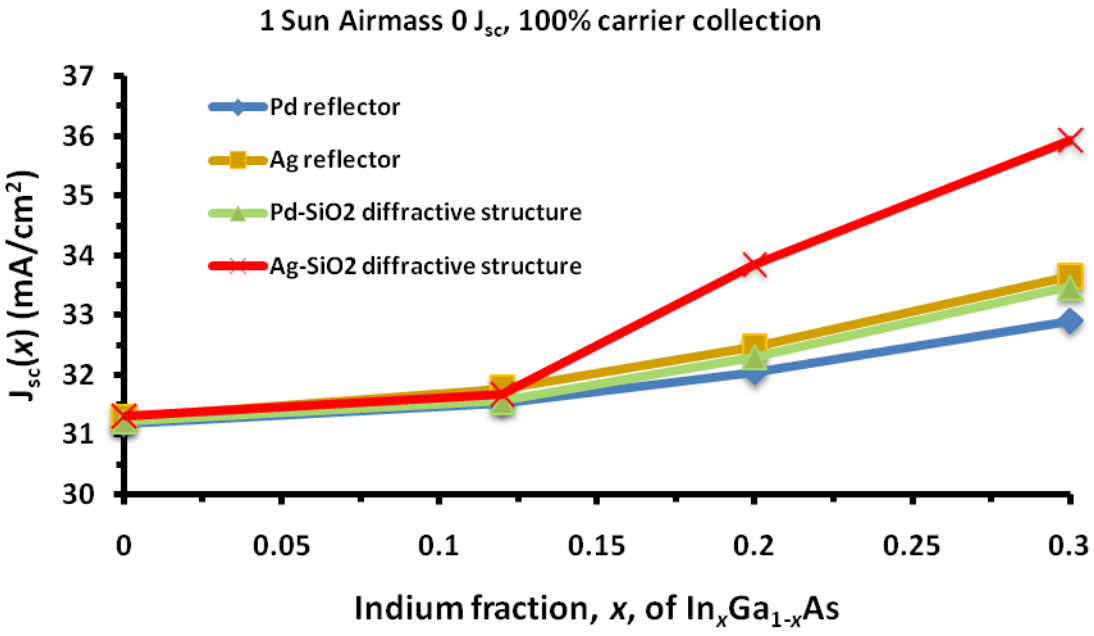

Figure 5.10: A comparison of the simulated 1 Sun AM 0 short-circuit current density, assuming normally incident light and 100% carrier collection, as a function of quantum well composition (x in $In_xGa_{1-x}As$) for ~2.3 μm thick quantum well solar cells, for x = 0.12, 0.20, and 0.30. The dielectric function of each composition of quantum well was calculated and used in the simulations to accurately model its optical properties. Devices were simulated with different back side geometries: a planar Pd reflector/contact ("Pd reflector"); a planar Ag reflector/contact ("Ag reflector"); and optimized diffractive structures that consist of Pd and SiO_2 ('Pd-SiO_2') or Ag and SiO_2 ('Ag-SiO_2').

J_{sc} (mA/cm^2)	GaAs homojunction	$In_{0.12}Ga_{0.88}As$	$In_{0.2}Ga_{0.8}As$	$In_{0.3}Ga_{0.7}As$
Pd reflector	31.2	31.5	32.0	32.9
Pd-SiO_2 diffractive structure	31.2	31.6	32.3	33.5
Ag reflector	31.3	31.8	32.5	33.7
Ag-SiO_2 diffractive structure	31.3	31.7	33.9	35.9

Table 5.1: The simulated 1 Sun AM 0 short-circuit current density, assuming normally incident illumination and 100% carrier collection, for ~2.3 μm thick quantum well solar cells with the quantum well compositions indicated by the column labels, and for a reference device with no quantum wells ('GaAs homojunction'). The table summarizes the data of Fig. 5.10 and has row labels identical to the labels in the legend of that figure, which identify the back side geometry of devices.

Four important conclusions can be drawn from Fig. 5.10, which is summarized in Table 5.1:

(1) Inserting relatively few InGaAs/GaAs quantum wells (<10 periods) into the intrinsic region of a thin film *p-i-n* GaAs homojunction device is significantly more beneficial when the diffractive structures investigated in this work are used instead of planar back side reflectors/contacts. Compared to GaAs homojunction devices, the 1 Sun AM 0 J_{sc} increases by up to 4.6 mA/cm^2 (15%) for the range of diffractive structures investigated when they are implemented with low-loss Ag and SiO_2. The greatest improvement occurs for the most strongly absorbing quantum wells that were simulated ($In_{0.3}Ga_{0.7}As$). Thus, the J_{sc} of thin film GaAs solar cells can be significantly increased by

incorporating strongly absorbing quantum wells in a *p-i-n* device and simultaneously engineering light trapping structures to minimize strain and the overall device thickness.

(2) Planar, symmetric back side diffractive structures, such as those investigated in this and the previous chapter, can substantially improve the photocurrent of thin film quantum well/dot solar cells. For the range of structures studied, they improve the simulated 1 Sun AM 0 J_{sc} of quantum well devices by up to 2.2 mA/cm^2 (7%) relative to the same quantum well device structures with planar metal reflectors. Again, the greatest improvement occurs for the most strongly absorbing quantum wells that were simulated ($In_{0.3}Ga_{0.7}As$).

(3) The metal used to implement the diffractive structures significantly influences their light trapping efficacy. If Ag is used in the diffractive structure instead of Pd, $J_{sc}(x)$ improves considerably when $x > 0.15$ due to reduced absorption in Ag compared to Pd. This enables more light to be diffracted at all orders when Ag is used, because the diffractive structure is less absorbing. The net benefit of using Ag-SiO_2 diffractive structures is an increase in the 1 Sun AM 0 J_{sc} of ~2.3 μm thick quantum well solar cells, with $In_xGa_{1-x}As$/GaAs quantum wells, by at least 1 mA/cm^2 compared to devices with Ag reflectors/contacts, when $x > 0.2$.

(4) To make explicit a point that has already been summarized: $J_{sc}(x)$ benefits most from light trapping when diffractive structures are used with $In_xGa_{1-x}As$/GaAs quantum wells that have large atomic fractions of indium, because the absorption coefficient of $In_xGa_{1-x}As$ increases, and its bandgap decreases, with x

The result that $J_{sc}(x)$ increases in proportion to the absorption coefficient of $In_xGa_{1-x}As$ suggests that significant averaging of Fabry-Perot and diffraction effects occurs over the absorption bandwidth of the quantum wells, so that, ultimately, the greatest benefit is realized when quantum wells with relatively large atomic fractions of

indium (or, potentially, quantum dots) are used. The averaging likely relates to the narrow range of wavelengths at which diffractive structures can strongly couple incident light to waveguide modes of a device structure, which is a fundamental aspect of their periodicity. Nevertheless, diffractive structures with multiple periods, such as those used here, can outperform single-period diffractive structures (i.e., linear gratings),[188] and additional optimization of their geometry, and of device structures, should yield further improvement.

5.3. Consideration of the Symmetry of Light Trapping Structures

The optical response characteristics of planar, symmetric diffractive structures, such as those explored in this and the previous chapters are potentially more likely to produce Fabry-Perot interference in devices than non-planar and/or asymmetric diffractive structures. Planar, symmetric structures diffract equal intensities of light into positive and negative orders (i.e., right- and left-moving waves). Thus, by reciprocity, waves incident normally on the diffractive structure (i.e., zero order incidence) that couple to guided modes can also couple out of those modes via the zero order if they encounter the diffractive structure subsequent to their in-coupling. This may result in stronger zero order diffraction from symmetric diffractive structures than from asymmetric diffractive structures, for which light in guided modes can only couple out via the zero order when it is incident from one direction (either right or left). By using asymmetric structures, therefore, it may be possible to couple light efficiently to waveguide modes of solar cells while limiting the probability of guided waves coupling out of waveguide modes. The potential benefits offered by optimized asymmetric light trapping structures merit further investigation of their ability to enhance solar cell performance.

5.4. SUMMARY

In summary, thin film InGaAs/GaAs quantum well solar cells benefit from the use of planar, multi-periodic back side diffractive structures, which diffract light into waveguide modes of the device structures, and which minimize loss associated with planar metal reflectors/contacts. The shape of the device response spectrum is largely determined by the Fabry-Perot characteristics of the thin device film. For the range of diffractive structures studied, they improved the simulated 1 Sun AM 0 J_{sc} of ~2.3 μm thick quantum well solar cells by up to 2.2 mA/cm^2 (7%) relative to the same devices with planar metal reflectors, and by up to 4.6 mA/cm^2 (15%) compared to ~2.3 μm thick GaAs homojunction devices. The improvements resulted equally from coupling of diffracted light into waveguide modes of the device structures and from reduced parasitic absorption in the diffractive structures than in planar metal reflectors. Additionally, irrespective of using a diffractive structure or a planar reflector, the greatest benefit for J_{sc} is realized by using $In_xGa_{1-x}As$/GaAs quantum wells with relatively large atomic fractions of indium (x), assuming that photogenerated carriers are collected from the quantum wells, due to the fact that the quantum well absorption coefficient increases, and its absorption edge increases to longer wavelengths, with x.

These results indicate that the benefits of light trapping can potentially be as sensitive to the absorptive properties of a scattering/diffractive structure as they are to the efficiency with which scattered/diffracted light couples to waveguide modes of a solar cell. If light trapping structures affect the electrical performance of a solar cell, then selection of appropriate materials and processing techniques are essential to achieving low electrical resistance and minimizing optical losses while realizing a physically robust device. Planar, symmetric, periodic structures, such as the diffractive structures investigated in this work, are potentially susceptible to light coupling out of waveguide

modes via the inverse process by which they couple into those modes, as dictated by reciprocity. However, as demonstrated in this work, such structures are attractive because they can be fabricated using standard techniques for film deposition, lithography, and etching, without damaging the semiconductor, enabling substantial improvement of the spectral response of thin film quantum well and/or quantum dot solar cells, and correspondingly large increases in their short-circuit current density.

---

[176] G.J. Bauhuis, P. Mulder, J.J. Schermer, E.J. Haverkamp, J. van Deelen and P.K. Larsen, *Proc. 20th European Photovolt. Solar Energy Conf.*, p.468 (2005).
[177] G.J. Bauhuis, P. Mulder, E.J. Haverkamp, J.C.C.M. Huijben and J.J. Schermer, *Solar Energy Mater. Solar Cells* **93**, 1488 (2009).
[178] C.J. Hwang, *J. Appl. Phys.* **40**, 3731 (1969).
[179] E. Vigil and P. Diaz, *Crystal Res. and Tech.* **19**, 285 (1984).
[180] H.C. Casey Jr., B.I. Miller and E. Pinkas, *J. Appl. Phys.* **44**, 3 (1973).
[181] N. Braslau, J.B. Gunn and J.L. Staples, *Solid State Electron.* **10**, 381 (1967).
[182] S.P. Morgan and D.V. Morgan, *Semicond. Sci. Technol.* **9**, 2278 (1994).
[183] H.-C. Lin, S. Senanayake, K.-Y. Cheng, M. Hong, J.R. Kwo, B. Yang and J.P. Mannaerts, *IEEE Trans. Elec. Dev.* **50**, 880 (2003).
[184] R.H. Cox and H. Strack, *Solid State Electron.* **10**, 1213 (1967).
[185] D.C. Houghton, *J. Appl. Phys.* **70**, 2136 (1991).
[186] J.W. Matthews and A.E. Blakeslee, *J. Cryst. Growth* **27**, 118 (1974).
[187] N.J. Ekins-Daukes, K.W.J. Barnham, J.P. Connolly, J.S. Roberts, J.C. Clark, G. Hill and M. Mazzer, *Appl. Phys. Lett.* **75**, 4195 (1999).
[188] Z. Yu, A. Raman and S. Fan, *Opt. Express* **18**, A366 (2010).

Chapter 6: Conclusion

6.1. SUMMARY

This dissertation has shown that the simultaneous use of sub-bandgap light absorbing structures, and, more specifically, InGaAs/GaAs quantum wells and quantum dots, and of light trapping structures, can improve the bandwidth of the spectral response and the spectral absorptivity of GaAs *p-i-n* homojunction solar cells, substantially increasing their short-circuit current density. Light trapping by scattering of light by sub-wavelength metal and dielectric nanoparticles, and by diffraction of light by multi-periodic structures, occurs principally by coupling of the scattered/diffracted light to optical modes of bulk and thin film InGaAs/GaAs quantum dot-in-well solar cells, including waveguide modes of the device structures. The simple, benign deposition of sub-wavelength dielectric particles on top of optically thick quantum dot-in-well solar cells improved their measured J_{sc} by up to 16% compared to the same devices without nanoparticles. Nanoparticle deposition did not affect the fill factor or open-circuit voltage of devices, with the result that the increase in J_{sc} translates directly to improved efficiency. Incorporating optimized multi-period back side diffraction structures on ~800 nm thick InGaAs/GaAs quantum dot-in-well solar cells, which diffract light into waveguide modes of the thin device structure, improved their measured spectral response by up to a factor of 10, and by an average factor of 3, over the bandwidth $\lambda = 850$ nm to 1250 nm.

Electromagnetic simulations of the device structures confirm that the measured improvements in performance result from increased absorption in the device structures when the light trapping schemes are utilized. In particular, they confirm that both the nanoparticles and the optimized diffractive structures achieve absorption enhancement

over a broad band of wavelengths, including wavelengths at energies below the GaAs bandgap, where only the quantum wells or quantum dots are absorbing, relative to structures that omit them. Finite element simulations of optically thick device structures with a monolayer of dense nanoparticles on their top surfaces demonstrate absorption enhancement due to coupling of scattered light to waveguide modes of the device structure and to increased transmission of the incident field into the device structure, which resembles the anti-reflection effect of a textured dielectric layer. Simulations of thin film InGaAs/GaAs quantum well solar cell structures with optimized diffractive structures and a single-layer anti-reflection coating, and of similar thin film device structures with planar metal back reflectors, have been performed using rigorous coupled-wave analysis (RCWA). The simulation results confirm that absorption increases at wavelengths of 850 nm to >1200 nm in quantum-dot-in-well devices when the diffractive structures replace a back side reflector, which is responsible for the measured improvement of the spectral response of such devices when the optimized diffractive structure was fabricated on them instead of a back side reflector.

Simulations of additionally optimized InGaAs/GaAs quantum well solar cell structures with multi-periodic diffractive structures indicate that 1 Sun Airmass 0 current densities >35 mA/cm^2 are achievable in ~2.3 μm thick devices with six periods of 8 nm $In_{0.3}Ga_{0.8}As$/20 nm GaAs quantum wells, assuming 100% of carriers are collected. That represents an increase in J_{sc} of 15% compared to a GaAs homojunction device having the same thickness, and of 7% compared to the same quantum well device with a planar back side reflector. Optimization of the diffractive structures produced geometries that are essentially transparent at wavelengths shorter than the GaAs absorption edge at 850 nm. Thus, only quantum well and/or quantum dot device structures benefit from the

diffractive structure, which diffracts light into waveguide modes of the device structures at wavelengths >850 nm, increasing absorption in the quantum wells and/or dots.

Additionally, devices with optimized diffractive structures benefit both from coupling of diffracted waves into waveguide modes of the thin device structures and from reduction of the net power absorbed in the back side metal compared to devices with planar reflective back contacts. The diffractive structures were optimized using software algorithms that maximize the simulated J_{sc} of solar cells under arbitrary spectral conditions based on RCWA calculations of spectral absorption in the active device structures. The optimization consisted of a genetic search that spanned a broad range of geometries for the diffractive structure, and was followed by a Simplex algorithm that refined its parameters. The optimization incorporated quantum well optical data that were calculated using a quantum mechanical model for the absorption coefficient of an arbitrary quantum well. The model uses the envelope function approximation and a four band Kane model, which includes strain effects, to calculate the bound quantum well states and the associated wavefunctions, which are used in a realistic calculation of the absorption coefficient of a quantum well.

6.2. Outlook for the Application of Quantum Wells and Quantum Dots for Solar Cells

This dissertation has attempted to convey the idea that semiconductor heterostructures, including quantum wells and quantum dots, can be used to engineer consider improvement of the efficiency of homojunction solar cells, but that doing so is non-trivial. Each heterointerface potentially increases recombination, reduces carrier drift and/or diffusion mobility, and, in general, can have a significant effect on carrier dynamics and transport. Therefore, the use of light trapping techniques is promising for maximizing absorption in limited volumes of quantum well and/or dot materials while

minimizing the amount of strain and number of interfaces in devices. Furthermore, maintaining a thin intrinsic region, where the quantum wells and/or dots are located, generally increases the electrostatic potential across the junction of a *p-(i)-n* diode solar cell, which should improve carrier escape and collection from quantum confined sub-band states. Thus, incorporating quantum wells and/or dots in thin film devices is promising for optimizing overall device performance, and may enable the creation of flexible, low weight solar cells, which could find applications in the space photovoltaics market and in terrestrial markets, including transportation, defense, and for consumers.

Quantum wells and dots are also being investigated for the purpose of reducing the mismatch in photocurrent produced by different sub-cells of tandem multi-junction (MJ) devices. By varying the composition and/or the thickness of quantum wells, their absorptive properties can be engineered to optimize the photocurrent and thickness of, for example, an InGaAs sub-cell, which can additionally benefit from strong excitonic absorption in quantum confined semiconductors. If quantum dots are used, the ability to control their size via epitaxial growth offers an additional parameter for absorption optimization. Nominally, such structures would be grown coherently strained, or potentially lattice-matched,[189] to the substrate, offering an appealing alternative to metamorphic layers.[**] Commercial entities are demonstrating interest in quantum wells[190] and quantum dots,[191] indicating that the technologies have matured considerably in the past decade.

[**] 'Metamorphic' material consists of epitaxially grown layers with graded lattice constants, achieved by gradually varying the material composition, which connect two nominally adjacent sub-cells in a MJ solar cell. The metamorphic material is dislocated, but its graded lattice constant protects the sub-cells that it connects from dislocations by minimizing strain in the sub-cell materials. However, the dislocations in the metamorphic material, which is electrically and optically active, are deleterious to device performance.

6.3. PROMISING AREAS FOR RELATED WORK

Light trapping has become a very active topic in solar cell research and development. This dissertation has investigated the use of nanoparticles and planar, symmetric diffractive structures for coupling of light to waveguide modes of InGaAs/GaAs quantum dot-in-well solar cells and demonstrated considerable broadband photocurrent improvement with both. More complicated structures are likely to improve the angular and polarization response of light trapping,[192] and may further improve coupling of light to waveguide modes of devices. Using, for example, asymmetric diffractive structures, such as a blazed ('sawtooth') profile, could reduce zero order diffraction and improve coupling to guided modes via the ± 1 or higher orders. Randomly structured light scatterers are also promising for broadband coupling of light. As periodic structures become increasingly complex with the goal of efficient coupling to modes at multiple wavelengths and for unpolarized sunlight, they may converge at performance resembling that of random structures. However, until more options are established for creating random geometries that contain many sub-wavelength features over a large area, periodic structures are likely to receive considerable attention.

The spatial overlap of quantum confined absorbing materials and the electromagnetic field inside a device is a topic that has received little focus to the author's knowledge. The overlap is essentially a function of the spectral bandwidth of illumination and the optical properties of a solar cell structure. If light trapping is utilized, this increases the number of parameters that affect the overlap, and it may affect the relative significance of parameters: if light couples weakly to waveguide modes of a device structure, then optimizing its thickness and, if they are used, the position within it of quantum wells and/or dots with respect to Fabry-Perot effects is reasonable. If light couples strongly to waveguide modes of a device structure, especially over a broad

spectral band, then the overlap of quantum wells and/or dots with the guided mode fields may be very important for maximizing their absorption of light. Understanding the tradeoffs involved in such optimization may be important for quantifying the benefits of different schemes for light trapping in thin film solar cells.

Strain-balancing, which has been used to produce quantum well[193] and quantum dot solar cells[194] with substantially higher open-circuit voltages than not-strain-balanced devices, has not been investigated in this work. Investigating strain-balancing in thin film devices similar to those of this work could proceed in three parts: (1) optical simulations of device structures; (2) electrical simulations of devices; and (3) experimental investigation of device structures and devices. Indeed, though every device structure investigated in this work has been designed not to exceed the critical thickness for dislocations, all quantum well and dot-in-well devices exhibit decreases in open-circuit voltage of magnitudes that are likely to prevent efficiency improvements relative to homojunction devices if they are not mitigated. This may reflect the presence of more subtle or complex effects than those directly related to strain. Our work with thin AlAs capping layers grown on InAs quantum dots in In(Ga)As quantum-dot-in-well solar cells demonstrates that V_{oc} improves compared to devices without capping layers.[195] That work supports the claim that AlAs capping layers improved the ordering of In-containing materials, which improved the overall material quality and, as a result, the electrical performance of devices. A complementary argument for the improved V_{oc} is that the wide bandgap AlAs capping layers increase the confinement energy of carriers in the quantum dots, potentially reducing the number of confined states through which carriers can recombine and, therefore, improving V_{oc}.[196] It is plausible that such an effect is at least partially responsible for improvements in many strain-balanced devices, because the strain compensating barriers typically consist of wide bandgap materials.

Finally, but of great importance, much insight into both bulk and thin film heterostructure solar cells, and device structures with light trapping, can be gained by thorough characterization. With regard to the thin film devices of this work, for example, the effects of various processing steps (such as wafer bonding and substrate removal) on material quality and the optoelectronic properties of devices could be investigated, which may identify avenues for improvement. As discussed in Sec. 4.6.2, many techniques are available for characterizing devices and device structures. In general, it is beneficial to characterize, at a minimum, as-grown device structures and end-of-process devices. Experimental samples should be compared to one or more standard reference devices. This is a reasonable approach to understanding the performance of complicated devices, such as quantum well and quantum dot solar cells. It also offers a methodical approach to improving their performance.

---

[189] R.J. Walters, *et al.*, *Proc. 37th IEEE Photovolt. Spec. Conf.* **3**, 150 (2011).
[190] R.E. Welser, *et al.*, *Proc. SPIE* **8111**, 8111-01 (2011).
[191] C.E. Valdivia, *et al.*, *Proc. 35th IEEE Photovolt. Spec. Conf.* p. 001253 (2010).
[192] Z. Yu, A. Raman and S. Fan, arXiv:1004.2902v2 [physics.optics] (2010). http://arxiv.org/abs/1004.2902v2
[193] N.J. Ekins-Daukes, D.B. Bushnell, J.P. Connolly, K.W.J. Barnham, M. Mazzer, J.S. Roberts, G. Hill and R. Airey, *Physica E* **14**, 132 (2002).
[194] S.M. Hubbard, C.D. Cress, C.G. Bailey, R.P. Raffaelle, S.G. Bailey and D.M. Wilt, *Appl. Phys. Lett.* **92**, 123512 (2008).
[195] D. Hu, C.O. McPheeters, E.T. Yu and D.M. Schaadt, *Nanoscale. Res. Lett.* **6**, 83 (2011).
[196] G. Wei and S.R. Forrest, *Nano Lett.* **7**, 218 (2007).

Appendix 1: A Brief Overview of Relevant Quantum Mechanics

A.1.1. The Matrix Formalism of Quantum Mechanics

The matrix formalism of quantum mechanics is important due to the vectorial nature of many physical properties. Thus, evaluating quantum mechanical expressions involving such properties is most readily performed using linear algebra. In quantum mechanics, the physical properties of a particle, such as its position, momentum, or energy, are "observed" by using "operators," which act upon the particle, producing an eigenvalue that contains the quantity of interest and a corresponding eigenstate, which, in general, is not the same state that the particle was in prior to observation. The wavefunction of a particle [$\psi(\mathbf{k}, \mathbf{r})$, sometimes abbreviated to simply ψ] contains all of the information about the particle, and it is itself a probability function that embodies the statistical nature of particles in quantum mechanics. While a particle's properties can vary in time, for simplicity, time-independent formulae are used here, which are suitable for demonstrative and many analytical purposes.

"Bra-ket" notation is used to simplify the algebra of matrix quantum mechanics. A particle in a quantum state with associated wavefunction ψ is denoted by a "bra" element, $|\psi\rangle$, which is defined as:

$$|\psi\rangle \equiv \psi(\mathbf{k}, \mathbf{r}). \tag{A1.1}$$

The complex conjugate of the wavefunction, ψ^*, is denoted by a "ket" element, $\langle\psi|$. A fundamental property of the wavefunction is that it is normalized over all space, which means that the probability of finding a particle somewhere in space is equal to unity. If the total volume of space is denoted V, then the normalization property can be expressed as follows:

$$\int_V \psi^* \psi \, d\mathbf{r} \equiv \langle\psi|\psi\rangle = 1. \tag{A1.2}$$

An important and frequently applied operator is the energy operator, which is known as the Hamiltonian, $\hat{H}$, and which appears in Schrödinger's equation:

$$\hat{H}|\psi\rangle = E|\psi\rangle, \tag{A1.3}$$

where E is the energy eigenvalue that corresponds to the energy of the particle. A comprehensive Hamiltonian must account for both kinetic and potential energy. Therefore, the Hamiltonian may be taken to be of the form

$$\hat{H} = \hat{T} + \hat{V}, \tag{A1.4}$$

where the potential energy operator has the form

$$\hat{V} = V(\mathbf{r}), \tag{A1.5}$$

and the kinetic energy operator has the form

$$\hat{T} = -\frac{\hat{\mathbf{p}} \cdot \hat{\mathbf{p}}}{2m} = -\frac{\hbar^2}{2m}\boldsymbol{\nabla}^2, \tag{A1.6}$$

where $\hat{\mathbf{p}} = -i\hbar\boldsymbol{\nabla}$ is the momentum operator, $\boldsymbol{\nabla}$ is the Laplacian operator, and

$$\boldsymbol{\nabla}^2 = \frac{\partial^2}{\partial x^2} + \frac{\partial^2}{\partial y^2} + \frac{\partial^2}{\partial z^2}. \tag{A1.7}$$

Thus, if we consider the Schrödinger equation in the x direction, it has the explicit form, based on Eq. A1.3, of

$$\left[-\frac{\hbar^2}{2m}\boldsymbol{\nabla}^{\mathbf{2}} + V(\mathbf{r})\right]\psi(\mathbf{k},\mathbf{r}) = E\,\psi(\mathbf{k},\mathbf{r}). \tag{A1.8}$$

If $V(\mathbf{r}) = 0$, corresponding to an unbound particle, the solution to Eq. A1.8 takes on the familiar form of a plane wave:

$$\psi(\mathbf{k},\mathbf{r}) = A\exp(i\mathbf{k}\cdot\mathbf{r}) + B\exp(-i\mathbf{k}\cdot\mathbf{r}), \tag{A1.9}$$

where the coefficients, A and B, are used to normalize the wavefunction, such that Eq. A1.2 is satisfied. If a particle is acted upon by a non-zero potential, or if additional effects, such as electrostatic screening by neighboring particles, are incorporated into the Hamiltonian operator, the form of the wavefunction changes. However, the plane wave form of Eq. A1.9 can often be modified to yield appropriate solutions in such cases.

A1.2. $\mathbf{k} \cdot \mathbf{p}$ THEORY

$\mathbf{k} \cdot \mathbf{p}$ theory is an approach to solving Schrodinger's equation by calculating the wavefunctions and energy eigenvalues of states near the edge of semiconductor electronic bands via slight perturbations to a set of known states at the band edge (i.e., at $\mathbf{k} = 0$). As many transitions between electronic bands occur near their edges (i.e., near $\mathbf{k} = 0$ in GaAs and other direct bandgap materials), it is important to accurately model these states. For modeling states at $\mathbf{k} = 0$, it is convenient to use Bloch waves, $u(\mathbf{k}, \mathbf{r})$, which are assumed to be approximately constant over a small region of k-space, where the band structure is to be calculated. $\mathbf{k} \cdot \mathbf{p}$ theory uses the Bloch states as a basis for energy band calculations at $\mathbf{k} \neq 0$ by modifying the standard Hamiltonian to explicitly include the wavevector. This is referred to as a 'perturbation' to the basis states, and it appears in Schrödinger's equation as:

$$\widehat{H}_{\mathbf{k}\cdot\mathbf{p}}(\mathbf{k}) = \left\{\left[\frac{\widehat{\mathbf{p}}^2}{2m_0} + V(\mathbf{r})\right] + \left[\frac{\hbar}{m_0}\mathbf{k}\cdot\widehat{\mathbf{p}} + \frac{\hbar^2 k^2}{2m_0}\right]\right\} u_n(\mathbf{k}, \mathbf{r}) = E_n(\mathbf{k}) u_n(\mathbf{k}, \mathbf{r}), \quad \text{(A1.10)}$$

where $\widehat{\mathbf{p}} = -i\hbar\boldsymbol{\nabla}$, V(r) is the periodic potential energy function of the crystal lattice, and *n* denotes the band index.

Perturbation theory mixes the states at $\mathbf{k} = 0$ in non-degenerate bands to produce the perturbed state. Perturbation theory assumes that an exact solution exists to the expression

$$\widehat{H}^0 \phi_n^0 = E_n^0 \phi_n^0, \quad \text{(A1.11)}$$

where $\widehat{H}^0$ is the unperturbed Hamiltonian, $\{\phi_n^0\}$ are a complete basis of orthonormal states (e.g., the Bloch waves in $\mathbf{k} \cdot \mathbf{p}$ theory), and E_n^0 are the energies of the basis states. The complete Hamiltonian has the form $\widehat{H} = \widehat{H}^0 + \alpha\widehat{H}^1$, with corresponding wavefunctions $\phi = \phi_n^0 + \alpha\phi_n^1 + \alpha^2\phi_n^2 + \cdots$ and energies $E_n = E_n^0 + \alpha E_n^0 + \alpha^2\phi_n^2 + \cdots$, where the superscript numeral denotes the order of the perturbation. In $\mathbf{k} \cdot \mathbf{p}$ theory, $\widehat{H}^0 = \frac{\hbar^2 k^2}{2m_0}$ and $\widehat{H}^1 = \mathbf{k} \cdot \mathbf{p}$. Thus, the first order perturbation is given by:

$$\widehat{H}^0 \sum_{n\prime \neq n} a_{n\prime} |\phi^0_{n\prime}\rangle + \widehat{H}^1 |\phi^0_{n'}\rangle = E^0_n \sum_{n' \neq n} a_{n'} |\phi^0_{n'}\rangle + E^1_n |\phi^0_{n'}\rangle, \tag{A1.12}$$

where $a_{n\prime}$ are coefficients for the linear combination of basis sets that yield the perturbed wavefunction: $\phi^1_n = \sum_{n' \neq n} a_{n'} |\phi^0_{n'}\rangle$. Solving Eq. A1.12 for E^1_n yields

$$E^1_n = \langle \phi^0_n | \widehat{H}^1 | \phi^0_n \rangle. \tag{A1.13}$$

However, as Eq. A1.13 shows, the first order perturbation in energy doesn't mix any of the states in other bands, and it is generally insufficient for calculations of states at $\mathbf{k} \neq 0$. Thus, a second order perturbation is required. After assembling the first and second order perturbation results, the energy of a state k near the edge of a band is given by:

$$E_n(\mathbf{k}) \approx E_n(0) + \frac{\hbar^2 k^2}{2m_0} + \frac{\hbar^2}{m_0^2} \sum_{m,m \neq n} \frac{\langle \phi^0_m | \mathbf{k} \cdot \mathbf{p} | \phi^0_n \rangle}{E^0_n - E^0_m}. \tag{A1.14}$$

If bands *m* and *n* are degenerate, then it can be seen that the denominator in the last term of Eq. A1.14 will cause the expression to be meaningless. Non-degenerate perturbation theory is needed in such a situation, which is commonly encountered in calculations of the valence band structure. While this appendix does not cover non-degenerate perturbation theory, the approach is very similar to that demonstrated here. The reader who desires additional information may refer to numerous quantum mechanics texts, including Ref. 197.

[197] E. Merzbacher, *Quantum Mechanics (3 ed.)* (Wiley, 1997).

Appendix 2: Matlab Scripts

The following software programs consist of code that is designed to run in Matlab. They have been tested for compatibility in Matlab v.R2009b running on both Mac OS X and Windows 7 operating systems and the results of all tests indicate that the software performed properly. Comments are provided in the code to assist the user in understanding and using it.

A2.1. SOLLERHALL_COM.M

```
function x = sollerhall_com()
% Adapted by COM from Appendix B.2, "Soller and Hall Analysis,"
% Ph.D. thesis of D. Derkacs (Univ of California, San Diego, 2009).

clear all;
h=6.62602896e-34;
c = 3e8;
q=1.6e-19;
indicator = 1;
count=0;

%%%%%%%%%%%%%%%%%%%%%%%%%%%%%%%%%%%%%%%%%%%%%%%%%%%%%%%%%%%%%%%%
% DONT CHANGE
%%%%%%%%%%%%%%%%%%%%%%%%%%%%%%%%%%%%%%%%%%%%%%%%%%%%%%%%%%%%%%%%
div = 1001;
data = zeros(4,div+1);
u = 0:6/div:6;
data(1,:) = u;

%%%%%%%%%%%%%%%%%%%%%%%%%%%%%%%%%%%%%%%%%%%%%%%%%%%%%%%%%%%%%%%%
% CHANGE 'lambda' sweep wavelength or ''d'' to sweep over dipole
distance from surface
%%%%%%%%%%%%%%%%%%%%%%%%%%%%%%%%%%%%%%%%%%%%%%%%%%%%%%%%%%%%%%%%

% Define the wavelength
for lambda = 400e-9:2e-9:1100e-9;
    indicator = indicator+1;
    count = count + 1;
    lambdav(count)=lambda; % vector of wavelengths in m

    d=20e-9;    % thickness of barrier

    % Define the height xs of the dipole above the substrate
    xs = 0e-9;
```

```
    nu_emwh = 3e8./lambda;
    index = 0;
    % Si
    n_Si = materials(lambda,'si');
    % Au
    n_Au = materials(lambda,'au');
    % a-Si
    n_aSi = materials(lambda,'as');
    % Ag
    n_ag = materials(lambda,'ag');
    % ITO
    n_ITO = materials(lambda,'it');
    % GaAs
    n_GaAs = materials(lambda,'ga');
    % PECVD SiO2
    n_SiO2 = materials(lambda,'so');

    % In.1Ga.9As
    realn_In10GaAs(1,:) = 1e-9*[300 305 310 315 320 325 330 335 340 345
350 355 360 365 370 375 380 385 390 395 400 405 410 415 420 425 430 435
440 445 450 455 460 465 470 475 480 485 490 495 500 505 510 515 520 525
530 535 540 545 550 555 560 565 570 575 580 585 590 595 600 605 610 615
620 625 630 635 640 645 650 655 660 665 670 675 680 685 690 695 700 705
710 715 720 725 730 735 740 745 750 755 760 765 770 775 780 785 790 795
800 805 810 815 820 825 830 835 840 845 850 855 860 865 870 875 880 885
890 895 900 905 910 915 920 925 930 935 940 945 950 955 960 965 970 975
980 985 990 995 1000 1005 1010 1015 1020 1025 1030 1035 1040 1045 1050
1055 1060 1065 1070 1075 1080 1085 1090 1095 1100 1105 1110 1115 1120
1125 1130 1135 1140 1145 1150 1155 1160 1165 1170 1175 1180 1185 1190
1195 1200];
    realn_In10GaAs(2,:) = [3.7968 3.7296 3.6687 3.6161 3.5776 3.5504
3.53 3.5146 3.5143 3.5179 3.5247 3.537 3.5566 3.5831 3.6146 3.6544
3.709 3.7812 3.8631 3.9751 4.0845 4.1911 4.2743 4.32 4.3811 4.4661
4.6169 4.7739 4.9217 4.9771 4.9453 4.8917 4.8257 4.7466 4.6809 4.6222
4.5684 4.5192 4.4696 4.4189 4.3762 4.3354 4.3014 4.2678 4.2347 4.2018
4.175 4.1514 4.1278 4.1056 4.0837 4.0625 4.0443 4.026 4.0079 3.9906
3.9734 3.9562 3.943 3.931 3.919 3.907 3.8944 3.8818 3.8691 3.8565 3.846
3.8354 3.8249 3.8144 3.8053 3.7974 3.7896 3.7817 3.7739 3.7677 3.7622
3.7568 3.7513 3.7458 3.7408 3.7363 3.7318 3.7272 3.7227 3.7182 3.7134
3.7073 3.7011 3.695 3.6888 3.6827 3.6765 3.6735 3.6707 3.6679 3.665
3.6622 3.6594 3.6567 3.6543 3.652 3.6497 3.6474 3.6451 3.6428 3.6405
3.6381 3.6358 3.63 3.63 3.63 3.63 3.63 3.63 3.63 3.63 3.63 3.63 3.63
3.63 3.63 3.63 3.63 3.63 3.63 3.63 3.63 3.63 3.63 3.63 3.63 3.63 3.63
3.63 3.63 3.63 3.63 3.63 3.63 3.63 3.63 3.63 3.63 3.63 3.63 3.63 3.63
3.63 3.63 3.63 3.63 3.63 3.63 3.63 3.63 3.63 3.63 3.63 3.63 3.63 3.63
3.63 3.63 3.63 3.63 3.63 3.63 3.63 3.63 3.63 3.63 3.63 3.63 3.63 3.63
3.63 3.63 3.63 3.63 3.63];
    imagn_In10GaAs(1,:) = 1e-9*[300 305 310 315 320 325 330 335 340 345
350 355 360 365 370 375 380 385 390 395 400 405 410 415 420 425 430 435
440 445 450 455 460 465 470 475 480 485 490 495 500 505 510 515 520 525
530 535 540 545 550 555 560 565 570 575 580 585 590 595 600 605 610 615
```

```
620 625 630 635 640 645 650 655 660 665 670 675 680 685 690 695 700 705
710 715 720 725 730 735 740 745 750 755 760 765 770 775 780 785 790 795
800 805 810 815 820 825 830 835 840 845 850 855 860 865 870 875 880 885
890 895 900 905 910 915 920 925 930 935 940 945 950 955 960 965 970 975
980 985 990 995 1000 1005 1010 1015 1020 1025 1030 1035 1040 1045 1050
1055 1060 1065 1070 1075 1080 1085 1090 1095 1100 1105 1110 1115 1120
1125 1130 1135 1140 1145 1150 1155 1160 1165 1170 1175 1180 1185 1190
1195 1200];
    imagn_In10GaAs(2,:) = [2.0142 1.9498 1.9128 1.8941 1.8761 1.8706
1.8745 1.8828 1.8908 1.9029 1.9185 1.9428 1.9611 1.975 2.0031 2.0295
2.0486 2.0715 2.0985 2.1106 2.1171 2.0734 2.0236 1.9699 1.9389 1.9102
1.892 1.8757 1.7725 1.5791 1.3879 1.1745 1.0397 0.9196 0.8324 0.7587
0.6943 0.6419 0.6037 0.5673 0.5353 0.5034 0.4805 0.4614 0.4422 0.4261
0.4116 0.3972 0.3831 0.3696 0.356 0.3425 0.3325 0.323 0.3135 0.3048
0.2995 0.2941 0.2888 0.2835 0.2759 0.2676 0.2593 0.2511 0.2447 0.2401
0.2355 0.2309 0.2263 0.2226 0.2203 0.2179 0.2155 0.2132 0.2102 0.2063
0.2024 0.1985 0.1946 0.1907 0.1875 0.1855 0.1835 0.1815 0.1795 0.1775
0.1738 0.1683 0.1628 0.1573 0.1518 0.1463 0.1411 0.1396 0.1381 0.1366
0.1351 0.1336 0.1321 0.1306 0.1294 0.1294 0.1294 0.1294 0.1294 0.1294
0.1294 0.1294 0.1294 0.129 0.129 0.129 0.129 0.129 0.129 0.129 0.129
0.129 0.129 0.129 0.129 0.129 0.129 0.129 0.129 0.129 0.129 0.129 0.129
0.129 0.129 0.129 0.129 0.129 0.129 0.129 0.129 0.129 0.129 0.129 0.129
0.129 0.129 0.129 0.129 0.129 0.129 0.129 0.129 0.129 0.129 0.129 0.129
0.129 0.129 0.129 0.129 0.129 0.129 0.129 0.129 0.129 0.129 0.129 0.129
0.129 0.129 0.129 0.129 0.129 0.129 0.129 0.129 0.129 0.129 0.129 0.129
0.129 0.129 0.129 0.129 ];
    rn_In10GaAs = interp1(realn_In10GaAs(1,:), realn_In10GaAs(2,:),
lambda, 'pchip');
    in_In10GaAs = j*interp1(imagn_In10GaAs(1,:), imagn_In10GaAs(2,:),
lambda, 'pchip');
    n_In10GaAs = rn_In10GaAs+in_In10GaAs;

    % In.2Ga.8As
    realn_In20GaAs(1,:) = 1e-9*[300 305 310 315 320 325 330 335 340 345
350 355 360 365 370 375 380 385 390 395 400 405 410 415 420 425 430 435
440 445 450 455 460 465 470 475 480 485 490 495 500 505 510 515 520 525
530 535 540 545 550 555 560 565 570 575 580 585 590 595 600 605 610 615
620 625 630 635 640 645 650 655 660 665 670 675 680 685 690 695 700 705
710 715 720 725 730 735 740 745 750 755 760 765 770 775 780 785 790 795
800 805 810 815 820 825 830 835 840 845 850 855 860 865 870 875 880 885
890 895 900 905 910 915 920 925 930 935 940 945 950 955 960 965 970 975
980 985 990 995 1000 1005 1010 1015 1020 1025 1030 1035 1040 1045 1050
1055 1060 1065 1070 1075 1080 1085 1090 1095 1100 1105 1110 1115 1120
1125 1130 1135 1140 1145 1150 1155 1160 1165 1170 1175 1180 1185 1190
1195 1200];
    realn_In20GaAs(2,:) = [3.7233 3.6604 3.609 3.551 3.5172 3.4845
3.4656 3.4544 3.4477 3.4412 3.4454 3.4581 3.464 3.481 3.5072 3.5439
3.585 3.6318 3.6831 3.7707 3.8583 3.9509 4.0286 4.0801 4.1215 4.1653
4.2455 4.4025 4.5625 4.7207 4.8182 4.8615 4.8355 4.7982 4.7416 4.68
4.6194 4.5599 4.5018 4.4557 4.4141 4.3738 4.3337 4.2951 4.2565 4.2194
4.1823 4.1589 4.1361 4.112 4.0865 4.0611 4.0393 4.0181 3.997 3.9786
3.9615 3.9444 3.9276 3.9115 3.8953 3.8792 3.8659 3.8532 3.8405 3.828
```

```
3.8174 3.8069 3.7963 3.7858 3.7767 3.7689 3.761 3.7532 3.7453 3.7379
3.7306 3.7233 3.716 3.7087 3.7017 3.695 3.6882 3.6815 3.6748 3.668
3.6633 3.6592 3.655 3.6508 3.6467 3.6425 3.6383 3.6354 3.6326 3.6298
3.6269 3.6241 3.6213 3.6188 3.6177 3.6165 3.6153 3.6142 3.613 3.6119
3.6107 3.6095 3.6084 3.6072 3.6061 3.6049 3.6038 3.6026 3.6014 3.6003
3.5991 3.598 3.5968 3.5956 3.5945 3.5933 3.5922 3.591 3.5899 3.5887
3.5875 3.5864 3.5852 3.5841 3.5829 3.5817 3.5806 3.5794 3.5783 3.5771
3.576 3.5748 3.5736 3.5725 3.5713 3.5702 3.569 3.5678 3.5667 3.5655
3.5644 3.5632 3.5621 3.5609 3.5597 3.5586 3.5574 3.5563 3.5551 3.5539
3.5528 3.5516 3.5505 3.5493 3.5482 3.547 3.5458 3.5447 3.5435 3.5424
3.5412 3.54 3.5389 3.5377 3.5366 3.5354 3.5343 3.5331 3.5319 3.5308
3.5296 3.5285 3.5273 3.5261 3.525];
    imagn_In20GaAs(1,:) = 1e-9*[300 305 310 315 320 325 330 335 340 345
350 355 360 365 370 375 380 385 390 395 400 405 410 415 420 425 430 435
440 445 450 455 460 465 470 475 480 485 490 495 500 505 510 515 520 525
530 535 540 545 550 555 560 565 570 575 580 585 590 595 600 605 610 615
620 625 630 635 640 645 650 655 660 665 670 675 680 685 690 695 700 705
710 715 720 725 730 735 740 745 750 755 760 765 770 775 780 785 790 795
800 805 810 815 820 825 830 835 840 845 850 855 860 865 870 875 880 885
890 895 900 905 910 915 920 925 930 935 940 945 950 955 960 965 970 975
980 985 990 995 1000 1005 1010 1015 1020 1025 1030 1035 1040 1045 1050
1055 1060 1065 1070 1075 1080 1085 1090 1095 1100 1105 1110 1115 1120
1125 1130 1135 1140 1145 1150 1155 1160 1165 1170 1175 1180 1185 1190
1195 1200];
    imagn_In20GaAs(2,:) = [2.0155 1.9448 1.9009 1.8766 1.857 1.8368
1.8353 1.8364 1.846 1.8541 1.8653 1.881 1.8961 1.9139 1.9353 1.9499
1.9621 1.9866 2.0147 2.0394 2.0462 2.0341 2.0069 1.9497 1.935 1.9299
1.9386 1.9688 1.9584 1.8662 1.745 1.5772 1.3902 1.2241 1.1161 0.9966
0.9047 0.8143 0.7416 0.6866 0.6433 0.6078 0.5772 0.5502 0.526 0.5033
0.482 0.4631 0.4473 0.4336 0.4208 0.4077 0.3942 0.381 0.3688 0.3583
0.3489 0.3402 0.3319 0.3237 0.3156 0.3079 0.3006 0.2941 0.2883 0.2829
0.278 0.2732 0.2685 0.2636 0.2588 0.2543 0.2503 0.2471 0.2447 0.2428
0.2411 0.2395 0.2376 0.2353 0.2321 0.2282 0.2239 0.2194 0.215 0.2112
0.2076 0.2043 0.201 0.1978 0.1945 0.1913 0.188 0.1845 0.1807 0.1769
0.1733 0.1699 0.1669 0.1646 0.1628 0.1612 0.1597 0.1584 0.1572 0.156
0.1548 0.1536 0.1523 0.1511 0.1498 0.1485 0.1473 0.1461 0.1449 0.1437
0.1425 0.1413 0.1402 0.139 0.1379 0.1368 0.1357 0.1347 0.1336 0.1326
0.1316 0.1306 0.1297 0.1288 0.1278 0.1269 0.1261 0.1252 0.1244 0.1236
0.1228 0.1221 0.1213 0.1206 0.12 0.1193 0.1187 0.1181 0.1175 0.117
0.1165 0.116 0.1155 0.1151 0.1147 0.1144 0.114 0.1137 0.1135 0.1132
0.113 0.1128 0.1127 0.1126 0.1125 0.1125 0.1125 0.1125 0.1126 0.1127
0.1128 0.113 0.1132 0.1135 0.1138 0.1141 0.1145 0.1149 0.1153 0.1158
0.1164 0.1169 0.1176 0.1182 0.1189 ];
    rn_In20GaAs = interp1(realn_In20GaAs(1,:), realn_In20GaAs(2,:),
lambda, 'pchip');
    in_In20GaAs = j*interp1(imagn_In20GaAs(1,:), imagn_In20GaAs(2,:),
lambda, 'pchip');
    n_In20GaAs = rn_In20GaAs+in_In20GaAs;

    % In.24Ga.76As
    realn_In24GaAs(1,:) = 1e-9*[300 305 310 315 320 325 330 335 340 345
350 355 360 365 370 375 380 385 390 395 400 405 410 415 420 425 430 435
```

```
440 445 450 455 460 465 470 475 480 485 490 495 500 505 510 515 520 525
530 535 540 545 550 555 560 565 570 575 580 585 590 595 600 605 610 615
620 625 630 635 640 645 650 655 660 665 670 675 680 685 690 695 700 705
710 715 720 725 730 735 740 745 750 755 760 765 770 775 780 785 790 795
800 805 810 815 820 825 830 835 840 845 850 855 860 865 870 875 880 885
890 895 900 905 910 915 920 925 930 935 940 945 950 955 960 965 970 975
980 985 990 995 1000 1005 1010 1015 1020 1025 1030 1035 1040 1045 1050
1055 1060 1065 1070 1075 1080 1085 1090 1095 1100 1105 1110 1115 1120
1125 1130 1135 1140 1145 1150 1155 1160 1165 1170 1175 1180 1185 1190
1195 1200];
    realn_In24GaAs(2,:) = [3.7044 3.6415 3.5854 3.5392 3.5004 3.4697
3.4465 3.4327 3.4239 3.421 3.428 3.4342 3.4445 3.4621 3.4851 3.5132
3.5536 3.6032 3.663 3.7344 3.816 3.8923 3.9512 3.9962 4.0324 4.0649
4.1561 4.261 4.4102 4.5526 4.6904 4.7759 4.8005 4.8142 4.7676 4.7143
4.6539 4.6013 4.5458 4.4903 4.4492 4.4064 4.3588 4.3173 4.279 4.2453
4.2138 4.1836 4.1573 4.131 4.1055 4.0804 4.0558 4.038 4.0201 4.0022
3.9802 3.9577 3.9351 3.9224 3.9106 3.8988 3.8869 3.8745 3.862 3.8496
3.837 3.8229 3.8088 3.7947 3.7808 3.7738 3.7669 3.7599 3.7529 3.7459
3.7383 3.7303 3.7222 3.7141 3.706 3.7 3.6943 3.6887 3.683 3.6773 3.6729
3.6687 3.6645 3.6604 3.6562 3.652 3.6478 3.6449 3.6421 3.6393 3.6365
3.6336 3.6308 3.6283 3.6272 3.626 3.6249 3.6237 3.6225 3.6214 3.6202
3.6191 3.6179 3.6168 3.6156 3.6144 3.6133 3.6121 3.611 3.6098 3.6087
3.6075 3.6063 3.6052 3.604 3.6029 3.6017 3.6006 3.5994 3.5982 3.5971
3.5959 3.5948 3.5936 3.5925 3.5913 3.5901 3.589 3.5878 3.5867 3.5855
3.5844 3.5832 3.582 3.5809 3.5797 3.5786 3.5774 3.5763 3.5751 3.5739
3.5728 3.5716 3.5705 3.5693 3.5682 3.567 3.5658 3.5647 3.5635 3.5624
3.5612 3.5601 3.5589 3.5577 3.5566 3.5554 3.5543 3.5531 3.552 3.5508
3.5496 3.5485 3.5473 3.5462 3.545 3.5439 3.5427 3.5415 3.5404 3.5392
3.5381 3.5369 3.5358 3.5346];
    imagn_In24GaAs(1,:) = 1e-9*[300 305 310 315 320 325 330 335 340 345
350 355 360 365 370 375 380 385 390 395 400 405 410 415 420 425 430 435
440 445 450 455 460 465 470 475 480 485 490 495 500 505 510 515 520 525
530 535 540 545 550 555 560 565 570 575 580 585 590 595 600 605 610 615
620 625 630 635 640 645 650 655 660 665 670 675 680 685 690 695 700 705
710 715 720 725 730 735 740 745 750 755 760 765 770 775 780 785 790 795
800 805 810 815 820 825 830 835 840 845 850 855 860 865 870 875 880 885
890 895 900 905 910 915 920 925 930 935 940 945 950 955 960 965 970 975
980 985 990 995 1000 1005 1010 1015 1020 1025 1030 1035 1040 1045 1050
1055 1060 1065 1070 1075 1080 1085 1090 1095 1100 1105 1110 1115 1120
1125 1130 1135 1140 1145 1150 1155 1160 1165 1170 1175 1180 1185 1190
1195 1200];
    imagn_In24GaAs(2,:) = [1.999 1.9304 1.8899 1.8531 1.8341 1.8175
1.8111 1.8111 1.8111 1.8216 1.8363 1.8517 1.8655 1.8793 1.9004 1.92
1.9382 1.9571 1.9764 1.988 1.999 1.9788 1.9555 1.9242 1.9 1.9 1.9
1.9091 1.9191 1.882 1.8183 1.7116 1.5526 1.3847 1.237 1.0988 0.9734
0.8687 0.8036 0.744 0.6882 0.6432 0.5988 0.5706 0.5424 0.5168 0.4977
0.4786 0.4606 0.4446 0.4286 0.4126 0.4002 0.3882 0.3762 0.365 0.3565
0.3481 0.3397 0.3316 0.3246 0.3175 0.3105 0.3034 0.2963 0.289 0.2818
0.2745 0.2672 0.2648 0.2628 0.2608 0.2588 0.2568 0.2539 0.2498 0.2457
0.2415 0.2374 0.2333 0.2299 0.2265 0.2231 0.2197 0.2163 0.2129 0.2094
0.206 0.2025 0.1991 0.1956 0.1921 0.1887 0.1859 0.183 0.1802 0.1774
0.1745 0.1717 0.1689 0.1661 0.1635 0.161 0.1584 0.1558 0.1533 0.1507
0.1482 0.1456 0.1451 0.1447 0.1442 0.1438 0.1433 0.1429 0.1424 0.142
```

```
0.1415 0.141 0.1406 0.1401 0.1397 0.1392 0.1388 0.1383 0.1378 0.1374
0.1369 0.1365 0.136 0.1356 0.1351 0.1346 0.1342 0.1337 0.1333 0.1328
0.1324 0.1319 0.1315 0.131 0.1305 0.1301 0.1296 0.1292 0.1287 0.1283
0.1278 0.1273 0.1269 0.1264 0.126 0.1255 0.1251 0.1246 0.1242 0.1237
0.1232 0.1228 0.1223 0.1219 0.1214 0.121 0.1205 0.12 0.1196 0.1191
0.1187 0.1182 0.1178 0.1173 0.1168 0.1164 0.1159 0.1155 0.115 0.1146
0.1141 0.1137 0.1132 0.1127 ];
    rn_In24GaAs = interp1(realn_In24GaAs(1,:), realn_In24GaAs(2,:),
lambda, 'pchip');
    in_In24GaAs = j*interp1(imagn_In24GaAs(1,:), imagn_In24GaAs(2,:),
lambda, 'pchip');
    n_In24GaAs = rn_In24GaAs+in_In24GaAs;

    % Al0.8Ga0.2As
    realn_a8(1,:) = 1e-9*[300   305 310 315 320 325 330 335 340 345 350
355 360 365 370 375 380 385 390 395 400 405 410 415 420 425 430 435 440
445 450 455 460 465 470 475 480 485 490 495 500 505 510 515 520 525 530
535 540 545 550 555 560 565 570 575 580 585 590 595 600 605 610 615 620
625 630 635 640 645 650 655 660 665 670 675 680 685 690 695 700 705 710
715 720 725 730 735 740 745 750 755 760 765 770 775 780 785 790 795 800
805 810 815 820 825 830 835 840 845 850 855 860 865 870 875 880 885 890
895 900 905 910 915 920 925 930 935 940 945 950 955 960 965 970 975 980
985 990 995 1000    1005    1010    1015    1020    1025    1030
1035    1040    1045    1050    1055    1060    1065    1070    1075
1080    1085    1090    1095    1100];
    realn_a8(2,:) = [4.014  3.991   3.999   4.035   4.109   4.250
4.415   4.558   4.700   4.868   5.020   5.031   4.954   4.835   4.683
4.563   4.464   4.380   4.308   4.245   4.189   4.138   4.093   4.053
4.016   3.983   3.953   3.920   3.888   3.859   3.832   3.807   3.784
3.763   3.743   3.725   3.709   3.700   3.688   3.662   3.631   3.603
3.576   3.554   3.533   3.514   3.498   3.482   3.467   3.453   3.440
3.427   3.415   3.404   3.393   3.383   3.373   3.363   3.354   3.345
3.336   3.328   3.320   3.313   3.305   3.298   3.291   3.285   3.279
3.273   3.267   3.261   3.255   3.250   3.245   3.240   3.235   3.230
3.226   3.221   3.217   3.212   3.208   3.204   3.200   3.197   3.193
3.189   3.186   3.183   3.179   3.176   3.173   3.170   3.167   3.164
3.161   3.158   3.155   3.153   3.150   3.147   3.145   3.142   3.140
3.138   3.135   3.133   3.131   3.129   3.127   3.125   3.123   3.121
3.119   3.117   3.115   3.113   3.111   3.110   3.108   3.106   3.105
3.103   3.101   3.100   3.098   3.097   3.095   3.094   3.092   3.091
3.090   3.088   3.087   3.086   3.084   3.083   3.082   3.081   3.079
3.078   3.077   3.076   3.075   3.074   3.073   3.071   3.070   3.069
3.068   3.067   3.066   3.065   3.064   3.063   3.063   3.062   3.061
3.060   3.059];
    imagn_a8(1,:) = realn_a8(1,:);
    imagn_a8(2,:) = [2.012  2.008   2.018   2.052   2.085   2.087
2.056   1.980   1.859   1.680   1.453   1.169   0.876   0.690   0.576
0.494   0.445   0.403   0.369   0.340   0.315   0.293   0.274   0.257
0.240   0.222   0.205   0.188   0.172   0.160   0.149   0.139   0.129
0.120   0.111   0.102   0.093   0.080   0.063   0.040   0.020   0.012
0.008   0.007   0.006   0.005   0.005   0.004   0.004   0.004   0.003
0.003   0.002   0.002   0.002   0.001   0.001   0.001   0.000   0.000
```

```
0.000   0.000   0.000   0.000   0.000   0.000   0.000   0.000   0.000
0.000   0.000   0.000   0.000   0.000   0.000   0.000   0.000   0.000
0.000   0.000   0.000   0.000   0.000   0.000   0.000   0.000   0.000
0.000   0.000   0.000   0.000   0.000   0.000   0.000   0.000   0.000
0.000   0.000   0.000   0.000   0.000   0.000   0.000   0.000   0.000
0.000   0.000   0.000   0.000   0.000   0.000   0.000   0.000   0.000
0.000   0.000   0.000   0.000   0.000   0.000   0.000   0.000   0.000
0.000   0.000   0.000   0.000   0.000   0.000   0.000   0.000   0.000
0.000   0.000   0.000   0.000   0.000   0.000   0.000   0.000   0.000
0.000   0.000   0.000   0.000   0.000   0.000   0.000   0.000   0.000
0.000   0.000];
    rn_a8 = interp1(realn_a8(1,:), realn_a8(2,:), lambda, 'pchip');
    in_a8 = j*interp1(imagn_a8(1,:), imagn_a8(2,:), lambda, 'pchip');
    n_a8 = rn_a8 + in_a8;

    % Pd
    realn_Pd(1,:) = 1e-9*[300.9   310.7 320.4   331.5   342.5   354.2
367.9   381.5   397.4   413.3   430.5   450.8   471.4   495.9   520.9
548.6   582.1   616.8   659.5   704.4   756.0   821.1   892.0   984.0
1087.6  1215.5  1393.1  1610.2  1937.2];
    realn_Pd(2,:) = [1.2    1.21    1.21    1.2 1.22    1.23    1.24
1.26    1.3 1.33    1.37    1.41    1.46    1.52    1.57    1.64
1.68    1.75    1.8 1.86    1.95    2.06    2.33    2.34    2.52
2.66    2.8 3.01    3.34];
    imagn_Pd(1,:) = realn_Pd(1,:);
    imagn_Pd(2,:) = [2.29   2.35    2.42    2.5 2.57    2.65    2.74
2.83    2.93    3.03    3.14    3.26    3.39    3.54    3.68    3.84
4.02    4.21    4.42    4.65    4.89    5.19    5.5 5.89    6.33    6.9
7.65    8.59    9.89];
    rn_Pd = interp1(realn_Pd(1,:), realn_Pd(2,:), lambda, 'pchip');
    in_Pd = j*interp1(imagn_Pd(1,:), imagn_Pd(2,:), lambda, 'pchip');
    n_Pd = rn_Pd + in_Pd;


    % SPECIFY composition In(x)Ga(1-x)As here, if used
    % x = atomic fraction of Indium
    x = 0.12;

    % RSoft GaAs n-k data (from luxpop.com): S. Zollner, "Optical
constants
    % and critical-point parameters of GaAs from 0.73 to 6.60 eV", J.
Appl. Phys., Vol. 90, No. 1, 1 July 2001, pp. 515-517.
    realn_RGaAs(1,:) = 1e-9*[200 210 220 230 240 245 250 255 260 270
280 290 300 310 320 330 340 350 360 370 380 390 400 420 440 460 480 500
520 540 560 580 600 650 700 750 800 810 820 830 840 845 850 900 1000
1100 1200 1300 1400 1500 1600 1700 1800 1900 2000 1000000];
    realn_RGaAs(2,:) = [1.323 1.298 1.373 1.512 1.788 2.137 2.686 3.253
3.645 3.98 4.142 4.039 3.844 3.694 3.613 3.576 3.57 3.592 3.642 3.726
3.869 4.102 4.443 4.818 4.995 4.698 4.465 4.304 4.183 4.087 4.013 3.953
3.904 3.813 3.756 3.703 3.664 3.659 3.653 3.648 3.644 3.642 3.631 3.59
3.509 3.464 3.433 3.41 3.393 3.379 3.369 3.36 3.352 3.346 3.341 3.341];
```

```
    imagn_RGaAs(1,:) = 1e-9*[200 210 220 230 240 245 250 255 260 270
280 290 300 310 320 330 340 350 360 370 380 390 400 420 440 460 480 500
520 540 560 580 600 650 700 750 800 810 820 830 840 845 850 900 1000
1100 1200 1300 1400 1500 1600 1700 1800 1900 2000 1000000];
    imagn_RGaAs(2,:) = [2.438 2.649 2.917 3.247 3.741 4.048 4.196 4.062
3.741 3.164 2.62 2.171 1.952 1.872 1.862 1.878 1.907 1.95 2.004 2.072
2.158 2.2 2.093 1.762 1.059 0.622 0.471 0.385 0.326 0.286 0.259 0.236
0.217 0.18 0.145 0.111 0.089 0.085 0.081 0.074 0.061 0.055 0 0 0 0 0 0
0 0 0 0 0 0 0 0 ];
    rn_RGaAs = interp1(realn_RGaAs(1,:), realn_RGaAs(2,:), lambda,
'pchip');
    in_RGaAs = j*interp1(imagn_RGaAs(1,:), imagn_RGaAs(2,:), lambda,
'pchip');



    % RSoft InAs n-k data (from luxpop.com): S. Adachi, "Model
dielectric constants of Gap, GaAs, GaSb, InP, InAs, and InSb," Phys.
Rev. B Vol. 35, No. 14, 15 May, 1987, pp. 7454-7463.
    realn_RInAs(1,:) = 1e-9*[210 220 230 240 250 260 270 280 290 300
310 320 330 340 350 400 450 490 500 510 520 530 550 600 650 700 750 800
850 900 950 1000 1050 1100 1200 1300 1400 1500 1600 1700 1800 1900 2000
2500 3000 3000.1 1000000];
    realn_RInAs(2,:) = [1.399 1.311 1.387 1.507 1.574 1.793 2.472 3.53
3.581 3.356 3.249 3.149 3.088 3.043 3.011 3.042 3.637 4.426 4.597 4.533
4.471 4.405 4.295 4.076 3.916 3.841 3.812 3.775 3.752 3.724 3.691 3.646
3.612 3.596 3.569 3.545 3.528 3.527 3.522 3.516 3.508 3.497 3.488 3.469
3.515 3.515 3.515];
    imagn_RInAs(1,:) = 1e-9*[210 220 230 240 250 260 270 280 290 300
310 320 330 340 350 400 450 490 500 510 520 530 550 600 650 700 750 800
850 900 950 1000 1050 1100 1200 1300 1400 1500 1600 1700 1800 1900 2000
2500 3000 3000.1 1000000];
    imagn_RInAs(2,:) = [2.11 2.26 2.5 2.72 3.01 3.33 3.22 3.03 2.11
1.71 1.66 1.68 1.69 1.71 1.73 1.86 1.89 1.55 1.45 1.29 1.15 1.04 0.85
0.67 0.54 0.52 0.47 0.42 0.4 0.36 0.33 0.3 0.29 0.28 0.26 0.24 0.22 0.2
0.18 0.17 0.17 0.16 0.16 0.13 0.09 0 0 ];
    rn_RInAs = interp1(realn_RInAs(1,:), realn_RInAs(2,:), lambda,
'pchip');
    in_RInAs = j*interp1(imagn_RInAs(1,:), imagn_RInAs(2,:), lambda,
'pchip');



    % Linear interpolation of the bulk GaAs and InAs refractive index
    conc=[0.0 1.0];
    rnx=[rn_RGaAs rn_RInAs];
    inx=[in_RGaAs in_RInAs];
    rn_InxGaAs = interp1(conc, rnx, x, 'linear');
    in_InxGaAs = interp1(conc, inx, x, 'linear');
    n_InxGaAs = rn_InxGaAs + in_InxGaAs;
```

```
    % Calculate the refractive index of InP or InGaAsP, if used
    %%%%%%%%%%%%%%%%%%%%%%%%%%%%%%%%%%%%%%%%%%%%%%%%%%%%%%%%
    % CHANGE Interpolation between InP and InGaAs
    % y to indicate concentration of As for one or more concentrations
    % (e.g., 3 specified below: 0, 0.2, 0.4)
    %%%%%%%%%%%%%%%%%%%%%%%%%%%%%%%%%%%%%%%%%%%%%%%%%%%%%%%%
    for y = [0 .2 .4]; % for InP, 20% InGaAs0.2P0.8, InGaAs structure
        index = index+1;
        e_current = h*c/lambda/q;
        eV = 0.56;
        lambda_new = h*c/q/(e_current+y.*eV);
        lambda_new2 = h*c/q/(e_current-(1-y).*eV);
        n_InP = materials(lambda_new,'ip');
        n_InGaAs = materials(lambda_new2,'ig');
        n_InGaAsP(index) = (1-y).*(n_InP.*(1+.045.*y))+ y.*n_InGaAs;
    end;

    %%%%%%%%%%%%%%%%%%%%%%%%%%%%%%%%%%%%%%%%%%%%%%%%%%%%%%%%
    % CHANGE to structure to be modeled in calculations
    %%%%%%%%%%%%%%%%%%%%%%%%%%%%%%%%%%%%%%%%%%%%%%%%%%%%%%%%
    % EXAMPLE INPUT:
    %
    % Dennis Hall (30nm above substrate)
    % n_sub = [1.0+j*realmin 3.662+j*.0052 1.5375+j*realmin
3.662+j*.0052];
    % n_subl = [(3.662)*160e-9/lambda (1.5375)*205e-9/lambda];
    % Dennis Hall II(LiF spacer 15nm)
    % d = 167e-9;
    % n_sub = [1.0 1.38 n_Si 1.48 n_Si];
    % n_subl = [(1.38)*15e-9/lambda n_Si*d/lambda (1.48)*205e-
9/lambda];

    % ACTUAL INPUT STRUCTURE:
    nbar = n_GaAs;
    nwell = n_InxGaAs;
    n_sub = [1.0-j*realmin n_SiO2 nbar n_a8 nbar nwell nbar nwell nbar
nwell nbar nwell nbar nwell nbar nwell nbar nwell nbar nwell nbar
n_Pd];
    nw1 = real(nwell)*8e-9/lambda;  % index scaled by well thickness
over lambda
    nb1 = real(nbar)*d/lambda;      % index scaled by barrier thickness
over lambda
    n_subl = [real(n_SiO2)*100e-9/lambda (nb1/d)*100e-9 real(n_a8)*40e-
9/lambda (nb1/d)*220e-9 nw1 nb1 nw1 nb1 nw1 nb1 nw1 nb1 nw1 nb1 nw1 nb1
nw1 nb1 nw1 (nb1/d)*220e-9]; % (nb1/d)*220e-9

    %%%%%%%%%%%%%%%%%%%%%%%%%%%%%%%%%%%%%%%%%%%%%%%%%%%%%%%%
    % CHANGE u TO REFLECT correct highest index bounding substrate
    %%%%%%%%%%%%%%%%%%%%%%%%%%%%%%%%%%%%%%%%%%%%%%%%%%%%%%%%
    %         n_barrier = find(u>=real(n_Au)); % for lower bounding
index of Au
    n_barrier = find(u>=real(n_Pd)); % for lower bounding index of Pd
```

```
    n_one = find(u>=1); % u > 1, corresponding to all evanescent modes

    %%%%%%%%%%%%%%%%%%%%%%%%%%%%%%%%%%%%%%%%%%%%%%%%%%%%%%%%
    % DONT CHANGE
    %%%%%%%%%%%%%%%%%%%%%%%%%%%%%%%%%%%%%%%%%%%%%%%%%%%%%%%%
    ks = 2*pi./lambda;
    costh = sqrt((1 - (u).^2-j*realmin));
    ksx = ks.*costh;

    % Multiple substrate method Fresnel coefficient calculation
    for ind = 1:1:length(u);
        rs(ind) = calc_reflection(n_sub,n_subl,1,u(ind),'te');
        rp(ind) = calc_reflection(n_sub,n_subl,1,u(ind),'tm');
    end;

    Su_VED = (u.^3)./sqrt(1-u.^2-j*realmin).*(1+rp.*exp(-2*j*xs*ksx));
    Su_HED = (u)./sqrt(1-u.^2-j*realmin).*(((1-u.^2).*(1-rp.*exp(-
2*j*xs*ksx)))+(1+rs.*exp(-2*j*xs*ksx)));


    % my calculations / plots for fractions into guided and leaky modes
    gmpHED = sum((real(Su_HED(n_barrier(1):length(u))))); % power in
guided modes for HED
    tmpHED = sum((real(Su_HED(1:length(u))))); % total power in
structure for HED
    fgmpHED(count) = gmpHED/tmpHED;   % fraction power into guided
modes of structure for HED

    gmpVED = sum((real(Su_VED(n_barrier(1):length(u))))); % power in
guided modes for VED
    tmpVED = sum((real(Su_VED(1:length(u))))); % total power in
structure for VED
    fgmpVED(count) = gmpVED/tmpVED; % fraction of power into guided
modes of structure for VED

    lmpHED = sum((real(Su_HED(n_one(1):n_barrier(1))))); % power in
leaky modes for HED
    flmpHED(count) = lmpHED/tmpHED; % fraction of total power in leaky
modes for HED

    lmpVED = sum((real(Su_VED(n_one(1):n_barrier(1))))); % power in
leaky modes for VED
    flmpVED(count) = lmpVED/tmpVED; % fraction of total power in leaky
modes for VED

    empHED = sum((real(Su_HED(n_one(1):length(u)))));
    fempHED(count) = empHED/tmpHED;

    % PLOTTING part 1:
```

```
    % REMOVE COMMENT when plotting a function of d instead of lambda
    % Otherwise, keep commented
    %         figure(21);
    %         plot(d,HED,'-*r','LineWidth',3,'MarkerSize',2);hold on;
    %         xlabel('guide thickness');
    %         ylabel('guided');
    %         legend('HED');
    %         title(strcat('\lambda = ',num2str(lambda), ' InGaAsP on
InP versus layer thickness'));
    %         subplot(4,2,8);
    %         plot(d,VED,'-*k','LineWidth',3,'MarkerSize',2);hold on;
    %         xlabel('guide thickness');
    %         ylabel('% guided');
    %         legend('VED');
    %         title(strcat('\lambda = ',num2str(lambda), ' InGaAsP on
InP versus layer thickness'));
    %%% close d loop %%%
    %     end;

end;

% PLOTTING part 2: coupling efficiency as a function of lambda
% COMMENT OUT if not plotting coupling efficiency vs. lambda
%
figure(18);
hold on;
xlim([400 1100]);
%     plot(lambda,fgmpHED,'-*r','LineWidth',3,'MarkerSize',2);hold on;
%     %     plot(lambda,fgmpVED,'-
*k','LineWidth',3,'MarkerSize',2);hold on;
%
plot(lambdav/1e-9,fgmpHED,'r','LineWidth',3);
%     plot(lambdav/1e-9,flmpHED,'k','LineWidth',3);
% %     plot(lambdav,fgmpVED,'b','LineWidth',3);
% %     plot(lambdav,flmpVED,'g','LineWidth',3);
%     legend('Guided','Leaky');
xlabel('Wavelength [nm]','FontWeight','b');
ylabel('Fraction into modes','FontWeight','b');
title('Ultrathin 8x (In0.12Ga0.88As)/GaAs QW / Pd back');

%     figure(19);
%     hold on;
%     %     plot(lambda,fgmpHED,'-
*r','LineWidth',3,'MarkerSize',2);hold on;
%     %     plot(lambda,fgmpVED,'-
*k','LineWidth',3,'MarkerSize',2);hold on;
%
%     plot(lambdav,fgmpVED,'b','LineWidth',3);
%     plot(lambdav,flmpVED,'g','LineWidth',3);
%     legend('Guided','Leaky');
%     xlabel('lambda [m]');
%     ylabel('Fraction into VED modes');
```

```
%     title('10x (In_0_._3Ga_0_._7As)/GaAs QW for VED');

%%%%%%%%%%%%%%%%%%%%%%%%%%%%%%%%%%%%%%%%%%%%%%%%%%%%%%%%
% DATA OUTPUT SECTION
% REMOVE COMMENT and modify file name ('data.txt') if desired
%
% data = data';
% save('data.txt', 'data', '-ascii', '-double');


%%%%%%%%%%%%%%%%%%%%%%%%%%%%%%%%%%%%%%%%%%%%%%%%%%%%%%%%
% Calculate Reflection
% DONT CHANGE
%%%%%%%%%%%%%%%%%%%%%%%%%%%%%%%%%%%%%%%%%%%%%%%%%%%%%%%%

    function output = calc_reflection(n,L,lambda,sintheta,pol)

        if nargin==0, help multidiel1; return; end
        if nargin<=4, pol='te'; end
        M = length(n)-2; % number of slabs
        if M==0, L = []; end % single interface, no slabs
        theta= acos(sqrt(1-sintheta.^2));
        costh = (sqrt(conj(1 - (n(1) * sintheta ./ n).^2)-j*realmin));

        % conj needed when na>n(i) and theta>th_c

        if pol=='te' | pol=='TE',
            nT = n .* costh; % transverse refractive indices
            r = -diff(nT) ./ (diff(nT) + 2*nT(1:M+1)); % r(i) = (n(i-
1)-n(i)) / (n(i-1)+n(i))
        else
            nT = n ./ costh; % TM case, fails at 90 deg for left medium
            r = diff(nT) ./ (diff(nT) + 2*nT(1:M+1));
        end

        if M>0,
            L = (sqrt(conj((L).^2-j*realmin)));
            L = L .* costh(2:M+1); % n(i)*l(i)*cos(th(i))
        end

        Gamma1 = r(M+1) * ones(1,length(lambda)); % initialize Gamma at
right-most interface

        for i = M:-1:1,
            delta = 2*pi*L(i)./lambda; % phase thickness in i-th layer
            z = exp(-2*j*delta);
            Gamma1 = (r(i) + Gamma1.*z) ./ (1 + r(i)*Gamma1.*z);
        end

        output = Gamma1;
```

```
    end;

end
```

A2.2. CALC_QW_ABS.M

```
function [alpha_qw_xx_yy, alpha_qw_zz] = calc_QW_abs(qw_mat, bar_mat,
x, lambdav, L, nu_l, nu_h, gam_broad_l, gam_broad_h, beta, F)
%%%%%%%%%%%%%%%%%%%%%%%%%%%%%%%%%%%%%%%%%%%%%%%%%%%%%%%%%%%%%%%%%%%%%%%%
%
% Calculate the anisotropic absorption coefficient of a quantum well
% Based on Ch.6, "Low Dimensional Semiconductor Structures," ed. K.
% Barnham and D. Vvedensky, Cambridge (2001), and on P. Kailuweit et
% al, JAP 107, 064317 (2010).
% Updated Aug 2010 by Clay McPheeters
%
% INPUT ARGUMENTS
% qw_mat = two-character string identifying the quantum well material
% (strings need to be the same as those used in materials.m)
% bar_mat = two-character string identifying the barrier material
% x = atomic fraction of designated element in alloy material
% [e.g., In(x)Ga(1-x)As]
% lambdav = vector of wavelengths (in meters) over which the absorption
%           coefficient will be calculated
% L = quantum well width (in meters)
% nu_l = light hole exciton oscillator strength fitting parameter
%           (nu = 0 corresponds to 3D, nu=0.5 corresponds to 2D; for a
%           practical quantum well, the value will be between.
% nu_h = heavy hole exciton oscillator strength fitting parameter
% gam_broad_l = light hole exciton homogeneous broadening term
%                 (generally on the order of 0.001 to 0.01 eV;
%                 specifies half-width at half-maximum)
% gam_broad_h = heavy hole exciton homogeneous broadening term
%                 (generally on the order of 0.001 to 0.01 eV;
%                 specifies half-width at half-maximum)
% beta = linear scaling parameter to fit calculated absorption to
%           measured data
% F = electric field strength in undoped (QW) region [kV/cm]
%
% OUTPUT
% alpha_qw_xx_yy = absorption coefficient (1/meter) of quantum well
%                 material, calculated over the specified wavelength
%                 range (lambdav), for x- and y-polarized light
% alpha_qw_zz = absorption coefficient (1/meter) of quantum well
%                 material, calculated over the specified wavelength
%                 range (lambdav), for z-polarized light
%
%%%%%%%%%%%%%%%%%%%%%%%%%%%%%%%%%%%%%%%%%%%%%%%%%%%%%%%%%%%%%%%%%%%%%%%%
%%%%
```

```
%%%%%%%%% CONSTANTS
c = 3e8;                        % speed of light, m/s
hbar = 1.0546e-34;              % (Plack's constant)/(2pi), J*s

% wavlength-dependent quantum well absorption to be calculated
alpha_qw_xx_yy = zeros(size(lambdav));
alpha_qw_zz = zeros(size(lambdav));


%%%%%%%%% Load material properties
[m_nb, m_nw, m_plb, m_plw, m_phb, m_phw, Eg_bar, Eg_lh, Eg_hh, V_en,
V_epl, V_eph, V_enj, V_eplj, V_ephj, Ry_pl, Ry_ph] = bulk_data(qw_mat,
bar_mat, x);


%%%%%%%%% Perform QW sub-band calculations
[k_n, E_n] = calc_QW_bs(m_nw, m_nb, V_en, L);
[k_ml, E_ml] = calc_QW_bs(m_plw, m_plb, V_epl, L);
[k_mh, E_mh] = calc_QW_bs(m_phw, m_phb, V_eph, L);

n = length(E_n);      % # of confined CB states
m_l = length(E_ml);   % # of confined light hole states
m_h = length(E_mh);   % # of confined heavy hole states


%%%%%%%%% Calculate Stark shifts
[dEstk_n, dEstk_lh, dEstk_hh] = calc_stark(L, F, E_n(1), E_mh(1),
E_ml(1));
% Apply Stark shifts to the first sub-band state, which is generally
% the only one that lies in the triangular portion of the QW
E_n(1) = E_n(1) + dEstk_n;
E_ml(1) = E_ml(1) + dEstk_lh;
E_mh(1) = E_mh(1) + dEstk_hh;


%%%%%%%%% Load bulk QW optical data
nt_well = materials(lambdav, qw_mat, x);
k_well = imag(nt_well);
al_well = 4*pi*k_well./(lambdav*10^2);  % calculate bulk QW material
absorption coefficient


%%%%%%%%% Calculate exciton oscillator strengths
Ry_pl_e = Ry_pl*6.24e18;            % note: Ry (atomic hydrogen) ~13eV,
                                    % loaded in bulk_data(...) function
                                    % call above
Ry_ph_e = Ry_ph*6.24e18
r_oscpl_e = 2*Ry_pl_e/(1-nu_l)^3;   % light hole oscillator strength
r_oscph_e = 2*Ry_ph_e/(1-nu_h)^3;   % heavy hole oscillator strength
```

```
E_bl_e = -Ry_pl_e/(1-nu_l)^2;       % light hole exciton binding energy
in eV
E_bh_e = -Ry_ph_e/(1-nu_h)^2;       % heavy hole exciton ....


%%%%%%%%% Calculate the absorption edge of the QW, accounting for sub-
band
%%%%%%%%% confinement energies
lambda_edge = ((hbar*6.24e18)*2*pi)*c/(Eg_hh + E_n(n) + E_mh(m_h));
% the wavelength corresponding to the absorption edge
abs_edge = interp1(lambdav, al_well, lambda_edge,'pchip');
% the bulk QW material absorption coefficient at the QW absorption edge


%%%%%%%%%%%%%%% CALCULATE SPECTRAL ABSORPTION COEFFICIENT
%%%%%%%%%%%%%%%%

%%%%%%%%% Wavelength sweep
for ctr = 1:length(lambdav)
    freq = c/lambdav(ctr);      % frequency, Hz
    omega = freq*(2*pi);        % angular frequency, 1/s
    qw_abs_l = 0;
    qw_abs_h = 0;
    qw_edge_l = 0;              % changes to 1 if hbar*omega > QW
bandgap, indicating light hole transitions possible in QW
    qw_edge_h = 0;              % changes to 1 if hbar*omega > QW
bandgap, indicating heavy hole transitions possible in QW
    lambda_edge_l = 0;
    lambda_edge_h = 0;
    k_edge_l = 0;
    k_edge_h = 0;
    abs_edge_l = 0;
    abs_edge_h = 0;


    if lambdav(ctr) <= 850e-9
        % If the wavelength is shorter than the GaAs absorption edge,
carriers are generated in the continuum of states at energies greater
than the GaAs bandgap. It is assumed that the bulk material absorption
applies at these wavelengths/energies.
        qw_abs_l = al_well(ctr);
        qw_abs_h = qw_abs_l;

    else
        % Otherwise, carriers are excited in bound states of the QW and
the modified absorption coefficient applies.

        %%%%%%%%% sum over conduction band (n) and valence band (m)
sub-band states
        for indn = 1:n
```

```
            %%%%%%%%%%%%%%%%%% HEAVY HOLES %%%%%%%%%%%%%%%%%%
            for indm_h = 1:m_h

                qw_edge_h = 0;
                pa_h=0;

                pa_h = inner_prod(m_nw, m_nb, m_phw, m_phb, V_en,
V_eph, L, k_mh(indm_h), E_mh(indm_h), k_n(indn), E_n(indn), indm_h,
indn);


                % The mimumum (unscaled) value of alpha is the bulk
value at the QW band edge wavelength. The QW density of states
determines if it takes on a higher base alue (i.e., if photon energy is
sufficient for transitions to higher than n=1 or m=1 sub-bands) and how
it scales according to excitonic absorption and envelope function
overlap.
                abs_edge_h = interp1(lambdav, al_well, lambdav(ctr),
'pchip');

                if ((hbar*6.24e18)*omega >= (Eg_hh + E_n(indn) +
E_mh(indm_h) + E_bh_e))
                    % Determine if photon energy is larger enough to
excite into a given sub-band
                    qw_edge_h = 1;
                    lambda_edge_h = (hbar*6.24e18*2*pi)*c/(Eg_hh +
E_n(1) + E_mh(1) + E_bh_e);
                    abs_edge_h = interp1(lambdav, al_well,
lambda_edge_h, 'pchip','extrap');
                end

                % model the exciton peak as a Lorentzian
                lor_h = (gam_broad_h)/(pi*(((hbar*6.24e18)*omega -
Eg_hh - E_n(indn) - E_mh(indm_h) - E_bh_e)^2 + gam_broad_h^2));

                % calculate the QW absorption coefficient for heavy
hole transitions, including transition probability and excitonic
absorption
                qw_abs_h = qw_abs_h + pa_h*(qw_edge_h +
r_oscph_e*lor_h)*abs_edge_h;

            end

            %%%%%%%%%%%%%%% LIGHT HOLES %%%%%%%%%%%%%%%%
            for indm_l = 1:m_l

                qw_edge_l = 0;
                pa_l=0;
```

```
                % The mimumum (unscaled) value of alpha is the bulk
value at the QW band edge wavelength. The QW density of states
determines if it takes on a higher base alue (i.e., if photon energy is
sufficient for transitions to higher than n=1 or m=1 sub-bands) and how
it scales according to excitonic absorption and envelope function
overlap.
                abs_edge_l = interp1(lambdav, al_well, lambdav(ctr),
'pchip');

                pa_l = inner_prod(m_nw, m_nb, m_plw, m_plb, V_en,
V_epl, L, k_ml(indm_l), E_ml(indm_l), k_n(indn), E_n(indn), indm_l,
indn);

                if ((hbar*6.24e18)*omega >= (Eg_lh + E_n(indn) +
E_ml(indm_l) + E_bl_e))
                    % Determine if photon energy is larger enough to
excite into a given sub-band
                    qw_edge_l = 1;
                    lambda_edge_l = (hbar*6.24e18*2*pi)*c/(Eg_lh +
E_n(1) + E_ml(1) + E_bl_e);
                    abs_edge_l = interp1(lambdav, al_well,
lambda_edge_l, 'pchip','extrap');
                end

                % model the exciton peak as a Lorentzian
                lor_l = (gam_broad_l)/(pi*(((hbar*6.24e18)*omega -
Eg_lh - E_n(indn) - E_ml(indm_l) - E_bl_e)^2 + gam_broad_l^2));

                % calculate the QW absorption coefficient for light
hole transitions, including transition probability and excitonic
absorption
                qw_abs_l = qw_abs_l + pa_l*(qw_edge_l +
r_oscpl_e*lor_l)*abs_edge_l;

            end
        end
    end

    % the ratio of transition strengths for (1,0,0) and (0,1,0)
polarized light is HH:LH = 3:1 (=> weighting 0.75 and 0.25)
    alpha_qw_xx_yy(ctr) = beta*(0.75*qw_abs_h + 0.25*qw_abs_l);


    % HH transitions are forbidden for (0,0,1) polarized light,
    % though the net oscillator strength is the same as the sum of
    % HH+LH oscillator strengths for other polarizations; so, no
weighting
    alpha_qw_zz(ctr) = beta*qw_abs_l;

end
```

```
%%%%%%%%% Assemble the wavelength (in nm) and QW absorption
coefficients for x- and y-polarized (_xx_yy), and for z-polarized (_zz)
light,in an output array.
qw_a_spec = [lambdav'/1e-9 alpha_qw_xx_yy' alpha_qw_zz'];


%%%%%%%%% PLOTTING
%%%%%%%%% Comment the following text if no plots are desired.
figure();
plot(lambdav/1e-9, alpha_qw_xx_yy,'LineWidth',1.5);
hold on;
plot(lambdav/1e-9, alpha_qw_zz, 'k','LineWidth',1.5);
plot(lambdav/1e-9, al_well, 'g','LineWidth',1.5);
legend('\alpha_x_x_,_y_y','\alpha_z_z','bulk');
xlabel('Wavelegth
(nm)','FontSize',14,'FontWeight','bold');ylabel('\alpha','FontSize',14,
'FontWeight','bold')

%%%%%%%%% ASCII FILE OUTPUT OF QW ABSORPTION COEFFICIENT
%%%%%%%%% Un-comment the following text if file output is desired.

save 'QW_alpha.txt' qw_a_spec -ascii;
```

A2.3. CALC_QW_BS.M

```
function [ksub, Esub] = calc_QW_bs(m_w, m_b, V_o, L)
%%%%%%%%%%%%%%%%%%%%%%%%%%%%%%%%%%%%%%%%%%%%%%%%%%%%%%%%%%%%%%%%%%%%%%%%%%%
%
% Solve for QW sub-band energies and wavenumbers
%
% INPUT ARGUMENTS
% m_w = effective mass of carrier in quantum well (kg)
% m_b = effective mass of carrier in barrier (kg)
% V_o = potential barrier (band offset at heterointerface, in eV)
% L = width of QW (in m)
%
% OUTPUT
% ksub = sub-band state wavenumber (m^-1)
% Esub (in eV)
%
%%%%%%%%%%%%%%%%%%%%%%%%%%%%%%%%%%%%%%%%%%%%%%%%%%%%%%%%%%%%%%%%%%%%%%%%%%%

hbar = 1.0546e-34;            % hbar in J*s
q = 1.602e-19;      % electronic charge, in coulombs

Vsteps = linspace(0, V_o, 50);
REsym = [];
REant = [];
```

```
options=optimset('TolFun',1E-100,'TolX',1E-
100,'MaxIter',100,'MaxFunEvals',100,'Display','off');


%%%%%%%%%%%% DO THE SYMMETRIC SUBBAND STATES
a=1;

for step=1:length(Vsteps)

    Esym(step) = fsolve(@(E_n1)
((sqrt((2*m_w*E_n1*q)/(hbar^2)))/m_w).*tan((sqrt((2*m_w*E_n1*q)/(hbar^2
)))*L/2)-(sqrt((2*m_b*(V_o-E_n1)*q)/(hbar^2)))/m_b, Vsteps(step),
options);
    if isreal(Esym(step))
        REsym(a)=Esym(step);
        a=a+1;
    end
end

Esym = REsym([find(REsym > 1e-4)]);
dup = [];
% if there are any duplicate states, remove them
for trk = 1:(length(Esym)-1)
    if abs(Esym(trk) - Esym(trk+1)) < 0.005
        dup = [dup, trk+1];
    end
end

Esym(dup) = [];   % remove the duplicates
Esym = sort(Esym);
Esymj = Esym*q;   % subband energies in Joules
ksym = sqrt(2*m_w*Esymj)/hbar;


%%%%%%%%%%%%%% DO THE ANTI-SYMMETRIC SUBBAND STATES
a=1;
for step=1:length(Vsteps)

    Eant(step) = fsolve(@(E_n1)
((sqrt((2*m_w*E_n1*q)/(hbar^2)))/m_w).*cot((sqrt((2*m_w*E_n1*q)/(hbar^2
)))*L/2)+(sqrt((2*m_b*(V_o-E_n1)*q)/(hbar^2)))/m_b, Vsteps(step),
options);
    if isreal(Eant(step))
        REant(a)=Eant(step);
        a=a+1;
    end
end

Eant = REant([find(REant > 1e-4)]);
dup = [];
```

```
% if there are any duplicate states or energies below first subband
(symmetric), remove them
for trk = 1:(length(Eant)-1)
    if abs(Eant(trk) - Eant(trk+1)) < 0.005
        dup = [dup, trk+1];
    end
end

Eant(dup) = [];   % remove the duplicates
Eant = sort(Eant);
Eantj = Eant*q;   % subband energies in Joules
kant = sqrt(2*m_w*Eantj)/hbar;

%%%%%%%%%%%%%% Assemble the symmetric and anti-symmetric subband data
Esub=zeros(1,(length(Esym)+length(Eant)));
ksub=zeros(1,(length(ksym)+length(kant)));
a=1;
y=1;
z=1;
while((y <= length(Esym)) || (z <= length(Eant)))
    if (rem(a,2)) == 1
        Esub(a) = Esym(y);
        ksub(a) = ksym(y);
        y=y+1;
    else
        Esub(a) = Eant(z);
        ksub(a) = kant(z);
        z=z+1;
    end
    a=a+1;

end
```

A2.4. INNER_PROD.M

```
function pa = inner_prod(m_nw, m_nb, m_pw, m_pb, V_en, V_ep, L, k_m,
E_m, k_n, E_n, m, n)
%
% Calculate the probability of transitions based on the overlap
intergral
% of initial (CB) and final (VB) state envelope functions.
%
% INPUT ARGUMENTS
% m_nw = effective mass of the electron in the QW (kg)
% m_nb = effective mass of the electron in the barrier (kg)
% m_pw = effective mass of the hole in the well (kg)
% m_pb = effective mass of the hole in the barrier (kg)
% V_en = QW conduction band offset (eV)
% V_ep = QW valence band offset (eV)
% L = QW width (m)
```

```
% k_m = valence sub-band state wavenumber (m^-1)
% E_m = valence sub-band state energy (eV)
% k_n = conduction sub-band state wavenumber (m^-1)
% E_n = conduction sub-band state energy (eV)
% m = valence sub-band index
% n = conduction sub-band index
%
% OUTPUT
% pa = probability of the transition
%

hbar = 1.0546e-34;              % hbar in J*s

z = (-L/2):(L/50):(L/2);

V_enj = V_en*1.6e-19;           % convert V_e to Joules
K_n = sqrt(2*m_nb*(V_enj-E_n)/(hbar^2));

% Enevelope function normalization coefficients
A=1;
B=1;

% Sum over the subbands
count=1;

% Determine the parity of the subband states
for indn = 1:length(k_n)
    for indm = 1:length(k_m)
        A = 1; B = 1;

        if rem(m,2) == 1
            Fm = B*cos(k_m(indm)*z);
        else
            Fm = B*sin(k_m(indm)*z);
        end

        if rem(n,2) == 1
            Fn = A*cos(k_n(indn)*z);
        else
            Fn = A*sin(k_n(indn)*z);
        end

        % Calculation the envelope function normalization
        A = sqrt(1/trapz(z, conj(Fn).*Fn));
        Fn = A*Fn;

        B = sqrt(1/trapz(z, conj(Fm).*Fm));
        Fm = B*Fm;
```

```
        % calculate the inner product of VB state m and CB state n,
        % then the probability amplitude
        ip = trapz(z, conj(Fn).*Fm);
        pa(count) = abs(ip)^2;
        count=count+1;
    end
end

end
```

A2.5. BULK_DATA.M

```
function [m_nb, m_nw, m_plb, m_plw, m_phb, m_phw, Eg_bar, Eg_lh, Eg_hh,
V_en, V_epl, V_eph, V_enj, V_eplj, V_ephj, Ry_pl, Ry_ph] =
bulk_data(qw_mat, bar_mat, x)
%%%%%%%%%%%%%%%%%%%%%%%%%%%%%%%%%%%%%%%%%%%%%%%%%%%%%%%%%%%%%%%%%%%%%%%%
%
% Load bulk material data
%
% INPUT ARGUMENTS
% qw_mat = a string designating the QW material
% bar_mat = a string designating the barrier material
% x = atomic fraction of elemental material in QW, as designated in
% material labels below
%
% OUTPUT
% m_nb = electron effective mass in barrier (kg)
% m_nw = electron effective mass in well (kg)
% m_plb = light hole effective mass in barrier (kg)
% m_plw = light hole effective mass in well (kg)
% m_phb = heavy hole effective mass in barrier (kg)
% m_phw = heavy hole effective mass in well (kg)
% Eg_bar = barrier bandgap (eV)
% Eg_lh = QW light hole bandgap, including sub-band confinement energy
(eV)
% Eg_hh = QW heavy hole bandgap, including sub-band confinement energy
(eV)
% V_en = QW conduction band offset (eV)
% V_epl = QW light hole band offset (eV)
% V_eph = QW heavy hole band offset (eV)
% V_enj = QW conduction band offset (J)
% V_eplj = QW light hole band offset (J)
% V_ephj = QW heavy hole band offset (J)
% Ry_pl = light hole Rydberg constant (J)
% Ry_ph = heavy hole Rydberg constant (J)
%
%%%%%%%%%%%%%%%%%%%%%%%%%%%%%%%%%%%%%%%%%%%%%%%%%%%%%%%%%%%%%%%%%%%%%%%%

m_0 = 9.109e-31;        % electron rest mass, kg
```

```
qe = 1.602e-19;          % electronic charge, coulombs
c = 2.998e8;             % speed of light, m/s
hbar = 1.055e-34;        % (Plack's constant)/(2pi), J*s
eps_0 = 8.854e-12;       % free space permittivity, F/m


mat = [qw_mat bar_mat];

% In(x)Ga(1-x)As QW and GaAs barrier
if mat == 'inga'
    % In(x)Ga(1-x)As data -
http://jap.aip.org/resource/1/japiau/v66/i4/p1739_s1
    % m_nw = 0.067(1-.426x)m0
    % m_phw = .34(1+.117x)m0
    % m_plw = .094(1-.660x)m0

    % GaAs data from NSM archive website
    m_nb = 0.063*m_0;
    m_nw = (0.063-0.04*x)*m_0;
    m_plb = 0.082*m_0;
    m_plw = (0.082-0.056*x)*m_0;        % (0.026+0.056*(1-x))
    m_phb = 0.51*m_0;
    m_phw = (0.51-0.1*x)*m_0;           % (0.41+0.1*(1-x))
    m_phwip = (0.11-0.075*x)*m_0;       % in-plane heavy hole effective
mass

    %%%%%%%%%%%%%%%% VB/CB OFFSET DATA %%%%%%%%%%%%%%%%%%%%%%%%
    % http://iopscience.iop.org/0953-8984/3/50/004: dEc = 0.95*dEv and
dEv = .02 eV
    % http://jap.aip.org/resource/1/japiau/v66/i4/p1739_s1: dEc =
0.85*dEg,
    % dEv = 0.15*dEg
    Eg_bar = 1.42;                          % bandgap of bulk barrier
material
    % UNSTRAINED GAAS -
http://jap.aip.org/resource/1/japiau/v66/i4/p1739_s1

    %%%%% STRAIN CALCULATIONS
    D = x*1.088 + (1-x)*0.934;              % an elastic constant for
the (001) direction
    a_par = 5.65e-10;                       % the in-plane (parallel)
lattice constant, assumed to be equal to GaAs
    a0 = x*6.08e-10 + (1-x)*5.65e-10;       % the unstrained lattice
constant of the QW material
    a_per = a0*(1 - D*(a_par/a0 - 1));      % the perpendicular lattice
constant of the QW material

    eps_par = (a_par - a0)/a0;              % the parallel component of
the strain tensor
    eps_per = (a_per - a0)/a0;              % the perpendicular
component of the strain tensor
```

```
    ac = x*(-5.08) + (1-x)*(-7.17);         % conduction band
deformation potential
    av = x*1.00 + (1-x)*1.16;               % valence band deformation
potential

    delta0 = x*0.38 + (1-x)*0.34;           % spin-orbit splitting
energy
    b = x*(-1.8) + (1-x)*(-1.7);            % shear deformation
potential for a strain of tetragonal symmetry
    delE = 2*b*(eps_per - eps_par);         % an energy shift term for
the (001) direction

    dEstr_cb = ac*(2*eps_par + eps_per);    % conduction band edge
hydrostatic strain shift - this is the only CB strain component for
direct bandgap materials
    dEstr_vbh = av*(2*eps_par + eps_per);   % valence band edges'
hydrostatic strain shift

    dEstr_hhs = 1/3*delta0 - 1/2*delE;
% heavy hole shear strain shift
    dEstr_lhs = -1/6*delta0 + 1/4*delE + 1/2*sqrt(delta0^2 +
delta0*delE + 9/4*delE^2);     % light hole shear strain shift
    dEstr_hh = dEstr_vbh + dEstr_hhs - 1/3*delta0;
% total heavy hole band strain shift
    dEstr_lh = dEstr_vbh + dEstr_lhs - 1/3*delta0;
% total light hole band strain shift


    % UNSTRAINED BANDGAPS, PLUS STRAIN SHIFTS
    if x==0
        Eg_qw=1.42;
        Eg_lh = Eg_qw + (dEstr_cb - dEstr_lh);
        Eg_hh = Eg_qw + (dEstr_cb - dEstr_hh);
    else
        Eg_qw = 1.42-1.07*x;    % bulk interpolation: 1.42-1.07*x   %
linear fit to spire InxGa(1-x)As absorption edge data gives smaller
bandgaps: 1.42-1.3465*x




%%%%%%%%%%%%%%%%%%%%%%%%%%%%%%%%%%%%%%%%%%%%%%%%%%%%%%%%%%%%%%%%%%%%%%%%
%%%%
        % NOTE:
        % COMMENT/UN-COMMENT THE IMMEDIATELY FOLLOWING 3 LINES OF CODE
        % TO INCORPORATE/UN-INCORPORATE STRAIN SHIFTS.
        % Strain shifts are based on the formalism used by Van de Walle
and
        % may or may not represent strain in GROWN quantum wells!
Adjust
```

```
        % use of the strain parameters accordingly.
        % Reference: C.G. Van de Walle, Phys. Rev. B vol. 39, p. 1871
(1989).

%%%%%%%%%%%%%%%%%%%%%%%%%%%%%%%%%%%%%%%%%%%%%%%%%%%%%%%%%%%%%%%%%%%%%%%%%%%%
%%%%
%         dEstr_cb=0;
%         dEstr_lh=0;
%         dEstr_hh=0;

        Eg_lh = Eg_qw + (dEstr_cb - dEstr_lh);
        Eg_hh = Eg_qw + (dEstr_cb - dEstr_hh);
    end

    % Total band offsets
    dEg_hh = Eg_bar - Eg_hh;
    dEg_lh = Eg_bar - Eg_lh;
    V_en = 0.6*dEg_hh;
    V_epl = 0.4*dEg_lh;
    V_eph = 0.4*dEg_hh;


    % reduced masses for exciton calculations
    mu_ip_nlh = (m_nw*m_plw)/(m_nw + m_plw);        % electron-light
hole reduced mass
    mu_ip_nhh = (m_nw*m_phwip)/(m_nw + m_phwip);    % electron-heavy
hole reduced mass

    % PERMITTIVITY
    % GaAs: epsr(static) = 12.9
    % In(1-x)Ga(x)As = 15.1-2.87x+0.67x^2 (NSM archive)
    eps_w = (12.9+2.25*x)*eps_0;
    eps_b = 12.9*eps_0;
    epsav = (eps_w + eps_b)/2;
end

% Al(x)Ga(1-x)As
if mat == 'gaal'

    m_nb = (0.063+0.083*x)*m_0;     % AlGaAs and GaAs data from NSM
archive
    m_nw = 0.063*m_0;
    m_plb = (0.082+0.068*x)*m_0;
    m_plw = 0.082*m_0;
    m_phb = (0.51+0.25*x)*m_0;
    m_phw = 0.51*m_0;
    m_phwip = 0.11*m_0;

    if x >= 0.45
        Eg_bar = 1.9+0.125*x+0.143*x^2;
    else
```

```
        Eg_bar = 1.42+1.247*x;      % bandgap of bulk barrier material
    end

    % UNSTRAINED GAAS -
http://jap.aip.org/resource/1/japiau/v66/i4/p1739_s1
    Eg_qw = 1.42;                   % bandgap of bulk well material:
based on attenuation coeff of 'bt' (In0.3Ga0.7As) in materials.m, which
is nonzero > 1260nm
    dEg = Eg_bar - Eg_qw;           % total band offset
    if x > 0.41
        V_en = 0.475-0.335*x+0.143*x^2;
    else
        V_en = 0.79*x;
    end
    V_ep = dEg-V_en;


    % reduced masses for exciton calculations
    mu_ip_nlh = (m_nw*m_plw)/(m_nw + m_plw);              % electron-
light hole reduced mass
    mu_ip_nhh = (m_nw*m_phwip)/(m_nw + m_phwip);          % electron-
heavy hole reduced mass

    % PERMITTIVITY
    % GaAs: epsr(static) = 12.9
    % In(1-x)Ga(x)As = 15.1-2.87x+0.67x^2 (NSM archive)
    eps_w = 12.9*eps_0;
    eps_b = (12.90-2.84*x)*eps_0;
    epsav = (eps_w + eps_b)/2;
end

% In(x)Ga(1-x)As QW and In0.3GaAs barrier
if mat == 'inbt'
    % In(x)Ga(1-x)As data -
http://jap.aip.org/resource/1/japiau/v66/i4/p1739_s1
    % m_nw = 0.067(1-.426x)m0
    % m_phw = .34(1+.117x)m0
    % m_plw = .094(1-.660x)m0

    % GaAs data from NSM archive

    m_nb = (0.063-0.04*.3)*m_0;
    m_nw = (0.063-0.04*x)*m_0;
    m_plb = (0.082-0.056*.3)*m_0;
    m_plw = (0.082-0.056*x)*m_0;
    m_phb = (0.51-0.1*.3)*m_0;
    m_phw = (0.51-0.1*x)*m_0;
    m_phwip = (0.11-0.075*x)*m_0;


    dEstr_cb = 0;
```

```
    dEstr_lh = 0;
    dEstr_hh = 0;

    % VB/CB OFFSET DATA
    % http://iopscience.iop.org/0953-8984/3/50/004: dEc = 0.95*dEv and
dEv = .02 eV
    % http://jap.aip.org/resource/1/japiau/v66/i4/p1739_s1: dEc =
0.85*dEg,
    % dEv = 0.15*dEg

    Eg_bar = 0.992;     % bandgap of In0.3GaAs
    % UNSTRAINED GAAS -
http://jap.aip.org/resource/1/japiau/v66/i4/p1739_s1
    % Eg_qw = 1.424-1.07*x; bandgap of bulk well material: based on
attenuation coeff of 'bt' (In0.3Ga0.7As) in materials.m, which is
nonzero > 1260nm

    if x==0
        Eg_qw=1.42;
    else if x==0.05
            Eg_qw=1.356;
        else if x==0.1
                Eg_qw = 1.283;
            else if x==0.3
                    Eg_qw = .992;
                else if x==0.4
                        Eg_qw = .896;
                    else
                        Eg_qw = 1.42-1.3465*x;
                    end
                end
            end
        end
    end

    Eg_lh = Eg_qw + (dEstr_cb - dEstr_lh);
    Eg_hh = Eg_qw + (dEstr_cb - dEstr_hh);

    dEg = Eg_bar-Eg_qw;     % total band offset
    V_en = 0.6*dEg;
    V_epl = 0.4*dEg;
    V_eph = 0.4*dEg;


    % reduced masses for exciton calculations
    mu_ip_nlh = (m_nw*m_plw)/(m_nw + m_plw);            % electron-
light hole reduced mass
    mu_ip_nhh = (m_nw*m_phwip)/(m_nw + m_phwip);        % electron-
heavy hole reduced mass

    % PERMITTIVITY
```

```
    % GaAs: epsr(static) = 12.9
    % In(1-x)Ga(x)As = 15.1-2.87x+0.67x^2 (NSM archive)
    eps_w = (12.9+2.25*x)*eps_0;
    eps_b = (12.9+2.25*.3)*eps_0;
    epsav = (eps_w + eps_b)/2;
end

% Calculate Rydberg cosntants for excitons
V_enj = V_en*1.6e-19;                                    % V_e in J
V_eplj = V_epl*1.6e-19;
V_ephj = V_eph*1.6e-19;
Ry_pl = (qe^4*mu_ip_nlh)/(8*epsav^2*(hbar*2*pi)^2);     % Light hole
Rydberg constant, J

Ry_ph = (qe^4*mu_ip_nhh)/(8*epsav^2*(hbar*2*pi)^2);       % Light hole

Rydberg constant, J
```

A2.6. CALC_STARK.M

```
function [dEstk_n, dEstk_lh, dEstk_hh] = calc_stark(L, F, E1n, E1hh,
E1lh)
% Estimates the shifts in energy of the first confined conduction band,
% light hole and heavy hole states due to the field present across
them.
% The estimation formula comes from the perturbation theory expansion
of energy, for which the second order term is an infinite sum over
subband states (excluding the first subband) describing the effect of
the mixing of the states due to the presence of the electric field. The
sum is simplified by assuming that:
%   - we only consider mixing of the first and second subband states
%   because it is much stronger than others
%   - we can use a simplification from an infinite barrier QW such that
the
%   denominator only depends on the first subband energy (instead of
E2-E1)
%
% INPUTS:
%   L = width of QW in meters
%   F = electric field strength [kV/cm]
%   E1n = first conduction band confined state energy [eV]
%   E1hh = first heavy hole confined state energy [eV]
%   E1lh = first light hole confined state energy [eV]
%
% OUTPUTS
%   dEstk_n = Stark shift to first conduction subband energy [eV]
%   dEstk_lh = Stark shift to first light hole subband energy [eV]
%   dEstk_hh =  Stark shift to first heavy hole subband energy

dEstk_n = (-256/(243*pi^4))*(((F*10^5)*L)^2)/E1n;
```

```
dEstk_lh = (-256/(243*pi^4))*(((F*10^5)*L)^2)/E1lh;

dEstk_hh = (-256/(243*pi^4))*(((F*10^5)*L)^2)/E1hh;
```

A2.7. MATERIALS.M

```
function x = materials(lambda, mat, mf)
%
% INPUT ARGUMENTS
% lambda = vector of wavelength(s) to be used in calculations (m)
% mat = a two-character string designating the material, as indicated
% in the material labels below
% mf = atomic fraction of elemental material in QW [e.g., see material
% 'in' below, which is In(x)Ga(1-x)As, and for which mf = x]
%
% OUTPUT
% x = the complex refractive index of the material at the wavelength
% specified by 'lambda'

nu_emwh = 2.998e8./lambda;

if mat=='si'
    realn_Si(1,:) = [1.146E+15 1.141E+15 1.136E+15 1.132E+15 1.127E+15
1.122E+15 1.117E+15 1.112E+15 1.107E+15 1.103E+15 1.098E+15 1.093E+15
1.088E+15 1.083E+15 1.078E+15 1.074E+15 1.069E+15 1.064E+15 1.059E+15
1.054E+15 1.049E+15 1.045E+15 1.040E+15 1.035E+15 1.030E+15 1.025E+15
1.020E+15 1.016E+15 1.011E+15 1.006E+15 1.001E+15 9.962E+14 9.914E+14
9.866E+14 9.817E+14 9.769E+14 9.720E+14 9.672E+14 9.624E+14 9.575E+14
9.527E+14 9.479E+14 9.430E+14 9.382E+14 9.334E+14 9.285E+14 9.237E+14
9.188E+14 9.140E+14 9.092E+14 9.043E+14 8.995E+14 8.947E+14 8.898E+14
8.850E+14 8.802E+14 8.753E+14 8.705E+14 8.657E+14 8.608E+14 8.560E+14
8.511E+14 8.463E+14 8.415E+14 8.366E+14 8.318E+14 8.270E+14 8.221E+14
8.173E+14 8.125E+14 8.076E+14 8.028E+14 7.979E+14 7.931E+14 7.883E+14
7.834E+14 7.786E+14 7.738E+14 7.689E+14 7.641E+14 7.593E+14 7.544E+14
7.496E+14 7.448E+14 7.399E+14 7.351E+14 7.302E+14 7.254E+14 7.206E+14
7.157E+14 7.109E+14 7.061E+14 7.012E+14 6.964E+14 6.916E+14 6.867E+14
6.819E+14 6.770E+14 6.722E+14 6.674E+14 6.625E+14 6.577E+14 6.529E+14
6.480E+14 6.432E+14 6.384E+14 6.335E+14 6.287E+14 6.239E+14 6.190E+14
6.142E+14 6.093E+14 6.045E+14 5.997E+14 5.948E+14 5.900E+14 5.852E+14
5.803E+14 5.755E+14 5.707E+14 5.658E+14 5.610E+14 5.561E+14 5.513E+14
5.465E+14 5.416E+14 5.368E+14 5.320E+14 5.271E+14 5.223E+14 5.175E+14
5.126E+14 5.078E+14 5.029E+14 4.981E+14 4.933E+14 4.884E+14 4.836E+14
4.788E+14 4.739E+14 4.691E+14 4.643E+14 4.594E+14 4.546E+14 4.498E+14
4.449E+14 4.401E+14 4.352E+14 4.304E+14 4.256E+14 4.207E+14 4.159E+14
4.111E+14 4.062E+14 4.014E+14 3.966E+14 3.917E+14 3.869E+14 3.820E+14
3.772E+14 3.724E+14 3.675E+14 3.627E+14 2.677E+14 2.621E+14 2.498E+14
2.185E+14 2.141E+14 1.957E+14 1.874E+14 1.768E+14];
    realn_Si(2,:) = [1.713 1.737 1.764 1.794 1.831 1.874 1.927 1.988
2.059 2.140 2.234 2.339 2.451 2.572 2.700 2.833 2.974 3.120 3.277 3.444
3.634 3.849 4.086 4.318 4.525 4.686 4.805 4.888 4.941 4.977 4.999 5.012
```

```
5.020 5.021 5.020 5.018 5.015 5.010 5.009 5.010 5.009 5.012 5.016 5.021
5.029 5.040 5.052 5.065 5.079 5.095 5.115 5.134 5.156 5.179 5.204 5.231
5.261 5.296 5.336 5.383 5.442 5.515 5.610 5.733 5.894 6.089 6.308 6.522
6.695 6.796 6.829 6.799 6.709 6.585 6.452 6.316 6.185 6.062 5.948 5.842
5.744 5.654 5.570 5.493 5.420 5.349 5.284 5.222 5.164 5.109 5.058 5.001
4.961 4.916 4.872 4.831 4.791 4.753 4.718 4.682 4.648 4.615 4.583 4.553
4.522 4.495 4.466 4.442 4.416 4.391 4.367 4.343 4.320 4.298 4.277 4.255
4.235 4.215 4.196 4.177 4.159 4.140 4.123 4.106 4.089 4.073 4.057 4.042
4.026 4.012 3.997 3.983 3.969 3.956 3.943 3.930 3.918 3.906 3.893 3.882
3.870 3.858 3.847 3.837 3.826 3.815 3.805 3.796 3.787 3.778 3.768 3.761
3.752 3.749 3.736 3.728 3.721 3.714 3.705 3.697 3.688 3.681 3.673
3.5361 3.5295 3.35193 3.5007 3.4876 3.4784 3.471 3.4644];
    imagn_Si(1,:) = [1.146E+15 1.141E+15 1.136E+15 1.132E+15 1.127E+15
1.122E+15 1.117E+15 1.112E+15 1.107E+15 1.103E+15 1.098E+15 1.093E+15
1.088E+15 1.083E+15 1.078E+15 1.074E+15 1.069E+15 1.064E+15 1.059E+15
1.054E+15 1.049E+15 1.045E+15 1.040E+15 1.035E+15 1.030E+15 1.025E+15
1.020E+15 1.016E+15 1.011E+15 1.006E+15 1.001E+15 9.962E+14 9.914E+14
9.866E+14 9.817E+14 9.769E+14 9.720E+14 9.672E+14 9.624E+14 9.575E+14
9.527E+14 9.479E+14 9.430E+14 9.382E+14 9.334E+14 9.285E+14 9.237E+14
9.188E+14 9.140E+14 9.092E+14 9.043E+14 8.995E+14 8.947E+14 8.898E+14
8.850E+14 8.802E+14 8.753E+14 8.705E+14 8.657E+14 8.608E+14 8.560E+14
8.511E+14 8.463E+14 8.415E+14 8.366E+14 8.318E+14 8.270E+14 8.221E+14
8.173E+14 8.125E+14 8.076E+14 8.028E+14 7.979E+14 7.931E+14 7.883E+14
7.834E+14 7.786E+14 7.738E+14 7.689E+14 7.641E+14 7.593E+14 7.544E+14
7.496E+14 7.448E+14 7.399E+14 7.351E+14 7.302E+14 7.254E+14 7.206E+14
7.157E+14 7.109E+14 7.061E+14 7.012E+14 6.964E+14 6.916E+14 6.867E+14
6.819E+14 6.770E+14 6.722E+14 6.674E+14 6.625E+14 6.577E+14 6.529E+14
6.480E+14 6.432E+14 6.384E+14 6.335E+14 6.287E+14 6.239E+14 6.190E+14
6.142E+14 6.093E+14 6.045E+14 5.997E+14 5.948E+14 5.900E+14 5.852E+14
5.803E+14 5.755E+14 5.707E+14 5.658E+14 5.610E+14 5.561E+14 5.513E+14
5.465E+14 5.416E+14 5.368E+14 5.320E+14 5.271E+14 5.223E+14 5.175E+14
5.126E+14 5.078E+14 5.029E+14 4.981E+14 4.933E+14 4.884E+14 4.836E+14
4.788E+14 4.739E+14 4.691E+14 4.643E+14 4.594E+14 4.546E+14 4.498E+14
4.449E+14 4.401E+14 4.352E+14 4.304E+14 4.256E+14 4.207E+14 4.159E+14
4.111E+14 4.062E+14 4.014E+14 3.966E+14 3.917E+14 3.869E+14 3.820E+14
3.772E+14 3.724E+14 3.675E+14 3.627E+14 2.677E+14 2.621E+14 2.498E+14
2.185E+14 2.141E+14 1.957E+14 1.874E+14 1.768E+14];
    imagn_Si(2,:) = [4.149 4.211 4.278 4.350 4.426 4.506 4.590 4.678
4.764 4.849 4.933 5.011 5.082 5.148 5.206 5.257 5.304 5.344 5.381 5.414
5.435 5.439 5.395 5.301 5.158 4.989 4.812 4.639 4.480 4.335 4.204 4.086
3.979 3.885 3.798 3.720 3.650 3.587 3.529 3.477 3.429 3.386 3.346 3.310
3.275 3.242 3.211 3.182 3.154 3.128 3.103 3.079 3.058 3.039 3.021 3.007
2.995 2.987 2.983 2.984 2.989 2.999 3.014 3.026 3.023 2.982 2.881 2.705
2.456 2.169 1.870 1.577 1.321 1.110 0.945 0.815 0.714 0.630 0.561 0.505
0.456 0.416 0.387 0.355 0.329 0.313 0.291 0.269 0.255 0.244 0.228 0.211
0.203 0.194 0.185 0.185 0.170 0.163 0.149 0.149 0.133 0.131 0.130 0.131
0.134 0.120 0.120 0.090 0.094 0.083 0.079 0.077 0.073 0.073 0.066 0.072
0.060 0.060 0.056 0.053 0.043 0.045 0.048 0.044 0.044 0.032 0.038 0.032
0.034 0.030 0.027 0.030 0.030 0.027 0.025 0.025 0.024 0.022 0.022 0.019
0.018 0.017 0.016 0.016 0.015 0.014 0.013 0.013 0.013 0.012 0.011 0.011
0.010 0.010 0.009 0.009 0.008 0.008 0.007 0.007 0.006 0.006 0.005
0.0005 0.00005 0.000005 0.0000005 0.00000005 0.000000005 0.0000000005
0.00000000005];
```

```
    rn_Si = interp1(realn_Si(1,:), realn_Si(2,:), nu_emwh, 'pchip');
    in_Si = j*interp1(imagn_Si(1,:), imagn_Si(2,:), nu_emwh, 'pchip');
    x = rn_Si+in_Si;
end

if mat=='au'
    %Gold
    realn_Au(1,:) = [1.84E14    1.89E14 1.93E14 1.98E14 2.03E14 2.08E14
2.13E14 2.18E14 2.22E14 2.27E14 2.32E14 2.37E14 2.42E14 2.66E14 2.9E14
3.14E14 3.39E14 3.63E14 3.87E14 4.11E14 4.35E14 4.59E14 5.32E14 5.56E14
5.8E14  6.05E14 6.29E14 6.53E14 6.77E14 7.01E14 7.25E14 7.5E14  7.74E14
7.98E14 8.22E14 8.46E14 8.7E14  8.95E14 9.19E14 9.43E14 9.67E14 9.91E14
1.02E15 1.04E15 1.06E15 1.09E15 1.11E15 1.14E15 1.16E15 1.18E15 1.21E15
1.23E15 1.26E15 1.28E15 1.31E15 1.33E15 1.35E15 1.38E15 1.4E15  1.43E15
1.45E15];
    realn_Au(2,:) = [0.609  0.583   0.559   0.537   0.515   0.493
0.473   0.454   0.436   0.419   0.403   0.389   0.372   0.312   0.272
0.236   0.21    0.188   0.174   0.164   0.16    0.166   0.306   0.402
0.608   0.916   1.242   1.426   1.562   1.616   1.636   1.658   1.674
1.696   1.716   1.74    1.766   1.798   1.824   1.84    1.83    1.812
1.776   1.742   1.69    1.648   1.598   1.546   1.504   1.49    1.484
1.478   1.47    1.462   1.454   1.452   1.442   1.438   1.432   1.43
1.422];
    imagn_Au(1,:) = [1.84E14    1.89E14 1.93E14 1.98E14 2.03E14 2.08E14
2.13E14 2.18E14 2.22E14 2.27E14 2.32E14 2.37E14 2.42E14 2.66E14 2.9E14
3.14E14 3.39E14 3.63E14 3.87E14 4.11E14 4.35E14 4.59E14 5.32E14 5.56E14
5.8E14  6.05E14 6.29E14 6.53E14 6.77E14 7.01E14 7.25E14 7.5E14  7.74E14
7.98E14 8.22E14 8.46E14 8.7E14  8.95E14 9.19E14 9.43E14 9.67E14 9.91E14
1.02E15 1.04E15 1.06E15 1.09E15 1.11E15 1.14E15 1.16E15 1.18E15 1.21E15
1.23E15 1.26E15 1.28E15 1.31E15 1.33E15 1.35E15 1.38E15 1.4E15  1.43E15
1.45E15];
    imagn_Au(2,:) = [10.3   10.1    9.81    9.58    9.36    9.15
8.96    8.77    8.59    8.42    8.25    8.09    8.77    7.93    7.07
6.47    5.88    5.39    4.86    4.35    3.8 3.15    2.88    2.54
2.12    1.84    1.796   1.846   1.904   1.94    1.958   1.956   1.936
1.906   1.862   1.848   1.846   1.86    1.878   1.904   1.916   1.92
1.918   1.9 1.882   1.852   1.822   1.784   1.748   1.698   1.636
1.59    1.55    1.51    1.478   1.442   1.418   1.388   1.364   1.334
1.306];
    rn_Au = interp1(realn_Au(1,:), realn_Au(2,:), nu_emwh, 'pchip');
    in_Au = j*interp1(imagn_Au(1,:), imagn_Au(2,:), nu_emwh, 'pchip');
    x = rn_Au+in_Au;
end

if mat=='ag'
    %Silver
    realn_Ag(1,:) = [1.8377E14  1.88606E14  1.93442E14  1.98278E14
2.03114E14  2.0795E14   2.12786E14  2.17622E14  2.22458E14  2.27294E14
2.3213E14   2.36966E14  2.41803E14  2.65983E14  2.90163E14  3.14343E14
3.38524E14  3.62704E14  3.86884E14  4.11064E14  4.35245E14  4.59425E14
4.83605E14  5.07785E14  5.31966E14  5.56146E14  5.80326E14  6.04506E14
6.28687E14  6.52867E14  6.77047E14  7.01227E14  7.25408E14  7.49588E14
```

```
7.73768E14  7.97948E14  8.22129E14  8.46309E14  8.70489E14  8.82579E14
8.94669E14  9.01923E14  9.06759E14  9.1885E14   9.26104E14  9.3094E14
9.38194E14  9.4303E14   9.50284E14  9.5512E14   9.62374E14  9.6721E14
9.793E14    9.9139E14   1.00348E15  1.01557E15  1.03975E15  1.06393E15
1.08811E15  1.11229E15  1.13647E15  1.16065E15  1.18483E15  1.20901E15
1.25737E15  1.30573E15  1.35409E15  1.40245E15  1.45082E15];
    realn_Ag(2,:) = [0.501  0.485   0.469   0.455   0.442   0.431
0.421   0.411   0.401   0.392   0.383   0.375   0.329   0.251   0.226
0.198   0.163   0.145   0.143   0.148   0.14    0.14    0.131   0.121
0.12    0.129   0.13    0.13    0.132   0.144   0.157   0.16    0.173
0.173   0.192   0.2 0.186   0.209   0.238   0.259   0.294   0.321
0.371   0.526   0.616   0.708   0.815   0.93    1.044   1.149   1.246
1.323   1.432   1.496   1.522   1.519   1.502   1.476   1.441   1.404
1.372   1.343   1.32    1.298   1.265   1.238   1.208   1.173   1.125];
    imagn_Ag(1,:) = [1.8377E14  1.88606E14  1.93442E14  1.98278E14
2.03114E14  2.0795E14   2.12786E14  2.17622E14  2.22458E14  2.27294E14
2.3213E14   2.36966E14  2.41803E14  2.65983E14  2.90163E14  3.14343E14
3.38524E14  3.62704E14  3.86884E14  4.11064E14  4.35245E14  4.59425E14
4.83605E14  5.07785E14  5.31966E14  5.56146E14  5.80326E14  6.04506E14
6.28687E14  6.52867E14  6.77047E14  7.01227E14  7.25408E14  7.49588E14
7.73768E14  7.97948E14  8.22129E14  8.46309E14  8.70489E14  8.82579E14
8.94669E14  9.01923E14  9.06759E14  9.1885E14   9.26104E14  9.3094E14
9.38194E14  9.4303E14   9.50284E14  9.5512E14   9.62374E14  9.6721E14
9.793E14    9.9139E14   1.00348E15  1.01557E15  1.03975E15  1.06393E15
1.08811E15  1.11229E15  1.13647E15  1.16065E15  1.18483E15  1.20901E15
1.25737E15  1.30573E15  1.35409E15  1.40245E15  1.45082E15];
    imagn_Ag(2,:) = [9.84   9.57    9.32    9.08    8.88    8.7 8.37
8.37    8.21    8.06    7.92    7.78    8.49    7.67    6.99    6.43
5.95    5.5 5.09    4.74    4.44    4.15    3.88    3.66    3.45
3.25    3.07    2.88    2.72    2.56    2.4 2.26    2.11    1.95
1.81    1.67    1.61    1.44    1.24    1.12    0.986   0.902   0.813
0.663   0.609   0.565   0.526   0.504   0.514   0.54    0.586   0.647
0.766   0.882   0.992   1.08    1.19    1.26    1.31    1.33    1.35
1.35    1.35    1.35    1.33    1.31    1.3 1.29    1.27];
    rn_Ag = interp1(realn_Ag(1,:), realn_Ag(2,:), nu_emwh, 'pchip');
    in_Ag = j*interp1(imagn_Ag(1,:), imagn_Ag(2,:), nu_emwh, 'pchip');
    x = rn_Ag+in_Ag;
end

if mat=='ni'
    % Nickel
    realn_InP(1,:) = 1e-6*[0.3 0.55 0.6 0.65 0.7 0.75 0.8 0.85 0.9 0.95
1 1.05 1.1 1.15 1.2 1.25 1.3 1.35 1.4 1.45 1.5 1.55 1.6 1.65 1.7 1.75
1.8 1.85 1.9 1.95 2 2.05 2.1 2.15 2.2 2.25 2.3 2.35 2.4 2.45 2.5 2.55
2.6 2.65 2.7 2.75 2.8 2.85 2.9 2.95 3 3.05 3.1 3.15 3.2 3.25 3.3 3.35
3.4 3.45 3.5 3.55 3.6 3.65 3.7 3.75 3.8 3.85 3.9 3.95 4 4.05 4.1 4.15
4.2 4.25 4.3 4.35 4.4 4.45 4.5 4.55 4.6 4.65 4.7 4.75 4.8 4.85 4.9 4.95
5 5.05 5.1 5.15 5.2 5.25 5.3 5.35 5.4 5.45 5.5 5.55 5.6 5.65 5.7 5.75
5.8 5.85 5.9 5.95 6 6.05 6.1 6.15 6.2 6.25 6.3 6.35 6.4 6.45 6.5];
    realn_InP(2,:) = [4.03 3.9 3.84 3.69 3.59 3.49 3.38 3.27 3.18 3.11
3.06 3.02125 2.97 2.91125 2.85 2.793125 2.74 2.695625 2.65 2.590625
2.53 2.481875 2.43 2.3575 2.28 2.208125 2.14 2.0775 2.02 1.966875 1.92
```

```
1.881875 1.85 1.82375 1.8 1.774375 1.75 1.729375 1.71 1.68875 1.67
1.658125 1.65 1.644375 1.64 1.635 1.63 1.625 1.62 1.614375 1.61
1.609375 1.61 1.61 1.61 1.609375 1.61 1.614375 1.62 1.625 1.63 1.634375
1.64 1.64875 1.66 1.674375 1.69 1.70625 1.72 1.72625 1.73 1.735625 1.74
1.74125 1.74 1.73625 1.73 1.721875 1.71 1.69125 1.67 1.65 1.63 1.61125
1.59 1.56125 1.53 1.500625 1.47 1.435625 1.4 1.364375 1.33 1.299375
1.27 1.239375 1.21 1.18375 1.16 1.13875 1.12 1.104375 1.09 1.074375
1.06 1.049375 1.04 1.029375 1.02 1.013125 1.01 1.006792 1.003833
1.001458 1 1.001797 1.004375 1.007266 1.01 1.012109 1.013125];
    imagn_InP(1,:) = 1e-6*[0.3 0.55 0.6 0.65 0.7 0.75 0.8 0.85 0.9 0.95
1 1.05 1.1 1.15 1.2 1.25 1.3 1.35 1.4 1.45 1.5 1.55 1.6 1.65 1.7 1.75
1.8 1.85 1.9 1.95 2 2.05 2.1 2.15 2.2 2.25 2.3 2.35 2.4 2.45 2.5 2.55
2.6 2.65 2.7 2.75 2.8 2.85 2.9 2.95 3 3.05 3.1 3.15 3.2 3.25 3.3 3.35
3.4 3.45 3.5 3.55 3.6 3.65 3.7 3.75 3.8 3.85 3.9 3.95 4 4.05 4.1 4.15
4.2 4.25 4.3 4.35 4.4 4.45 4.5 4.55 4.6 4.65 4.7 4.75 4.8 4.85 4.9 4.95
5 5.05 5.1 5.15 5.2 5.25 5.3 5.35 5.4 5.45 5.5 5.55 5.6 5.65 5.7 5.75
5.8 5.85 5.9 5.95 6 6.05 6.1 6.15 6.2 6.25 6.3 6.35 6.4 6.45 6.5];
    imagn_InP(2,:) = [9.64 8.92 8.35 7.92 7.48 7.13 6.82 6.51 6.23 5.98
5.74 5.546875 5.38 5.233125 5.1 4.97125 4.85 4.734375 4.63 4.54625 4.47
4.388125 4.31 4.245625 4.18 4.09875 4.01 3.915 3.82 3.73375 3.65
3.56375 3.48 3.403125 3.33 3.25875 3.19 3.124375 3.06 2.994375 2.93
2.868125 2.81 2.75875 2.71 2.659375 2.61 2.56375 2.52 2.479375 2.44
2.39875 2.36 2.329375 2.3 2.265 2.23 2.199375 2.17 2.13875 2.11
2.089375 2.07 2.044375 2.02 2.0025 1.99 1.983125 1.98 1.978125 1.98
1.989375 2 2.005 2.01 2.01875 2.03 2.045625 2.06 2.065625 2.07 2.08
2.09 2.095625 2.1 2.105625 2.11 2.11125 2.11 2.106875 2.1 2.08625 2.07
2.05625 2.04 2.01625 1.99 1.965625 1.94 1.91 1.88 1.854375 1.83 1.805
1.78 1.755625 1.73 1.699375 1.67 1.645625 1.63 1.6105 1.58825 1.564375
1.54 1.518672 1.498125 1.478516 1.46 1.442735 1.426875];
    rn_InP = interp1(realn_InP(1,:), realn_InP(2,:), lambda, 'pchip');
    in_InP = j*interp1(imagn_InP(1,:), imagn_InP(2,:), lambda,
'pchip');
    x = rn_InP+in_InP;
end

if mat=='it'
    %ITO
    reale_ITO(1,:) = [2.25E14 3E14 4.5E14 6E14 7.5E14 9E14 9.6E14
1.05E15];
    reale_ITO(2,:) = [1.8 2.8 3.6 4 4.4 5.1 5.6 5.5];
    image_ITO(1,:) = [2.25E14 3E14 4.5E14 6E14 7.5E14 9E14 9.6E14
1.05E15];
    image_ITO(2,:) = [0.4 0.2 0.1 0 0.1 0.2 0.5 1.3];
    re_ITO = interp1(reale_ITO(1,:), reale_ITO(2,:), nu_emwh, 'pchip');
    ie_ITO = j*interp1(image_ITO(1,:), image_ITO(2,:), nu_emwh,
'pchip');
    x = sqrt(re_ITO+ie_ITO);
end

if mat=='as'
    %a-Si
```

```
    realn_Asi(1,:) = [1.69262E14    1.93442E14  2.17622E14  2.41803E14
2.65983E14  2.90163E14  3.14343E14  3.38524E14  3.62704E14  3.86884E14
4.11064E14  4.35245E14  4.59425E14  4.83605E14  5.31966E14  5.80326E14
6.04506E14  6.28687E14  6.77047E14  7.25408E14  7.73768E14  8.22129E14
8.46309E14  8.70489E14  9.1885E14   9.6721E14   1.01557E15  1.06393E15
1.11229E15  1.16065E15  1.20901E15  1.32991E15  1.45082E15];
    realn_Asi(2,:) = [3.45  3.48    3.5 3.54    3.57    3.61    3.68
3.77    3.86    3.931   4.01    4.09    4.17    4.23    4.36    4.46
4.47    4.49    4.47    4.38    4.17    3.9 3.73    3.55    3.21
2.97    2.56    2.3 2.07    1.86    1.69    1.35    1.11];
    imagn_Asi(1,:) = [1.69262E14    1.93442E14  2.17622E14  2.41803E14
2.65983E14  2.90163E14  3.14343E14  3.38524E14  3.62704E14  3.86884E14
4.11064E14  4.35245E14  4.59425E14  4.83605E14  5.31966E14  5.80326E14
6.04506E14  6.28687E14  6.77047E14  7.25408E14  7.73768E14  8.22129E14
8.46309E14  8.70489E14  9.1885E14   9.6721E14   1.01557E15  1.06393E15
1.11229E15  1.16065E15  1.20901E15  1.32991E15  1.45082E15];
    imagn_Asi(2,:) = [0 0   0   0   0   0   0   0   0.0812  0.136
0.199   0.271   0.363   0.461   0.69    0.969   1.12    1.28    1.64
2.02    2.38    2.66    2.79    2.88    3   3.06    3.04    2.99
2.93    2.85    2.76    2.51    2.28];
    rn_Asi = interp1(realn_Asi(1,:), realn_Asi(2,:), nu_emwh, 'pchip');
    in_Asi = j*interp1(imagn_Asi(1,:), imagn_Asi(2,:), nu_emwh,
'pchip');
    x = rn_Asi+in_Asi;
end

if mat=='ip'
    % InP
    realn_InP(1,:) = 1e-6*[0.2066 0.2084 0.2101 0.2119 0.2138 0.2156
0.2175 0.2194 0.2214 0.2234 0.2254 0.2275 0.2296 0.2317 0.2339 0.2362
0.2384 0.2407 0.2431 0.2455 0.2480 0.2505 0.2530 0.2556 0.2583 0.2610
0.2638 0.2666 0.2695 0.2725 0.2755 0.2786 0.2818 0.2850 0.2883 0.2917
0.2952 0.2988 0.3024 0.3061 0.3100 0.3139 0.3179 0.3220 0.3263 0.3306
0.3351 0.3397 0.3444 0.3493 0.3542 0.3594 0.3647 0.3701 0.3757 0.3815
0.3875 0.3936 0.4000 0.4065 0.4133 0.4203 0.4275 0.4350 0.4428 0.4509
0.4592 0.4679 0.4769 0.4862 0.4959 0.5061 0.5166 0.5276 0.5391 0.5510
0.5636 0.5767 0.5904 0.6048 0.6199 0.6358 0.6526 0.6702 0.6888 0.7085
0.7293 0.7514 0.7749 0.7999 0.8266 0.8551 0.8856 0.9184 0.9537 0.9919
1.0332 1.0781 1.1271 1.1808 1.2399 1.3051 1.3776 1.4586 1.5498 1.6531
1.7712 1.9075 2.0664 2.2543 2.4797];
    realn_InP(2,:) = [1.3360 1.3079 1.3010 1.2962 1.2990 1.3088 1.3250
1.3484 1.3750 1.4018 1.4260 1.4420 1.4550 1.4656 1.4820 1.5100 1.5580
1.6321 1.7450 1.9237 2.1310 2.3353 2.5460 2.7549 2.9840 3.2844 3.5600
3.7224 3.8000 3.7741 3.6970 3.6145 3.5270 3.4517 3.3840 3.3255 3.2750
3.2321 3.1960 3.1656 3.1410 3.1219 3.1080 3.0989 3.0950 3.0963 3.1030
3.1147 3.1330 3.1582 3.1930 3.2324 3.2990 3.4191 3.5760 3.7659 3.9760
4.2217 4.4150 4.4411 4.3950 4.3327 4.2560 4.1871 4.1210 4.0604 4.0040
3.9515 3.9030 3.8588 3.8180 3.7801 3.7450 3.7123 3.6820 3.6543 3.6290
3.6059 3.5850 3.5663 3.5490 3.5323 3.5170 3.5035 3.4920 3.4830 3.4760
3.4712 3.4670 3.4633 3.4560 3.4402 3.4186 3.3920 3.3620 3.3287 3.2970
3.2736 3.2540 3.2361 3.2200 3.2049 3.1910 3.1785 3.1670 3.1561 3.1460
3.1372 3.1290 3.1210 3.1140];
```

```
    imagn_InP(1,:) = 1e-6*[0.2066 0.2084 0.2101 0.2119 0.2138 0.2156
0.2175 0.2194 0.2214 0.2234 0.2254 0.2275 0.2296 0.2317 0.2339 0.2362
0.2384 0.2407 0.2431 0.2455 0.2480 0.2505 0.2530 0.2556 0.2583 0.2610
0.2638 0.2666 0.2695 0.2725 0.2755 0.2786 0.2818 0.2850 0.2883 0.2917
0.2952 0.2988 0.3024 0.3061 0.3100 0.3139 0.3179 0.3220 0.3263 0.3306
0.3351 0.3397 0.3444 0.3493 0.3542 0.3594 0.3647 0.3701 0.3757 0.3815
0.3875 0.3936 0.4000 0.4065 0.4133 0.4203 0.4275 0.4350 0.4428 0.4509
0.4592 0.4679 0.4769 0.4862 0.4959 0.5061 0.5166 0.5276 0.5391 0.5510
0.5636 0.5767 0.5904 0.6048 0.6199 0.6358 0.6526 0.6702 0.6888 0.7085
0.7293 0.7514 0.7749 0.7999 0.8266 0.8551 0.8856 0.9184 0.9537 0.9919
1.0332 1.0781 1.1271 1.1808 1.2399 1.3051 1.3776 1.4586 1.5498 1.6531
1.7712 1.9075 2.0664 2.2543 2.4797];
    imagn_InP(2,:) = [2.1130 2.1487 2.1830 2.2294 2.2800 2.3312 2.3830
2.4351 2.4840 2.5237 2.5620 2.6025 2.6520 2.7193 2.8020 2.9012 3.0160
3.1541 3.2910 3.4090 3.4950 3.5171 3.5140 3.5351 3.5170 3.4068 3.2230
2.9398 2.6370 2.3898 2.1860 2.0464 1.9480 1.8761 1.8260 1.7881 1.7620
1.7448 1.7350 1.7299 1.7300 1.7349 1.7440 1.7567 1.7730 1.7928 1.8160
1.8419 1.8720 1.9065 1.9480 1.9994 2.0600 2.1456 2.2090 2.2108 2.1430
1.9654 1.7350 1.4832 1.2470 1.0861 0.9640 0.8648 0.7860 0.7209 0.6670
0.6198 0.5790 0.5429 0.5110 0.4823 0.4570 0.4354 0.4160 0.3975 0.3800
0.3631 0.3470 0.3314 0.3170 0.3046 0.2930 0.2818 0.2700 0.2561 0.2420
0.2292 0.2180 0.2149 0.2030 0.1619 0.1090 0.0689 0.033 0.017 0.0056
0.00012 0 0 0 0 0 0 0 0 0 0 0 0 0];
    rn_InP = interp1(realn_InP(1,:), realn_InP(2,:), lambda, 'pchip');
    in_InP = j*interp1(imagn_InP(1,:), imagn_InP(2,:), lambda,
'pchip');
    x = rn_InP+in_InP;
end

if mat=='rg'
    % RSoft GaAs n-k data (from luxpop.com): S. Zollner, "Optical
constants and critical-point parameters of GaAs from 0.73 to 6.60 eV",
J. Appl. Phys., Vol. 90, No. 1, 1 July 2001, pp. 515-517.
    realn_RGaAs(1,:) = 1e-9*[200 210 220 230 240 245 250 255 260 270
280 290 300 310 320 330 340 350 360 370 380 390 400 420 440 460 480 500
520 540 560 580 600 650 700 750 800 810 820 830 840 845 850 900 1000
1100 1200 1300 1400 1500 1600 1700 1800 1900 2000 1000000];
    realn_RGaAs(2,:) = [1.323 1.298 1.373 1.512 1.788 2.137 2.686 3.253
3.645 3.98 4.142 4.039 3.844 3.694 3.613 3.576 3.57 3.592 3.642 3.726
3.869 4.102 4.443 4.818 4.995 4.698 4.465 4.304 4.183 4.087 4.013 3.953
3.904 3.813 3.756 3.703 3.664 3.659 3.653 3.648 3.644 3.642 3.631 3.59
3.509 3.464 3.433 3.41 3.393 3.379 3.369 3.36 3.352 3.346 3.341 3.341];
    imagn_RGaAs(1,:) = 1e-9*[200 210 220 230 240 245 250 255 260 270
280 290 300 310 320 330 340 350 360 370 380 390 400 420 440 460 480 500
520 540 560 580 600 650 700 750 800 810 820 830 840 845 850 900 1000
1100 1200 1300 1400 1500 1600 1700 1800 1900 2000 1000000];
    imagn_RGaAs(2,:) = [2.438 2.649 2.917 3.247 3.741 4.048 4.196 4.062
3.741 3.164 2.62 2.171 1.952 1.872 1.862 1.878 1.907 1.95 2.004 2.072
2.158 2.2 2.093 1.762 1.059 0.622 0.471 0.385 0.326 0.286 0.259 0.236
0.217 0.18 0.145 0.111 0.089 0.085 0.081 0.074 0.061 0.055 0 0 0 0 0 0
0 0 0 0 0 0 0 0 ];
```

```
    rn_RGaAs = interp1(realn_RGaAs(1,:), realn_RGaAs(2,:), lambda,
'pchip');
    in_RGaAs = j*interp1(imagn_RGaAs(1,:), imagn_RGaAs(2,:), lambda,
'pchip');
    x = rn_RGaAs+in_RGaAs;
end

if mat=='ri'
    % RSoft InAs n-k data (from luxpop.com): S. Adachi, "Model
dielectric constants of GaP, GaAs, GaSb, InP, InAs, and InSb," Phys.
Rev. B Vol. 35, No. 14, 15 May, 1987, pp. 7454-7463.
    realn_RInAs(1,:) = 1e-9*[210 220 230 240 250 260 270 280 290 300
310 320 330 340 350 400 450 490 500 510 520 530 550 600 650 700 750 800
850 900 950 1000 1050 1100 1200 1300 1400 1500 1600 1700 1800 1900 2000
2500 3000 3000.1 1000000];
    realn_RInAs(2,:) = [1.399 1.311 1.387 1.507 1.574 1.793 2.472 3.53
3.581 3.356 3.249 3.149 3.088 3.043 3.011 3.042 3.637 4.426 4.597 4.533
4.471 4.405 4.295 4.076 3.916 3.841 3.812 3.775 3.752 3.724 3.691 3.646
3.612 3.596 3.569 3.545 3.528 3.527 3.522 3.516 3.508 3.497 3.488 3.469
3.515 3.515 3.515];
    imagn_RInAs(1,:) = 1e-9*[210 220 230 240 250 260 270 280 290 300
310 320 330 340 350 400 450 490 500 510 520 530 550 600 650 700 750 800
850 900 950 1000 1050 1100 1200 1300 1400 1500 1600 1700 1800 1900 2000
2500 3000 3000.1 1000000];
    imagn_RInAs(2,:) = [2.11 2.26 2.5 2.72 3.01 3.33 3.22 3.03 2.11
1.71 1.66 1.68 1.69 1.71 1.73 1.86 1.89 1.55 1.45 1.29 1.15 1.04 0.85
0.67 0.54 0.52 0.47 0.42 0.4 0.36 0.33 0.3 0.29 0.28 0.26 0.24 0.22 0.2
0.18 0.17 0.17 0.16 0.16 0.13 0.09 0 0 ];
    rn_RInAs = interp1(realn_RInAs(1,:), realn_RInAs(2,:), lambda,
'pchip');
    in_RInAs = j*interp1(imagn_RInAs(1,:), imagn_RInAs(2,:), lambda,
'pchip');
    x = rn_RInAs+in_RInAs;
end

if mat=='ig'
    % InGaAs LM to InP
    realn_InGaAs(1,:) = 1e-9*[206.6420 207.3331 208.0288 208.7293
209.4344 210.1444 210.8592 211.5788 212.3034 213.0330 213.7676 214.5072
215.2521 216.0021 216.7573 217.5179 218.2838 219.0551 219.8319 220.6142
221.4021 222.1957 222.9949 223.8000 224.6108 225.4276 226.2503 227.0791
227.9139 228.7549 229.6022 230.4557 231.3156 232.1820 233.0549 233.9343
234.8204 235.7133 236.6129 237.5195 238.4330 239.3536 240.2814 241.2163
242.1586 243.1082 244.0653 245.0300 246.0023 246.9824 247.9704 248.9662
249.9701 250.9821 252.0024 253.0310 254.0680 255.1135 256.1677 257.2307
258.3025 259.3832 260.4731 261.5721 262.6805 263.7983 264.9256 266.0626
267.2094 268.3662 269.5330 270.7100 271.8973 273.0951 274.3035 275.5226
276.7526 277.9937 279.2459 280.5095 281.7845 283.0712 284.3697 285.6801
287.0027 288.3376 289.6850 291.0450 292.4179 293.8037 295.2028 296.6153
298.0413 299.4811 300.9349 302.4029 303.8852 305.3822 306.8940 308.4208
309.9630 311.5206 313.0939 314.6832 316.2887 317.9107 319.5494 321.2051
322.8781 324.5685 326.2768 328.0031 329.7478 331.5112 333.2935 335.0951
```

```
336.9163 338.7573 340.6186 342.5005 344.4033 346.3273 348.2730 350.2406
352.2306 354.2434 356.2793 358.3387 360.4220 362.5298 364.6623 366.8201
369.0035 371.2131 373.4493 375.7127 378.0036 380.3226 382.6703 385.0471
387.4537 389.8905 392.3582 394.8573 397.3884 399.9522 402.5493 405.1803
407.8460 410.5470 413.2839 416.0577 418.8689 421.7183 424.6068 427.5351
430.5041 433.5146 436.5675 439.6638 442.8042 445.9899 449.2217 452.5007
455.8279 459.2044 462.6313 466.1097 469.6408 473.2259 476.8661 480.5627
484.3171 488.1306 492.0047 495.9407 499.9402 504.0048 508.1360 512.3355
516.6049 520.9461 525.3609 529.8512 534.4189 539.0660 543.7947 548.6070
553.5053 558.4918 563.5690 568.7394 574.0055 579.3700 584.8358 590.4056
596.0826 601.8698 607.7705 613.7880 619.9259 626.1878 632.5775 639.0989
645.7562 652.5536 659.4956 666.5870 673.8325 681.2373 688.8066 696.5460
704.4613 712.5585 720.8441 729.3246 738.0070 746.8987 756.0072 765.3406
774.9074 784.7163 794.7768 805.0986 815.6920 826.5679 855.1 885.6 918.4
953.7 991.9 1033.2 1078.1 1127.1 1180.8 1239.9 1305.1 1377.6 1458.6
1549.8 1653.1 1771.2 1907.5 2066.4 2254.3 2479.7];
    realn_InGaAs(2,:) = [1.3440 1.3251 1.3066 1.3217 1.3044 1.3202
1.3125 1.3074 1.3055 1.2993 1.3033 1.3008 1.3000 1.3020 1.3028 1.3044
1.3022 1.3081 1.3102 1.3124 1.3164 1.3216 1.3279 1.3325 1.3380 1.3449
1.3523 1.3597 1.3685 1.3769 1.3877 1.3977 1.4078 1.4196 1.4312 1.4434
1.4572 1.4691 1.4834 1.4975 1.5139 1.5299 1.5470 1.5643 1.5829 1.6015
1.6231 1.6456 1.6691 1.6953 1.7248 1.7565 1.7909 1.8293 1.8704 1.9161
1.9642 2.0183 2.0752 2.1372 2.2027 2.2725 2.3452 2.4205 2.4970 2.5766
2.6566 2.7362 2.8151 2.8926 2.9664 3.0371 3.1039 3.1665 3.2258 3.2806
3.3349 3.3834 3.4300 3.4700 3.5060 3.5359 3.5590 3.5754 3.5866 3.5934
3.5963 3.5957 3.5931 3.5878 3.5805 3.5719 3.5618 3.5497 3.5373 3.5250
3.5128 3.5005 3.4885 3.4766 3.4646 3.4532 3.4421 3.4312 3.4214 3.4113
3.4018 3.3932 3.3851 3.3771 3.3693 3.3623 3.3558 3.3509 3.3453 3.3404
3.3363 3.3327 3.3291 3.3269 3.3249 3.3234 3.3224 3.3216 3.3213 3.3220
3.3233 3.3249 3.3269 3.3295 3.3333 3.3373 3.3422 3.3478 3.3542 3.3616
3.3694 3.3782 3.3880 3.3986 3.4109 3.4244 3.4389 3.4552 3.4725 3.4915
3.5126 3.5360 3.5623 3.5903 3.6227 3.6571 3.6956 3.7392 3.7865 3.8386
3.8942 3.9510 4.0058 4.0568 4.1028 4.1433 4.1792 4.2123 4.2431 4.2728
4.3047 4.3393 4.3824 4.4319 4.4840 4.5334 4.5749 4.6021 4.6144 4.6128
4.6005 4.5810 4.5562 4.5281 4.4994 4.4693 4.4389 4.4085 4.3795 4.3509
4.3233 4.2968 4.2709 4.2461 4.2231 4.2002 4.1776 4.1560 4.1348 4.1142
4.0944 4.0757 4.0578 4.0401 4.0231 4.0065 3.9901 3.9733 3.9580 3.9427
3.9277 3.9127 3.8996 3.8869 3.8739 3.8616 3.8503 3.8387 3.8280 3.8163
3.8059 3.7967 3.7859 3.7741 3.7636 3.7536 3.7443 3.7338 3.7262 3.7203
3.7203 3.6987 3.6721 3.6421 3.6088 3.5771 3.5537 3.5341 3.5162 3.5001
3.4850 3.4711 3.4586 3.4471 3.4362 3.4261 3.4173 3.4091 3.4011 3.3941];
    imagn_InGaAs(1,:) = 1e-9*[206.6420 207.3331 208.0288 208.7293
209.4344 210.1444 210.8592 211.5788 212.3034 213.0330 213.7676 214.5072
215.2521 216.0021 216.7573 217.5179 218.2838 219.0551 219.8319 220.6142
221.4021 222.1957 222.9949 223.8000 224.6108 225.4276 226.2503 227.0791
227.9139 228.7549 229.6022 230.4557 231.3156 232.1820 233.0549 233.9343
234.8204 235.7133 236.6129 237.5195 238.4330 239.3536 240.2814 241.2163
242.1586 243.1082 244.0653 245.0300 246.0023 246.9824 247.9704 248.9662
249.9701 250.9821 252.0024 253.0310 254.0680 255.1135 256.1677 257.2307
258.3025 259.3832 260.4731 261.5721 262.6805 263.7983 264.9256 266.0626
267.2094 268.3662 269.5330 270.7100 271.8973 273.0951 274.3035 275.5226
276.7526 277.9937 279.2459 280.5095 281.7845 283.0712 284.3697 285.6801
287.0027 288.3376 289.6850 291.0450 292.4179 293.8037 295.2028 296.6153
```

```
298.0413 299.4811 300.9349 302.4029 303.8852 305.3822 306.8940 308.4208
309.9630 311.5206 313.0939 314.6832 316.2887 317.9107 319.5494 321.2051
322.8781 324.5685 326.2768 328.0031 329.7478 331.5112 333.2935 335.0951
336.9163 338.7573 340.6186 342.5005 344.4033 346.3273 348.2730 350.2406
352.2306 354.2434 356.2793 358.3387 360.4220 362.5298 364.6623 366.8201
369.0035 371.2131 373.4493 375.7127 378.0036 380.3226 382.6703 385.0471
387.4537 389.8905 392.3582 394.8573 397.3884 399.9522 402.5493 405.1803
407.8460 410.5470 413.2839 416.0577 418.8689 421.7183 424.6068 427.5351
430.5041 433.5146 436.5675 439.6638 442.8042 445.9899 449.2217 452.5007
455.8279 459.2044 462.6313 466.1097 469.6408 473.2259 476.8661 480.5627
484.3171 488.1306 492.0047 495.9407 499.9402 504.0048 508.1360 512.3355
516.6049 520.9461 525.3609 529.8512 534.4189 539.0660 543.7947 548.6070
553.5053 558.4918 563.5690 568.7394 574.0055 579.3700 584.8358 590.4056
596.0826 601.8698 607.7705 613.7880 619.9259 626.1878 632.5775 639.0989
645.7562 652.5536 659.4956 666.5870 673.8325 681.2373 688.8066 696.5460
704.4613 712.5585 720.8441 729.3246 738.0070 746.8987 756.0072 765.3406
774.9074 784.7163 794.7768 805.0986 815.6920 826.5679 855.1 885.6 918.4
953.7 991.9 1033.2 1078.1 1127.1 1180.8 1239.9 1305.1 1377.6 1458.6
1549.8 1653.1 1771.2 1907.5 2066.4 2254.3 2479.7];
    imagn_InGaAs(2,:) = [2.2677 2.2142 2.2876 2.2733 2.2630 2.2694
2.2905 2.2793 2.2876 2.2999 2.3091 2.3257 2.3412 2.3536 2.3639 2.3771
2.3937 2.4114 2.4246 2.4446 2.4617 2.4767 2.4932 2.5113 2.5297 2.5468
2.5646 2.5862 2.6051 2.6247 2.6457 2.6648 2.6854 2.7058 2.7269 2.7489
2.7705 2.7951 2.8169 2.8400 2.8647 2.8895 2.9143 2.9396 2.9665 2.9946
3.0233 3.0522 3.0831 3.1146 3.1481 3.1826 3.2168 3.2521 3.2879 3.3222
3.3554 3.3875 3.4171 3.4442 3.4676 3.4872 3.5024 3.5126 3.5168 3.5156
3.5079 3.4947 3.4751 3.4489 3.4174 3.3808 3.3405 3.2973 3.2514 3.2022
3.1513 3.0969 3.0396 2.9794 2.9166 2.8524 2.7868 2.7229 2.6610 2.6021
2.5459 2.4923 2.4425 2.3956 2.3520 2.3109 2.2730 2.2379 2.2052 2.1746
2.1465 2.1203 2.0963 2.0744 2.0540 2.0351 2.0177 2.0016 1.9873 1.9745
1.9626 1.9512 1.9408 1.9316 1.9234 1.9160 1.9097 1.9033 1.8984 1.8937
1.8900 1.8865 1.8836 1.8814 1.8795 1.8784 1.8776 1.8773 1.8778 1.8784
1.8798 1.8814 1.8835 1.8862 1.8891 1.8930 1.8967 1.9012 1.9065 1.9122
1.9181 1.9242 1.9310 1.9383 1.9460 1.9544 1.9632 1.9724 1.9816 1.9913
2.0013 2.0115 2.0220 2.0327 2.0432 2.0526 2.0613 2.0663 2.0692 2.0669
2.0578 2.0410 2.0171 1.9865 1.9518 1.9145 1.8767 1.8390 1.8040 1.7720
1.7416 1.7127 1.6777 1.6381 1.5866 1.5230 1.4447 1.3582 1.2677 1.1807
1.1017 1.0290 0.9631 0.9042 0.8503 0.8056 0.7652 0.7292 0.6939 0.6646
0.6382 0.6122 0.5868 0.5651 0.5437 0.5246 0.5075 0.4920 0.4791 0.4658
0.4522 0.4406 0.4277 0.4135 0.4015 0.3901 0.3794 0.3734 0.3650 0.3563
0.3508 0.3473 0.3400 0.3313 0.3267 0.3175 0.3092 0.3067 0.2978 0.2974
0.2912 0.2902 0.2892 0.2873 0.2868 0.2856 0.2828 0.2814 0.2807 0.2799
0.2789 0.2770 0.2760 0.2750 0.2738 0.2710 0.2676 0.2604 0.2519 0.2290
0.2089 0.1633 0.1017 0.0456 0.01600 0.00530 0.00020 0.00010 0.00005 0
];
    rn_InGaAs = interp1(realn_InGaAs(1,:), realn_InGaAs(2,:), lambda,
'pchip');
    in_InGaAs = j*interp1(imagn_InGaAs(1,:), imagn_InGaAs(2,:), lambda,
'pchip');
    x = rn_InGaAs+in_InGaAs;
end
```

```
if mat=='i1'
    % In.1Ga.9As
    realn_In10GaAs(1,:) = 1e-9*[300 305 310 315 320 325 330 335 340 345
350 355 360 365 370 375 380 385 390 395 400 405 410 415 420 425 430 435
440 445 450 455 460 465 470 475 480 485 490 495 500 505 510 515 520 525
530 535 540 545 550 555 560 565 570 575 580 585 590 595 600 605 610 615
620 625 630 635 640 645 650 655 660 665 670 675 680 685 690 695 700 705
710 715 720 725 730 735 740 745 750 755 760 765 770 775 780 785 790 795
800 805 810 815 820 825 830 835 840 845 850 855 860 865 870 875 880 885
890 895 900 905 910 915 920 925 930 935 940 945 950 955 960 965 970 975
980 985 990 995 1000 1005 1010 1015 1020 1025 1030 1035 1040 1045 1050
1055 1060 1065 1070 1075 1080 1085 1090 1095 1100 1105 1110 1115 1120
1125 1130 1135 1140 1145 1150 1155 1160 1165 1170 1175 1180 1185 1190
1195 1200];
    realn_In10GaAs(2,:) = [3.7968 3.7296 3.6687 3.6161 3.5776 3.5504
3.53 3.5146 3.5143 3.5179 3.5247 3.537 3.5566 3.5831 3.6146 3.6544
3.709 3.7812 3.8631 3.9751 4.0845 4.1911 4.2743 4.32 4.3811 4.4661
4.6169 4.7739 4.9217 4.9771 4.9453 4.8917 4.8257 4.7466 4.6809 4.6222
4.5684 4.5192 4.4696 4.4189 4.3762 4.3354 4.3014 4.2678 4.2347 4.2018
4.175 4.1514 4.1278 4.1056 4.0837 4.0625 4.0443 4.026 4.0079 3.9906
3.9734 3.9562 3.943 3.931 3.919 3.907 3.8944 3.8818 3.8691 3.8565 3.846
3.8354 3.8249 3.8144 3.8053 3.7974 3.7896 3.7817 3.7739 3.7677 3.7622
3.7568 3.7513 3.7458 3.7408 3.7363 3.7318 3.7272 3.7227 3.7182 3.7134
3.7073 3.7011 3.695 3.6888 3.6827 3.6765 3.6735 3.6707 3.6679 3.665
3.6622 3.6594 3.6567 3.6543 3.652 3.6497 3.6474 3.6451 3.6428 3.6405
3.6381 3.6358 3.63 3.63 3.63 3.63 3.63 3.63 3.63 3.63 3.63 3.63 3.63
3.63 3.63 3.63 3.63 3.63 3.63 3.63 3.63 3.63 3.63 3.63 3.63 3.63 3.63
3.63 3.63 3.63 3.63 3.63 3.63 3.63 3.63 3.63 3.63 3.63 3.63 3.63 3.63
3.63 3.63 3.63 3.63 3.63 3.63 3.63 3.63 3.63 3.63 3.63 3.63 3.63 3.63
3.63 3.63 3.63 3.63 3.63 3.63 3.63 3.63 3.63 3.63 3.63 3.63 3.63 3.63
3.63 3.63 3.63 3.63 3.63];
    imagn_In10GaAs(1,:) = 1e-9*[300 305 310 315 320 325 330 335 340 345
350 355 360 365 370 375 380 385 390 395 400 405 410 415 420 425 430 435
440 445 450 455 460 465 470 475 480 485 490 495 500 505 510 515 520 525
530 535 540 545 550 555 560 565 570 575 580 585 590 595 600 605 610 615
620 625 630 635 640 645 650 655 660 665 670 675 680 685 690 695 700 705
710 715 720 725 730 735 740 745 750 755 760 765 770 775 780 785 790 795
800 805 810 815 820 825 830 835 840 845 850 855 860 865 870 875 880 885
890 895 900 905 910 915 920 925 930 935 940 945 950 955 960 965 970 975
980 985 990 995 1000 1005 1010 1015 1020 1025 1030 1035 1040 1045 1050
1055 1060 1065 1070 1075 1080 1085 1090 1095 1100 1105 1110 1115 1120
1125 1130 1135 1140 1145 1150 1155 1160 1165 1170 1175 1180 1185 1190
1195 1200];
    imagn_In10GaAs(2,:) = [2.0142 1.9498 1.9128 1.8941 1.8761 1.8706
1.8745 1.8828 1.8908 1.9029 1.9185 1.9428 1.9611 1.975 2.0031 2.0295
2.0486 2.0715 2.0985 2.1106 2.1171 2.0734 2.0236 1.9699 1.9389 1.9102
1.892 1.8757 1.7725 1.5791 1.3879 1.1745 1.0397 0.9196 0.8324 0.7587
0.6943 0.6419 0.6037 0.5673 0.5353 0.5034 0.4805 0.4614 0.4422 0.4261
0.4116 0.3972 0.3831 0.3696 0.356 0.3425 0.3325 0.323 0.3135 0.3048
0.2995 0.2941 0.2888 0.2835 0.2759 0.2676 0.2593 0.2511 0.2447 0.2401
0.2355 0.2309 0.2263 0.2226 0.2203 0.2179 0.2155 0.2132 0.2102 0.2063
0.2024 0.1985 0.1946 0.1907 0.1875 0.1855 0.1835 0.1815 0.1795 0.1775
0.1738 0.1683 0.1628 0.1573 0.1518 0.1463 0.1411 0.1396 0.1381 0.1366
```

```
0.1351 0.1336 0.1321 0.1306 0.1294 0.1294 0.1294 0.1294 0.1294 0.1294
0.1294 0.1294 0.1294 0.129 0.129 0.129 0.129 0.129 0.129 0.129 0.129
0.129 0.129 0.129 0.129 0.129 0.129 0.129 0.129 0.129 0.129 0.129 0.129
0.129 0.129 0.129 0.129 0.129 0.129 0.129 0.129 0.129 0.129 0.129 0.129
0.129 0.129 0.129 0.129 0.129 0.129 0.129 0.129 0.129 0.129 0.129 0.129
0.129 0.129 0.129 0.129 0.129 0.129 0.129 0.129 0.129 0.129 0.129 0.129
0.129 0.129 0.129 0.129 0.129 0.129 0.129 0.129 0.129 0.129 0.129 0.129
0.129 0.129 0.129 0.129 ];
    rn_In10GaAs = interp1(realn_In10GaAs(1,:), realn_In10GaAs(2,:),
lambda, 'pchip');
    in_In10GaAs = j*interp1(imagn_In10GaAs(1,:), imagn_In10GaAs(2,:),
lambda, 'pchip');
    x = rn_In10GaAs+in_In10GaAs;
end

if mat=='i2'
    % In.2Ga.8As
    realn_In20GaAs(1,:) = 1e-9*[300 305 310 315 320 325 330 335 340 345
350 355 360 365 370 375 380 385 390 395 400 405 410 415 420 425 430 435
440 445 450 455 460 465 470 475 480 485 490 495 500 505 510 515 520 525
530 535 540 545 550 555 560 565 570 575 580 585 590 595 600 605 610 615
620 625 630 635 640 645 650 655 660 665 670 675 680 685 690 695 700 705
710 715 720 725 730 735 740 745 750 755 760 765 770 775 780 785 790 795
800 805 810 815 820 825 830 835 840 845 850 855 860 865 870 875 880 885
890 895 900 905 910 915 920 925 930 935 940 945 950 955 960 965 970 975
980 985 990 995 1000 1005 1010 1015 1020 1025 1030 1035 1040 1045 1050
1055 1060 1065 1070 1075 1080 1085 1090 1095 1100 1105 1110 1115 1120
1125 1130 1135 1140 1145 1150 1155 1160 1165 1170 1175 1180 1185 1190
1195 1200];
    realn_In20GaAs(2,:) = [3.7233 3.6604 3.609 3.551 3.5172 3.4845
3.4656 3.4544 3.4477 3.4412 3.4454 3.4581 3.464 3.481 3.5072 3.5439
3.585 3.6318 3.6831 3.7707 3.8583 3.9509 4.0286 4.0801 4.1215 4.1653
4.2455 4.4025 4.5625 4.7207 4.8182 4.8615 4.8355 4.7982 4.7416 4.68
4.6194 4.5599 4.5018 4.4557 4.4141 4.3738 4.3337 4.2951 4.2565 4.2194
4.1823 4.1589 4.1361 4.112 4.0865 4.0611 4.0393 4.0181 3.997 3.9786
3.9615 3.9444 3.9276 3.9115 3.8953 3.8792 3.8659 3.8532 3.8405 3.828
3.8174 3.8069 3.7963 3.7858 3.7767 3.7689 3.761 3.7532 3.7453 3.7379
3.7306 3.7233 3.716 3.7087 3.7017 3.695 3.6882 3.6815 3.6748 3.668
3.6633 3.6592 3.655 3.6508 3.6467 3.6425 3.6383 3.6354 3.6326 3.6298
3.6269 3.6241 3.6213 3.6188 3.6177 3.6165 3.6153 3.6142 3.613 3.6119
3.6107 3.6095 3.6084 3.6072 3.6061 3.6049 3.6038 3.6026 3.6014 3.6003
3.5991 3.598 3.5968 3.5956 3.5945 3.5933 3.5922 3.591 3.5899 3.5887
3.5875 3.5864 3.5852 3.5841 3.5829 3.5817 3.5806 3.5794 3.5783 3.5771
3.576 3.5748 3.5736 3.5725 3.5713 3.5702 3.569 3.5678 3.5667 3.5655
3.5644 3.5632 3.5621 3.5609 3.5597 3.5586 3.5574 3.5563 3.5551 3.5539
3.5528 3.5516 3.5505 3.5493 3.5482 3.547 3.5458 3.5447 3.5435 3.5424
3.5412 3.54 3.5389 3.5377 3.5366 3.5354 3.5343 3.5331 3.5319 3.5308
3.5296 3.5285 3.5273 3.5261 3.525];
    imagn_In20GaAs(1,:) = 1e-9*[300 305 310 315 320 325 330 335 340 345
350 355 360 365 370 375 380 385 390 395 400 405 410 415 420 425 430 435
440 445 450 455 460 465 470 475 480 485 490 495 500 505 510 515 520 525
530 535 540 545 550 555 560 565 570 575 580 585 590 595 600 605 610 615
```

```
620 625 630 635 640 645 650 655 660 665 670 675 680 685 690 695 700 705
710 715 720 725 730 735 740 745 750 755 760 765 770 775 780 785 790 795
800 805 810 815 820 825 830 835 840 845 850 855 860 865 870 875 880 885
890 895 900 905 910 915 920 925 930 935 940 945 950 955 960 965 970 975
980 985 990 995 1000 1005 1010 1015 1020 1025 1030 1035 1040 1045 1050
1055 1060 1065 1070 1075 1080 1085 1090 1095 1100 1105 1110 1115 1120
1125 1130 1135 1140 1145 1150 1155 1160 1165 1170 1175 1180 1185 1190
1195 1200];
    imagn_In20GaAs(2,:) = [2.0155 1.9448 1.9009 1.8766 1.857 1.8368
1.8353 1.8364 1.846 1.8541 1.8653 1.881 1.8961 1.9139 1.9353 1.9499
1.9621 1.9866 2.0147 2.0394 2.0462 2.0341 2.0069 1.9497 1.935 1.9299
1.9386 1.9688 1.9584 1.8662 1.745 1.5772 1.3902 1.2241 1.1161 0.9966
0.9047 0.8143 0.7416 0.6866 0.6433 0.6078 0.5772 0.5502 0.526 0.5033
0.482 0.4631 0.4473 0.4336 0.4208 0.4077 0.3942 0.381 0.3688 0.3583
0.3489 0.3402 0.3319 0.3237 0.3156 0.3079 0.3006 0.2941 0.2883 0.2829
0.278 0.2732 0.2685 0.2636 0.2588 0.2543 0.2503 0.2471 0.2447 0.2428
0.2411 0.2395 0.2376 0.2353 0.2321 0.2282 0.2239 0.2194 0.215 0.2112
0.2076 0.2043 0.201 0.1978 0.1945 0.1913 0.188 0.1845 0.1807 0.1769
0.1733 0.1699 0.1669 0.1646 0.1628 0.1612 0.1597 0.1584 0.1572 0.156
0.1548 0.1536 0.1523 0.1511 0.1498 0.1485 0.1473 0.1461 0.1449 0.1437
0.1425 0.1413 0.1402 0.139 0.1379 0.1368 0.1357 0.1347 0.1336 0.1326
0.1316 0.1306 0.1297 0.1288 0.1278 0.1269 0.1261 0.1252 0.1244 0.1236
0.1228 0.1221 0.1213 0.1206 0.12 0.1193 0.1187 0.1181 0.1175 0.117
0.1165 0.116 0.1155 0.1151 0.1147 0.1144 0.114 0.1137 0.1135 0.1132
0.113 0.1128 0.1127 0.1126 0.1125 0.1125 0.1125 0.1125 0.1126 0.1127
0.1128 0.113 0.1132 0.1135 0.1138 0.1141 0.1145 0.1149 0.1153 0.1158
0.1164 0.1169 0.1176 0.1182 0.1189 ];
    rn_In20GaAs = interp1(realn_In20GaAs(1,:), realn_In20GaAs(2,:),
lambda, 'pchip');
    in_In20GaAs = j*interp1(imagn_In20GaAs(1,:), imagn_In20GaAs(2,:),
lambda, 'pchip');
    x = rn_In20GaAs+in_In20GaAs;
end

if mat=='bt'
    % In0.3Ga70As
    realn_InGaAs(1,:) = 1e-9*[300.000 310.000 320.000 330.000 340.000
350.000 360.000 370.000 380.000 390.000 400.000 410.000 420.000 430.000
440.000 450.000 460.000 470.000 480.000 490.000 500.000 510.000 520.000
530.000 540.000 550.000 560.000 570.000 580.000 590.000 600.000 610.000
620.000 630.000 640.000 650.000 660.000 670.000 680.000 690.000 700.000
710.000 720.000 730.000 740.000 750.000 760.000 770.000 780.000 790.000
800.000 810.000 820.000 830.000 840.000 850.000 860.000 870.000 880.000
890.000 900.000 910.000 920.000 930.000 940.000 950.000 960.000 970.000
980.000 990.000 1000.000 1010.000 1020.000 1030.000 1040.000 1050.000
1060.000 1070.000 1080.000 1090.000 1100.000 1110.000 1120.000 1130.000
1140.000 1150.000 1160.000 1170.000 1180.000 1190.000 1200.000 1210.000
1220.000 1230.000 1240.000 1250.000 1260.000 1270.000 1280.000 1290.000
1300.000 ];
    realn_InGaAs(2,:) = [3.545 3.464 3.399 3.355 3.330 3.322 3.326
3.345 3.377 3.425 3.492 3.584 3.712 3.885 4.062 4.187 4.280 4.387 4.526
4.610 4.600 4.544 4.476 4.408 4.345 4.289 4.239 4.195 4.154 4.116 4.082
```

```
4.051 4.023 3.997 3.971 3.948 3.927 3.906 3.889 3.872 3.857 3.842 3.829
3.815 3.804 3.793 3.781 3.769 3.758 3.749 3.739 3.730 3.723 3.720 3.720
3.720 3.719 3.713 3.703 3.695 3.687 3.679 3.671 3.662 3.654 3.645 3.637
3.628 3.619 3.610 3.602 3.594 3.586 3.579 3.573 3.567 3.562 3.557 3.553
3.548 3.544 3.540 3.537 3.533 3.529 3.526 3.523 3.520 3.516 3.513 3.511
3.508 3.505 3.503 3.500 3.498 3.495 3.493 3.490 3.488 3.486 ];
    imagn_InGaAs(1,:) = 1e-9*[300.000 310.000 320.000 330.000 340.000
350.000 360.000 370.000 380.000 390.000 400.000 410.000 420.000 430.000
440.000 450.000 460.000 470.000 480.000 490.000 500.000 510.000 520.000
530.000 540.000 550.000 560.000 570.000 580.000 590.000 600.000 610.000
620.000 630.000 640.000 650.000 660.000 670.000 680.000 690.000 700.000
710.000 720.000 730.000 740.000 750.000 760.000 770.000 780.000 790.000
800.000 810.000 820.000 830.000 840.000 850.000 860.000 870.000 880.000
890.000 900.000 910.000 920.000 930.000 940.000 950.000 960.000 970.000
980.000 990.000 1000.000 1010.000 1020.000 1030.000 1040.000 1050.000
1060.000 1070.000 1080.000 1090.000 1100.000 1110.000 1120.000 1130.000
1140.000 1150.000 1160.000 1170.000 1180.000 1190.000 1200.000 1210.000
1220.000 1230.000 1240.000 1250.000 1260.000 1270.000 1280.000 1290.000
1300.000 ];
    imagn_InGaAs(2,:) = [2.166 1.994 1.899 1.849 1.824 1.817 1.823
1.839 1.863 1.895 1.931 1.971 2.004 2.000 1.923 1.808 1.705 1.614 1.473
1.254 1.041 0.876 0.755 0.668 0.599 0.545 0.499 0.460 0.430 0.407 0.384
0.362 0.341 0.323 0.312 0.299 0.291 0.284 0.272 0.266 0.253 0.248 0.238
0.237 0.231 0.230 0.228 0.227 0.226 0.224 0.221 0.216 0.211 0.206 0.199
0.193 0.187 0.181 0.176 0.172 0.168 0.164 0.161 0.158 0.154 0.151 0.149
0.145 0.142 0.140 0.137 0.134 0.131 0.129 0.126 0.123 0.121 0.118 0.116
0.113 0.111 0.108 0.106 0.104 0.102 0.099 0.096 0.093 0.088 0.081 0.073
0.061 0.048 0.036 0.027 0.008 1.94623E-05 1.9618E-08 1.97737E-11 0 0 ];
    rn_InGaAs = interp1(realn_InGaAs(1,:), realn_InGaAs(2,:), lambda,
'pchip');
    in_InGaAs = j*interp1(imagn_InGaAs(1,:), imagn_InGaAs(2,:), lambda,
'pchip');
    x = rn_InGaAs+in_InGaAs;
end

if mat=='gp'
    % In0.5 Ga0.5 P
    realn_InGaP(1,:) = 1e-9*[249.9 250.4 250.9 251.4 251.9 252.4 253.0
253.5 254.0 254.5 255.0 255.6 256.1 256.6 257.1 257.7 258.2 258.8 259.3
259.8 260.4 260.9 261.5 262.0 262.6 263.1 263.7 264.3 264.8 265.4 266.0
266.5 267.1 267.7 268.3 268.8 269.4 270.0 270.6 271.2 271.8 272.4 273.0
273.6 274.2 274.8 275.4 276.0 276.6 277.2 277.9 278.5 279.1 279.7 280.4
281.0 281.6 282.3 282.9 283.6 284.2 284.9 285.5 286.2 286.8 287.5 288.2
288.8 289.5 290.2 290.9 291.5 292.2 292.9 293.6 294.3 295.0 295.7 296.4
297.1 297.8 298.6 299.3 300.0 300.7 301.5 302.2 302.9 303.7 304.4 305.2
305.9 306.7 307.4 308.2 309.0 309.7 310.5 311.3 312.1 312.8 313.6 314.4
315.2 316.0 316.8 317.6 318.5 319.3 320.1 320.9 321.8 322.6 323.4 324.3
325.1 326.0 326.8 327.7 328.6 329.4 330.3 331.2 332.1 333.0 333.9 334.8
335.7 336.6 337.5 338.4 339.3 340.3 341.2 342.1 343.1 344.0 345.0 346.0
346.9 347.9 348.9 349.9 350.8 351.8 352.8 353.8 354.9 355.9 356.9 357.9
359.0 360.0 361.0 362.1 363.2 364.2 365.3 366.4 367.5 368.5 369.6 370.7
371.9 373.0 374.1 375.2 376.4 377.5 378.7 379.8 381.0 382.2 383.3 384.5
```

```
385.7 386.9 388.1 389.3 390.6 391.8 393.0 394.3 395.5 396.8 398.1 399.4
400.6 401.9 403.2 404.6 405.9 407.2 408.6 409.9 411.3 412.6 414.0 415.4
416.8 418.2 419.6 421.0 422.4 423.9 425.3 426.8 428.3 429.8 431.3 432.8
434.3 435.8 437.3 438.9 440.4 442.0 443.6 445.2 446.8 448.4 450.0 451.6
453.3 454.9 456.6 458.3 460.0 461.7 463.4 465.2 466.9 468.7 470.5 472.2
474.0 475.9 477.7 479.5 481.4 483.3 485.2 487.1 489.0 490.9 492.9 494.8
496.8 498.8 500.8 502.8 504.9 506.9 509.0 511.1 513.2 515.4 517.5 519.7
521.8 524.1 526.3 528.5 530.8 533.0 535.3 537.7 540.0 542.4 544.7 547.1
549.6 552.0 554.5 557.0 559.5 562.0 564.5 567.1 569.7 572.4 575.0 577.7
580.4 583.1 585.8 588.6 591.4 594.3 597.1 600.0 602.9 605.9 608.8 611.8
614.9 617.9 621.0 624.1 627.3 630.5 633.7 636.9 640.2 643.5 646.9 650.3
653.7 657.1 660.6 664.2 667.7 671.4 675.0 678.7 682.4 686.2 690.0 693.9
697.8 701.7 705.7 709.7 713.8 717.9 722.1 726.3 730.6 734.9 739.3 743.7
748.2 752.7 757.3 762.0 766.7 771.4 776.3 781.1 786.1 791.1 796.2 801.3
806.5 811.8 817.1 822.5 828.0 833.6 839.2 844.9 850.7 856.6 862.5 868.5
874.6 880.9 887.1 893.5 900.0 906.6 913.2 920.0 926.9 933.8 940.9 948.1
955.4 962.8 970.3 978.0 985.7 993.6 1001.6 1009.8 1018.0 1026.4 1035.0
1043.7 1052.5 1061.5 1070.7 1080.0 1089.5 1099.1 1108.9 1118.9 1129.1
1139.4 1150.0 1160.7 1171.7 1182.9 1194.2 1205.8 1217.6 1229.7 1242.0
1254.5 1267.3 1280.4 1293.8 1307.4 1321.3 1335.5 1350.0 1364.8 1380.0
1395.5 1411.4 1427.6 1444.2 1461.2 1478.6 1496.4 1514.6 1533.3 1552.5
1572.2 1592.3 1613.0 1634.2 1656.0 1678.4 1701.4 1725.0 1749.3 1774.3
1800.0 1826.5 1853.7 1881.8 1910.8 1940.6 1971.4 2003.2 2036.1 2070.0
2105.1 2141.4 2178.9 2217.9 2258.2 2300.0];
    realn_InGaP(2,:) = [2.745  2.817  2.911  2.997  3.071  3.138  3.187
3.224  3.257  3.287  3.318  3.361  3.406  3.455  3.506  3.551  3.591
3.626  3.651  3.676  3.703  3.725  3.747  3.769  3.783  3.798  3.819
3.840  3.861  3.881  3.898  3.911  3.920  3.924  3.926  3.927  3.927
3.927  3.927  3.927  3.927  3.927  3.927  3.927  3.927  3.927  3.927
3.927  3.926  3.925  3.922  3.917  3.907  3.896  3.888  3.881  3.875
3.870  3.864  3.860  3.857  3.852  3.846  3.837  3.828  3.819  3.809
3.799  3.790  3.781  3.772  3.763  3.755  3.750  3.745  3.742  3.739
3.736  3.733  3.729  3.726  3.722  3.719  3.715  3.713  3.710  3.709
3.709  3.709  3.709  3.709  3.709  3.709  3.709  3.709  3.709  3.709
3.709  3.709  3.709  3.709  3.709  3.709  3.709  3.709  3.709  3.709
3.709  3.709  3.709  3.709  3.709  3.709  3.709  3.709  3.709  3.709
3.709  3.709  3.709  3.709  3.709  3.709  3.709  3.709  3.709  3.709
3.711  3.716  3.724  3.733  3.740  3.749  3.759  3.768  3.779  3.790
3.801  3.813  3.828  3.841  3.856  3.871  3.888  3.906  3.927  3.947
3.965  3.985  4.007  4.029  4.056  4.091  4.129  4.165  4.195  4.223
4.250  4.272  4.292  4.314  4.336  4.375  4.420  4.462  4.502  4.540
4.568  4.584  4.597  4.610  4.621  4.628  4.635  4.641  4.645  4.650
4.650  4.648  4.643  4.639  4.634  4.630  4.626  4.621  4.615  4.608
4.593  4.574  4.555  4.536  4.515  4.496  4.477  4.456  4.441  4.434
4.426  4.414  4.400  4.380  4.359  4.341  4.320  4.301  4.282  4.263
4.241  4.224  4.216  4.210  4.201  4.192  4.182  4.172  4.161  4.150
4.137  4.120  4.107  4.095  4.083  4.072  4.061  4.049  4.037  4.023
4.001  3.981  3.968  3.959  3.953  3.947  3.940  3.933  3.926  3.918
3.909  3.899  3.888  3.877  3.867  3.858  3.855  3.855  3.855  3.850
3.840  3.829  3.818  3.806  3.794  3.783  3.773  3.761  3.751  3.743
3.735  3.727  3.721  3.715  3.709  3.703  3.698  3.693  3.687  3.682
3.676  3.670  3.663  3.656  3.649  3.642  3.637  3.633  3.631  3.626
3.623  3.620  3.615  3.612  3.608  3.605  3.602  3.601  3.600  3.600
```

```
3.600  3.600  3.600  3.600  3.600  3.600  3.600  3.598  3.596  3.593
3.589  3.584  3.580  3.576  3.570  3.564  3.555  3.543  3.523  3.503
3.493  3.485  3.478  3.472  3.466  3.459  3.452  3.441  3.429  3.418
3.411  3.405  3.399  3.394  3.389  3.386  3.382  3.379  3.375  3.369
3.365  3.360  3.354  3.348  3.340  3.332  3.322  3.314  3.309  3.304
3.301  3.296  3.292  3.287  3.282  3.278  3.274  3.272  3.268  3.264
3.259  3.254  3.250  3.244  3.241  3.238  3.236  3.236  3.236  3.236
3.235  3.234  3.232  3.230  3.226  3.220  3.215  3.208  3.203  3.199
3.195  3.191  3.186  3.182  3.178  3.173  3.169  3.166  3.164  3.164
3.164  3.164  3.164  3.164  3.164  3.164  3.163  3.161  3.157  3.153
3.149  3.143  3.138  3.135  3.131  3.128  3.127  3.127  3.127  3.127
3.127  3.127  3.127  3.127  3.126  3.125  3.123  3.119  3.110  3.096
3.091  3.091  3.091  3.091  3.091  3.091  3.091  3.091  3.091  3.090
3.089  3.088  3.087  3.085  3.084  3.083  3.082  3.080  3.078  3.077
3.076  3.075  3.073  3.072  3.071  3.070  3.068  3.066  3.066  3.064
3.062  3.061  3.060  3.059  3.057  3.055  3.055];
    imagn_InGaP(1,:) = 1e-9*[249.9 250.4 250.9 251.4 251.9 252.4 253.0
253.5 254.0 254.5 255.0 255.6 256.1 256.6 257.1 257.7 258.2 258.8 259.3
259.8 260.4 260.9 261.5 262.0 262.6 263.1 263.7 264.3 264.8 265.4 266.0
266.5 267.1 267.7 268.3 268.8 269.4 270.0 270.6 271.2 271.8 272.4 273.0
273.6 274.2 274.8 275.4 276.0 276.6 277.2 277.9 278.5 279.1 279.7 280.4
281.0 281.6 282.3 282.9 283.6 284.2 284.9 285.5 286.2 286.8 287.5 288.2
288.8 289.5 290.2 290.9 291.5 292.2 292.9 293.6 294.3 295.0 295.7 296.4
297.1 297.8 298.6 299.3 300.0 300.7 301.5 302.2 302.9 303.7 304.4 305.2
305.9 306.7 307.4 308.2 309.0 309.7 310.5 311.3 312.1 312.8 313.6 314.4
315.2 316.0 316.8 317.6 318.5 319.3 320.1 320.9 321.8 322.6 323.4 324.3
325.1 326.0 326.8 327.7 328.6 329.4 330.3 331.2 332.1 333.0 333.9 334.8
335.7 336.6 337.5 338.4 339.3 340.3 341.2 342.1 343.1 344.0 345.0 346.0
346.9 347.9 348.9 349.9 350.8 351.8 352.8 353.8 354.9 355.9 356.9 357.9
359.0 360.0 361.0 362.1 363.2 364.2 365.3 366.4 367.5 368.5 369.6 370.7
371.9 373.0 374.1 375.2 376.4 377.5 378.7 379.8 381.0 382.2 383.3 384.5
385.7 386.9 388.1 389.3 390.6 391.8 393.0 394.3 395.5 396.8 398.1 399.4
400.6 401.9 403.2 404.6 405.9 407.2 408.6 409.9 411.3 412.6 414.0 415.4
416.8 418.2 419.6 421.0 422.4 423.9 425.3 426.8 428.3 429.8 431.3 432.8
434.3 435.8 437.3 438.9 440.4 442.0 443.6 445.2 446.8 448.4 450.0 451.6
453.3 454.9 456.6 458.3 460.0 461.7 463.4 465.2 466.9 468.7 470.5 472.2
474.0 475.9 477.7 479.5 481.4 483.3 485.2 487.1 489.0 490.9 492.9 494.8
496.8 498.8 500.8 502.8 504.9 506.9 509.0 511.1 513.2 515.4 517.5 519.7
521.8 524.1 526.3 528.5 530.8 533.0 535.3 537.7 540.0 542.4 544.7 547.1
549.6 552.0 554.5 557.0 559.5 562.0 564.5 567.1 569.7 572.4 575.0 577.7
580.4 583.1 585.8 588.6 591.4 594.3 597.1 600.0 602.9 605.9 608.8 611.8
614.9 617.9 621.0 624.1 627.3 630.5 633.7 636.9 640.2 643.5 646.9 650.3
653.7 657.1 660.6 664.2 667.7 671.4 675.0 678.7 682.4 686.2 690.0 693.9
697.8 701.7 705.7 709.7 713.8 717.9 722.1 726.3 730.6 734.9 739.3 743.7
748.2 752.7 757.3 762.0 766.7 771.4 776.3 781.1 786.1 791.1 796.2 801.3
806.5 811.8 817.1 822.5 828.0 833.6 839.2 844.9 850.7 856.6 862.5 868.5
874.6 880.9 887.1 893.5 900.0 906.6 913.2 920.0 926.9 933.8 940.9 948.1
955.4 962.8 970.3 978.0 985.7 993.6 1001.6 1009.8 1018.0 1026.4 1035.0
1043.7 1052.5 1061.5 1070.7 1080.0 1089.5 1099.1 1108.9 1118.9 1129.1
1139.4 1150.0 1160.7 1171.7 1182.9 1194.2 1205.8 1217.6 1229.7 1242.0
1254.5 1267.3 1280.4 1293.8 1307.4 1321.3 1335.5 1350.0 1364.8 1380.0
1395.5 1411.4 1427.6 1444.2 1461.2 1478.6 1496.4 1514.6 1533.3 1552.5
1572.2 1592.3 1613.0 1634.2 1656.0 1678.4 1701.4 1725.0 1749.3 1774.3
```

```
1800.0 1826.5 1853.7 1881.8 1910.8 1940.6 1971.4 2003.2 2036.1 2070.0
2105.1 2141.4 2178.9 2217.9 2258.2 2300.0];
    imagn_InGaP(2,:) = [3.760 3.753 3.746 3.739 3.730 3.720 3.710 3.699
3.684 3.669 3.654 3.634 3.615 3.591 3.557 3.512 3.459 3.404 3.360 3.328
3.304 3.277 3.252 3.227 3.200 3.169 3.139 3.103 3.067 3.031 2.995 2.963
2.935 2.906 2.875 2.847 2.818 2.784 2.749 2.712 2.675 2.641 2.607 2.578
2.552 2.523 2.499 2.477 2.458 2.439 2.419 2.402 2.385 2.365 2.347 2.332
2.318 2.304 2.290 2.274 2.258 2.243 2.228 2.217 2.210 2.204 2.196 2.186
2.174 2.160 2.146 2.132 2.118 2.104 2.091 2.077 2.065 2.055 2.047 2.043
2.040 2.037 2.033 2.030 2.025 2.021 2.015 2.009 2.002 1.994 1.986 1.981
1.974 1.969 1.965 1.964 1.964 1.963 1.961 1.958 1.954 1.951 1.947 1.943
1.941 1.940 1.938 1.937 1.936 1.934 1.933 1.931 1.929 1.926 1.923 1.919
1.915 1.912 1.910 1.909 1.909 1.909 1.909 1.909 1.909 1.909 1.909 1.911
1.913 1.916 1.920 1.923 1.926 1.930 1.933 1.936 1.939 1.944 1.950 1.955
1.961 1.968 1.974 1.981 1.989 1.998 2.006 2.013 2.015 2.017 2.017 2.017
2.015 2.013 2.006 1.996 1.982 1.966 1.951 1.934 1.915 1.893 1.866 1.833
1.799 1.759 1.715 1.672 1.641 1.612 1.582 1.547 1.500 1.450 1.414 1.383
1.351 1.315 1.279 1.242 1.204 1.170 1.137 1.105 1.077 1.048 1.016 0.987
0.954 0.921 0.888 0.856 0.824 0.793 0.766 0.746 0.731 0.708 0.683 0.660
0.640 0.622 0.603 0.587 0.571 0.556 0.541 0.527 0.515 0.504 0.496 0.491
0.487 0.482 0.477 0.470 0.463 0.455 0.448 0.440 0.432 0.423 0.414 0.405
0.397 0.389 0.384 0.380 0.378 0.375 0.372 0.369 0.366 0.362 0.358 0.353
0.348 0.342 0.335 0.329 0.326 0.321 0.316 0.311 0.305 0.301 0.300 0.300
0.299 0.297 0.295 0.292 0.288 0.285 0.281 0.276 0.272 0.267 0.261 0.256
0.251 0.245 0.240 0.236 0.231 0.227 0.225 0.222 0.221 0.220 0.218 0.218
0.217 0.215 0.212 0.209 0.206 0.201 0.197 0.195 0.193 0.191 0.191 0.190
0.188 0.186 0.180 0.172 0.165 0.159 0.154 0.150 0.146 0.143 0.139 0.137
0.134 0.129 0.123 0.116 0.108 0.096 0.081 0.066 0.051 0.039 0.025 0.013
0.004 0.001 0.000 0.000 0.000 0.000 0.000 0.000 0.000 0.000 0.000 0.000
0.000 0.000 0.000 0.000 0.000 0.000 0.000 0.000 0.000 0.000 0.000 0.000
0.000 0.000 0.000 0.000 0.000 0.000 0.000 0.000 0.000 0.000 0.000 0.000
0.000 0.000 0.000 0.000 0.000 0.000 0.000 0.000 0.000 0.000 0.000 0.000
0.000 0.000 0.000 0.000 0.000 0.000 0.000 0.000 0.000 0.000 0.000 0.000
0.000 0.000 0.000 0.000 0.000 0.000 0.000 0.000 0.000 0.000 0.000 0.000
0.000 0.000 0.000 0.000 0.000 0.000 0.000 0.000 0.000 0.000 0.000 0.000
0.000 0.000 0.000 0.000 0.000 0.000 0.000 0.000 0.000 0.000 0.000 0.000
0.000 0.000 0.000 0.000 0.000 0.000 0.000 0.000 0.000 0.000 0.000 0.000
0.000 0.000 0.000 0.000 0.000 0.000 0.000 0.000 0.000 0.000 0.000 0.000
0.000 0.000 0.000 0.000 ];
    rn_InGaP = interp1(realn_InGaP(1,:), realn_InGaP(2,:), lambda,
'pchip');
    in_InGaP = j*interp1(imagn_InGaP(1,:), imagn_InGaP(2,:), lambda,
'pchip');
    x = rn_InGaP+in_InGaP;
end

if mat=='ti'
    % Ti
    realn_Ti(1,:) = 1e-9*[206.6 208.4 210.1 211.9 213.8 215.6 217.5
219.4 221.4 223.4 225.4 227.5 229.6 231.7 233.9 236.2 238.4 240.7 243.1
245.5 248.0 250.5 253.0 255.6 258.3 261.0 263.8 266.6 269.5 272.5 275.5
```

```
278.6 281.8 285.0 288.3 291.7 295.2 298.8 302.4 306.1 310.0 313.9 317.9
322.0 326.3 330.6 335.1 339.7 344.4 349.3 354.2 359.4 364.7 370.1 375.7
381.5 387.5 393.6 400.0 406.5 413.3 420.3 427.5 435.0 442.8 450.9 459.2
467.9 476.9 486.2 495.9 506.1 516.6 527.6 539.1 551.0 563.6 576.7 590.4
604.8 619.9 635.8 652.6 670.2 688.8 708.5 729.3 751.4 774.9 799.9 826.6
855.1 885.6 918.4 953.7 991.9 1033.2 1078.1 1127.1 1180.8 1239.9];
    realn_Ti(2,:) = [1.16 1.17 1.18 1.20 1.21 1.22 1.23 1.24 1.24 1.24
1.24 1.20 1.18 1.27 1.35 1.32 1.26 1.25 1.25 1.25 1.24 1.23 1.22 1.22
1.21 1.20 1.18 1.17 1.17 1.16 1.15 1.14 1.13 1.12 1.10 1.07 1.05 1.04
1.04 1.04 1.04 1.05 1.06 1.08 1.11 1.14 1.17 1.21 1.24 1.27 1.30 1.33
1.37 1.41 1.44 1.47 1.50 1.53 1.55 1.57 1.59 1.61 1.63 1.66 1.68 1.70
1.71 1.73 1.75 1.77 1.78 1.79 1.81 1.83 1.86 1.89 1.92 1.96 2.01 2.06
2.11 2.16 2.22 2.29 2.36 2.45 2.54 2.64 2.74 2.86 2.98 3.08 3.17 3.23
3.28 3.31 3.35 3.41 3.47 3.54 3.62];
    imagn_Ti(1,:) = 1e-9*[206.6 208.4 210.1 211.9 213.8 215.6 217.5
219.4 221.4 223.4 225.4 227.5 229.6 231.7 233.9 236.2 238.4 240.7 243.1
245.5 248.0 250.5 253.0 255.6 258.3 261.0 263.8 266.6 269.5 272.5 275.5
278.6 281.8 285.0 288.3 291.7 295.2 298.8 302.4 306.1 310.0 313.9 317.9
322.0 326.3 330.6 335.1 339.7 344.4 349.3 354.2 359.4 364.7 370.1 375.7
381.5 387.5 393.6 400.0 406.5 413.3 420.3 427.5 435.0 442.8 450.9 459.2
467.9 476.9 486.2 495.9 506.1 516.6 527.6 539.1 551.0 563.6 576.7 590.4
604.8 619.9 635.8 652.6 670.2 688.8 708.5 729.3 751.4 774.9 799.9 826.6
855.1 885.6 918.4 953.7 991.9 1033.2 1078.1 1127.1 1180.8 1239.9];
    imagn_Ti(2,:) = [1.21 1.22 1.22 1.22 1.22 1.22 1.21 1.21 1.21 1.20
1.19 1.17 1.15 1.18 1.21 1.21 1.20 1.20 1.20 1.20 1.21 1.22 1.22 1.22
1.23 1.24 1.25 1.26 1.28 1.30 1.31 1.32 1.33 1.35 1.37 1.40 1.44 1.48
1.53 1.57 1.61 1.67 1.73 1.78 1.83 1.87 1.90 1.93 1.96 1.99 2.01 2.04
2.06 2.08 2.09 2.11 2.12 2.14 2.15 2.16 2.17 2.19 2.21 2.23 2.25 2.27
2.29 2.31 2.34 2.36 2.39 2.43 2.47 2.51 2.56 2.61 2.67 2.72 2.77 2.82
2.88 2.93 2.99 3.05 3.11 3.17 3.23 3.27 3.30 3.32 3.32 3.30 3.28 3.26
3.25 3.27 3.30 3.35 3.40 3.46 3.52];
    rn_Ti = interp1(realn_Ti(1,:), realn_Ti(2,:), lambda, 'pchip');
    in_Ti = j*interp1(imagn_Ti(1,:), imagn_Ti(2,:), lambda, 'pchip');
    x = rn_Ti+in_Ti;

end

if mat=='cr'
    % Chromium
    realn_Cr(1,:) = 1e-9*[206.64 208.38 210.14 211.94 213.77 215.63
217.52 219.44 221.40 223.40 225.43 227.50 229.60 231.75 233.93 236.16
238.43 240.75 243.11 245.52 247.97 250.48 253.03 255.64 258.30 261.02
263.80 266.63 269.53 272.49 275.52 278.62 281.78 285.02 288.34 291.73
295.20 298.76 302.40 306.14 309.96 313.89 317.91 322.04 326.28 330.63
335.10 339.69 344.40 349.25 354.24 359.38 364.66 370.11 375.71 381.49
387.45 393.60 399.95 406.51 413.28 420.29 427.54 435.04 442.80 450.86
459.20 467.87 476.87 486.22 495.94 506.06 516.60 527.60 539.07 551.05
563.57 576.68 590.41 604.81 619.93 635.82 652.55 670.19 688.81 708.49
729.32 751.43 774.91 799.90 826.57 855.07 885.61 918.41 953.73 991.88
1033.21 1078.13 1127.14 1180.81 1239.85 2000];
    realn_Cr(2,:) = [1.460 1.458 1.460 1.465 1.470 1.472 1.470 1.461
1.450 1.440 1.430 1.420 1.410 1.400 1.390 1.379 1.370 1.364 1.360 1.359
```

```
1.360 1.364 1.370 1.376 1.380 1.380 1.380 1.383 1.390 1.410 1.430 1.436
1.440 1.448 1.460 1.479 1.500 1.520 1.540 1.559 1.580 1.605 1.630 1.651
1.670 1.689 1.710 1.738 1.770 1.808 1.840 1.852 1.860 1.878 1.900 1.924
1.950 1.979 2.010 2.043 2.080 2.123 2.170 2.218 2.270 2.331 2.400 2.476
2.560 2.655 2.750 2.829 2.910 3.013 3.110 3.178 3.220 3.225 3.210 3.188
3.160 3.129 3.100 3.076 3.060 3.054 3.060 3.079 3.110 3.158 3.210 3.251
3.290 3.327 3.370 3.433 3.500 3.564 3.620 3.661 3.680 3.680];
    imagn_Cr(1,:) = 1e-9*[206.64 208.38 210.14 211.94 213.77 215.63
217.52 219.44 221.40 223.40 225.43 227.50 229.60 231.75 233.93 236.16
238.43 240.75 243.11 245.52 247.97 250.48 253.03 255.64 258.30 261.02
263.80 266.63 269.53 272.49 275.52 278.62 281.78 285.02 288.34 291.73
295.20 298.76 302.40 306.14 309.96 313.89 317.91 322.04 326.28 330.63
335.10 339.69 344.40 349.25 354.24 359.38 364.66 370.11 375.71 381.49
387.45 393.60 399.95 406.51 413.28 420.29 427.54 435.04 442.80 450.86
459.20 467.87 476.87 486.22 495.94 506.06 516.60 527.60 539.07 551.05
563.57 576.68 590.41 604.81 619.93 635.82 652.55 670.19 688.81 708.49
729.32 751.43 774.91 799.90 826.57 855.07 885.61 918.41 953.73 991.88
1033.21 1078.13 1127.14 1180.81 1239.85 2000];
    imagn_Cr(2,:) = [1.710 1.717 1.720 1.721 1.720 1.719 1.720 1.724
1.730 1.734 1.740 1.749 1.760 1.769 1.780 1.794 1.810 1.829 1.850 1.874
1.900 1.925 1.950 1.975 2.000 2.026 2.050 2.070 2.090 2.114 2.140 2.165
2.190 2.214 2.240 2.270 2.300 2.326 2.350 2.375 2.400 2.425 2.450 2.475
2.500 2.526 2.550 2.570 2.590 2.615 2.640 2.661 2.680 2.699 2.720 2.743
2.770 2.808 2.850 2.889 2.930 2.975 3.020 3.061 3.100 3.140 3.180 3.223
3.260 3.283 3.300 3.318 3.330 3.333 3.330 3.326 3.320 3.309 3.300 3.297
3.300 3.313 3.330 3.350 3.370 3.385 3.400 3.419 3.440 3.460 3.480 3.500
3.520 3.541 3.560 3.573 3.580 3.579 3.580 3.591 3.620 3.620];
    rn_Cr = interp1(realn_Cr(1,:), realn_Cr(2,:), lambda, 'pchip');
    in_Cr = j*interp1(imagn_Cr(1,:), imagn_Cr(2,:), lambda, 'pchip');
    x = rn_Cr+in_Cr;
end

if mat=='mf'
    % Mgf2
    realn_MgF(1,:) = 1e-9*[300 310 320 330 340 350 360 370 380 390 400
410 420 430 440 450 460 470 480 490 500 510 520 530 540 550 560 570 580
590 600 610 620 630 640 650 660 670 680 690 700 710 720 730 740 750 760
770 780 790 800 810 820 830 840 850 860 870 880 890 900 910 920 930 940
950 960 970 980 990 1000 1010 1020 1030 1040 1050 1060 1070 1080 1090
1100 1110 1120 1130 1140 1150 1160 1170 1180 1190 1200 1210 1220 1230
1240 1250 1260 1270 1280 1290 1300 1310 1320 1330 1340 1350 1360 1370
1380 1390 1400 1410 1420 1430 1440 1450 1460 1470 1480 1490 1500 1510
1520 1530 1540 1550 1560 1570 1580 1590 1600 ];
    realn_MgF(2,:) = [1.41472 1.41307 1.41142 1.40977 1.40812 1.40647
1.40482 1.40317 1.40152 1.39987 1.39822 1.39657 1.39497 1.39345 1.39199
1.3906 1.38927 1.38799 1.38677 1.38561 1.3845 1.38344 1.38242 1.38145
1.38051 1.37963 1.37878 1.37797 1.37718 1.37644 1.37573 1.37504 1.37438
1.37375 1.37315 1.37257 1.37202 1.37148 1.37096 1.37046 1.36999 1.36954
1.36909 1.36866 1.36825 1.36786 1.36748 1.36711 1.36676 1.36642 1.36608
1.36577 1.36546 1.36516 1.36487 1.3646 1.36433 1.36406 1.36382 1.36357
1.36333 1.3631 1.36288 1.36266 1.36245 1.36225 1.36205 1.36186 1.36167
1.36149 1.36132 1.36115 1.36098 1.36082 1.36066 1.36051 1.36036 1.36022
```

```
1.36007 1.35994 1.3598 1.35967 1.35955 1.35942 1.3593 1.35919 1.35907
1.35896 1.35885 1.35875 1.35864 1.35854 1.35844 1.35834 1.35825 1.35816
1.35807 1.35798 1.35789 1.35781 1.35773 1.35765 1.35758 1.35749 1.35742
1.35735 1.35728 1.3572 1.35714 1.35707 1.35701 1.35694 1.35688 1.35681
1.35675 1.35669 1.35663 1.35658 1.35652 1.35647 1.35641 1.35636 1.35631
1.35626 1.3562 1.35616 1.35611 1.35606 1.35602 1.35597 1.35592];
    imagn_MgF(1,:) = 1e-9*[300 310 320 330 340 350 360 370 380 390 400
410 420 430 440 450 460 470 480 490 500 510 520 530 540 550 560 570 580
590 600 610 620 630 640 650 660 670 680 690 700 710 720 730 740 750 760
770 780 790 800 810 820 830 840 850 860 870 880 890 900 910 920 930 940
950 960 970 980 990 1000 1010 1020 1030 1040 1050 1060 1070 1080 1090
1100 1110 1120 1130 1140 1150 1160 1170 1180 1190 1200 1210 1220 1230
1240 1250 1260 1270 1280 1290 1300 1310 1320 1330 1340 1350 1360 1370
1380 1390 1400 1410 1420 1430 1440 1450 1460 1470 1480 1490 1500 1510
1520 1530 1540 1550 1560 1570 1580 1590 1600 ];
    imagn_MgF(2,:) = [0.007666217 0.006231196 0.005913826 0.001217208 0
0 0 0 0 0 0 0 0 0 0 0 0 0 0 0 0 0 0 0 0 0 0 0 0 0 0 0 0 0 0 0 0 0 0 0
0 0 0 0 0 0 0 0 0 0 0 0 0 0 0 0 0 0 0 0 0 0 0 0 0 0 0 0 0 0 0 0 0 0 0
0 0 0 0 0 0 0 0 0 0 0 0 0 0 0 0 0 0 0 0 0 0 0 0 0 0 0 0 0 0 0 0 0 0 0
0 0 0 0 0 0 0 0 0 0 0 0 0 0 0 0 0 0];
    rn_MgF = interp1(realn_MgF(1,:), realn_MgF(2,:), lambda, 'pchip');
    in_MgF = j*interp1(imagn_MgF(1,:), imagn_MgF(2,:), lambda,
'pchip');
    x = rn_MgF+in_MgF;
end

if mat=='so'
    % SiO2 PECVD
    realn_sio(1,:) = 1e-9*[300 310 320 330 340 350 360 370 380 390 400
410 420 430 440 450 460 470 480 490 500 510 520 530 540 550 560 570 580
590 600 610 620 630 640 650 660 670 680 690 700 710 720 730 740 750 760
770 780 790 800 810 820 830 840 850 860 870 880 890 900 910 920 930 940
950 960 970 980 990 1000 1010 1020 1030 1040 1050 1060 1070 1080 1090
1100 1110 1120 1130 1140 1150 1160 1170 1180 1190 1200 1210 1220 1230
1240 1250 1260 1270 1280 1290 1300 1310 1320 1330 1340 1350 1360 1370
1380 1390 1400 1410 1420 1430 1440 1450 1460 1470 1480 1490 1500 1510
1520 1530 1540 1550 1560 1570 1580 1590 1600 2000];
    realn_sio(2,:) = [1.43842 1.4391 1.43978 1.44046 1.44114 1.44182
1.4425 1.44318 1.44386 1.44454 1.44522 1.4459 1.44636 1.44663 1.44676
1.44676 1.44666 1.44649 1.44624 1.44594 1.4456 1.44522 1.44482 1.4444
1.44397 1.44352 1.44307 1.44261 1.44216 1.4417 1.44124 1.4408 1.44036
1.43992 1.43949 1.43906 1.43865 1.43824 1.43784 1.43745 1.43707 1.43671
1.43634 1.43598 1.43564 1.43531 1.43498 1.43466 1.43434 1.43404 1.43374
1.43346 1.43318 1.4329 1.43263 1.43238 1.43212 1.43188 1.43164 1.43141
1.43118 1.43095 1.43074 1.43053 1.43033 1.43012 1.42993 1.42974 1.42956
1.42938 1.4292 1.42903 1.42886 1.4287 1.42854 1.42838 1.42823 1.42809
1.42794 1.4278 1.42766 1.42752 1.4274 1.42727 1.42714 1.42702 1.4269
1.42678 1.42667 1.42656 1.42645 1.42634 1.42624 1.42613 1.42603 1.42594
1.42584 1.42575 1.42565 1.42556 1.42547 1.42539 1.42531 1.42522 1.42514
1.42506 1.42499 1.42491 1.42484 1.42476 1.42469 1.42462 1.42456 1.42448
1.42441 1.42435 1.42429 1.42423 1.42416 1.42411 1.42405 1.42398 1.42393
1.42387 1.42382 1.42377 1.42371 1.42366 1.42361 1.42356 1.4235 1.4235];
```

```
    imagn_sio(1,:) = 1e-9*[300 310 320 330 340 350 360 370 380 390 400
410 420 430 440 450 460 470 480 490 500 510 520 530 540 550 560 570 580
590 600 610 620 630 640 650 660 670 680 690 700 710 720 730 740 750 760
770 780 790 800 810 820 830 840 850 860 870 880 890 900 910 920 930 940
950 960 970 980 990 1000 1010 1020 1030 1040 1050 1060 1070 1080 1090
1100 1110 1120 1130 1140 1150 1160 1170 1180 1190 1200 1210 1220 1230
1240 1250 1260 1270 1280 1290 1300 1310 1320 1330 1340 1350 1360 1370
1380 1390 1400 1410 1420 1430 1440 1450 1460 1470 1480 1490 1500 1510
1520 1530 1540 1550 1560 1570 1580 1590 1600 2000 ];
    imagn_sio(2,:) = [0.003659191 0.003294136 0.003452309 0.002155259 0
0 0 0 0 0 0 0 0 0 0 0 0 0 0 0 0 0 0 0 0 0 0 0 0 0 0 0 0 0 0 0 0 0 0 0
0 0 0 0 0 0 0 0 0 0 0 0 0 0 0 0 0 0 0 0 0 0 0 0 0 0 0 0 0 0 0 0 0 0 0
0 0 0 0 0 0 0 0 0 0 0 0 0 0 0 0 0 0 0 0 0 0 0 0 0 0 0 0 0 0 0 0 0 0 0
0 0 0 0 0 0 0 0 0 0 0 0 0 0 0 0 0 0 0];
    rn_sio = interp1(realn_sio(1,:), realn_sio(2,:), lambda, 'pchip');
    in_sio = j*interp1(imagn_sio(1,:), imagn_sio(2,:), lambda,
'pchip');
    x = rn_sio+in_sio;
end

if mat=='sn'
    % SiN 2.1
    realn_sio(1,:) = 1e-9*[300 310 320 330 340 350 360 370 380 390 400
410 420 430 440 450 460 470 480 490 500 510 520 530 540 550 560 570 580
590 600 610 620 630 640 650 660 670 680 690 700 710 720 730 740 750 760
770 780 790 800 810 820 830 840 850 860 870 880 890 900 910 920 930 940
950 960 970 980 990 1000 1010 1020 1030 1040 1050 1060 1070 1080 1090
1100 1110 1120 1130 1140 1150 1160 1170 1180 1190 1200 1210 1220 1230
1240 1250 1260 1270 1280 1290 1300 1310 1320 1330 1340 1350 1360 1370
1380 1390 1400 1410 1420 1430 1440 1450 1460 1470 1480 1490 1500 1510
1520 1530 1540 1550 1560 1570 1580 1590 1600 ];
    realn_sio(2,:) = [2.44212 2.42493 2.40774 2.39055 2.37336 2.35617
2.33898 2.32179 2.3046 2.28741 2.27022 2.25303 2.23786 2.22438 2.21231
2.20143 2.19158 2.18261 2.17443 2.16693 2.16003 2.15366 2.14777 2.1423
2.13722 2.13249 2.12807 2.12394 2.12007 2.11643 2.11302 2.10981 2.10677
2.10391 2.1012 2.09864 2.09622 2.09392 2.09174 2.08966 2.08768 2.0858
2.08401 2.0823 2.08067 2.07911 2.07762 2.0762 2.07482 2.07352 2.07226
2.07106 2.0699 2.06879 2.06772 2.0667 2.06571 2.06476 2.06385 2.06296
2.06211 2.06129 2.0605 2.05973 2.05899 2.05828 2.05759 2.05692 2.05627
2.05565 2.05504 2.05446 2.05389 2.05334 2.05281 2.05229 2.05178 2.0513
2.05083 2.05036 2.04992 2.04948 2.04906 2.04865 2.04825 2.04786 2.04748
2.04712 2.04676 2.04641 2.04607 2.04574 2.04542 2.04511 2.0448 2.0445
2.04421 2.04393 2.04365 2.04338 2.04312 2.04286 2.0426 2.04236 2.04212
2.04189 2.04166 2.04143 2.04121 2.04099 2.04079 2.04058 2.04039 2.04019
2.03999 2.03981 2.03962 2.03944 2.03926 2.03909 2.03892 2.03876 2.03859
2.03843 2.03828 2.03812 2.03797 2.03783 2.03768 2.03754 2.03741];
    imagn_sio(1,:) = 1e-9*[300 310 320 330 340 350 360 370 380 390 400
410 420 430 440 450 460 470 480 490 500 510 520 530 540 550 560 570 580
590 600 610 620 630 640 650 660 670 680 690 700 710 720 730 740 750 760
770 780 790 800 810 820 830 840 850 860 870 880 890 900 910 920 930 940
950 960 970 980 990 1000 1010 1020 1030 1040 1050 1060 1070 1080 1090
1100 1110 1120 1130 1140 1150 1160 1170 1180 1190 1200 1210 1220 1230
```

```
1240 1250 1260 1270 1280 1290 1300 1310 1320 1330 1340 1350 1360 1370
1380 1390 1400 1410 1420 1430 1440 1450 1460 1470 1480 1490 1500 1510
1520 1530 1540 1550 1560 1570 1580 1590 1600 ];
    imagn_sio(2,:) = [0.357835629 0.312426633 0.277736964 0.243341633
0.208405781 0.176633527 0.146838897 0.119516769 0.096607329 0.078221562
0.065329626 0.055617248 0.046330479 0.035342394 0.02208462 0.008494003
0 0 0 0 0 0 0 0 0 0 0 0 0 0 0 0 0 0 0 0 0 0 0 0 0 0 0 0 0 0 0 0 0 0 0 0
0 0 0 0 0 0 0 0 0 0 0 0 0 0 0 0 0 0 0 0 0 0 0 0 0 0 0 0 0 0 0 0 0 0 0 0
0 0 0 0 0 0 0 0 0 0 0 0 0 0 0 0 0 0 0 0 0 0 0 0 0 0 0 0 0 0 0 0 0 0 0 0
0 0 0 0 0 0 0 ];
    rn_sio = interp1(realn_sio(1,:), realn_sio(2,:), lambda, 'pchip');
    in_sio = j*interp1(imagn_sio(1,:), imagn_sio(2,:), lambda,
'pchip');
    x = rn_sio+in_sio;
end


if mat=='ga'
    % GaAs
    realn_GaAs(1,:) = 1e-9*[207 208 210 212 214 216 218 219 221 223 225
227 230 232 234 236 238 241 243 246 248 250 253 256 258 261 264 267 270
272 276 279 282 285 288 292 295 299 302 306 310 314 318 322 326 331 335
340 344 349 354 359 365 370 376 381 387 394 400 407 413 420 428 435 443
451 459 468 477 486 496 506 517 528 539 551 564 577 590 605 620 636 653
670 689 708 729 751 775 800 827 855 886 918 954 992 1033 1078 1127 1181
1240 1305 1378 1459 1550 1653 1771 1907 2066 2254 2480];
    realn_GaAs(2,:) = [1.264 1.273 1.288 1.300 1.311 1.318 1.325 1.336
1.349 1.365 1.383 1.404 1.430 1.461 1.499 1.541 1.599 1.677 1.802 2.012
2.273 2.583 2.890 3.139 3.342 3.488 3.598 3.691 3.769 3.845 3.913 3.978
4.015 3.991 3.939 3.877 3.810 3.749 3.692 3.643 3.601 3.566 3.538 3.517
3.501 3.490 3.485 3.487 3.495 3.510 3.531 3.559 3.596 3.642 3.709 3.803
3.938 4.161 4.373 4.434 4.509 4.795 5.052 5.056 4.959 4.833 4.694 4.586
4.492 4.408 4.333 4.266 4.205 4.150 4.100 4.055 4.013 3.975 3.940 3.908
3.878 3.851 3.826 3.805 3.785 3.764 3.742 3.720 3.700 3.684 3.666 3.643
3.614 3.576 3.539 3.513 3.492 3.472 3.455 3.438 3.423 3.409 3.397 3.385
3.374 3.364 3.354 3.346 3.338 3.331 3.324];
    imagn_GaAs(1,:) = 1e-9*[207 208 210 212 214 216 218 219 221 223 225
227 230 232 234 236 238 241 243 246 248 250 253 256 258 261 264 267 270
272 276 279 282 285 288 292 295 299 302 306 310 314 318 322 326 331 335
340 344 349 354 359 365 370 376 381 387 394 400 407 413 420 428 435 443
451 459 468 477 486 496 506 517 528 539 551 564 577 590 605 620 636 653
670 689 708 729 751 775 800 827 855 886 918 954 992 1033 1078 1127 1181
1240 1305 1378 1459 1550 1653 1771 1907 2066 2254 2480];
    imagn_GaAs(2,:) = [2.4720E+00 2.5210E+00 2.5570E+00 2.5910E+00
2.6250E+00 2.6650E+00 2.7100E+00 2.7600E+00 2.8150E+00 2.8730E+00
2.9360E+00 3.0040E+00 3.0790E+00 3.1620E+00 3.2550E+00 3.3610E+00
3.4840E+00 3.6360E+00 3.7950E+00 3.9610E+00 4.0840E+00 4.1010E+00
4.0470E+00 3.9260E+00 3.7700E+00 3.6110E+00 3.4520E+00 3.3060E+00
3.1690E+00 3.0490E+00 2.9190E+00 2.7440E+00 2.5630E+00 2.4010E+00
2.2600E+00 2.1520E+00 2.0690E+00 2.0100E+00 1.9690E+00 1.9390E+00
1.9200E+00 1.9090E+00 1.9040E+00 1.9040E+00 1.9090E+00 1.9180E+00
1.9310E+00 1.9460E+00 1.9650E+00 1.9870E+00 2.0130E+00 2.0420E+00
```

```
2.0760E+00 2.1150E+00 2.1620E+00 2.2390E+00 2.2880E+00 2.2370E+00
2.1460E+00 2.0520E+00 1.9480E+00 1.8680E+00 1.7210E+00 1.3600E+00
9.9100E-01 8.0800E-01 6.9600E-01 6.0500E-01 5.3900E-01 4.8500E-01
4.4100E-01 4.0300E-01 3.7100E-01 3.4400E-01 3.2000E-01 2.9700E-01
2.7600E-01 2.5700E-01 2.4000E-01 2.2500E-01 2.1100E-01 1.9500E-01
1.7900E-01 1.6500E-01 1.5100E-01 1.3100E-01 1.1200E-01 1.0000E-01
9.1000E-02 8.9000E-02 8.0000E-02 4.0000E-02 4.0000E-05 0.0000E+00
0.0000E+00 0.0000E+00 0.0000E+00 0.0000E+00 0.0000E+00 0.0000E+00
0.0000E+00 0.0000E+00 0.0000E+00 0.0000E+00 0.0000E+00 0.0000E+00
0.0000E+00 0.0000E+00 0.0000E+00 0.0000E+00 0.0000E+00 ];
    rn_GaAs = interp1(realn_GaAs(1,:), realn_GaAs(2,:), lambda,
'pchip');
    in_GaAs = j*interp1(imagn_GaAs(1,:), imagn_GaAs(2,:), lambda,
'pchip');
    x = rn_GaAs+in_GaAs;
end

if mat=='gf'
    % GaAs w/ free carrier 5E17
    realn_GaAs(1,:) = 1e-9*[207 208 210 212 214 216 218 219 221 223 225
227 230 232 234 236 238 241 243 246 248 250 253 256 258 261 264 267 270
272 276 279 282 285 288 292 295 299 302 306 310 314 318 322 326 331 335
340 344 349 354 359 365 370 376 381 387 394 400 407 413 420 428 435 443
451 459 468 477 486 496 506 517 528 539 551 564 577 590 605 620 636 653
670 689 708 729 751 775 800 827 855 886 918 954 992 1033 1078 1127 1181
1240 1305 1378 1459 1550 1653 1771 1907 2066 2254 2480];
    realn_GaAs(2,:) = [1.264 1.273 1.288 1.300 1.311 1.318 1.325 1.336
1.349 1.365 1.383 1.404 1.430 1.461 1.499 1.541 1.599 1.677 1.802 2.012
2.273 2.583 2.890 3.139 3.342 3.488 3.598 3.691 3.769 3.845 3.913 3.978
4.015 3.991 3.939 3.877 3.810 3.749 3.692 3.643 3.601 3.566 3.538 3.517
3.501 3.490 3.485 3.487 3.495 3.510 3.531 3.559 3.596 3.642 3.709 3.803
3.938 4.161 4.373 4.434 4.509 4.795 5.052 5.056 4.959 4.833 4.694 4.586
4.492 4.408 4.333 4.266 4.205 4.150 4.100 4.055 4.013 3.975 3.940 3.908
3.878 3.851 3.826 3.805 3.785 3.764 3.742 3.720 3.700 3.684 3.666 3.643
3.614 3.576 3.539 3.513 3.492 3.472 3.455 3.438 3.423 3.409 3.397 3.385
3.374 3.364 3.354 3.346 3.338 3.331 3.324];
    imagn_GaAs(1,:) = 1e-9*[207 208 210 212 214 216 218 219 221 223 225
227 230 232 234 236 238 241 243 246 248 250 253 256 258 261 264 267 270
272 276 279 282 285 288 292 295 299 302 306 310 314 318 322 326 331 335
340 344 349 354 359 365 370 376 381 387 394 400 407 413 420 428 435 443
451 459 468 477 486 496 506 517 528 539 551 564 577 590 605 620 636 653
670 689 708 729 751 775 800 827 855 886 918 954 992 1033 1078 1127 1181
1240 1305 1378 1459 1550 1653 1771 1907 2066 2254 2480];
    imagn_GaAs(2,:) = [2.47E+00 2.52E+00    2.56E+00    2.59E+00
2.63E+00    2.67E+00    2.71E+00    2.76E+00    2.82E+00    2.87E+00
2.94E+00    3.00E+00    3.08E+00    3.16E+00    3.26E+00    3.36E+00
3.48E+00    3.64E+00    3.80E+00    3.96E+00    4.08E+00    4.10E+00
4.05E+00    3.93E+00    3.77E+00    3.61E+00    3.45E+00    3.31E+00
3.17E+00    3.05E+00    2.92E+00    2.74E+00    2.56E+00    2.40E+00
2.26E+00    2.15E+00    2.07E+00    2.01E+00    1.97E+00    1.94E+00
1.92E+00    1.91E+00    1.90E+00    1.90E+00    1.91E+00    1.92E+00
1.93E+00    1.95E+00    1.97E+00    1.99E+00    2.01E+00    2.04E+00
```

```
2.08E+00    2.12E+00    2.16E+00    2.24E+00    2.29E+00    2.24E+00
2.15E+00    2.05E+00    1.95E+00    1.87E+00    1.72E+00    1.36E+00
9.91E-01    8.08E-01    6.96E-01    6.05E-01    5.39E-01    4.85E-01
4.41E-01    4.03E-01    3.71E-01    3.44E-01    3.20E-01    2.97E-01
2.76E-01    2.57E-01    2.40E-01    2.25E-01    2.11E-01    1.95E-01
1.79E-01    1.65E-01    1.51E-01    1.31E-01    1.12E-01    1.00E-01
9.10E-02    8.90E-02    8.00E-02    4.00E-02    4.00E-05    2.95E-05
2.48E-05    2.49E-05    2.58E-05    2.66E-05    2.75E-05    2.91E-05
3.06E-05    3.24E-05    3.49E-05    3.61E-05    3.81E-05    4.06E-05
4.34E-05    4.67E-05    5.07E-05    5.33E-05    5.74E-05];
    rn_GaAs = interp1(realn_GaAs(1,:), realn_GaAs(2,:), lambda,
'pchip');
    in_GaAs = j*interp1(imagn_GaAs(1,:), imagn_GaAs(2,:), lambda,
'pchip');
    x = rn_GaAs+in_GaAs;
end

if mat=='ap'
    % InAlP (Al1 Ga0)0.5 In0.5 P
    realn_InAlP(1,:) = 1e-9*[192 194 195 197 198 200 201 203 205 206
208 209 211 213 214 216 217 219 221 222 224 225 227 229 230 232 233 235
237 238 240 241 243 245 246 248 249 251 253 254 256 257 259 261 262 264
265 267 269 270 272 273 275 277 278 280 281 283 285 286 288 289 291 293
294 296 297 299 301 302 304 305 307 309 310 312 313 315 317 318 320 321
323 325 326 328 329 331 333 334 336 337 339 341 342 344 345 347 349 350
352 353 355 357 358 360 361 363 365 366 368 369 371 373 374 376 377 379
381 382 384 385 387 389 390 392 393 395 397 398 400 401 403 405 406 408
409 411 412 414 416 417 419 420 422 424 425 427 428 430 432 433 435 436
438 440 441 443 444 446 448 449 451 452 454 456 457 459 460 462 464 465
467 468 470 472 473 475 476 478 480 481 483 484 486 488 489 491 492 494
496 497 499 500 502 504 505 507 508 510 512 513 515 516 518 520 521 523
524 526 528 529 531 532 534 536 537 539 540 542 544 545 547 548 550 551
553 555 556 558 559 561 563 564 566 567 569 571 572 574 575 577 579 580
582 583 585 587 588 590 591 593 595 596 598 599 601 603 604 606 607 609
611 612 614 615 617 618 620 622 623 625 626 628 630 631 633 634 636 638
639 641 642 644 646 647 649 650 652 654 655 657 658 660 661 663 665 666
668 669 671 673 674 676 677 679 681 682 684 685 687 689 690 692 693 695
696 698 700 701 703 704 706 708 709 711 712 714 716 717 719 720 722 723
725 727 728 730 731 733 735 736 738 739 741 743 744 746 747 749 750 752
754 755 757 758 760 762 763 765 766 768 770 771 773 774 776 777 779 781
782 784 785 787 789 790 792 793 795 796 798 800 801 803 804 806 808 809
811 812 814 815 817 819 820 822 823 825 827 828 830 831 833 834 836 838
839 841 842 844 845 847 849 850 852 853 855 857 858 860 861 863 864 866
868 869 871 872 874 875 877 879 880 882 883 885 887 888 890 891 893 894
896 898 899 901 902 904 905 907 909 910 912 913 915 916 918 920 921 923
924 926 927 929 931 932 934 935 937 938 940 942 943 945 946 948 949 951
953 954 956 957 959 960 962 964 965 967 968 970 971 973 975 976 978 979
981 982 984 986 987 989 990 992 993 995 996 998 1000 1013 1017 1020
1023 1027 1030 1034 1037 1041 1044 1048 1051 1055 1058 1061 1065 1068
1072 1075 1079 1082 1086 1089 1092 1096 1099 1103 1106 1110 1113 1117
1120 1123 1127 1130 1134 1137 1141 1144 1147 1151 1154 1158 1161 1165
1168 1171 1175 1178 1182 1185 1189 1192 1195 1199 1202 1206 1209 1213
```

```
1216 1219 1223 1226 1230 1233 1237 1240 1243 1247 1250 1254 1257 1261
1264 1267 1271 1274 1278 1281 1285 1288 1291 1295 1298 1302 1305 1308
1312 1315 1319 1322 1326 1329 1332 1336 1339 1343 1346 1350 1353 1356
1360 1363 1367 1370 1373 1377 1380 1384 1387 1391 1394 1397 1401 1404
1408 1411 1415 1418 1421 1425 1428 1432 1435 1438 1442 1445 1449 1452
1456 1459 1462 1466 1469 1473 1476 1480 1483 1486 1490 1493 1497 1500
1504 1507 1510 1514 1517 1521 1524 1528 1531 1535 1538 1541 1545 1548
1552 1555 1559 1562 1565 1569 1572 1576 1579 1583 1586 1590 1593 1596
1600 1603 1607 1610 1614 1617 1621 1624 1627 1631 1634 1638 1641 1645
1648 1652 1655 1659 1662 1666 1669 1672 1676 1679 1683 1686 1690 1693
1697];
    realn_InAlP(2,:) = [1.2920 1.3210 1.3453 1.3641 1.3771 1.3842
1.3860 1.3839 1.3795 1.3747 1.3715 1.3715 1.3758 1.3851 1.3996 1.4195
1.4444 1.4743 1.5078 1.5438 1.5825 1.6239 1.6685 1.7165 1.7686 1.8252
1.8869 1.9546 2.0290 2.1110 2.2013 2.3009 2.4101 2.5294 2.6584 2.7961
2.9407 3.0892 3.2379 3.3821 3.5171 3.6387 3.7435 3.8295 3.8964 3.9450
3.9772 3.9953 4.0020 3.9997 3.9906 3.9768 3.9599 3.9411 3.9214 3.9016
3.8824 3.8642 3.8474 3.8323 3.8190 3.8077 3.7985 3.7917 3.7871 3.7850
3.7854 3.7883 3.7938 3.8020 3.8129 3.8265 3.8428 3.8618 3.8835 3.9078
3.9346 3.9637 3.9950 4.0283 4.0632 4.0994 4.1366 4.1743 4.2121 4.2494
4.2859 4.3209 4.3540 4.3847 4.4126 4.4370 4.4575 4.4734 4.4839 4.4883
4.4862 4.4782 4.4666 4.4560 4.4460 4.4350 4.4228 4.4094 4.3949 4.3794
4.3631 4.3462 4.3287 4.3109 4.2927 4.2744 4.2561 4.2377 4.2195 4.2014
4.1835 4.1658 4.1484 4.1314 4.1147 4.0983 4.0823 4.0667 4.0514 4.0366
4.0221 4.0080 3.9943 3.9810 3.9681 3.9555 3.9433 3.9315 3.9200 3.9089
3.8981 3.8877 3.8775 3.8677 3.8582 3.8490 3.8400 3.8314 3.8230 3.8149
3.8070 3.7994 3.7919 3.7848 3.7778 3.7710 3.7644 3.7580 3.7518 3.7457
3.7397 3.7339 3.7282 3.7225 3.7169 3.7114 3.7058 3.7003 3.6948 3.6893
3.6838 3.6783 3.6727 3.6672 3.6619 3.6568 3.6521 3.6479 3.6443 3.6415
3.6393 3.6373 3.6349 3.6317 3.6270 3.6205 3.6123 3.6025 3.5915 3.5795
3.5671 3.5545 3.5421 3.5307 3.5202 3.5103 3.5009 3.4919 3.4833 3.4750
3.4670 3.4593 3.4518 3.4446 3.4376 3.4309 3.4243 3.4179 3.4117 3.4057
3.3998 3.3941 3.3885 3.3830 3.3777 3.3725 3.3674 3.3624 3.3576 3.3528
3.3481 3.3436 3.3391 3.3347 3.3304 3.3261 3.3220 3.3179 3.3139 3.3100
3.3061 3.3023 3.2986 3.2949 3.2913 3.2877 3.2842 3.2808 3.2774 3.2741
3.2708 3.2676 3.2644 3.2613 3.2582 3.2551 3.2521 3.2492 3.2463 3.2434
3.2406 3.2378 3.2350 3.2323 3.2296 3.2270 3.2244 3.2218 3.2193 3.2167
3.2143 3.2118 3.2094 3.2070 3.2047 3.2023 3.2001 3.1978 3.1955 3.1933
3.1911 3.1890 3.1868 3.1847 3.1826 3.1806 3.1785 3.1765 3.1745 3.1726
3.1706 3.1687 3.1668 3.1649 3.1631 3.1612 3.1594 3.1576 3.1558 3.1540
3.1523 3.1506 3.1489 3.1472 3.1455 3.1438 3.1422 3.1406 3.1390 3.1374
3.1358 3.1343 3.1327 3.1312 3.1297 3.1282 3.1267 3.1252 3.1238 3.1223
3.1209 3.1195 3.1181 3.1167 3.1154 3.1140 3.1127 3.1113 3.1100 3.1087
3.1074 3.1061 3.1048 3.1036 3.1023 3.1011 3.0999 3.0987 3.0974 3.0963
3.0951 3.0939 3.0927 3.0916 3.0904 3.0893 3.0882 3.0871 3.0860 3.0849
3.0838 3.0827 3.0816 3.0806 3.0795 3.0785 3.0775 3.0764 3.0754 3.0744
3.0734 3.0724 3.0715 3.0705 3.0695 3.0686 3.0676 3.0667 3.0657 3.0648
3.0639 3.0630 3.0621 3.0612 3.0603 3.0594 3.0585 3.0576 3.0568 3.0559
3.0551 3.0542 3.0534 3.0526 3.0517 3.0509 3.0501 3.0493 3.0485 3.0477
3.0469 3.0461 3.0453 3.0446 3.0438 3.0430 3.0423 3.0415 3.0408 3.0401
3.0393 3.0386 3.0379 3.0372 3.0364 3.0357 3.0350 3.0343 3.0336 3.0330
3.0323 3.0316 3.0309 3.0303 3.0296 3.0289 3.0283 3.0276 3.0270 3.0263
3.0257 3.0251 3.0244 3.0238 3.0232 3.0226 3.0220 3.0214 3.0208 3.0202
```

```
3.0196 3.0190 3.0184 3.0178 3.0172 3.0166 3.0161 3.0155 3.0149 3.0144
3.0138 3.0133 3.0127 3.0122 3.0116 3.0111 3.0106 3.0100 3.0095 3.0090
3.0084 3.0079 3.0074 3.0069 3.0064 3.0059 3.0054 3.0049 3.0044 3.0039
3.0034 3.0029 3.0024 3.0019 3.0014 3.0010 3.0005 3.0000 2.9996 2.9991
2.9986 2.9982 2.9977 2.9973 2.9968 2.9964 2.9959 2.9955 2.9950 2.9946
2.9942 2.9937 2.9933 2.9929 2.9924 2.9920 2.9916 2.9912 2.9908 2.9904
2.9899 2.9895 2.9891 2.9887 2.9883 2.9879 2.9875 2.9871 2.9867 2.9863
2.9860 2.9856 2.9852 2.9848 2.9844 2.9841 2.9837 2.9833 2.9829 2.9826
2.9822 2.9818 2.9815 2.9811 2.9808 2.9804 2.9800 2.9797 2.9793 2.9790
2.9786 2.9783 2.9779 2.9751 2.9743 2.9736 2.9729 2.9722 2.9715 2.9709
2.9702 2.9695 2.9689 2.9682 2.9676 2.9670 2.9663 2.9657 2.9651 2.9645
2.9639 2.9633 2.9627 2.9621 2.9615 2.9610 2.9604 2.9598 2.9593 2.9588
2.9582 2.9577 2.9571 2.9566 2.9561 2.9556 2.9551 2.9546 2.9541 2.9536
2.9531 2.9526 2.9521 2.9517 2.9512 2.9507 2.9503 2.9498 2.9494 2.9489
2.9485 2.9480 2.9476 2.9472 2.9468 2.9463 2.9459 2.9455 2.9451 2.9447
2.9443 2.9439 2.9435 2.9431 2.9427 2.9423 2.9420 2.9416 2.9412 2.9408
2.9405 2.9401 2.9397 2.9394 2.9390 2.9387 2.9383 2.9380 2.9376 2.9373
2.9370 2.9366 2.9363 2.9360 2.9357 2.9353 2.9350 2.9347 2.9344 2.9341
2.9338 2.9335 2.9332 2.9329 2.9326 2.9323 2.9320 2.9317 2.9314 2.9311
2.9308 2.9305 2.9303 2.9300 2.9297 2.9294 2.9292 2.9289 2.9286 2.9284
2.9281 2.9278 2.9276 2.9273 2.9271 2.9268 2.9266 2.9263 2.9261 2.9258
2.9256 2.9253 2.9251 2.9249 2.9246 2.9244 2.9242 2.9239 2.9237 2.9235
2.9232 2.9230 2.9228 2.9226 2.9224 2.9221 2.9219 2.9217 2.9215 2.9213
2.9211 2.9209 2.9207 2.9205 2.9203 2.9201 2.9199 2.9197 2.9195 2.9193
2.9191 2.9189 2.9187 2.9185 2.9183 2.9181 2.9179 2.9177 2.9176 2.9174
2.9172 2.9170 2.9168 2.9167 2.9165 2.9163 2.9161 2.9160 2.9158 2.9156
2.9154 2.9153 2.9151 2.9149 2.9148 2.9146 2.9144 2.9143 2.9141 2.9140
2.9138 2.9136 2.9135 2.9133 2.9132 2.9130 2.9129 2.9127 2.9126 2.9124
2.9123 2.9121 2.9120 2.9118 2.9117 2.9115 2.9114 2.9112 2.9111 2.9110
2.9108 2.9107 2.9105 ];
    imagn_InAlP(1,:) = 1e-9*[192 194 195 197 198 200 201 203 205 206
208 209 211 213 214 216 217 219 221 222 224 225 227 229 230 232 233 235
237 238 240 241 243 245 246 248 249 251 253 254 256 257 259 261 262 264
265 267 269 270 272 273 275 277 278 280 281 283 285 286 288 289 291 293
294 296 297 299 301 302 304 305 307 309 310 312 313 315 317 318 320 321
323 325 326 328 329 331 333 334 336 337 339 341 342 344 345 347 349 350
352 353 355 357 358 360 361 363 365 366 368 369 371 373 374 376 377 379
381 382 384 385 387 389 390 392 393 395 397 398 400 401 403 405 406 408
409 411 412 414 416 417 419 420 422 424 425 427 428 430 432 433 435 436
438 440 441 443 444 446 448 449 451 452 454 456 457 459 460 462 464 465
467 468 470 472 473 475 476 478 480 481 483 484 486 488 489 491 492 494
496 497 499 500 502 504 505 507 508 510 512 513 515 516 518 520 521 523
524 526 528 529 531 532 534 536 537 539 540 542 544 545 547 548 550 551
553 555 556 558 559 561 563 564 566 567 569 571 572 574 575 577 579 580
582 583 585 587 588 590 591 593 595 596 598 599 601 603 604 606 607 609
611 612 614 615 617 618 620 622 623 625 626 628 630 631 633 634 636 638
639 641 642 644 646 647 649 650 652 654 655 657 658 660 661 663 665 666
668 669 671 673 674 676 677 679 681 682 684 685 687 689 690 692 693 695
696 698 700 701 703 704 706 708 709 711 712 714 716 717 719 720 722 723
725 727 728 730 731 733 735 736 738 739 741 743 744 746 747 749 750 752
754 755 757 758 760 762 763 765 766 768 770 771 773 774 776 777 779 781
782 784 785 787 789 790 792 793 795 796 798 800 801 803 804 806 808 809
811 812 814 815 817 819 820 822 823 825 827 828 830 831 833 834 836 838
```

```
839 841 842 844 845 847 849 850 852 853 855 857 858 860 861 863 864 866
868 869 871 872 874 875 877 879 880 882 883 885 887 888 890 891 893 894
896 898 899 901 902 904 905 907 909 910 912 913 915 916 918 920 921 923
924 926 927 929 931 932 934 935 937 938 940 942 943 945 946 948 949 951
953 954 956 957 959 960 962 964 965 967 968 970 971 973 975 976 978 979
981 982 984 986 987 989 990 992 993 995 996 998 1000 1013 1017 1020
1023 1027 1030 1034 1037 1041 1044 1048 1051 1055 1058 1061 1065 1068
1072 1075 1079 1082 1086 1089 1092 1096 1099 1103 1106 1110 1113 1117
1120 1123 1127 1130 1134 1137 1141 1144 1147 1151 1154 1158 1161 1165
1168 1171 1175 1178 1182 1185 1189 1192 1195 1199 1202 1206 1209 1213
1216 1219 1223 1226 1230 1233 1237 1240 1243 1247 1250 1254 1257 1261
1264 1267 1271 1274 1278 1281 1285 1288 1291 1295 1298 1302 1305 1308
1312 1315 1319 1322 1326 1329 1332 1336 1339 1343 1346 1350 1353 1356
1360 1363 1367 1370 1373 1377 1380 1384 1387 1391 1394 1397 1401 1404
1408 1411 1415 1418 1421 1425 1428 1432 1435 1438 1442 1445 1449 1452
1456 1459 1462 1466 1469 1473 1476 1480 1483 1486 1490 1493 1497 1500
1504 1507 1510 1514 1517 1521 1524 1528 1531 1535 1538 1541 1545 1548
1552 1555 1559 1562 1565 1569 1572 1576 1579 1583 1586 1590 1593 1596
1600 1603 1607 1610 1614 1617 1621 1624 1627 1631 1634 1638 1641 1645
1648 1652 1655 1659 1662 1666 1669 1672 1676 1679 1683 1686 1690 1693
1697];
    imagn_InAlP(2,:) = [2.404 2.405 2.403 2.401 2.400 2.401 2.407 2.418
2.436 2.461 2.494 2.532 2.576 2.624 2.674 2.726 2.779 2.831 2.882 2.933
2.984 3.035 3.087 3.140 3.194 3.248 3.303 3.359 3.414 3.468 3.521 3.570
3.614 3.651 3.677 3.692 3.691 3.672 3.634 3.576 3.499 3.405 3.299 3.184
3.066 2.948 2.834 2.726 2.626 2.535 2.453 2.380 2.315 2.259 2.209 2.166
2.129 2.097 2.069 2.046 2.027 2.011 1.998 1.987 1.979 1.972 1.968 1.964
1.962 1.960 1.959 1.957 1.956 1.955 1.952 1.949 1.944 1.937 1.928 1.917
1.903 1.886 1.865 1.841 1.814 1.783 1.748 1.709 1.667 1.621 1.572 1.520
1.466 1.409 1.351 1.292 1.235 1.181 1.133 1.091 1.049 1.008 0.968 0.930
0.894 0.859 0.825 0.794 0.763 0.735 0.708 0.683 0.659 0.636 0.615 0.595
0.576 0.558 0.541 0.525 0.510 0.495 0.482 0.469 0.457 0.445 0.435 0.424
0.414 0.405 0.396 0.387 0.379 0.371 0.363 0.356 0.348 0.341 0.335 0.328
0.322 0.316 0.310 0.304 0.298 0.292 0.287 0.281 0.276 0.270 0.265 0.260
0.254 0.249 0.243 0.238 0.233 0.227 0.222 0.216 0.210 0.205 0.199 0.193
0.188 0.182 0.176 0.171 0.165 0.160 0.155 0.150 0.145 0.141 0.136 0.131
0.124 0.117 0.108 0.098 0.087 0.075 0.064 0.053 0.043 0.035 0.029 0.023
0.020 0.017 0.015 0.014 0.012 0.011 0.010 0.009 0.008 0.007 0.007 0.006
0.005 0.005 0.005 0.004 0.004 0.004 0.003 0.003 0.003 0.003 0.002 0.002
0.002 0.002 0.002 0.002 0.002 0.002 0.001 0.001 0.001 0.001 0.001 0.001
0.001 0.001 0.001 0.001 0.001 0.001 0.001 0.001 0.001 0.001 0.001 0.001
0.001 0.000 0.000 0.000 0.000 0.000 0.000 0.000 0.000 0.000 0.000 0.000
0.000 0.000 0.000 0.000 0.000 0.000 0.000 0.000 0.000 0.000 0.000 0.000
0.000 0.000 0.000 0.000 0.000 0.000 0.000 0.000 0.000 0.000 0.000 0.000
0.000 0.000 0.000 0.000 0.000 0.000 0.000 0.000 0.000 0.000 0.000 0.000
0.000 0.000 0.000 0.000 0.000 0.000 0.000 0.000 0.000 0.000 0.000 0.000
0.000 0.000 0.000 0.000 0.000 0.000 0.000 0.000 0.000 0.000 0.000 0.000
0.000 0.000 0.000 0.000 0.000 0.000 0.000 0.000 0.000 0.000 0.000 0.000
0.000 0.000 0.000 0.000 0.000 0.000 0.000 0.000 0.000 0.000 0.000 0.000
0.000 0.000 0.000 0.000 0.000 0.000 0.000 0.000 0.000 0.000 0.000 0.000
0.000 0.000 0.000 0.000 0.000 0.000 0.000 0.000 0.000 0.000 0.000 0.000
0.000 0.000 0.000 0.000 0.000 0.000 0.000 0.000 0.000 0.000 0.000 0.000
0.000 0.000 0.000 0.000 0.000 0.000 0.000 0.000 0.000 0.000 0.000 0.000
```

```
0.000 0.000 0.000 0.000 0.000 0.000 0.000 0.000 0.000 0.000 0.000 0.000
```

```
2.33938 2.33692 2.33457 2.33233 2.33018 2.32812 2.32615 2.32427 2.32245
2.32071 2.31904 2.31743 2.31589 2.31441 2.31298 2.31161 2.31028 2.30901
2.30777 2.30659 2.30545 2.30434 2.30326 2.30223 2.30123 2.30027 2.29933
2.29843 2.29756 2.29671 2.29588 2.29509 2.29432 2.29357 2.29284 2.29214
2.29145 2.29079 2.29014 2.28951 2.2889 2.28831 2.28773 2.28717 2.28662
2.2861 2.28558 2.28508 2.28458 2.28411 2.28364 2.28319 2.28274 2.28231
2.28189 2.28149 2.28108 2.2807 2.28031 2.27994 2.27957 2.27922 2.27887
2.27854 2.2782 2.27788 2.27756 2.27726 2.27695 2.27665 2.27637 2.27608
2.27581 2.27553 2.27527 2.27501 2.27475 2.27451 2.27427 2.27402 2.27379
2.27356 2.27333 2.27311 2.27289 2.27268 2.27248 2.27227 2.27207];
    imagn_ZnS(1,:) = 1e-9*[300 310 320 330 340 350 360 370 380 390 400
410 420 430 440 450 460 470 480 490 500 510 520 530 540 550 560 570 580
590 600 610 620 630 640 650 660 670 680 690 700 710 720 730 740 750 760
770 780 790 800 810 820 830 840 850 860 870 880 890 900 910 920 930 940
950 960 970 980 990 1000 1010 1020 1030 1040 1050 1060 1070 1080 1090
1100 1110 1120 1130 1140 1150 1160 1170 1180 1190 1200 1210 1220 1230
1240 1250 1260 1270 1280 1290 1300 1310 1320 1330 1340 1350 1360 1370
1380 1390 1400 1410 1420 1430 1440 1450 1460 1470 1480 1490 1500 1510
1520 1530 1540 1550 1560 1570 1580 1590 1600 ];
    imagn_ZnS(2,:) = [0.335962564 0.289731848 0.255079695 0.200010064
0.099973396 0.008410666 0 0 0 0 0 0 0 0 0 0 0 0 0 0 0 0 0 0 0 0 0 0 0
0 0 0 0 0 0 0 0 0 0 0 0 0 0 0 0 0 0 0 0 0 0 0 0 0 0 0 0 0 0 0 0 0 0 0
0 0 0 0 0 0 0 0 0 0 0 0 0 0 0 0 0 0 0 0 0 0 0 0 0 0 0 0 0 0 0 0 0 0 0
0 0 0 0 0 0 0 0 0 0 0 0 0 0 0 0 0 0 0 0 0 0 0 0 0 0 0 0 0 0 0 0 0 0 0
0 0 0 0 0 0 0 0 0 0 0 0 0 0 0 0 0 0 0 0 0 0 0 0 0 0 0 0 0 0 0 0 0 0 0 ];
    rn_ZnS = interp1(realn_ZnS(1,:), realn_ZnS(2,:), lambda, 'pchip');
    in_ZnS = j*interp1(imagn_ZnS(1,:), imagn_ZnS(2,:), lambda,
'pchip');
    x = rn_ZnS+in_ZnS;
end

if mat=='ta'
    % TaO5
    realn_ZnS(1,:) = 1e-9*[300 314 328 346 367 393 420 460 501 561 633
737 881 1098 1436 1600 2000];
    realn_ZnS(2,:) = [2.330 2.281 2.231 2.189 2.159 2.127 2.101 2.074
2.054 2.034 2.017 2.007 1.992 1.977 1.975 1.972 1.970];
    imagn_ZnS(1,:) = 1e-9*[300 314 328 346 367 393 420 460 501 561 633
737 881 1098 1436 1600 2000];
    imagn_ZnS(2,:) = [0 0 0 0 0 0 0 0 0 0 0 0 0 0 0 0 0 0];
    rn_ZnS = interp1(realn_ZnS(1,:), realn_ZnS(2,:), lambda, 'pchip');
    in_ZnS = j*interp1(imagn_ZnS(1,:), imagn_ZnS(2,:), lambda,
'pchip');
    x = rn_ZnS+in_ZnS;
end

if mat=='ge'
    % Ge
    realn_Ge(1,:) = 1e-9*[206.64 208.38 210.14 211.94 213.77 215.63
217.52 219.44 221.40 223.40 225.43 227.50 229.60 231.75 233.93 236.16
238.43 240.75 243.11 245.52 247.97 250.48 253.03 255.64 258.30 261.02
263.80 266.63 269.53 272.49 275.52 278.62 281.78 285.02 288.34 291.73
295.20 298.76 302.40 306.14 309.96 313.89 317.91 322.04 326.28 330.63
```

```
335.10 339.69 344.40 349.25 354.24 359.38 364.66 370.11 375.71 381.49
387.45 393.60 399.95 406.51 413.28 420.29 427.54 435.04 442.80 450.86
459.20 467.87 476.87 486.22 495.94 506.06 516.60 527.60 539.07 551.05
563.57 576.68 590.41 604.81 619.93 635.82 652.55 670.19 688.81 708.49
729.32 751.43 774.91 799.90 826.57 855.07 885.61 918.41 953.73 991.88
1033.21 1078.13 1127.14 1180.81 1239.85 1305.11 1377.61 1458.65 1549.81
1653.14 1771.22 1907.46 2066.42 2254.28 2479.70 ];
    realn_Ge(2,:) = [1.023 1.0625 1.108 1.1575 1.209 1.262688 1.31
1.340062 1.36 1.372937 1.38 1.3835 1.383 1.377625 1.371 1.366375 1.364
1.365062 1.37 1.379812 1.394 1.412063 1.435 1.463563 1.498 1.537563
1.586 1.643937 1.72 1.809687 1.953 2.197689 2.516 2.936752 3.338
3.585125 3.745 3.830187 3.869 3.893812 3.905 3.91375 3.92 3.927562
3.936 3.946312 3.958 3.970687 3.985 4.001062 4.02 4.043563 4.07
4.100312 4.128 4.147125 4.157 4.1545 4.141 4.113312 4.082 4.055938
4.037 4.03025 4.035 4.05225 4.082 4.123937 4.18 4.24925 4.34 4.45675
4.61 4.839063 5.062 5.171687 5.283 5.539312 5.748 5.715437 5.588
5.445188 5.294 5.17275 5.067 4.976187 4.897 4.82625 4.763 4.705437
4.653 4.603687 4.56 4.526375 4.495 4.455625 4.42 4.401563 4.385
4.355312 4.325 4.301875 4.285 4.283437 4.275 4.231625 4.18 4.133125
4.104 4.086 4.074 ];
    imagn_Ge(1,:) = 1e-9*[206.64 208.38 210.14 211.94 213.77 215.63
217.52 219.44 221.40 223.40 225.43 227.50 229.60 231.75 233.93 236.16
238.43 240.75 243.11 245.52 247.97 250.48 253.03 255.64 258.30 261.02
263.80 266.63 269.53 272.49 275.52 278.62 281.78 285.02 288.34 291.73
295.20 298.76 302.40 306.14 309.96 313.89 317.91 322.04 326.28 330.63
335.10 339.69 344.40 349.25 354.24 359.38 364.66 370.11 375.71 381.49
387.45 393.60 399.95 406.51 413.28 420.29 427.54 435.04 442.80 450.86
459.20 467.87 476.87 486.22 495.94 506.06 516.60 527.60 539.07 551.05
563.57 576.68 590.41 604.81 619.93 635.82 652.55 670.19 688.81 708.49
729.32 751.43 774.91 799.90 826.57 855.07 885.61 918.41 953.73 991.88
1033.21 1078.13 1127.14 1180.81 1239.85 1305.11 1377.61 1458.65 1549.81
1653.14 1771.22 1907.46 2066.42 2254.28 2479.70 ];
    imagn_Ge(2,:) = [2.774 2.80225 2.831 2.856 2.873 2.873375 2.866
2.855812 2.846 2.842 2.842 2.845062 2.854 2.8715 2.897 2.931438 2.973
3.02 3.073 3.132187 3.197 3.266813 3.342 3.422063 3.509 3.60375 3.709
3.825937 3.96 4.120937 4.297 4.514188 4.669 4.642375 4.507 4.272563
4.009 3.797751 3.614 3.462751 3.336 3.228563 3.137 3.05675 2.986
2.921562 2.863 2.809062 2.759 2.712 2.667 2.624125 2.579 2.526562 2.469
2.405437 2.34 2.273813 2.215 2.1725 2.145 2.135563 2.14 2.1565 2.181
2.20875 2.24 2.2735 2.309 2.346375 2.384 2.43275 2.455 2.40775 2.318
2.200875 2.049 1.8685 1.634 1.276 9.33E-01 7.50E-01 6.38E-01 5.57E-01
5.00E-01 4.45E-01 4.01E-01 3.70E-01 3.45E-01 3.25E-01 2.98E-01 2.43E-01
1.90E-01 1.75E-01 1.67E-01 1.45E-01 1.23E-01 1.12E-01 1.03E-01 9.11E-02
8.09E-02 8.06E-02 7.45E-02 4.00E-02 5.67E-03 1.31E-03 2.80E-04 3.15E-03
0 0 0 ];
    rn_Ge = interp1(realn_Ge(1,:), realn_Ge(2,:), lambda, 'pchip');
    in_Ge = j*interp1(imagn_Ge(1,:), imagn_Ge(2,:), lambda, 'pchip');
    x = rn_Ge+in_Ge;
end

if mat=='to'
    % TiO2
```

```
    realn_T(1,:) = 1e-9*[300 310 320 330 340 350 360 370 380 390 400
410 420 430 440 450 460 470 480 490 500 510 520 530 540 550 560 570 580
590 600 610 620 630 640 650 660 670 680 690 700 710 720 730 740 750 760
770 780 790 800 810 820 830 840 850 860 870 880 890 900 910 920 930 940
950 960 970 980 990 1000 1010 1020 1030 1040 1050 1060 1070 1080 1090
1100 1110 1120 1130 1140 1150 1160 1170 1180 1190 1200 1210 1220 1230
1240 1250 1260 1270 1280 1290 1300 1310 1320 1330 1340 1350 1360 1370
1380 1390 1400 1410 1420 1430 1440 1450 1460 1470 1480 1490 1500 1510
1520 1530 1540 1550 1560 1570 1580 1590 1600];
    realn_T(2,:) = [2.99229 2.95622 2.92015 2.88408 2.84801 2.81194
2.77587 2.7398 2.70373 2.66766 2.63159 2.59552 2.56507 2.53891 2.51612
2.49606 2.47823 2.46229 2.44795 2.43497 2.42318 2.41241 2.40254 2.39348
2.3851 2.37737 2.37019 2.36353 2.35731 2.35151 2.34608 2.34099 2.33622
2.33173 2.3275 2.32352 2.31976 2.31619 2.31282 2.30963 2.3066 2.30372
2.30098 2.29838 2.29589 2.29353 2.29127 2.28911 2.28705 2.28508 2.28319
2.28138 2.27965 2.27799 2.27639 2.27486 2.27338 2.27197 2.2706 2.26929
2.26802 2.26681 2.26564 2.2645 2.26341 2.26235 2.26133 2.26035 2.25939
2.25848 2.25759 2.25672 2.25588 2.25508 2.25429 2.25353 2.2528 2.25208
2.25138 2.25071 2.25006 2.24943 2.24881 2.24821 2.24762 2.24706 2.24651
2.24598 2.24545 2.24495 2.24445 2.24397 2.2435 2.24304 2.24259 2.24216
2.24174 2.24133 2.24092 2.24054 2.24015 2.23977 2.23941 2.23905 2.23871
2.23837 2.23803 2.23771 2.23739 2.23708 2.23677 2.23648 2.23619 2.23591
2.23563 2.23535 2.23509 2.23483 2.23457 2.23432 2.23408 2.23384 2.23361
2.23337 2.23315 2.23293 2.23271 2.2325 2.23229 2.23209 2.23189];
    imagn_T(1,:) = 1e-9*[300 310 320 330 340 350 360 370 380 390 400
410 420 430 440 450 460 470 480 490 500 510 520 530 540 550 560 570 580
590 600 610 620 630 640 650 660 670 680 690 700 710 720 730 740 750 760
770 780 790 800 810 820 830 840 850 860 870 880 890 900 910 920 930 940
950 960 970 980 990 1000 1010 1020 1030 1040 1050 1060 1070 1080 1090
1100 1110 1120 1130 1140 1150 1160 1170 1180 1190 1200 1210 1220 1230
1240 1250 1260 1270 1280 1290 1300 1310 1320 1330 1340 1350 1360 1370
1380 1390 1400 1410 1420 1430 1440 1450 1460 1470 1480 1490 1500 1510
1520 1530 1540 1550 1560 1570 1580 1590 1600];
    imagn_T(2,:) = [0.853144245 0.64743964 0.461947111 0.295625754
0.13606909 0.023511325 0 0 0 0 0 0 0 0 0 0 0 0 0 0 0 0 0 0 0 0 0 0 0 0 0
0 0 0 0 0 0 0 0 0 0 0 0 0 0 0 0 0 0 0 0 0 0 0 0 0 0 0 0 0 0 0 0 0 0 0 0 0
0 0 0 0 0 0 0 0 0 0 0 0 0 0 0 0 0 0 0 0 0 0 0 0 0 0 0 0 0 0 0 0 0 0 0 0 0
0 0 0 0 0 0 0 0 0 0 0 0 0 0 0 0 0 0 0 0 0 0 0 0 0 0 0 0 0 0 0 0 0 0 0 0 ];
    rn_T = interp1(realn_T(1,:), realn_T(2,:), lambda, 'pchip');
    in_T = j*interp1(imagn_T(1,:), imagn_T(2,:), lambda, 'pchip');
    x = rn_T+in_T;
end

if mat=='al'
    % Al2O3
    realn_T(1,:) = 1e-9*[379.5 380.2 381.0 381.7 382.5 383.2 384.0
384.7 385.5 386.2 387.0 387.7 388.5 389.2 390.0 390.7 391.5 392.2 393.0
393.7 394.5 395.2 396.0 396.7 397.5 398.2 399.0 399.7 400.5 401.2 402.0
402.7 403.5 404.2 405.0 405.7 406.5 407.2 408.0 408.7 409.5 410.2 411.0
411.7 412.5 413.2 414.0 414.7 415.5 416.2 417.0 417.7 418.5 419.2 420.0
420.7 421.4 422.2 422.9 423.7 424.4 425.2 425.9 426.7 427.4 428.2 428.9
429.7 430.4 431.2 431.9 432.6 433.4 434.1 434.9 435.6 436.4 437.1 437.9
```

438.6 439.4 440.1 440.9 441.6 442.3 443.1 443.8 444.6 445.3 446.1 446.8
447.6 448.3 449.0 449.8 450.5 451.3 452.0 452.8 453.5 454.3 455.0 455.7
456.5 457.2 458.0 458.7 459.5 460.2 460.9 461.7 462.4 463.2 463.9 464.7
465.4 466.1 466.9 467.6 468.4 469.1 469.8 470.6 471.3 472.1 472.8 473.6
474.3 475.0 475.8 476.5 477.3 478.0 478.7 479.5 480.2 481.0 481.7 482.4
483.2 483.9 484.7 485.4 486.1 486.9 487.6 488.4 489.1 489.8 490.6 491.3
492.1 492.8 493.5 494.3 495.0 495.8 496.5 497.2 498.0 498.7 499.5 500.2
500.9 501.7 502.4 503.1 503.9 504.6 505.4 506.1 506.8 507.6 508.3 509.0
509.8 510.5 511.3 512.0 512.7 513.5 514.2 514.9 515.7 516.4 517.2 517.9
518.6 519.4 520.1 520.8 521.6 522.3 523.0 523.8 524.5 525.3 526.0 526.7
527.5 528.2 528.9 529.7 530.4 531.1 531.9 532.6 533.3 534.1 534.8 535.5
536.3 537.0 537.7 538.5 539.2 539.9 540.7 541.4 542.2 542.9 543.6 544.4
545.1 545.8 546.6 547.3 548.0 548.8 549.5 550.2 550.9 551.7 552.4 553.1
553.9 554.6 555.3 556.1 556.8 557.5 558.3 559.0 559.7 560.5 561.2 561.9
562.7 563.4 564.1 564.9 565.6 566.3 567.0 567.8 568.5 569.2 570.0 570.7
571.4 572.2 572.9 573.6 574.4 575.1 575.8 576.5 577.3 578.0 578.7 579.5
580.2 580.9 581.6 582.4 583.1 583.8 584.6 585.3 586.0 586.8 587.5 588.2
588.9 589.7 590.4 591.1 591.8 592.6 593.3 594.0 594.8 595.5 596.2 596.9
597.7 598.4 599.1 599.9 600.6 601.3 602.0 602.8 603.5 604.2 604.9 605.7
606.4 607.1 607.8 608.6 609.3 610.0 610.7 611.5 612.2 612.9 613.7 614.4
615.1 615.8 616.6 617.3 618.0 618.7 619.5 620.2 620.9 621.6 622.4 623.1
623.8 624.5 625.2 626.0 626.7 627.4 628.1 628.9 629.6 630.3 631.0 631.8
632.5 633.2 633.9 634.7 635.4 636.1 636.8 637.5 638.3 639.0 639.7 640.4
641.2 641.9 642.6 643.3 644.0 644.8 645.5 646.2 646.9 647.7 648.4 649.1
649.8 650.5 651.3 652.0 652.7 653.4 654.1 654.9 655.6 656.3 657.0 657.8
658.5 659.2 659.9 660.6 661.4 662.1 662.8 663.5 664.2 665.0 665.7 666.4
667.1 667.8 668.5 669.3 670.0 670.7 671.4 672.1 672.9 673.6 674.3 675.0
675.7 676.5 677.2 677.9 678.6 679.3 680.0 680.8 681.5 682.2 682.9 683.6
684.4 685.1 685.8 686.5 687.2 687.9 688.7 689.4 690.1 690.8 691.5 692.2
693.0 693.7 694.4 695.1 695.8 696.5 697.2 698.0 698.7 699.4 700.1 700.8
701.5 702.3 703.0 703.7 704.4 705.1 705.8 706.5 707.3 708.0 708.7 709.4
710.1 710.8 711.5 712.3 713.0 713.7 714.4 715.1 715.8 716.5 717.3 718.0
718.7 719.4 720.1 720.8 721.5 722.3 723.0 723.7 724.4 725.1 725.8 726.5
727.2 728.0 728.7 729.4 730.1 730.8 731.5 732.2 732.9 733.6 734.4 735.1
735.8 736.5 737.2 737.9 738.6 739.3 740.0 740.8 741.5 742.2 742.9 743.6
744.3 745.0 745.7 746.4 747.2 747.9 748.6 749.3 750.0 750.7 751.4 752.1
752.8 753.5 754.2 755.0 755.7 756.4 757.1 757.8 758.5 759.2 759.9 760.6
761.3 762.0 762.8 763.5 764.2 764.9 765.6 766.3 767.0 767.7 768.4 769.1
769.8 770.5 771.2 772.0 772.7 773.4 774.1 774.8 775.5 776.2 776.9 777.6
778.3 779.0 779.7 780.4 781.1 781.8 782.5 783.3 784.0 784.7 785.4 786.1
786.8 787.5 788.2 788.9 789.6 790.3 791.0 791.7 792.4 793.1 793.8 794.5
795.2 795.9 796.6 797.4 798.1 798.8 799.5 800.2 800.9 801.6 802.3 803.0
803.7 804.4 805.1 805.8 806.5 807.2 807.9 808.6 809.3 810.0 810.7 811.4
812.1 812.8 813.5 814.2 814.9 815.6 816.3 817.0 817.7 818.4 819.1 819.8
820.5 821.2 821.9 822.6 823.3 824.0 824.7 825.4 826.1 826.9 827.6 828.3
829.0 829.7 830.4 831.1 831.8 832.5 833.2 833.9 834.6 835.3 836.0 836.7
837.3 838.0 838.7 839.4 840.1 840.8 841.5 842.2 842.9 843.6 844.3 845.0
845.7 846.4 847.1 847.8 848.5 849.2 849.9 850.6 851.3 852.0 852.7 853.4
854.1 854.8 855.5 856.2 856.9 857.6 858.3 859.0 859.7 860.4 861.1 861.8
862.5 863.2 863.9 864.6 865.3 866.0 866.6 867.3 868.0 868.7 869.4 870.1
870.8 871.5 872.2 872.9 873.6 874.3 875.0 875.7 876.4 877.1 877.8 878.5
879.2 879.9 880.5 881.2 881.9 882.6 883.3 884.0 884.7 885.4 886.1 886.8
887.5 888.2 888.9 889.6 890.3 890.9 891.6 892.3 893.0 893.7 894.4 895.1

```
895.8 896.5 897.2 897.9 898.6 899.3 899.9 900.6 901.3 902.0 902.7 903.4
904.1 904.8 905.5 906.2 906.9 907.6 908.2 908.9 909.6 910.3 911.0 911.7
912.4 913.1 913.8 914.5 915.1 915.8 916.5 917.2 917.9 918.6 919.3 920.0
920.7 921.4 922.0 922.7 923.4 924.1 924.8 925.5 926.2 926.9 927.6 928.2
928.9 929.6 930.3 931.0 931.7 932.4 933.1 933.7 934.4 935.1 935.8 936.5
937.2 937.9 938.6 939.2 939.9 940.6 941.3 942.0 942.7 943.4 944.7 946.5
947.8 949.5 951.3 952.6 954.3 956.1 957.4 959.1 960.8 962.5 964.2 965.6
967.3 969.0 970.4 972.1 973.8 975.2 976.9 978.6 980.0 981.7 983.4 985.1
986.7 988.2 989.8 991.5 993.0 994.6 996.3 997.7 999.4 1001.1 1002.5
1004.2 1005.8 1007.5 1009.2 1010.6 1012.3 1013.9 1015.4 1017.1 1018.7
1020.2 1021.8 1023.5 1025.1 1026.8 1028.2 1029.9 1031.5 1033.0 1034.7
1036.3 1037.9 1039.6 1041.1 1042.7 1044.3 1045.8 1047.5 1049.1 1050.6
1052.2 1053.8 1055.5 1057.1 1058.6 1060.2 1061.8 1063.4 1065.0 1066.6
1068.2 1069.8 1071.4 1073.0 1074.6 1076.1 1077.7 1079.3 1080.9 1082.5
1084.1 1085.7 1087.3 1088.9 1090.5 1092.0 1093.6 1095.2 1096.8 1098.4
1100.0 1101.6 1103.2 1104.7 1106.3 1107.9 1109.5 1111.1 1112.7 1114.3
1115.8 1117.4 1119.0 1120.6 1122.2 1123.8 1125.3 1126.9 1128.5 1130.1
1131.7 1133.2 1134.8 1136.4 1138.0 1139.6 1141.1 1142.7 1144.3 1145.9
1147.5 1149.0 1150.6 1152.2 1153.8 1155.3 1156.9 1158.5 1160.1 1161.7
1163.2 1164.8 1166.4 1168.0 1169.5 1171.1 1172.7 1174.2 1175.8 1177.4
1179.0 1180.5 1182.1 1183.7 1185.3 1186.8 1188.4 1190.0 1191.5 1193.1
1194.7 1196.2 1197.8 1199.4 1201.0 1202.5 1204.1 1205.7 1207.2 1208.8
1210.4 1211.9 1213.5 1215.1 1216.6 1218.2 1219.8 1221.3 1222.9 1224.5
1226.0 1227.6 1229.1 1230.7 1232.3 1233.8 1235.4 1237.0 1238.5 1240.1
1241.6 1243.2 1244.8 1246.3 1247.9 1249.4 1251.0 1252.6 1254.1 1255.7
1257.2 1258.8 1260.4 1261.9 1263.5 1265.0 1266.6 1268.1 1269.7 1271.2
1272.8 1274.4 1275.9 1277.5 1279.0 1280.6 1282.1 1283.7 1285.2 1286.8
1288.3 1289.9 1291.4 1293.0 1294.5 1296.1 1297.7 1299.2 1300.8 1302.3
1303.9 1305.4 1307.0 1308.5 1310.0 1311.6 1313.1 1314.7 1316.2 1317.8
1319.3 1320.9 1322.4 1324.0 1325.5 1327.1 1328.6 1330.2 1331.7 1333.2
1334.8 1336.3 1337.9 1339.4 1341.0 1342.5 1344.0 1345.6 1347.1 1348.7
1350.2 1351.8 1353.3 1354.8 1356.4 1357.9 1359.5 1361.0 1362.5 1364.1
1365.6 1367.1 1368.7 1370.2 1371.8 1373.3 1374.8 1376.4 1377.9 1379.4
1381.0 1382.5 1384.0 1385.6 1387.1 1388.6 1390.2 1391.7 1393.2 1394.8
1396.3 1397.8 1399.4 1400.9 1402.4 1404.0 1405.5 1407.0 1408.6 1410.1
1411.6 1413.1 1414.7 1416.2 1417.7 1419.3 1420.8 1422.3 1423.8 1425.4
1426.9 1428.4 1430.0 1431.5 1433.0 1434.5 1436.1 1437.6 1439.1 1440.6
1442.2 1443.7 1445.2 1446.7 1448.2 1449.8 1451.3 1452.8 1454.3 1455.9
1457.4 1458.9 1460.4 1461.9 1463.5 1465.0 1466.5 1468.0 1469.5 1471.1
1472.6 1474.1 1475.6 1477.1 1478.6 1480.2 1481.7 1483.2 1484.7 1486.2
1487.7 1489.2 1490.8 1492.3 1493.8 1495.3 1496.8 1498.3 1499.8 1501.4
1502.9 1504.4 1505.9 1507.4 1508.9 1510.4 1511.9 1513.5 1515.0 1516.5
1518.0 1519.5 1521.0 1522.5 1524.0 1525.5 1527.0 1528.5 1530.0 1531.6
1533.1 1534.6 1536.1 1537.6 1539.1 1540.6 1542.1 1543.6 1545.1 1546.6
1548.1 1549.6 1551.1 1552.6 1554.1 1555.6 1557.1 1558.6 1560.1 1561.6
1563.1 1564.6 1566.1 1567.6 1569.1 1570.6 1572.1 1573.6 1575.1 1576.6
1578.1 1579.6 1581.1 1582.6 1584.1 1585.6 1587.1 1588.6 1590.1 1591.6
1593.1 1594.6 1596.1 1597.6 1599.1];
    realn_T(2,:) = [1.650 1.651 1.651 1.651 1.651 1.652 1.652 1.652
1.652 1.652 1.653 1.653 1.653 1.653 1.653 1.653 1.654 1.654 1.654 1.654
1.654 1.655 1.655 1.655 1.655 1.655 1.655 1.655 1.656 1.656 1.656 1.656
1.656 1.656 1.656 1.657 1.657 1.657 1.657 1.657 1.657 1.657 1.657 1.658
1.658 1.658 1.658 1.658 1.658 1.658 1.658 1.658 1.658 1.659 1.659 1.659
```

1.659 1.659 1.659 1.659 1.659 1.659 1.659 1.659 1.659 1.660 1.660 1.660
1.660 1.660 1.660 1.660 1.660 1.660 1.660 1.660 1.660 1.660 1.660 1.660
1.660 1.661 1.661 1.661 1.661 1.661 1.661 1.661 1.661 1.661 1.661 1.661
1.661 1.661 1.661 1.661 1.661 1.661 1.661 1.661 1.661 1.661 1.661 1.661
1.661 1.661 1.662 1.662 1.662 1.662 1.662 1.662 1.662 1.662 1.662 1.662
1.662 1.662 1.662 1.662 1.662 1.662 1.662 1.662 1.662 1.662 1.662 1.662
1.662 1.662 1.662 1.662 1.662 1.662 1.662 1.662 1.662 1.662 1.662 1.662
1.662 1.662 1.662 1.662 1.662 1.662 1.662 1.662 1.662 1.662 1.662 1.662
1.662 1.662 1.662 1.662 1.662 1.662 1.662 1.662 1.662 1.662 1.662 1.662
1.662 1.662 1.662 1.662 1.662 1.662 1.662 1.662 1.662 1.662 1.662 1.662
1.662 1.662 1.662 1.662 1.662 1.662 1.662 1.662 1.662 1.662 1.662 1.662
1.661 1.661 1.661 1.661 1.661 1.661 1.661 1.661 1.661 1.661 1.661 1.661
1.661 1.661 1.661 1.661 1.661 1.661 1.661 1.661 1.661 1.661 1.661 1.661
1.661 1.661 1.661 1.661 1.661 1.661 1.661 1.661 1.661 1.661 1.661 1.661
1.661 1.661 1.661 1.661 1.661 1.661 1.661 1.661 1.661 1.660 1.660 1.660
1.660 1.660 1.660 1.660 1.660 1.660 1.660 1.660 1.660 1.660 1.660 1.660
1.660 1.660 1.660 1.660 1.660 1.660 1.660 1.660 1.660 1.660 1.660 1.660
1.660 1.660 1.660 1.660 1.660 1.660 1.660 1.660 1.660 1.660 1.659 1.659
1.659 1.659 1.659 1.659 1.659 1.659 1.659 1.659 1.659 1.659 1.659 1.659
1.659 1.659 1.659 1.659 1.659 1.659 1.659 1.659 1.659 1.659 1.659 1.659
1.659 1.659 1.659 1.659 1.659 1.659 1.659 1.659 1.659 1.658 1.658 1.658
1.658 1.658 1.658 1.658 1.658 1.658 1.658 1.658 1.658 1.658 1.658 1.658
1.658 1.658 1.658 1.658 1.658 1.658 1.658 1.658 1.658 1.658 1.658 1.658
1.658 1.658 1.658 1.658 1.658 1.658 1.658 1.658 1.657 1.657 1.657 1.657
1.657 1.657 1.657 1.657 1.657 1.657 1.657 1.657 1.657 1.657 1.657 1.657
1.657 1.657 1.657 1.657 1.657 1.657 1.657 1.657 1.657 1.657 1.657 1.657
1.657 1.657 1.657 1.657 1.657 1.657 1.656 1.656 1.656 1.656 1.656 1.656
1.656 1.656 1.656 1.656 1.656 1.656 1.656 1.656 1.656 1.656 1.656 1.656
1.656 1.656 1.656 1.656 1.656 1.656 1.656 1.656 1.656 1.656 1.656 1.656
1.656 1.656 1.656 1.656 1.656 1.656 1.655 1.655 1.655 1.655 1.655 1.655
1.655 1.655 1.655 1.655 1.655 1.655 1.655 1.655 1.655 1.655 1.655 1.655
1.655 1.655 1.655 1.655 1.655 1.655 1.655 1.655 1.655 1.655 1.655 1.655
1.655 1.655 1.655 1.655 1.655 1.655 1.655 1.654 1.654 1.654 1.654 1.654
1.654 1.654 1.654 1.654 1.654 1.654 1.654 1.654 1.654 1.654 1.654 1.654
1.654 1.654 1.654 1.654 1.654 1.654 1.654 1.654 1.654 1.654 1.654 1.654
1.654 1.654 1.654 1.654 1.654 1.654 1.654 1.654 1.654 1.654 1.653 1.653
1.653 1.653 1.653 1.653 1.653 1.653 1.653 1.653 1.653 1.653 1.653 1.653
1.653 1.653 1.653 1.653 1.653 1.653 1.653 1.653 1.653 1.653 1.653 1.653
1.653 1.653 1.653 1.653 1.653 1.653 1.653 1.653 1.653 1.653 1.653 1.653
1.653 1.653 1.653 1.652 1.652 1.652 1.652 1.652 1.652 1.652 1.652 1.652
1.652 1.652 1.652 1.652 1.652 1.652 1.652 1.652 1.652 1.652 1.652 1.652
1.652 1.652 1.652 1.652 1.652 1.652 1.652 1.652 1.652 1.652 1.652 1.652
1.652 1.652 1.652 1.652 1.652 1.652 1.652 1.652 1.652 1.652 1.652 1.652
1.651 1.651 1.651 1.651 1.651 1.651 1.651 1.651 1.651 1.651 1.651 1.651
1.651 1.651 1.651 1.651 1.651 1.651 1.651 1.651 1.651 1.651 1.651 1.651
1.651 1.651 1.651 1.651 1.651 1.651 1.651 1.651 1.651 1.651 1.651 1.651
1.651 1.651 1.651 1.651 1.651 1.651 1.651 1.651 1.651 1.651 1.651 1.651
1.650 1.650 1.650 1.650 1.650 1.650 1.650 1.650 1.650 1.650 1.650 1.650
1.650 1.650 1.650 1.650 1.650 1.650 1.650 1.650 1.650 1.650 1.650 1.650
1.650 1.650 1.650 1.650 1.650 1.650 1.650 1.650 1.650 1.650 1.650 1.650
1.650 1.650 1.650 1.650 1.650 1.650 1.650 1.650 1.650 1.650 1.650 1.650
1.650 1.650 1.650 1.650 1.649 1.649 1.649 1.649 1.649 1.649 1.649 1.649

```
1.649 1.649 1.649 1.649 1.649 1.649 1.649 1.649 1.649 1.649 1.649 1.649
1.649 1.649 1.649 1.649 1.649 1.649 1.649 1.649 1.649 1.649 1.649 1.649
1.649 1.649 1.649 1.649 1.649 1.649 1.649 1.649 1.649 1.649 1.649 1.649
1.649 1.649 1.649 1.649 1.649 1.649 1.649 1.649 1.649 1.649 1.649 1.649
1.649 1.649 1.648 1.648 1.648 1.648 1.648 1.648 1.648 1.648 1.648 1.648
1.648 1.648 1.648 1.648 1.648 1.648 1.648 1.648 1.648 1.648 1.648 1.648
1.648 1.648 1.648 1.648 1.648 1.648 1.648 1.648 1.648 1.648 1.648 1.648
1.648 1.648 1.648 1.648 1.648 1.648 1.648 1.648 1.648 1.648 1.648 1.648
1.648 1.648 1.648 1.648 1.648 1.648 1.647 1.647 1.647 1.647 1.647 1.647
1.647 1.647 1.647 1.647 1.647 1.647 1.647 1.647 1.647 1.647 1.647 1.647
1.647 1.647 1.647 1.647 1.647 1.647 1.647 1.647 1.647 1.647 1.647 1.647
1.647 1.646 1.646 1.646 1.646 1.646 1.646 1.646 1.646 1.646 1.646 1.646
1.646 1.646 1.646 1.646 1.646 1.646 1.646 1.646 1.646 1.646 1.646 1.646
1.646 1.646 1.646 1.646 1.646 1.646 1.646 1.646 1.646 1.646 1.646 1.646
1.645 1.645 1.645 1.645 1.645 1.645 1.645 1.645 1.645 1.645 1.645 1.645
1.645 1.645 1.645 1.645 1.645 1.645 1.645 1.645 1.645 1.645 1.645 1.645
1.645 1.645 1.645 1.645 1.645 1.645 1.645 1.645 1.645 1.645 1.645 1.645
1.645 1.645 1.645 1.645 1.645 1.644 1.644 1.644 1.644 1.644 1.644 1.644
1.644 1.644 1.644 1.644 1.644 1.644 1.644 1.644 1.644 1.644 1.644 1.644
1.644 1.644 1.644 1.644 1.644 1.644 1.644 1.644 1.644 1.644 1.644 1.644
1.644 1.644 1.644 1.644 1.644 1.644 1.644 1.644 1.644 1.644 1.644 1.644
1.644 1.644 1.644 1.644 1.644 1.643 1.643 1.643 1.643 1.643 1.643 1.643
1.643 1.643 1.643 1.643 1.643 1.643 1.643 1.643 1.643 1.643 1.643 1.643
1.643 1.643 1.643 1.643 1.643 1.643 1.643 1.643 1.643 1.643 1.643 1.643
1.643 1.643 1.643 1.643 1.643 1.643 1.643 1.643 1.643 1.643 1.643 1.643
1.643 1.643 1.643 1.643 1.643 1.643 1.643 1.643 1.643 1.643 1.643 1.643
1.643 1.643 1.643 1.642 1.642 1.642 1.642 1.642 1.642 1.642 1.642 1.642
1.642 1.642 1.642 1.642 1.642 1.642 1.642 1.642 1.642 1.642 1.642 1.642
1.642 1.642 1.642 1.642 1.642 1.642 1.642 1.642 1.642 1.642 1.642 1.642
1.642 1.642 1.642 1.642 1.642 1.642 1.642 1.642 1.642 1.642 1.642 1.642
1.642 1.642 1.642 1.642 1.642 1.642 1.642 1.642 1.642 1.642 1.642 1.642
1.642 1.642 1.642 1.642 1.641 1.641 1.641 1.641 1.641 1.641 1.641 1.641
1.641 1.641 1.641 1.641 1.641 1.641 1.641 1.641 1.641 1.641 1.641 1.641
1.641 1.641 1.641 1.641 1.641 1.641 1.641 1.641 1.641 1.641 1.641 1.641
1.641 1.641 1.641 1.641 1.641 1.641 1.641 1.641 1.641 1.641 1.641 1.641
1.641 1.641 1.641 1.641 1.641 1.641 1.641 1.641 1.641 1.641 1.641 1.641
1.641 1.641 1.641 1.641 1.641 1.641 1.641 1.641 1.641 1.641 1.641 1.641
1.641 1.641 1.641 1.641 1.641 1.641 1.641 1.641 1.641 1.641 1.641 1.641
1.641 1.641 1.640 1.640 1.640 1.640 1.640 1.640 1.640 1.640 1.640 1.640
1.640 1.640 1.640 1.640 1.640 1.640 1.640 1.640 1.640 1.640 1.640 1.640
1.640 1.640 1.640 1.640 1.640 1.640 1.640 1.640 1.640 1.640 1.640  ];
    imagn_T(1,:) = 1e-9*[379.5 380.2 381.0 381.7 382.5 383.2 384.0
384.7 385.5 386.2 387.0 387.7 388.5 389.2 390.0 390.7 391.5 392.2 393.0
393.7 394.5 395.2 396.0 396.7 397.5 398.2 399.0 399.7 400.5 401.2 402.0
402.7 403.5 404.2 405.0 405.7 406.5 407.2 408.0 408.7 409.5 410.2 411.0
411.7 412.5 413.2 414.0 414.7 415.5 416.2 417.0 417.7 418.5 419.2 420.0
420.7 421.4 422.2 422.9 423.7 424.4 425.2 425.9 426.7 427.4 428.2 428.9
429.7 430.4 431.2 431.9 432.6 433.4 434.1 434.9 435.6 436.4 437.1 437.9
438.6 439.4 440.1 440.9 441.6 442.3 443.1 443.8 444.6 445.3 446.1 446.8
447.6 448.3 449.0 449.8 450.5 451.3 452.0 452.8 453.5 454.3 455.0 455.7
456.5 457.2 458.0 458.7 459.5 460.2 460.9 461.7 462.4 463.2 463.9 464.7
```

465.4 466.1 466.9 467.6 468.4 469.1 469.8 470.6 471.3 472.1 472.8 473.6
474.3 475.0 475.8 476.5 477.3 478.0 478.7 479.5 480.2 481.0 481.7 482.4
483.2 483.9 484.7 485.4 486.1 486.9 487.6 488.4 489.1 489.8 490.6 491.3
492.1 492.8 493.5 494.3 495.0 495.8 496.5 497.2 498.0 498.7 499.5 500.2
500.9 501.7 502.4 503.1 503.9 504.6 505.4 506.1 506.8 507.6 508.3 509.0
509.8 510.5 511.3 512.0 512.7 513.5 514.2 514.9 515.7 516.4 517.2 517.9
518.6 519.4 520.1 520.8 521.6 522.3 523.0 523.8 524.5 525.3 526.0 526.7
527.5 528.2 528.9 529.7 530.4 531.1 531.9 532.6 533.3 534.1 534.8 535.5
536.3 537.0 537.7 538.5 539.2 539.9 540.7 541.4 542.2 542.9 543.6 544.4
545.1 545.8 546.6 547.3 548.0 548.8 549.5 550.2 550.9 551.7 552.4 553.1
553.9 554.6 555.3 556.1 556.8 557.5 558.3 559.0 559.7 560.5 561.2 561.9
562.7 563.4 564.1 564.9 565.6 566.3 567.0 567.8 568.5 569.2 570.0 570.7
571.4 572.2 572.9 573.6 574.4 575.1 575.8 576.5 577.3 578.0 578.7 579.5
580.2 580.9 581.6 582.4 583.1 583.8 584.6 585.3 586.0 586.8 587.5 588.2
588.9 589.7 590.4 591.1 591.8 592.6 593.3 594.0 594.8 595.5 596.2 596.9
597.7 598.4 599.1 599.9 600.6 601.3 602.0 602.8 603.5 604.2 604.9 605.7
606.4 607.1 607.8 608.6 609.3 610.0 610.7 611.5 612.2 612.9 613.7 614.4
615.1 615.8 616.6 617.3 618.0 618.7 619.5 620.2 620.9 621.6 622.4 623.1
623.8 624.5 625.2 626.0 626.7 627.4 628.1 628.9 629.6 630.3 631.0 631.8
632.5 633.2 633.9 634.7 635.4 636.1 636.8 637.5 638.3 639.0 639.7 640.4
641.2 641.9 642.6 643.3 644.0 644.8 645.5 646.2 646.9 647.7 648.4 649.1
649.8 650.5 651.3 652.0 652.7 653.4 654.1 654.9 655.6 656.3 657.0 657.8
658.5 659.2 659.9 660.6 661.4 662.1 662.8 663.5 664.2 665.0 665.7 666.4
667.1 667.8 668.5 669.3 670.0 670.7 671.4 672.1 672.9 673.6 674.3 675.0
675.7 676.5 677.2 677.9 678.6 679.3 680.0 680.8 681.5 682.2 682.9 683.6
684.4 685.1 685.8 686.5 687.2 687.9 688.7 689.4 690.1 690.8 691.5 692.2
693.0 693.7 694.4 695.1 695.8 696.5 697.2 698.0 698.7 699.4 700.1 700.8
701.5 702.3 703.0 703.7 704.4 705.1 705.8 706.5 707.3 708.0 708.7 709.4
710.1 710.8 711.5 712.3 713.0 713.7 714.4 715.1 715.8 716.5 717.3 718.0
718.7 719.4 720.1 720.8 721.5 722.3 723.0 723.7 724.4 725.1 725.8 726.5
727.2 728.0 728.7 729.4 730.1 730.8 731.5 732.2 732.9 733.6 734.4 735.1
735.8 736.5 737.2 737.9 738.6 739.3 740.0 740.8 741.5 742.2 742.9 743.6
744.3 745.0 745.7 746.4 747.2 747.9 748.6 749.3 750.0 750.7 751.4 752.1
752.8 753.5 754.2 755.0 755.7 756.4 757.1 757.8 758.5 759.2 759.9 760.6
761.3 762.0 762.8 763.5 764.2 764.9 765.6 766.3 767.0 767.7 768.4 769.1
769.8 770.5 771.2 772.0 772.7 773.4 774.1 774.8 775.5 776.2 776.9 777.6
778.3 779.0 779.7 780.4 781.1 781.8 782.5 783.3 784.0 784.7 785.4 786.1
786.8 787.5 788.2 788.9 789.6 790.3 791.0 791.7 792.4 793.1 793.8 794.5
795.2 795.9 796.6 797.4 798.1 798.8 799.5 800.2 800.9 801.6 802.3 803.0
803.7 804.4 805.1 805.8 806.5 807.2 807.9 808.6 809.3 810.0 810.7 811.4
812.1 812.8 813.5 814.2 814.9 815.6 816.3 817.0 817.7 818.4 819.1 819.8
820.5 821.2 821.9 822.6 823.3 824.0 824.7 825.4 826.1 826.9 827.6 828.3
829.0 829.7 830.4 831.1 831.8 832.5 833.2 833.9 834.6 835.3 836.0 836.7
837.3 838.0 838.7 839.4 840.1 840.8 841.5 842.2 842.9 843.6 844.3 845.0
845.7 846.4 847.1 847.8 848.5 849.2 849.9 850.6 851.3 852.0 852.7 853.4
854.1 854.8 855.5 856.2 856.9 857.6 858.3 859.0 859.7 860.4 861.1 861.8
862.5 863.2 863.9 864.6 865.3 866.0 866.6 867.3 868.0 868.7 869.4 870.1
870.8 871.5 872.2 872.9 873.6 874.3 875.0 875.7 876.4 877.1 877.8 878.5
879.2 879.9 880.5 881.2 881.9 882.6 883.3 884.0 884.7 885.4 886.1 886.8
887.5 888.2 888.9 889.6 890.3 890.9 891.6 892.3 893.0 893.7 894.4 895.1
895.8 896.5 897.2 897.9 898.6 899.3 899.9 900.6 901.3 902.0 902.7 903.4
904.1 904.8 905.5 906.2 906.9 907.6 908.2 908.9 909.6 910.3 911.0 911.7
912.4 913.1 913.8 914.5 915.1 915.8 916.5 917.2 917.9 918.6 919.3 920.0

```
920.7 921.4 922.0 922.7 923.4 924.1 924.8 925.5 926.2 926.9 927.6 928.2
928.9 929.6 930.3 931.0 931.7 932.4 933.1 933.7 934.4 935.1 935.8 936.5
937.2 937.9 938.6 939.2 939.9 940.6 941.3 942.0 942.7 943.4 944.7 946.5
947.8 949.5 951.3 952.6 954.3 956.1 957.4 959.1 960.8 962.5 964.2 965.6
967.3 969.0 970.4 972.1 973.8 975.2 976.9 978.6 980.0 981.7 983.4 985.1
986.7 988.2 989.8 991.5 993.0 994.6 996.3 997.7 999.4 1001.1 1002.5
1004.2 1005.8 1007.5 1009.2 1010.6 1012.3 1013.9 1015.4 1017.1 1018.7
1020.2 1021.8 1023.5 1025.1 1026.8 1028.2 1029.9 1031.5 1033.0 1034.7
1036.3 1037.9 1039.6 1041.1 1042.7 1044.3 1045.8 1047.5 1049.1 1050.6
1052.2 1053.8 1055.5 1057.1 1058.6 1060.2 1061.8 1063.4 1065.0 1066.6
1068.2 1069.8 1071.4 1073.0 1074.6 1076.1 1077.7 1079.3 1080.9 1082.5
1084.1 1085.7 1087.3 1088.9 1090.5 1092.0 1093.6 1095.2 1096.8 1098.4
1100.0 1101.6 1103.2 1104.7 1106.3 1107.9 1109.5 1111.1 1112.7 1114.3
1115.8 1117.4 1119.0 1120.6 1122.2 1123.8 1125.3 1126.9 1128.5 1130.1
1131.7 1133.2 1134.8 1136.4 1138.0 1139.6 1141.1 1142.7 1144.3 1145.9
1147.5 1149.0 1150.6 1152.2 1153.8 1155.3 1156.9 1158.5 1160.1 1161.7
1163.2 1164.8 1166.4 1168.0 1169.5 1171.1 1172.7 1174.2 1175.8 1177.4
1179.0 1180.5 1182.1 1183.7 1185.3 1186.8 1188.4 1190.0 1191.5 1193.1
1194.7 1196.2 1197.8 1199.4 1201.0 1202.5 1204.1 1205.7 1207.2 1208.8
1210.4 1211.9 1213.5 1215.1 1216.6 1218.2 1219.8 1221.3 1222.9 1224.5
1226.0 1227.6 1229.1 1230.7 1232.3 1233.8 1235.4 1237.0 1238.5 1240.1
1241.6 1243.2 1244.8 1246.3 1247.9 1249.4 1251.0 1252.6 1254.1 1255.7
1257.2 1258.8 1260.4 1261.9 1263.5 1265.0 1266.6 1268.1 1269.7 1271.2
1272.8 1274.4 1275.9 1277.5 1279.0 1280.6 1282.1 1283.7 1285.2 1286.8
1288.3 1289.9 1291.4 1293.0 1294.5 1296.1 1297.7 1299.2 1300.8 1302.3
1303.9 1305.4 1307.0 1308.5 1310.0 1311.6 1313.1 1314.7 1316.2 1317.8
1319.3 1320.9 1322.4 1324.0 1325.5 1327.1 1328.6 1330.2 1331.7 1333.2
1334.8 1336.3 1337.9 1339.4 1341.0 1342.5 1344.0 1345.6 1347.1 1348.7
1350.2 1351.8 1353.3 1354.8 1356.4 1357.9 1359.5 1361.0 1362.5 1364.1
1365.6 1367.1 1368.7 1370.2 1371.8 1373.3 1374.8 1376.4 1377.9 1379.4
1381.0 1382.5 1384.0 1385.6 1387.1 1388.6 1390.2 1391.7 1393.2 1394.8
1396.3 1397.8 1399.4 1400.9 1402.4 1404.0 1405.5 1407.0 1408.6 1410.1
1411.6 1413.1 1414.7 1416.2 1417.7 1419.3 1420.8 1422.3 1423.8 1425.4
1426.9 1428.4 1430.0 1431.5 1433.0 1434.5 1436.1 1437.6 1439.1 1440.6
1442.2 1443.7 1445.2 1446.7 1448.2 1449.8 1451.3 1452.8 1454.3 1455.9
1457.4 1458.9 1460.4 1461.9 1463.5 1465.0 1466.5 1468.0 1469.5 1471.1
1472.6 1474.1 1475.6 1477.1 1478.6 1480.2 1481.7 1483.2 1484.7 1486.2
1487.7 1489.2 1490.8 1492.3 1493.8 1495.3 1496.8 1498.3 1499.8 1501.4
1502.9 1504.4 1505.9 1507.4 1508.9 1510.4 1511.9 1513.5 1515.0 1516.5
1518.0 1519.5 1521.0 1522.5 1524.0 1525.5 1527.0 1528.5 1530.0 1531.6
1533.1 1534.6 1536.1 1537.6 1539.1 1540.6 1542.1 1543.6 1545.1 1546.6
1548.1 1549.6 1551.1 1552.6 1554.1 1555.6 1557.1 1558.6 1560.1 1561.6
1563.1 1564.6 1566.1 1567.6 1569.1 1570.6 1572.1 1573.6 1575.1 1576.6
1578.1 1579.6 1581.1 1582.6 1584.1 1585.6 1587.1 1588.6 1590.1 1591.6
1593.1 1594.6 1596.1 1597.6 1599.1];
    imagn_T(2,:) = [0 0 0 0 0 0 0 0 0 0 0 0 0 0 0 0 0 0 0 0 0 0 0 0 0 0 0 0
0 0 0 0 0 0 0 0 0 0 0 0 0 0 0 0 0 0 0 0 0 0 0 0 0 0 0 0 0 0 0 0 0 0 0 0 0
0 0 0 0 0 0 0 0 0 0 0 0 0 0 0 0 0 0 0 0 0 0 0 0 0 0 0 0 0 0 0 0 0 0 0 0 0
0 0 0 0 0 0 0 0 0 0 0 0 0 0 0 0 0 0 0 0 0 0 0 0 0 0 0 0 0 0 0 0 0 0 0 0 0
0 0 0 0 0 0 0 0 0 0 0 0 0 0 0 0 0 0 0 0 0 0 0 0 0 0 0 0 0 0 0 0 0 0 0 0 0
0 0 0 0 0 0 0 0 0 0 0 0 0 0 0 0 0 0 0 0 0 0 0 0 0 0 0 0 0 0 0 0 0 0 0 0 0
0 0 0 0 0 0 0 0 0 0 0 0 0 0 0 0 0 0 0 0 0 0 0 0 0 0 0 0 0 0 0 0 0 0 0 0 0
0 0 0 0 0 0 0 0 0 0 0 0 0 0 0 0 0 0 0 0 0 0 0 0 0 0 0 0 0 0 0 0 0 0 0 0 0
```

```
0 0 0 
```

```
3.770   3.762   3.753   3.745   3.737   3.730   3.723   3.716   3.710
3.704   3.698   3.693   3.687   3.682   3.677   3.673   3.668   3.664
3.660   3.656   3.653   3.650   3.648   3.646   3.647   3.649   3.649
3.648   3.639   3.626   3.613   3.599   3.588   3.579   3.571   3.563
3.556   3.550   3.544   3.538   3.532   3.527   3.522   3.517   3.513
3.508   3.504   3.500   3.496   3.492   3.488   3.484   3.481   3.477
3.474   3.471   3.468   3.464   3.461   3.459   3.456   3.453   3.450
3.447   3.445   3.442   3.440   3.437   3.435   3.433   3.430   3.428
3.426   3.424   3.421   3.419   3.417   3.415   3.413   3.412   3.410
3.408   3.406   3.404   3.402   3.401   3.399   3.397   3.396   3.394
3.392];
    imagn_a1 = [1.965   1.932   1.910   1.901   1.901   1.906   1.914
1.927   1.943   1.962   1.985   2.012   2.042   2.076   2.114   2.160
2.201   2.177   2.110   2.013   1.909   1.872   1.839   1.682   1.466
1.235   1.017   0.874   0.777   0.699   0.639   0.591   0.551   0.518
0.489   0.463   0.439   0.418   0.399   0.382   0.366   0.351   0.338
0.326   0.315   0.305   0.295   0.286   0.278   0.270   0.262   0.255
0.249   0.242   0.236   0.230   0.224   0.219   0.213   0.208   0.203
0.198   0.193   0.188   0.183   0.178   0.173   0.167   0.161   0.154
0.148   0.143   0.138   0.134   0.130   0.126   0.123   0.120   0.117
0.113   0.110   0.107   0.104   0.101   0.098   0.095   0.092   0.089
0.086   0.083   0.081   0.078   0.075   0.072   0.068   0.062   0.051
0.037   0.023   0.011   0.005   0.002   0.000   0.000   0.000   0.000
0.000   0.000   0.000   0.000   0.000   0.000   0.000   0.000   0.000
0.000   0.000   0.000   0.000   0.000   0.000   0.000   0.000   0.000
0.000   0.000   0.000   0.000   0.000   0.000   0.000   0.000   0.000
0.000   0.000   0.000   0.000   0.000   0.000   0.000   0.000   0.000
0.000   0.000   0.000   0.000   0.000   0.000   0.000   0.000   0.000
0.000   0.000   0.000   0.000   0.000   0.000   0.000   0.000   0.000
0.000];
    rn_a1 = interp1(wl_a1, realn_a1, lambda, 'pchip');
    in_a1 = interp1(wl_a1, imagn_a1, lambda, 'pchip');
    x = rn_a1 + in_a1;
end

if mat=='a2'
    % Al0.2Ga0.8As
    wl_a2 = 1e-9*[300   305 310 315 320 325 330 335 340 345 350 355 360
365 370 375 380 385 390 395 400 405 410 415 420 425 430 435 440 445 450
455 460 465 470 475 480 485 490 495 500 505 510 515 520 525 530 535 540
545 550 555 560 565 570 575 580 585 590 595 600 605 610 615 620 625 630
635 640 645 650 655 660 665 670 675 680 685 690 695 700 705 710 715 720
725 730 735 740 745 750 755 760 765 770 775 780 785 790 795 800 805 810
815 820 825 830 835 840 845 850 855 860 865 870 875 880 885 890 895 900
905 910 915 920 925 930 935 940 945 950 955 960 965 970 975 980 985 990
995 1000    1005    1010    1015    1020    1025    1030    1035
1040    1045    1050    1055    1060    1065    1070    1075    1080
1085    1090    1095    1100];
    realn_a2 = [3.788   3.727   3.681   3.650   3.632   3.623   3.622
3.628   3.642   3.663   3.693   3.732   3.784   3.857   3.952   4.089
4.251   4.371   4.470   4.563   4.658   4.799   4.933   4.949   4.900
4.822   4.730   4.652   4.580   4.517   4.460   4.409   4.363   4.321
```

```
4.282   4.245   4.211   4.180   4.150   4.122   4.096   4.072   4.049
4.027   4.007   3.987   3.969   3.952   3.936   3.921   3.906   3.893
3.880   3.867   3.855   3.844   3.834   3.824   3.815   3.806   3.796
3.786   3.775   3.765   3.754   3.744   3.735   3.727   3.719   3.711
3.703   3.696   3.689   3.683   3.677   3.671   3.665   3.660   3.655
3.651   3.648   3.646   3.647   3.648   3.646   3.636   3.619   3.603
3.588   3.575   3.565   3.555   3.547   3.539   3.531   3.524   3.517
3.511   3.505   3.499   3.494   3.488   3.483   3.478   3.473   3.469
3.464   3.460   3.455   3.451   3.447   3.443   3.440   3.436   3.432
3.429   3.426   3.422   3.419   3.416   3.413   3.410   3.407   3.404
3.401   3.399   3.396   3.393   3.391   3.388   3.386   3.383   3.381
3.379   3.376   3.374   3.372   3.370   3.368   3.366   3.364   3.362
3.360   3.358   3.356   3.354   3.352   3.351   3.349   3.347   3.346
3.344   3.342   3.341   3.339   3.338   3.336   3.335   3.333   3.332
3.331];
    imagn_a2 = [1.959   1.931   1.913   1.906   1.906   1.910   1.918
1.930   1.945   1.965   1.988   2.016   2.048   2.088   2.128   2.132
2.104   2.022   1.917   1.859   1.796   1.651   1.459   1.241   1.028
0.885   0.781   0.699   0.639   0.589   0.549   0.514   0.483   0.456
0.432   0.410   0.390   0.372   0.356   0.341   0.328   0.315   0.303
0.293   0.283   0.273   0.265   0.256   0.248   0.240   0.233   0.226
0.219   0.212   0.206   0.199   0.193   0.186   0.180   0.172   0.164
0.157   0.150   0.144   0.139   0.134   0.129   0.125   0.121   0.117
0.113   0.109   0.105   0.102   0.098   0.094   0.091   0.087   0.083
0.080   0.077   0.073   0.067   0.056   0.039   0.023   0.009   0.003
0.001   0.001   0.000   0.000   0.000   0.000   0.000   0.000   0.000
0.000   0.000   0.000   0.000   0.000   0.000   0.000   0.000   0.000
0.000   0.000   0.000   0.000   0.000   0.000   0.000   0.000   0.000
0.000   0.000   0.000   0.000   0.000   0.000   0.000   0.000   0.000
0.000   0.000   0.000   0.000   0.000   0.000   0.000   0.000   0.000
0.000   0.000   0.000   0.000   0.000   0.000   0.000   0.000   0.000
0.000   0.000   0.000   0.000   0.000   0.000   0.000   0.000   0.000
0.000];
    rn_a2 = interp1(wl_a2, realn_a2, lambda, 'pchip');
    in_a2 = interp1(wl_a2, imagn_a2, lambda, 'pchip');
    x = rn_a2 + in_a2;
end

if mat=='a3'
    % Al0.3Ga0.7As
    wl_a3 = 1e-9*[300   305 310 315 320 325 330 335 340 345 350 355 360
365 370 375 380 385 390 395 400 405 410 415 420 425 430 435 440 445 450
455 460 465 470 475 480 485 490 495 500 505 510 515 520 525 530 535 540
545 550 555 560 565 570 575 580 585 590 595 600 605 610 615 620 625 630
635 640 645 650 655 660 665 670 675 680 685 690 695 700 705 710 715 720
725 730 735 740 745 750 755 760 765 770 775 780 785 790 795 800 805 810
815 820 825 830 835 840 845 850 855 860 865 870 875 880 885 890 895 900
905 910 915 920 925 930 935 940 945 950 955 960 965 970 975 980 985 990
995 1000    1005    1010    1015    1020    1025    1030    1035
1040    1045    1050    1055    1060    1065    1070    1075    1080
1085    1090    1095    1100];
```

```
    realn_a3 = [3.792   3.738   3.699   3.675   3.662   3.658   3.663
3.675   3.694   3.723   3.763   3.817   3.890   4.004   4.145   4.276
4.400   4.497   4.586   4.723   4.851   4.889   4.867   4.802   4.711
4.631   4.556   4.490   4.431   4.379   4.331   4.287   4.247   4.210
4.176   4.143   4.113   4.085   4.058   4.034   4.011   3.989   3.969
3.949   3.931   3.914   3.898   3.883   3.869   3.856   3.843   3.831
3.820   3.808   3.796   3.783   3.770   3.758   3.746   3.735   3.725
3.715   3.706   3.697   3.689   3.681   3.673   3.666   3.660   3.654
3.648   3.645   3.644   3.645   3.643   3.633   3.613   3.593   3.576
3.562   3.550   3.540   3.530   3.521   3.512   3.504   3.497   3.489
3.482   3.476   3.469   3.463   3.457   3.452   3.446   3.441   3.436
3.431   3.426   3.421   3.417   3.413   3.408   3.404   3.400   3.396
3.392   3.389   3.385   3.382   3.378   3.375   3.372   3.369   3.365
3.362   3.359   3.357   3.354   3.351   3.348   3.346   3.343   3.341
3.338   3.336   3.333   3.331   3.329   3.326   3.324   3.322   3.320
3.318   3.316   3.314   3.312   3.310   3.308   3.306   3.305   3.303
3.301   3.299   3.298   3.296   3.294   3.293   3.291   3.290   3.288
3.287   3.285   3.284   3.282   3.281   3.280   3.278   3.277   3.276
3.274];
    imagn_a3 = [1.955   1.930   1.914   1.906   1.906   1.909   1.916
1.928   1.943   1.964   1.989   2.022   2.055   2.076   2.078   2.026
1.934   1.862   1.784   1.662   1.505   1.295   1.070   0.909   0.788
0.701   0.637   0.584   0.542   0.505   0.473   0.445   0.420   0.397
0.377   0.359   0.342   0.327   0.313   0.301   0.289   0.278   0.267
0.258   0.248   0.239   0.231   0.223   0.215   0.207   0.199   0.191
0.182   0.173   0.164   0.156   0.148   0.142   0.137   0.132   0.127
0.122   0.117   0.112   0.108   0.103   0.099   0.094   0.090   0.086
0.082   0.078   0.073   0.062   0.045   0.024   0.010   0.003   0.001
0.001   0.001   0.000   0.000   0.000   0.000   0.000   0.000   0.000
0.000   0.000   0.000   0.000   0.000   0.000   0.000   0.000   0.000
0.000   0.000   0.000   0.000   0.000   0.000   0.000   0.000   0.000
0.000   0.000   0.000   0.000   0.000   0.000   0.000   0.000   0.000
0.000   0.000   0.000   0.000   0.000   0.000   0.000   0.000   0.000
0.000   0.000   0.000   0.000   0.000   0.000   0.000   0.000   0.000
0.000   0.000   0.000   0.000   0.000   0.000   0.000   0.000   0.000
0.000   0.000   0.000   0.000   0.000   0.000   0.000   0.000   0.000
0.000];
    rn_a3 = interp1(wl_a3, realn_a3, lambda, 'pchip');
    in_a3 = interp1(wl_a3, imagn_a3, lambda, 'pchip');
    x = rn_a3 + in_a3;
end

if mat=='a4'
    % Al0.4Ga0.6As
    wl_a4 = 1e-9*[300   305 310 315 320 325 330 335 340 345 350 355 360
365 370 375 380 385 390 395 400 405 410 415 420 425 430 435 440 445 450
455 460 465 470 475 480 485 490 495 500 505 510 515 520 525 530 535 540
545 550 555 560 565 570 575 580 585 590 595 600 605 610 615 620 625 630
635 640 645 650 655 660 665 670 675 680 685 690 695 700 705 710 715 720
725 730 735 740 745 750 755 760 765 770 775 780 785 790 795 800 805 810
815 820 825 830 835 840 845 850 855 860 865 870 875 880 885 890 895 900
```

```
905 910 915 920 925 930 935 940 945 950 955 960 965 970 975 980 985 990
995 1000    1005    1010    1015    1020    1025    1030    1035
1040    1045    1050    1055    1060    1065    1070    1075    1080
1085    1090    1095    1100];
    realn_a4 = [3.806   3.760   3.727   3.708   3.702   3.702   3.712
3.730   3.758   3.798   3.854   3.943   4.057   4.186   4.325   4.434
4.526   4.655   4.782   4.845   4.857   4.803   4.708   4.624   4.543
4.473   4.411   4.355   4.306   4.260   4.218   4.180   4.144   4.111
4.080   4.051   4.024   3.999   3.976   3.954   3.934   3.914   3.897
3.880   3.864   3.849   3.836   3.821   3.807   3.791   3.776   3.762
3.748   3.735   3.724   3.712   3.702   3.692   3.682   3.673   3.665
3.657   3.650   3.645   3.642   3.644   3.641   3.627   3.603   3.581
3.563   3.548   3.535   3.523   3.512   3.502   3.493   3.484   3.475
3.467   3.460   3.452   3.445   3.438   3.432   3.426   3.420   3.414
3.408   3.403   3.398   3.392   3.387   3.383   3.378   3.374   3.369
3.365   3.361   3.357   3.353   3.349   3.345   3.342   3.338   3.335
3.331   3.328   3.325   3.322   3.319   3.316   3.313   3.310   3.307
3.304   3.302   3.299   3.297   3.294   3.292   3.289   3.287   3.285
3.282   3.280   3.278   3.276   3.274   3.272   3.270   3.268   3.266
3.264   3.262   3.260   3.259   3.257   3.255   3.253   3.252   3.250
3.249   3.247   3.245   3.244   3.242   3.241   3.240   3.238   3.237
3.235   3.234   3.233   3.231   3.230   3.229   3.228   3.226   3.225
3.224];
    imagn_a4 = [1.953   1.930   1.914   1.906   1.905   1.908   1.915
1.928   1.945   1.970   1.998   2.028   2.046   2.014   1.948   1.876
1.791   1.685   1.548   1.342   1.114   0.940   0.799   0.700   0.629
0.573   0.529   0.491   0.458   0.430   0.404   0.381   0.361   0.343
0.326   0.311   0.297   0.284   0.272   0.261   0.250   0.240   0.230
0.221   0.212   0.202   0.192   0.182   0.171   0.161   0.153   0.146
0.140   0.134   0.128   0.122   0.117   0.112   0.106   0.101   0.096
0.091   0.086   0.081   0.076   0.065   0.045   0.022   0.007   0.002
0.001   0.001   0.001   0.000   0.000   0.000   0.000   0.000   0.000
0.000   0.000   0.000   0.000   0.000   0.000   0.000   0.000   0.000
0.000   0.000   0.000   0.000   0.000   0.000   0.000   0.000   0.000
0.000   0.000   0.000   0.000   0.000   0.000   0.000   0.000   0.000
0.000   0.000   0.000   0.000   0.000   0.000   0.000   0.000   0.000
0.000   0.000   0.000   0.000   0.000   0.000   0.000   0.000   0.000
0.000   0.000   0.000   0.000   0.000   0.000   0.000   0.000   0.000
0.000   0.000   0.000   0.000   0.000   0.000   0.000   0.000   0.000
0.000   0.000   0.000   0.000   0.000   0.000   0.000   0.000   0.000
0.000];
    rn_a4 = interp1(wl_a4, realn_a4, lambda, 'pchip');
    in_a4 = interp1(wl_a4, imagn_a4, lambda, 'pchip');
    x = rn_a4 + in_a4;
end

if mat=='a5'
    % Al0.5Ga0.5As
    wl_a5 = 1e-9*[300   305 310 315 320 325 330 335 340 345 350 355 360
365 370 375 380 385 390 395 400 405 410 415 420 425 430 435 440 445 450
455 460 465 470 475 480 485 490 495 500 505 510 515 520 525 530 535 540
```

```
545 550 555 560 565 570 575 580 585 590 595 600 605 610 615 620 625 630
635 640 645 650 655 660 665 670 675 680 685 690 695 700 705 710 715 720
725 730 735 740 745 750 755 760 765 770 775 780 785 790 795 800 805 810
815 820 825 830 835 840 845 850 855 860 865 870 875 880 885 890 895 900
905 910 915 920 925 930 935 940 945 950 955 960 965 970 975 980 985 990
995 1000    1005    1010    1015    1020    1025    1030    1035
1040    1045    1050    1055    1060    1065    1070    1075    1080
1085    1090    1095    1100];
    realn_a5 = [3.834   3.794   3.768   3.754   3.753   3.759   3.776
3.803   3.845   3.914   4.008   4.134   4.275   4.388   4.490   4.616
4.748   4.829   4.860   4.811   4.716   4.628   4.538   4.462   4.395
4.336   4.284   4.236   4.192   4.152   4.115   4.081   4.050   4.020
3.993   3.968   3.944   3.923   3.902   3.884   3.866   3.849   3.832
3.814   3.796   3.779   3.762   3.747   3.733   3.720   3.707   3.695
3.684   3.673   3.664   3.654   3.647   3.645   3.643   3.634   3.618
3.597   3.574   3.556   3.539   3.525   3.511   3.499   3.488   3.477
3.467   3.458   3.449   3.441   3.433   3.425   3.417   3.410   3.403
3.397   3.390   3.384   3.378   3.373   3.367   3.362   3.356   3.351
3.346   3.342   3.337   3.333   3.328   3.324   3.320   3.316   3.312
3.308   3.304   3.301   3.297   3.294   3.291   3.287   3.284   3.281
3.278   3.275   3.272   3.269   3.266   3.264   3.261   3.258   3.256
3.253   3.251   3.249   3.246   3.244   3.242   3.240   3.237   3.235
3.233   3.231   3.229   3.227   3.225   3.224   3.222   3.220   3.218
3.216   3.215   3.213   3.211   3.210   3.208   3.207   3.205   3.204
3.202   3.201   3.199   3.198   3.197   3.195   3.194   3.193   3.191
3.190   3.189   3.188   3.186   3.185   3.184   3.183   3.182   3.181
3.179];
    imagn_a5 = [1.956   1.934   1.919   1.911   1.910   1.914   1.924
1.942   1.965   1.994   2.019   2.006   1.963   1.898   1.809   1.705
1.578   1.377   1.144   0.953   0.794   0.685   0.612   0.553   0.508
0.469   0.437   0.408   0.383   0.360   0.340   0.322   0.306   0.291
0.277   0.264   0.252   0.241   0.230   0.219   0.208   0.196   0.185
0.173   0.162   0.153   0.146   0.139   0.133   0.126   0.120   0.114
0.108   0.102   0.096   0.091   0.085   0.078   0.068   0.049   0.024
0.010   0.005   0.003   0.001   0.001   0.000   0.000   0.000   0.000
0.000   0.000   0.000   0.000   0.000   0.000   0.000   0.000   0.000
0.000   0.000   0.000   0.000   0.000   0.000   0.000   0.000   0.000
0.000   0.000   0.000   0.000   0.000   0.000   0.000   0.000   0.000
0.000   0.000   0.000   0.000   0.000   0.000   0.000   0.000   0.000
0.000   0.000   0.000   0.000   0.000   0.000   0.000   0.000   0.000
0.000   0.000   0.000   0.000   0.000   0.000   0.000   0.000   0.000
0.000   0.000   0.000   0.000   0.000   0.000   0.000   0.000   0.000
0.000   0.000   0.000   0.000   0.000   0.000   0.000   0.000   0.000
0.000   0.000   0.000   0.000   0.000   0.000   0.000   0.000   0.000
0.000   0.000   0.000   0.000   0.000   0.000   0.000   0.000   0.000
0.000];
    rn_a5 = interp1(wl_a5, realn_a5, lambda, 'pchip');
    in_a5 = interp1(wl_a5, imagn_a5, lambda, 'pchip');
    x = rn_a5 + in_a5;
end

if mat=='a6'
```

```
    % Al0.6Ga0.4As
    wl_a6 = 1e-9*[300   305 310 315 320 325 330 335 340 345 350 355 360
365 370 375 380 385 390 395 400 405 410 415 420 425 430 435 440 445 450
455 460 465 470 475 480 485 490 495 500 505 510 515 520 525 530 535 540
545 550 555 560 565 570 575 580 585 590 595 600 605 610 615 620 625 630
635 640 645 650 655 660 665 670 675 680 685 690 695 700 705 710 715 720
725 730 735 740 745 750 755 760 765 770 775 780 785 790 795 800 805 810
815 820 825 830 835 840 845 850 855 860 865 870 875 880 885 890 895 900
905 910 915 920 925 930 935 940 945 950 955 960 965 970 975 980 985 990
995 1000    1005    1010    1015    1020    1025    1030    1035
1040    1045    1050    1055    1060    1065    1070    1075    1080
1085    1090    1095    1100];
    realn_a6 = [3.877   3.844   3.824   3.816   3.821   3.836   3.867
3.922   4.002   4.121   4.263   4.383   4.497   4.633   4.771   4.854
4.886   4.832   4.727   4.629   4.531   4.449   4.379   4.317   4.262
4.212   4.167   4.125   4.088   4.053   4.021   3.991   3.964   3.939
3.916   3.895   3.875   3.854   3.833   3.811   3.791   3.772   3.755
3.739   3.724   3.709   3.696   3.683   3.672   3.661   3.653   3.652
3.646   3.626   3.603   3.580   3.557   3.539   3.524   3.509   3.496
3.484   3.472   3.460   3.449   3.439   3.429   3.420   3.412   3.403
3.395   3.388   3.380   3.373   3.367   3.360   3.354   3.348   3.342
3.336   3.330   3.325   3.320   3.315   3.310   3.305   3.300   3.296
3.292   3.287   3.283   3.279   3.275   3.272   3.268   3.264   3.261
3.257   3.254   3.251   3.247   3.244   3.241   3.238   3.235   3.233
3.230   3.227   3.224   3.222   3.219   3.217   3.214   3.212   3.210
3.207   3.205   3.203   3.201   3.199   3.197   3.195   3.193   3.191
3.189   3.187   3.185   3.184   3.182   3.180   3.178   3.177   3.175
3.173   3.172   3.170   3.169   3.167   3.166   3.164   3.163   3.162
3.160   3.159   3.158   3.156   3.155   3.154   3.153   3.151   3.150
3.149   3.148   3.147   3.146   3.144   3.143   3.142   3.141   3.140
3.139];
    imagn_a6 = [1.966   1.944   1.931   1.925   1.927   1.938   1.955
1.985   2.013   2.010   1.982   1.918   1.824   1.718   1.587   1.382
1.131   0.927   0.760   0.649   0.576   0.517   0.475   0.437   0.406
0.378   0.354   0.333   0.314   0.297   0.281   0.266   0.253   0.240
0.228   0.215   0.202   0.188   0.175   0.164   0.155   0.146   0.139
0.131   0.124   0.117   0.110   0.103   0.096   0.091   0.083   0.071
0.056   0.033   0.014   0.007   0.006   0.004   0.004   0.003   0.002
0.001   0.001   0.000   0.000   0.000   0.000   0.000   0.000   0.000
0.000   0.000   0.000   0.000   0.000   0.000   0.000   0.000   0.000
0.000   0.000   0.000   0.000   0.000   0.000   0.000   0.000   0.000
0.000   0.000   0.000   0.000   0.000   0.000   0.000   0.000   0.000
0.000   0.000   0.000   0.000   0.000   0.000   0.000   0.000   0.000
0.000   0.000   0.000   0.000   0.000   0.000   0.000   0.000   0.000
0.000   0.000   0.000   0.000   0.000   0.000   0.000   0.000   0.000
0.000   0.000   0.000   0.000   0.000   0.000   0.000   0.000   0.000
0.000   0.000   0.000   0.000   0.000   0.000   0.000   0.000   0.000
0.000   0.000   0.000   0.000   0.000   0.000   0.000   0.000   0.000
0.000];
    rn_a6 = interp1(wl_a6, realn_a6, lambda, 'pchip');
    in_a6 = interp1(wl_a6, imagn_a6, lambda, 'pchip');
    x = rn_a6 + in_a6;
```

```
end

if mat=='a7'
    % Al0.7Ga0.3As
    wl_a7 = 1e-9*[300   305 310 315 320 325 330 335 340 345 350 355 360
365 370 375 380 385 390 395 400 405 410 415 420 425 430 435 440 445 450
455 460 465 470 475 480 485 490 495 500 505 510 515 520 525 530 535 540
545 550 555 560 565 570 575 580 585 590 595 600 605 610 615 620 625 630
635 640 645 650 655 660 665 670 675 680 685 690 695 700 705 710 715 720
725 730 735 740 745 750 755 760 765 770 775 780 785 790 795 800 805 810
815 820 825 830 835 840 845 850 855 860 865 870 875 880 885 890 895 900
905 910 915 920 925 930 935 940 945 950 955 960 965 970 975 980 985 990
995 1000    1005    1010    1015    1020    1025    1030    1035
1040    1045    1050    1055    1060    1065    1070    1075    1080
1085    1090    1095    1100];
    realn_a7 = [3.947   3.920   3.909   3.911   3.933   3.979   4.057
4.187   4.334   4.462   4.591   4.748   4.881   4.946   4.947   4.854
4.725   4.614   4.512   4.428   4.355   4.292   4.235   4.184   4.138
4.097   4.059   4.024   3.993   3.964   3.938   3.912   3.887   3.861
3.836   3.813   3.791   3.772   3.753   3.736   3.720   3.704   3.691
3.682   3.673   3.661   3.645   3.618   3.589   3.567   3.547   3.529
3.513   3.498   3.484   3.470   3.458   3.446   3.435   3.424   3.414
3.404   3.395   3.386   3.378   3.370   3.362   3.354   3.347   3.340
3.333   3.326   3.320   3.314   3.308   3.302   3.296   3.291   3.286
3.281   3.276   3.271   3.266   3.262   3.258   3.253   3.249   3.245
3.241   3.237   3.234   3.230   3.227   3.223   3.220   3.216   3.213
3.210   3.207   3.204   3.201   3.198   3.196   3.193   3.190   3.188
3.185   3.183   3.180   3.178   3.176   3.173   3.171   3.169   3.167
3.165   3.163   3.161   3.159   3.157   3.155   3.153   3.151   3.149
3.148   3.146   3.144   3.143   3.141   3.139   3.138   3.136   3.135
3.133   3.132   3.130   3.129   3.128   3.126   3.125   3.124   3.122
3.121   3.120   3.119   3.117   3.116   3.115   3.114   3.113   3.112
3.111   3.110   3.108   3.107   3.106   3.105   3.104   3.103   3.102
3.102];
    imagn_a7 = [1.988   1.972   1.966   1.972   1.988   2.021   2.048
2.050   2.022   1.948   1.841   1.720   1.555   1.296   1.028   0.827
0.672   0.575   0.512   0.461   0.423   0.389   0.361   0.337   0.315
0.296   0.278   0.262   0.247   0.233   0.218   0.203   0.187   0.174
0.162   0.152   0.143   0.135   0.126   0.118   0.110   0.102   0.095
0.087   0.077   0.054   0.031   0.018   0.011   0.007   0.006   0.005
0.004   0.003   0.003   0.002   0.002   0.002   0.002   0.002   0.001
0.001   0.001   0.001   0.001   0.001   0.000   0.000   0.000   0.000
0.000   0.000   0.000   0.000   0.000   0.000   0.000   0.000   0.000
0.000   0.000   0.000   0.000   0.000   0.000   0.000   0.000   0.000
0.000   0.000   0.000   0.000   0.000   0.000   0.000   0.000   0.000
0.000   0.000   0.000   0.000   0.000   0.000   0.000   0.000   0.000
0.000   0.000   0.000   0.000   0.000   0.000   0.000   0.000   0.000
0.000   0.000   0.000   0.000   0.000   0.000   0.000   0.000   0.000
0.000   0.000   0.000   0.000   0.000   0.000   0.000   0.000   0.000
```

```
0.000   0.000   0.000   0.000   0.000   0.000   0.000   0.000   0.000
0.000];
    rn_a7 = interp1(wl_a7, realn_a7, lambda, 'pchip');
    in_a7 = interp1(wl_a7, imagn_a7, lambda, 'pchip');
    x = rn_a7 + in_a7;
end

if mat=='a8'
    % Al0.8Ga0.2As
    wl_a8 = 1e-9*[300   305 310 315 320 325 330 335 340 345 350 355 360
365 370 375 380 385 390 395 400 405 410 415 420 425 430 435 440 445 450
455 460 465 470 475 480 485 490 495 500 505 510 515 520 525 530 535 540
545 550 555 560 565 570 575 580 585 590 595 600 605 610 615 620 625 630
635 640 645 650 655 660 665 670 675 680 685 690 695 700 705 710 715 720
725 730 735 740 745 750 755 760 765 770 775 780 785 790 795 800 805 810
815 820 825 830 835 840 845 850 855 860 865 870 875 880 885 890 895 900
905 910 915 920 925 930 935 940 945 950 955 960 965 970 975 980 985 990
995 1000    1005    1010    1015    1020    1025    1030    1035
1040    1045    1050    1055    1060    1065    1070    1075    1080
1085    1090    1095    1100];
    realn_a8 = [4.014   3.991   3.999   4.035   4.109   4.250   4.415
4.558   4.700   4.868   5.020   5.031   4.954   4.835   4.683   4.563
4.464   4.380   4.308   4.245   4.189   4.138   4.093   4.053   4.016
3.983   3.953   3.920   3.888   3.859   3.832   3.807   3.784   3.763
3.743   3.725   3.709   3.700   3.688   3.662   3.631   3.603   3.576
3.554   3.533   3.514   3.498   3.482   3.467   3.453   3.440   3.427
3.415   3.404   3.393   3.383   3.373   3.363   3.354   3.345   3.336
3.328   3.320   3.313   3.305   3.298   3.291   3.285   3.279   3.273
3.267   3.261   3.255   3.250   3.245   3.240   3.235   3.230   3.226
3.221   3.217   3.212   3.208   3.204   3.200   3.197   3.193   3.189
3.186   3.183   3.179   3.176   3.173   3.170   3.167   3.164   3.161
3.158   3.155   3.153   3.150   3.147   3.145   3.142   3.140   3.138
3.135   3.133   3.131   3.129   3.127   3.125   3.123   3.121   3.119
3.117   3.115   3.113   3.111   3.110   3.108   3.106   3.105   3.103
3.101   3.100   3.098   3.097   3.095   3.094   3.092   3.091   3.090
3.088   3.087   3.086   3.084   3.083   3.082   3.081   3.079   3.078
3.077   3.076   3.075   3.074   3.073   3.071   3.070   3.069   3.068
3.067   3.066   3.065   3.064   3.063   3.063   3.062   3.061   3.060
3.059];
    imagn_a8 = [2.012   2.008   2.018   2.052   2.085   2.087   2.056
1.980   1.859   1.680   1.453   1.169   0.876   0.690   0.576   0.494
0.445   0.403   0.369   0.340   0.315   0.293   0.274   0.257   0.240
0.222   0.205   0.188   0.172   0.160   0.149   0.139   0.129   0.120
0.111   0.102   0.093   0.080   0.063   0.040   0.020   0.012   0.008
0.007   0.006   0.005   0.005   0.004   0.004   0.004   0.003   0.003
0.002   0.002   0.002   0.001   0.001   0.001   0.000   0.000   0.000
0.000   0.000   0.000   0.000   0.000   0.000   0.000   0.000   0.000
0.000   0.000   0.000   0.000   0.000   0.000   0.000   0.000   0.000
0.000   0.000   0.000   0.000   0.000   0.000   0.000   0.000   0.000
0.000   0.000   0.000   0.000   0.000   0.000   0.000   0.000   0.000
0.000   0.000   0.000   0.000   0.000   0.000   0.000   0.000   0.000
```

```
0.000   0.000   0.000   0.000   0.000   0.000   0.000   0.000   0.000
0.000   0.000   0.000   0.000   0.000   0.000   0.000   0.000   0.000
0.000   0.000   0.000   0.000   0.000   0.000   0.000   0.000   0.000
0.000   0.000   0.000   0.000   0.000   0.000   0.000   0.000   0.000
0.000   0.000   0.000   0.000   0.000   0.000   0.000   0.000   0.000
0.000];
    rn_a8 = interp1(wl_a8, realn_a8, lambda, 'pchip');
    in_a8 = interp1(wl_a8, imagn_a8, lambda, 'pchip');
    x = rn_a8 + in_a8;
end

if mat=='a9'
    % Al0.9Ga0.1As
    wl_a9 = 1e-9*[300   305 310 315 320 325 330 335 340 345 350 355 360
365 370 375 380 385 390 395 400 405 410 415 420 425 430 435 440 445 450
455 460 465 470 475 480 485 490 495 500 505 510 515 520 525 530 535 540
545 550 555 560 565 570 575 580 585 590 595 600 605 610 615 620 625 630
635 640 645 650 655 660 665 670 675 680 685 690 695 700 705 710 715 720
725 730 735 740 745 750 755 760 765 770 775 780 785 790 795 800 805 810
815 820 825 830 835 840 845 850 855 860 865 870 875 880 885 890 895 900
905 910 915 920 925 930 935 940 945 950 955 960 965 970 975 980 985 990
995 1000    1005    1010    1015    1020    1025    1030    1035
1040    1045    1050    1055    1060    1065    1070    1075    1080
1085    1090    1095    1100];
    realn_a9 = [4.1 4.160   4.258   4.433   4.636   4.824   4.989
5.128   5.184   5.056   4.868   4.713   4.574   4.465   4.376   4.297
4.229   4.170   4.117   4.071   4.029   3.987   3.947   3.910   3.875
3.844   3.816   3.789   3.765   3.748   3.729   3.702   3.670   3.636
3.602   3.574   3.549   3.526   3.505   3.485   3.467   3.450   3.434
3.419   3.405   3.391   3.379   3.366   3.355   3.343   3.332   3.322
3.312   3.303   3.294   3.285   3.277   3.269   3.261   3.254   3.247
3.240   3.233   3.227   3.220   3.214   3.208   3.203   3.197   3.192
3.187   3.182   3.177   3.172   3.167   3.163   3.158   3.154   3.150
3.146   3.142   3.139   3.135   3.131   3.128   3.124   3.121   3.118
3.115   3.112   3.109   3.106   3.103   3.100   3.097   3.095   3.092
3.090   3.087   3.085   3.082   3.080   3.078   3.076   3.074   3.071
3.069   3.067   3.065   3.063   3.061   3.060   3.058   3.056   3.054
3.052   3.051   3.049   3.047   3.046   3.044   3.043   3.041   3.040
3.038   3.037   3.036   3.034   3.033   3.031   3.030   3.029   3.028
3.026   3.025   3.024   3.023   3.022   3.020   3.019   3.018   3.017
3.016   3.015   3.014   3.013   3.012   3.011   3.010   3.009   3.008
3.007   3.006   3.005   3.005   3.004   3.003   3.002   3.001   3.000
3.000];
    imagn_a9 = [2.1 2.173   2.197   2.173   2.100   1.985   1.799
1.477   1.130   0.849   0.629   0.515   0.451   0.399   0.362   0.329
0.303   0.279   0.258   0.238   0.218   0.197   0.178   0.164   0.151
0.139   0.127   0.116   0.104   0.093   0.078   0.051   0.026   0.016
0.012   0.009   0.007   0.006   0.006   0.005   0.005   0.004   0.004
0.004   0.003   0.003   0.003   0.002   0.002   0.002   0.002   0.002
0.002   0.002   0.001   0.001   0.001   0.001   0.001   0.001   0.001
0.001   0.001   0.001   0.000   0.000   0.000   0.000   0.000   0.000
0.000   0.000   0.000   0.000   0.000   0.000   0.000   0.000   0.000
```

```
0.000   0.000   0.000   0.000   0.000   0.000   0.000   0.000   0.000
0.000   0.000   0.000   0.000   0.000   0.000   0.000   0.000   0.000
0.000   0.000   0.000   0.000   0.000   0.000   0.000   0.000   0.000
0.000   0.000   0.000   0.000   0.000   0.000   0.000   0.000   0.000
0.000   0.000   0.000   0.000   0.000   0.000   0.000   0.000   0.000
0.000   0.000   0.000   0.000   0.000   0.000   0.000   0.000   0.000
0.000   0.000   0.000   0.000   0.000   0.000   0.000   0.000   0.000
0.000   0.000   0.000   0.000   0.000   0.000   0.000   0.000   0.000
0.000];
    rn_a9 = interp1(wl_a9, realn_a9, lambda, 'pchip');
    in_a9 = interp1(wl_a9, imagn_a9, lambda, 'pchip');
    x = rn_a9 + in_a9;
end

if mat=='af'
    % AlAs
    wl_af = 1e-9*[300   305 310 315 320 325 330 335 340 345 350 355 360
365 370 375 380 385 390 395 400 405 410 415 420 425 430 435 440 445 450
455 460 465 470 475 480 485 490 495 500 505 510 515 520 525 530 535 540
545 550 555 560 565 570 575 580 585 590 595 600 605 610 615 620 625 630
635 640 645 650 655 660 665 670 675 680 685 690 695 700 705 710 715 720
725 730 735 740 745 750 755 760 765 770 775 780 785 790 795 800 805 810
815 820 825 830 835 840 845 850 855 860 865 870 875 880 885 890 895 900
905 910 915 920 925 930 935 940 945 950 955 960 965 970 975 980 985 990
995 1000    1005    1010    1015    1020    1025    1030    1035
1040    1045    1050    1055    1060    1065    1070    1075    1080
1085    1090    1095    1100];
    realn_af = [4.434   4.673   4.902   5.153   5.326   5.252   5.068
4.878   4.679   4.535   4.425   4.329   4.249   4.180   4.121   4.065
4.012   3.963   3.918   3.878   3.842   3.810   3.781   3.753   3.723
3.680   3.634   3.598   3.566   3.537   3.510   3.486   3.464   3.443
3.424   3.406   3.389   3.373   3.357   3.343   3.329   3.316   3.304
3.292   3.281   3.270   3.260   3.250   3.240   3.231   3.222   3.213
3.205   3.197   3.190   3.182   3.175   3.168   3.161   3.155   3.149
3.143   3.137   3.131   3.126   3.121   3.116   3.111   3.106   3.102
3.097   3.093   3.089   3.084   3.080   3.077   3.073   3.069   3.066
3.062   3.059   3.055   3.052   3.049   3.046   3.043   3.040   3.037
3.035   3.032   3.029   3.027   3.024   3.022   3.019   3.017   3.015
3.013   3.010   3.008   3.006   3.004   3.002   3.000   2.998   2.996
2.994   2.993   2.991   2.989   2.987   2.986   2.984   2.983   2.981
2.979   2.978   2.976   2.975   2.974   2.972   2.971   2.970   2.968
2.967   2.966   2.964   2.963   2.962   2.961   2.960   2.958   2.957
2.956   2.955   2.954   2.953   2.952   2.951   2.950   2.949   2.948
2.947   2.946   2.945   2.944   2.943   2.943   2.942   2.941   2.940
2.939   2.938   2.938   2.937   2.936   2.935   2.935   2.934   2.933
2.932];
    imagn_af = [2.307   2.241   2.081   1.819   1.485   1.083   0.714
0.535   0.456   0.389   0.349   0.313   0.285   0.259   0.235   0.210
0.186   0.168   0.152   0.137   0.123   0.110   0.095   0.068   0.039
0.024   0.016   0.011   0.009   0.007   0.007   0.006   0.006   0.005
0.005   0.005   0.005   0.004   0.004   0.004   0.003   0.003   0.003
```

```
0.003   0.002   0.002   0.002   0.002   0.001   0.001   0.001   0.001
0.001   0.000   0.000   0.000   0.000   0.000   0.000   0.000   0.000
0.000   0.000   0.000   0.000   0.000   0.000   0.000   0.000   0.000
0.000   0.000   0.000   0.000   0.000   0.000   0.000   0.000   0.000
0.000   0.000   0.000   0.000   0.000   0.000   0.000   0.000   0.000
0.000   0.000   0.000   0.000   0.000   0.000   0.000   0.000   0.000
0.000   0.000   0.000   0.000   0.000   0.000   0.000   0.000   0.000
0.000   0.000   0.000   0.000   0.000   0.000   0.000   0.000   0.000
0.000   0.000   0.000   0.000   0.000   0.000   0.000   0.000   0.000
0.000   0.000   0.000   0.000   0.000   0.000   0.000   0.000   0.000
0.000   0.000   0.000   0.000   0.000   0.000   0.000   0.000   0.000
0.000   0.000   0.000   0.000   0.000   0.000   0.000   0.000   0.000
0.000];
    rn_af = interp1(wl_af, realn_af, lambda, 'pchip');
    in_af = interp1(wl_af, imagn_af, lambda, 'pchip');
    x = rn_af + in_af;
end


if mat=='in'
% In(x)Ga(1-x)As
    rn_InxGaAs = zeros(size(lambda));
    in_InxGaAs = rn_InxGaAs;

    for ctr = 1:length(lambda)


    % GaAs n-k data (from luxpop.com): S. Zollner, "Optical constants
    % and critical-point parameters of GaAs from 0.73 to 6.60 eV", J.
Appl. Phys., Vol. 90, No. 1, 1 July 2001, pp. 515-517.
    realn_RGaAs(1,:) = 1e-9*[200 210 220 230 240 245 250 255 260 270
280 290 300 310 320 330 340 350 360 370 380 390 400 420 440 460 480 500
520 540 560 580 600 650 700 750 800 810 820 830 840 845 850 900 1000
1100 1200 1300 1400 1500 1600 1700 1800 1900 2000 1000000];
    realn_RGaAs(2,:) = [1.323 1.298 1.373 1.512 1.788 2.137 2.686 3.253
3.645 3.98 4.142 4.039 3.844 3.694 3.613 3.576 3.57 3.592 3.642 3.726
3.869 4.102 4.443 4.818 4.995 4.698 4.465 4.304 4.183 4.087 4.013 3.953
3.904 3.813 3.756 3.703 3.664 3.659 3.653 3.648 3.644 3.642 3.631 3.59
3.509 3.464 3.433 3.41 3.393 3.379 3.369 3.36 3.352 3.346 3.341 3.341];
    imagn_RGaAs(1,:) = 1e-9*[200 210 220 230 240 245 250 255 260 270
280 290 300 310 320 330 340 350 360 370 380 390 400 420 440 460 480 500
520 540 560 580 600 650 700 750 800 810 820 830 840 845 850 900 1000
1100 1200 1300 1400 1500 1600 1700 1800 1900 2000 1000000];
    imagn_RGaAs(2,:) = [2.438 2.649 2.917 3.247 3.741 4.048 4.196 4.062
3.741 3.164 2.62 2.171 1.952 1.872 1.862 1.878 1.907 1.95 2.004 2.072
2.158 2.2 2.093 1.762 1.059 0.622 0.471 0.385 0.326 0.286 0.259 0.236
0.217 0.18 0.145 0.111 0.089 0.085 0.081 0.074 0.061 0.055 0 0 0 0 0 0
0 0 0 0 0 0 0 0 ];
    rn_RGaAs = interp1(realn_RGaAs(1,:), realn_RGaAs(2,:), lambda(ctr),
'pchip');
```

```
    in_RGaAs = j*interp1(imagn_RGaAs(1,:), imagn_RGaAs(2,:),
lambda(ctr), 'pchip');



    % InAs n-k data (from luxpop.com): S. Adachi, "Model dielectric
    % constants of Gap, GaAs, GaSb, InP, InAs, and InSb," Phys. Rev. B
Vol. 35, No. 14, 15 May, 1987, pp. 7454-7463.
    realn_RInAs(1,:) = 1e-9*[210 220 230 240 250 260 270 280 290 300
310 320 330 340 350 400 450 490 500 510 520 530 550 600 650 700 750 800
850 900 950 1000 1050 1100 1200 1300 1400 1500 1600 1700 1800 1900 2000
2500 3000 3000.1 1000000];
    realn_RInAs(2,:) = [1.399 1.311 1.387 1.507 1.574 1.793 2.472 3.53
3.581 3.356 3.249 3.149 3.088 3.043 3.011 3.042 3.637 4.426 4.597 4.533
4.471 4.405 4.295 4.076 3.916 3.841 3.812 3.775 3.752 3.724 3.691 3.646
3.612 3.596 3.569 3.545 3.528 3.527 3.522 3.516 3.508 3.497 3.488 3.469
3.515 3.515 3.515];
    imagn_RInAs(1,:) = 1e-9*[210 220 230 240 250 260 270 280 290 300
310 320 330 340 350 400 450 490 500 510 520 530 550 600 650 700 750 800
850 900 950 1000 1050 1100 1200 1300 1400 1500 1600 1700 1800 1900 2000
2500 3000 3000.1 1000000];
    imagn_RInAs(2,:) = [2.11 2.26 2.5 2.72 3.01 3.33 3.22 3.03 2.11
1.71 1.66 1.68 1.69 1.71 1.73 1.86 1.89 1.55 1.45 1.29 1.15 1.04 0.85
0.67 0.54 0.52 0.47 0.42 0.4 0.36 0.33 0.3 0.29 0.28 0.26 0.24 0.22 0.2
0.18 0.17 0.17 0.16 0.16 0.13 0.09 0 0 ];
    rn_RInAs = interp1(realn_RInAs(1,:), realn_RInAs(2,:), lambda(ctr),
'pchip');
    in_RInAs = j*interp1(imagn_RInAs(1,:), imagn_RInAs(2,:),
lambda(ctr), 'pchip');



    conc=[0.0 1.0];
    rnx=[rn_RGaAs rn_RInAs];
    inx=[in_RGaAs in_RInAs];
    rn_InxGaAs(ctr) = interp1(conc, rnx, mf, 'linear');
    in_InxGaAs(ctr) = interp1(conc, inx, mf, 'linear');


    end

    x = rn_InxGaAs + in_InxGaAs;
end
```

References

"Electric Aircraft," accessed 11 February 2012 from http://en.wikipedia.org/wiki/Electric_aircraft.

"PC1D," http://www.pv.unsw.edu.au/info-about/our-school/products-services/pc1d. Accessed 5 February, 2012.

"UFM/Mauro Solar Riser," accessed 11 February 2012 from http://www.airventuremuseum.org/collection/aircraft/UFM-Mauro%20Solar%20Riser.asp

Adams, J.G.J., W. Elder, G. Hill, J.S. Roberts, K.W.J. Barnham and N.J. Ekins-Daukes, *Proc. SPIE* **7597***,* 759705 (2010).

Ahrenkiel, R.K. and M.S. Lundstrom, *Minority Carriers in III-V Semiconductors: Physics and Applications*. (Academic Press, 2003).

Alemu, A., J. A. H. Coaquira, and A. Freundlich, *J. Appl. Phys*. **99**, 084506 (2006).

Alemu, A., J.A.H. Coaquira and A. Freundlich, *J. Appl. Phys*. **99**, 084506 (2006).

Annual Energy Review, US Energy Information Administration (2011).

Araujo, G.L. and A. Martí, *Solar Energy Mater. and Solar Cells* **33**, 213 (1994).

Araujo, G.L., A. Martí, F.W. Ragay and J.H. Wolter, *Proc. 12th European Communities Solar Energy Conf.* p. 1481 (1994).

Araujo, G.L. and A. Martí, *Appl. Phys. Lett.* **66**, 894 (1995).

Bailey, C.G., D.V. Forbes, R.P. Raffaelle and S.M. Hubbard, *Appl. Phys. Lett.* **98**, 163105 (2011).

Barnham, K.W.J. and G. Duggan, *J. Appl. Phys.* **67**, 3490 (1990).

Barnham, K.W.J. and G. Duggan, *J. Appl. Phys*. **67**, 3490 (1990).

Barnham, K., I. Ballard, J. Barnes, J. Connolly, P. Griffin, B. Kluftinger, J. Nelson, I. Tsui and A. Zachariou, *Appl. Surf. Sci.* **113-114**, 722 (1997).

Bauhuis, G.J., P. Mulder, J.J. Schermer, E.J. Haverkamp, J. van Deelen and P.K. Larsen, *Proc. 20th European Photovolt. Solar Energy Conf.* , Barcelona, p.468 (June 2005).

Bauhuis, G.J., P. Mulder, J.J. Schermer, E.J. Haverkamp, J. van Deelen and P.K. Larsen, *Proc. 20th European Photovolt. Solar Energy Conf.*, p.468 (2005).

Bauhuis, G.J., P. Mulder, E.J. Haverkamp, J.C.C.M. Huijben and J.J. Schermer, *Solar Energy Mater. Solar Cells* **93**, 1488 (2009).

Braslau, N., J.B. Gunn and J.L. Staples, *Solid State Electron.* **10**, 381 (1967).

Bremner, S.P., R. Corkish and C.B. Honsberg, *IEEE Trans. Elec. Devices* **46**, 1932 (1999).

Brewer, S.H., W.R. Glomm, M.C. Johnson, M.K. Knag and S. Franzen, *Langmuir* **21**, 9303 (2005).

Bushnell, D.B., T.N.D. Tibbits, K.W.J. Barnham, J.P. Connolly, M. Mazzer, N.J. Ekins-Daukes, J.S. Roberts, G. Hill and R. Airey, *J. Appl. Phys.* **97**, 124908 (2005).

Carter-Coman, C., R. Bicknell-Tassius, R.G. Benz, A.S. Brown and N.M. Jokerst, *J. Electrochem. Soc.* **144**, L29 (1997).

Casey Jr., H.C., B.I. Miller and E. Pinkas, *J. Appl. Phys.* **44**, 3 (1973).

Chang, K.H., P.K. Bhattacharya and R. Gibala, *J. Appl. Phys.* **66**, 2993 (1989).

Chen, Y.C., P.K. Bhattacharya and J. Singh, *J. Vac. Sci. Tech. B* **10**, 769 (1992).

Cheng, J. and N.K. Dutta, eds., *Vertical-cavity Surface-emitting Lasers: Technology and Applications*, p. 302 (Overseas Publishers, 2000).

Cowell, A., "Solar-Powered Planes Flies for 26 Hours." *New York Times*, 8 July 2010.

Cox, R.H. and H. Strack, *Solid State Electron.* **10**, 1213 (1967).

Dahal, R., B. Pantha, J. Li, J.Y. Lin, and H.X. Jiang, *Appl. Phys. Lett*. **94**, 063505 (2009).

Derkacs, D., W.V. Chen, P.M. Matheu, S.H. Lim, P.K.L. Yu, and E.T. Yu, *Appl. Phys. Lett*. **93**, 091107 (2008).

Derkacs, D., Ph.D. thesis, Univ. of California, San Diego (2009).

Dries, J.G., M.R. Gokhale and S.R. Forrest, *Appl. Phys. Lett.* **74**, 2581 (1999).

Ekins-Daukes, N.J., K.W.J. Barnham, J.P. Connolly, J.S. Roberts, J.C. Clark, G. Hill and M. Mazzer, *Appl. Phys. Lett.* **75**, 4195 (1999).

Ekins-Daukes, N.J., J. Barnes, K.W.J. Barnham, J.P. Connolly, M. Mazzer, J.C. Clark, R. Grey, G. Hill, M. Pate and J.S. Roberts, *Solar Energy Mater. and Solar Cells* **68**, 71 (2001).

Ekins-Daukes, N.J., D.B. Bushnell, J.P. Connolly, K.W.J. Barnham, M. Mazzer, J.S. Roberts, G. Hill and R. Airey, *Physica E* **14**, 132 (2002).

Emery, K., *Handbook of Photovoltaic Science and Engineering (2nd ed.)*, ed. A. Luque and S. Hegedus, Ch. 18 (Wiley, 2011).

Fobelets, K., R. Vounckx and G. Borgs, *J. Micromech. Microeng.* **4**, 123 (1994).

Fry, P.W., J.J. Finley, L.R. Wilson, A. Lemaitre, D.J. Mowbray, M.S. Skolnick, M. Hopkinson, G. Hill and J.C. Clark, *Appl. Phys. Lett.* **77**, 4344 (2000).

Goldberg, D.E., *Genetic Algorithms in Search, Optimization, and Machine Learning* (Addison-Wesley, 1989).

Green, M.A., K. Emery, Y. Hishikawa, W. Warta and E.D. Dunlop, *Prog. Photovolt:. Res. Appl.* **19**, 565 (2011).

Gunapala, S.D., S.V. Bandara, C.J. Hill, D.Z. Ting, J.K. Liu, S.B. Rafol, E.R. Blazejewski, J.M. Mumolo, S.A. Keo, S. Krishna, Y.-C. Chang, and C.A. Shott, *IEEE J. Quantum Electronics* **43**, 230 (2007).

Han, W.Y., *et al*. *J. Appl. Phys.* **74**, 754 (1993).

Hegedus, S. and A. Luque, *Handbook of Photovoltaic Science and Engineering (2 ed.)* (Wiley, 2011) p. 6.

Henry, C.H., *J. Appl. Phys.* **51**, 4494 (1980).

Höglund, L., C. Asplund, Q. Wang, S. Almqvist, H. Malm, E. Petrini, J. Y. Andersson, P. O. Holtz, and H. Pettersson, *Appl. Phys. Lett*. **88**, 213510 (2006).

Houghton, D.C., *J. Appl. Phys.* **70**, 2136 (1991).

Hu, D., C.O. McPheeters, E.T. Yu and D.M. Schaadt, *Nanoscale. Res. Lett.* **6**, 83 (2011).

Hubbard, S.M., C.D. Cress, C.G. Bailey, R.P. Raffaelle, S.G. Bailey and D.M. Wilt, *Appl. Phys. Lett.* **92**, 123512 (2008).

Hwang, C.J., *J. Appl. Phys.* **40**, 3731 (1969).

Johnson, H.T., V. Nguyen, and A.F. Bower, *J. Appl. Phys*. **92**, 4653 (2002).

King, R.R., J.H. Ermer, D.E. Joslin, M. Haddad, J.W. Eldredge, N.H. Karam, B. Keyes and R.K. Ahrenkiel, *Proc. 2nd World Conf. Photovolt. Solar Ener. Conversion*, Vienna, Austria, p. 86 (1998).

Laghumavarapu, R.B., M. El-Emawy, N. Nuntawong, A. Moscho, L.F. Lester and D.L. Huffaker, *Appl. Phys. Lett.* **91**, 243115 (2007).

Lazzarini, L., L. Nasi, C.E. Norman, G. Salviati and S. Bertoni, *J. Cryst. Growth* **126**, 133 (1993).

Lee, C.C., C.Y. Wang and G. Matijasevic, *IEEE Trans. Comp., Hybrids, Manuf. Technol.* **16**, 311 (1993).

Lee, K., K.-T. Shiu, J.D. Zimmerman, C.K. Renshaw and S.R. Forrest, *Appl. Phys. Lett.* **97**, 101107 (2010).

Li, L., *J. Opt. Soc. Am. A*. **13**, 1870 (1996).

Li, L., *J. Opt. Soc. Am. A*. **14**, 2758 (1997).

Lim, S.H., W. Mar, P. Matheu, D. Derkacs, and E.T. Yu, *J. Appl. Phys*. **101**, 104309 (2007).

Lin, A.S., W. Wang and J.D. Phillips, *J. Appl. Phys.* **105**, 064512 (2009).

Lin, H.-C., S. Senanayake, K.-Y. Cheng, M. Hong, J.R. Kwo, B. Yang and J.P. Mannaerts, *IEEE Trans. Elec. Dev.* **50**, 880 (2003).

Luque, A. and A. Martí, *Phys. Rev. Lett.* **78**, 5014 (1997).

Luque, A., A. Martí and A.J. Nozik *MRS Bulletin* **32**, 236 (2007).

Ma, L.L., Y.C. Zhou, N. Jiang, X. Lu, J. Shao, W. Lu, J. Ge, X.M. Ding, and X.Y. Hou, *Appl. Phys. Lett*. **88**, 171907 (2006).

Martí, A., L. Cuadra, and A. Luque, *Proc. 28th Photovolt. Spec. Conf.* ,p.940 (2000).

Matthews, J.W. and A.E. Blakeslee, *J. Cryst. Growth* **27**, 118 (1974).

Merzbacher, E., *Quantum Mechanics (3 ed.)* (Wiley, 1997).

Metzger, W.K., D. Albin, D. Levi, P. Sheldon, X. Li, B.M. Keyes and R.K. Ahrenkiel, *J. Appl. Phys.* **94**, 3549 (2003).

Mialhe, P., J.P. Charles, A. Khoury and G. Bordure, *J. Phys. D.: Appl. Phys.* **19**, 483 (1986).

Miska, P., J. Even, C. Paranthoen, O. Dehaese, A. Jbeli, M. Senes, and X. Marie, *Appl. Phys. Lett*. **86**, 111905 (2005).

Mohaidat, J.M., K. Shum, W. B. Wang, and R. R. Alfano, *J. Appl. Phys.* **76**, 5533 (1994).

Moharam, M.G. and T.K. Gaylord, *J. Opt. Soc. Am. A.* **3**, 1780 (1986).

Monte, A.F.G., F. Qu and M. Hopkinson, *Appl. Phys. Lett*. **92**, 182102 (2008).

Morgan, S.P. and D.V. Morgan, *Semicond. Sci. Technol.* **9**, 2278 (1994).

Nozik, A.J., *Chem. Phys. Lett*. **457**, 3 (2008).

Okamoto, H. and T.B. Massalski, *Binary Alloy Phase Diagrams*, ed. T.B. Massalski, pp. 381-383 (ASM International, 1990).

Oshima, R., A. Takata, and Y. Okada, *Appl. Phys. Lett*. **93**, 083111 (2008)

Parker, E.H.C., ed., *The Technology and Physics of Molecular Beam Epitaxy* (Springer, 1985).

Petit, R., *Electromagnetic Theory of Gratings*, p. 174 (Springer-Verlag, 1989).

Polyakov, A.Y., *et al.*, *J. Elec. Mater.* **30**, 147 (2001).

Popescu, V., G. Bester, M.C. Hanna, A.G. Norman and A. Zunger *Phys. Rev. B* **78**, 205321 (2008).

Press, W.H., S.A. Teukolsky, W.T. Vetterling and B.P. Flannery, *Numerical Recipes in C*, 2 ed. (Cambridge University Press, 1995).

Ptak, A.J., D.J. Friedman and S. Kurtz, *J. Vac. Sci. Tech. B* **25**, 955 (2007).

Riordan, C. and R. Hulstron, *Record of 21st IEEE PV Spec. Conf.*, 1085 (1990).

RSoft Design Group, *DiffractMOD User Guide (v. 3.2)*, p.39 (2011).

Sambur, J.B., T. Novet and B.A. Parkinson, *Science* **330**, 63 (2010).

Schermer, J.J., P. Mulder, G.J. Bauhuis, M.M.A.J. Voncken, J. van Deelen, E. Haverkamp and P.K. Larsen, *Phys. Stat. Sol. (a)* **202**, 501 (2005)

Schubert, E.F., *Light-Emitting Diodes* (Cambridge Univ. Press, 2003).

Serdiukova, I., C. Monier, M.F. Viela and A. Freundlich, *Appl. Phys. Lett*. **74**, 2812 (1999).

Shahrjerdi, D., *et al.*, *Appl. Phys. Lett.* **100**, 053901 (2012).

Shockley, W. and H.J. Queisser *J. Appl. Phys.* **32,** 510 (1961).

Smith, J. M., P. A. Dalgarno, B. Urbaszek, E. J. McGhee, G. S. Buller, G. J. Nott, R. J. Warburton, J. M. Garcia, W. Schoenfeld, and P. M. Petroff, *Appl. Phys. Lett.* **82**, 3761 (2003).

Snider, G., *1D Poisson*, http://www.nd.edu/~gsnider/. Accessed 7 August 2011.

Soller, B.J. and D.G. Hall, *J. Opt. Soc. Am. A* **18**, 2577 (2001).

Stuart, H.R. and D.G. Hall, *Appl. Phys. Lett.* **69**, 2327 (1996).

Stuart, H.R. and D.G. Hall, *Appl. Phys. Lett.* **73**, 3815 (1998).

Tseng, M.-C., R.-H. Horng, Y.-L. Tsai, D.-S. Wuu and H.-H. Yu, *IEEE Elec. Dev. Lett.* **30**, 940 (2009).

Valdivia, C.E., *et al.*, *Proc. 35th IEEE Photovolt. Spec. Conf.* p. 001253 (2010).

Vigil, E. and P. Diaz, *Crystal Res. and Tech.* **19**, 285 (1984).

Walters, R.J., *et al.*, *Proc. 37th IEEE Photovolt. Spec. Conf.* **3**, 150 (2011).

Wang, T.B., Z.Z. Shen, R.Q. Ye, X.M. Xie, F. Subhan and J. Freytag, *J. Elec. Mater.* **29**, 443 (2000).

Wei, G. and S.R. Forrest, *Nano Lett.* **7**, 218 (2007).

Wei, G., K.-T. Shiu, N.C. Giebink, and S.R. Forrest, *Appl. Phys Lett*. **91**, 223507 (2007).

Welser, R.E., *et al.*, *Proc. SPIE* **8111**, 8111-01 (2011).

Wheeldon, J.F., et al., *Proc. SPIE* **7750**, 77502Q-1 (2010).

Yablonovitch, E., *J. Opt. Soc. Am.* **72**, 899 (1982).

Wheeldon, J.F., et al., *AIP Conf. Proc.* **1407**, 220 (2011).

Yablonovitch, E., T. Sands, D.M. Hwang, I. Schnitzer, T.J. Gmitter, S.K. Shastry, D.S. Hill and J.C.C. Fan, *Appl. Phys. Lett.* **59**, 3159 (1991).

Yazawa, Y., K. Tamura, S. Watahiki, T. Kitatani, J. Minemura and T. Warabisako, *Solar Energy Materials and Solar Cells* **50**, 229 (1998).

Yu, Z., A. Raman and S. Fan, arXiv:1004.2902v2 [physics.optics] (2010). http://arxiv.org/abs/1004.2902v2. Accessed 29 February 2012.

Yu, Z., A. Raman and S. Fan, *Opt. Express* **18**, A366 (2010).

Zhao, R., W.S. Lau, T.C. Chong and M.F. Li, *Jpn. J. Appl. Phys.* **35**, 22 (1996).

Zhao, J., A. Wang, M. A. Green, and F. Ferrazza, *Appl. Phys. Lett*. **73**, 1991 (1998).

Zou, J., D.J.H. Cockayne and B.F. Usher, *J. Appl. Phys.* **73**, 629 (1993).